Institut für Wasserbau · Universität Stuttgart

Mitteilungen

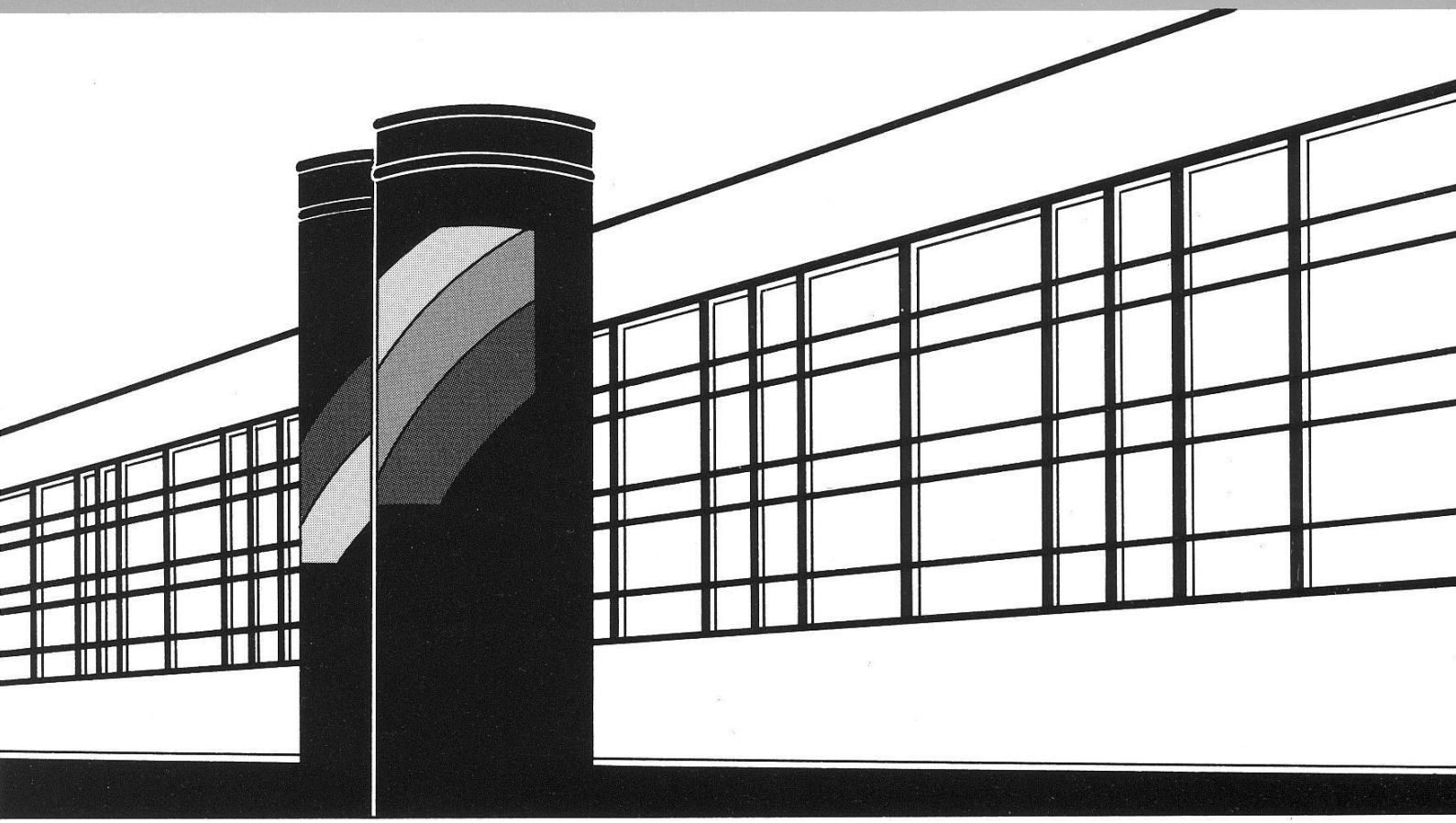

Heft 182 Andreas Kopp

Evaluation of CO_2 Injection Processes in Geological Formations for Site Screening

Evaluation of CO_2 Injection Processes in Geological Formations for Site Screening

Von der Fakultät Bau- und Umweltingenieurwissenschaften der Universität Stuttgart
zur Erlangung der Würde eines Doktors der
Ingenieurwissenschaften (Dr.-Ing.) genehmigte Abhandlung

Vorgelegt von

Andreas Kopp

aus Furtwangen

Hauptberichter:	Prof. Dr.-Ing. Rainer Helmig
Nebenberichter:	Prof. Dr. rer. nat. Christoph Clauser (RWTH Aachen)
Nebenberichter:	Prof. Dr. Helge Dahle (University of Bergen, Norway)

Tag der mündlichen Prüfung: 28.5.2009

Institut für Wasserbau
Lehrstuhl für Hydromechanik und Hydrosystemmodellierung
Universität Stuttgart

2009

Heft 182

Evaluation of CO_2 Injection Processes in Geological Formations for Site Screening

von
Dr.-Ing.
Andreas Kopp

Eigenverlag des Instituts für Wasserbau der Universität Stuttgart

D93 Evaluation of CO_2 Injection Processes in Geological Formations for Site Screening

Kopp, Andreas:

Evaluation of CO_2 Injection Processes in Geological Formations for Site Screening – / von Andreas Kopp. Institut für Wasserbau, Universität Stuttgart. - Stuttgart: Inst. für Wasserbau der Univ., 2009

(Mitteilungen / Institut für Wasserbau, Universität Stuttgart ; H. 182)
Zugl.: Stuttgart, Univ., Diss., 2009
ISBN 978-3-933761-86-6
NE: Institut für Wasserbau < Stuttgart >: Mitteilungen

Herausgegeben 2009 vom Eigenverlag des Instituts für Wasserbau, Universität Stuttgart
Druck: Document Center S. Kästl, Ostfildern

Danksagung

Ich möchte mich an dieser Stelle bei all den Personen bedanken, die zum Gelingen dieser Arbeit beigetagen haben.

Zuerst möchte ich mich bei meinem Hauptberichter Rainer Helmig bedanken. Er gab mir die Chance nach einjähriger beruflicher Tätigkeit an die Universität zurückzukehren und die Vorzüge einer unabhängigen Forschungsarbeit zu genießen. Die große Freiheit die er mir dabei gewährte und die konsequente Rückendeckung die ich permanent erfahren durfte waren ein großer Ansporn für mich und Grundlage für die Freude bei der Arbeit. Seine fundierte Fachkenntnis, die zahlreichen Kontakte zu anderen Forschungseinrichtungen und Institutionen die er mir vermittelte und die fortwährende Leidenschaft und Motivation die fachlichen Probleme zu lösen, haben diese Arbeit maßgeblich positiv beeinflusst. Bei Prof. Christoph Clauser (Aachen) und Prof. Helge Dahle (Bergen) möchte ich mich für die Übernahme der Mitberichte bedanken.

Mein besonderer Dank gilt Holger Class, der mir ständig mit fachlichen Ratschlägen und Problemlösungen den richtigen Weg gezeigt hat. Seine Ruhe und Besonnenheit in schwierigen Zeiten waren Grundpfeiler für die Durchführung der Arbeit. Unsere zahlreichen Reisen zu Konferenzen, Workshops, Tagungen, etc. waren nicht nur lehrreich, sondern haben auch viel Spaß gemacht.

Herzlicher Dank geht an meine Mitarbeiter am Institut für Wasserbau und insbesondere an die Kollegen am Lehrstuhl für Hydromechanik und Hydrosystemmodellierung. Es herrschte immer eine sehr gute Stimmung die sich teilweise im Privaten fortsetzte.

Besonders erwähnen möchte ich hierbei:

- Steffen Ochs, Anozie Ebigbo, Andreas Bielinski und Ulrich Ölmann, die mich auf dem Weg zur Promotion begleitet haben und die ich als Menschen in meinem Leben nicht missen möchte.
- Prudence Lawday für den Beistand bei allerlei organisatorischen Problemen mit der nötigen Portion Humor.
- Klaus Mosthaf, Peter Probst, und Jing Li für ihre Motivation und ihr Engagement während ihrer Diplomarbeit.

Zu guter Letzt möchte ich mich bei meiner Familie bedanken, die mich stets unterstützt hat und ohne die ich diese Ausbildung nicht geschafft hätte. Meinem Onkel Siegfried möchte ich besonders danken für stete Unterstützung und die finanzielle Hilfe während meines Studiums. Meiner Lebensgefährtin Andrea möchte ich für den Rückhalt und das Verständnis in den letzten Jahren und für unsere wundervolle Tochter Milena danken.

All religions, arts and sciences are branches of the same tree.
All these aspirations are directed toward ennobling man's life,
lifting it from the sphere of mere physical existence
and leading the individual towards freedom.

Albert Einstein
German-Swiss-American physicist
1879 - 1955

Contents

List of Figures

List of Tables

Nomenclature

The following table shows the symbols used in this thesis. Local notations are explained in the text. Vectors and matrices are written in bold type.

Symbol	Meaning	Dimension
A	cross-sectional area	[m^2]
A, B, C	dimensionless functions	[-]
$AnIso$	absolute permeability anisotropy	[-]
C	effective capacity coefficient	[-]
C_g	geometric capacity coefficient	[-]
C_h	heterogeneity capacity coefficient	[-]
C_i	intrinsic capacity coefficient	[-]
$C_{i,CO2}$	intrinsic capacity coefficient referring to the CO_2-rich phase	[-]
$C_{i,w}$	intrinsic capacity coefficient referring to the water-rich phase	[-]
Ca	dimensionless Capillary Number	[-]
D	diffusion coefficient	[m^2/s]
D	depth of reservoir below surface	[m]
D_i	damage of case i	[kg]
D_{50}	average grain diameter	[μm]
E	extensive fluid property	
EE	Elementary Effect	[-]
F	force	[N]
Gr	dimensionless Gravitational Number	[-]
H	enthalpy	[J]
H	height of the reservoir	[m]
II	injection interval in percent of total reservoir height	[-]
J	Jacobian matrix	
M	molecular weight	[kg/mol]
M_{eff}	effective CO_2 mass stored	[kg, -]
N	basis function	
Q	energy, heat	[J]
$\mathbf{R}(\mathbf{u})$	set of equations with primary variable vector $\mathbf{u}$	
R	ideal gas constant, $R = 8.31447$	[J/(mol·K)]
Re	dimensionless Reynolds number	[-]

S	salinity (mass fraction of salt in the water-rich phase)	[kg/kg]
S_α	saturation of phase α	[-]
$S^{\mathrm{t}}_{\mathrm{CO2}}$	CO_2 saturation at the tangential point of the fractional flow function	[-]
$S_{\alpha,\mathrm{e}}$	effective saturation of phase α	[-]
$S_{\alpha,\mathrm{r}}$	residual saturation of phase α	[-]
T	temperature	[K,°C]
U	internal energy	[J]
V	volume	[m^3]
$V_{\mathrm{CO2,e}}$	effective storage volume	[m^3]
$V_{\mathrm{CO2,t}}$	theoretical storage volume	[m^3]
V_{total}	total geometric reservoir volume (bulk volume)	[m^3]
W	work	[J]
W	weighting function	
X	mass fraction	[-]
c_{s}	specific heat capacity of the soil grains	[J/kg K]
$dTdz$	geothermal gradient	[K/m, °C/m]
e	intensive variable	
f	fractional flow function	
g	gravity constant (g = 9.81)	[m/s^2]
h	piezometric head	[m]
h	specific enthalpy	[J/kg]
Δh_L	heat of dissolution, enthalpy change due to dissolution	[J/kg]
k	absolute permeability scalar (isotropic)	[m^2]
$\mathrm{k_h}$	absolute horizontal permeability	[m^2]
$\mathrm{k_v}$	absolute vertical permeability	[m^2]
$\mathbf{k}$	absolute permeability tensor	[m^2]
$\mathbf{k_f}$	hydraulic conductivity tensor	[m/s]
$k_{r,\alpha}$	relative permeability of phase α	[-]
l	length	[m]
m	mass	[kg]
$\mathrm{m_i}$	thickness of layer i	[m]
n	number of moles	[mol]
n_{f}	number of cases that failed	[-]
$\mathbf{n}$	outer normal vector	
p	pressure	[Pa]
p_α	pressure of phase α	[Pa]
p_{c}	capillary pressure	[Pa]
p_{d}	capillary entry pressure	[Pa]
q	source/sink, injection rate	[kg/s, J/s]

$\mathbf{q}_\mathrm{h}$	heat flux	[J/s]
$\mathbf{q}^\mathrm{C}_{\alpha,\mathrm{a}}$	advective mass flux	[kg/s]
$\mathbf{q}^\mathrm{C}_{\alpha,\mathrm{d}}$	diffusive mass flux	[kg/s]
$\mathbf{q}^\mathrm{C}_{\mathrm{CO2,b}}$	mass flux due to buoyancy forces	[kg/s]
r	leaky well distance to injection well	[m]
t	time	[s]
u	specific internal energy	[J/mol, J/kg]
u	unknown variable	
$\mathbf{v}$	Darcy velocity vector	[m/s]
$\mathbf{v}_\mathrm{tot}$	total velocity	[m/s]
v	specific volume	[m^3/mol, m^3/kg]
v	flow velocity	[m/s]
$\mathrm{v_t}$	velocity at the tangential point of the fractional flow function	[m/s]
x	mole fraction	[-]
$\mathbf{x}$	normalised Morris Method input vector	[-]
y	normalised model result	[-]
z	elevation	[m]
Γ	control volume boundary	
Θ	contact angle	[rad,°]
ϕ	porosity	[-]
Ψ_α	total potential of phase α	[Pa]
Ω	control volume domain	
α	dip angle	[°]
λ	total mobility	[1/(Pa·s)]
λ_BC	Brooks-Corey model parameter, sorting factor	[-]
λ_i	heat conductivity	[J/(m·s·K)]
λ_pm	heat conductivity of porous medium	[J/(m·s·K)]
λ_α	mobility of phase α	[1/(Pa·s)]
μ	dynamic viscosity	[Pa·s]
μ^*	mean of the distribution of absolute values of the Elementary Effects	[-]
ν	kinematic viscosity	[m^2/s]
ϱ	mass density	[kg/m^3]
ϱ_mol	molar density	[mol/m^3]
ϱ_s	soil grain density	[kg/m^3]
σ	surface tension	[N/m]
σ	standard deviation of the distribution of Elementary Effects	[-]

subscripts

CO2	CO_2-rich phase
cr	characteristic value
crit	critical, at critical point
heat	referring to heat
mass	referring to mass
n	non-wetting phase
pm	porous medium
s	solid phase
w	water-rich phase
α, β	referring to phases α, β

superscripts

C	component
CO2	CO_2 component
NaCl	salt component
r	trajectory
t	at tangential point of fractional flow function
w	water component

Abstract

The concentration of greenhouse gases in the atmosphere has increased due to tremendous human fossil fuel consumption since the Industrial Revolution. This is most likely the cause for an observed global increase in the average temperature and for the changing climate. It is expected that further global warming will have drastic ecological and economic impacts. No single technology will be sufficient to achieve the necessary emission reductions. Carbon dioxide capture and storage (CCS) is a promising technology which could make a substantial contribution. It is a process which captures CO_2 from large local sources and then stores it away from the atmosphere. Storage capacity estimates for deep saline aquifers are most promising. The initial procedure for selecting a few aquifers for a CCS project is called site screening. Aquifers identified in site screening then have to prove their suitability in further investigations. Site screening is a challenging task, since usually few data are available and the prognosis of the complex processes occurring in a reservoir after CO_2 injection is difficult.

This study aims at improving the insight into CO_2 injection processes in geological formations to assist site screening. The criteria in site screening include the estimation of the storage capacity, which should be sufficient to store the long-term production of the CO_2 source, and the long-term ability to store CO_2, which is related to the efficiency of the project and risk arising due to possible CO_2 leakages.

At first, the statistical characteristics of storage sites in potential geological formations are calculated by analysis of a large database. The parameter ranges and distributions are used to define typical reservoirs and serve as a basis for generating random reservoir setups respecting statistical characteristics. The relation of forces occurring in reservoirs after CO_2 injection is analysed by dimensional analysis. By the identification of dominant forces and processes, reservoirs with different parameter setups are compared with respect to their potential CO_2 storage capacity and risk. A sophisticated concept for estimating the CO_2 storage capacity of geological formations is developed. Detailed, time-dependent storage-capacity estimates are calculated in numerical experiments. The results are interpreted using the simultaneously calculated ratios of forces. The influence of individual reservoir parameters on storage capacity and risk is investigated in a sensitivity analysis. Finally, a risk analysis on potential CO_2 leakage through pre-existing wells is performed. In numerous numerical experiments, individual parameters are randomly sampled from the statistical parameter distributions and leakage is calculated. A risk surface is derived which represents the average risk for CO_2 leakage through pre-existing wells for any site with unknown reservoir properties.

Zusammenfassung

Aufgrund des enormen Verbrauchs an fossilen Brennstoffen in den letzten 160 Jahren, stieg die Konzentration der Treibhausgase in der Atmosphäre stark an. Dieser Anstieg der Treibhausgaskonzentrationen ist mit größter Wahrscheinlichkeit die Ursache für den weltweiten Temperaturanstieg und die beobachteten Klimaveränderungen. Man erwartet, dass ein weiterer Temperaturanstieg zu tiefgreifenden ökologischen Veränderungen und ökonomischen Belastungen führen wird. Eine einzelne Technologie oder Maßnahme wird die nötige Verringerung der Treibhausgasemissionen nicht leisten können, deshalb muss gleichzeitig eine ganze Reihe an Maßnahmen ergriffen werden. Zu diesen Maßnahmen gehören z.B. eine effizientere Energiegewinnung und -nutzung, der Ausbau der Nutzung regenerativer Energien, die erhöhte Verwendung treibhausgasarmer Brennstoffe, die Abscheidung des CO_2 im Abgasstrom von großen CO_2-Produzenten und die anschließende Einlagerung in tiefe geologische Schichten oder der Tiefsee (CCS), eine Umstellung auf eine weniger klimabelastende Landwirtschaft, die Aufforstung, sowie der eventuelle Ausbau der Kernenergie zur Stromerzeugung.

Der Fokus dieser Arbeit liegt auf der Abscheidung und Speicherung von CO_2 in tiefen geologischen Schichten. Das CO_2 wird hierbei im Abgasstrom von z.B. Kohle, Gas oder Öl betriebenen Kraftwerken abgeschieden, mittels Rohrleitungen zur Speicherstätte geleitet und dann in eine mindestens 800 m unter der Tagesoberfläche liegende, poröse, mit Salzwasser gefüllte Gesteinsschicht eingepresst. Nach der Injektion breitet sich das CO_2 als freie Phase lateral aus. Gleichzeitig steigt es aufgrund der wesentlich geringeren Dichte gegenüber dem Salzwasser auf. Ein gewisser Anteil löst sich dabei im Salzwasser. Um ein weiteres Aufsteigen zu verhindern, werden Formationen für ein solches Vorhaben ausgewählt, die über eine geringdurchlässige Deckschicht (Caprock) verfügen. An dieser Deckschicht wird das CO_2 durch den nicht zu überwindenden Eindringdruck aufgehalten. Die Deckschicht kann jedoch auch geologische Schwachstellen aufweisen oder kann durch menschliche Aktivitäten, z.B. gebohrte Brunnen, potentielle Fließpfade für ein Entweichen des CO_2 aufweisen. Dies verursacht zum einen das Risiko für ein Scheitern des Vorhabens, nämlich das Abtrennen des CO_2 für geologische Zeiträume aus dem Kohlenstoffkreislauf und der Atmosphäre, zum anderen besteht ein Gesundheitsrisiko von Menschen die mit ausgetretenem CO_2 in Kontakt kommen sowie der Beeinträchtigung von Tieren, Pflanzen und ganzer Ökosysteme.

In Deutschland wird diese Technologie aktuell intensiv erforscht. Im GEOTECHNOLOGIEN Projekt, gefördert vom Bundesministerium für Bildung und Forschung (BMBF) und der Deutschen Forschungsgemeinschaft (DFG), werden in zwei Phasen "Technologien für eine sichere und dauerhafte Speicherung des Treibhausgases CO_2" erforscht und entwickelt. Wichtige Einzelprojekte sind hierbei CO2-TRAP (Entwicklung und Bewertung innovativer Strategien zur Speicherung und dauerhaften Fixierung von CO_2 in geologischen Formationen), CLEAN (Wissenschaftliches Begleitprogramm zur CO_2-Injektion im zweitgrößten Erdgasfeld Europas "Altmark" zur Steigerung der Erdgasförderraten), CO2-MoPa (Modellierung und Parametrisierung von CO_2-Speicherung in tiefen, salinen Formationen für Dimensionierungs- und Risikoanalysen), CO2SEALS (Abdichtungsprozesse bei der geologischen Speicherung von CO2: Ein integrierter Ansatz von Laborexperimenten zur numerischen Simulation auf der Reservoirskala) und COAST (Forschung und Entwicklung für die Standortexploration und –charakterisierung im Rahmen eines industrielles Demonstrationsprojektes zur Einlagerung von CO_2 in einem Buntsandstein-Salzwasseraquifer in Nordfriesland). Desweiteren wird, im Rahmen des von der Europäischen Union und der Industrie geförderten CO2SINK-Projekts, seit Juni 2008 CO_2 in eine salzwasserführende Schicht in Ketzin (nahe Berlin) eingepresst. Das Projekt will anhand eines in-Situ Labors die Lücke zwischen den zahlreichen wissenschaftlichen und ingenieurstechnischen Modellvorstellungen bezüglich der geologischen CO_2 Speicherung und einem vollwertigen Demonstrationsprojekt schließen.

Der Projektzyklus eines typischen CO_2 Speichervorhabens beinhaltet zunächst die Abschätzung der zu erwartenden Emissionen über den gesamten Produktionszeitraum des Kraftwerks (o.ä.). Anschließend erfolgt die Suche nach geeigneten Formationen in der Region. Wurde eine Vorauswahl getroffen, erfolgt für die identifizierten Standorte eine detaillierte Charakterisierung durch die Entwicklung eines geologischen Modells, die Untersuchung der CO_2 Ausbreitung und des Druckaufbaus durch numerische Simulationen, sowie eine umfassende Risikobewertung. Letztendlich wird ein geeigneter und sicherer Standort ausgewählt und ein Antrag über eine CO_2 Speicherung an die zuständige Genehmigungsbehörde gestellt. Nach erfolgter Genehmigung wird dann für bis zu mehreren Jahrzehnten CO_2 injiziert sowie die Ausbreitung des CO_2 und der Druckaufbau innerhalb der Formation überwacht. Abschließend wird der Standort stillgelegt und weiter überwacht.

Zielsetzung der Arbeit

Mit der vorliegenden Arbeit soll das Prozessverständnis von CO_2 Injektionen in geologische Formationen verbessert werden um die anfängliche Standortauswahl innerhalb einer Region zu unterstützen. Diese Phase eines Projekts ist typischerweise durch einen Mangel an detaillierten Standortinformationen gekennzeichnet. Um eine Vorauswahl treffen zu können, muss dennoch die Speicherkapazität einer Formation abgeschätzt werden. Außerdem sollte die Eignung der Formation das CO_2 über lange Zeiträume sicher verwahren zu können

nachgewiesen werden. Dieser Nachweis ist nötig um den Projekterfolg sicherzustellen sowie eventuelle Risiken zu vermeiden. Die Untersuchung dieser Fragestellungen erfolgt in dieser Arbeit über die statistische Analyse einer Datenbank relevanter Formationsparameter, sowie über analytische und numerische Experimente.

Ein wichtiger Aspekt ist hierbei die ausschließliche Betrachtung des Injektionszeitraumes, d.h. es werden Zeiträume bis zu ∼20 Jahren kontinuierlicher Injektion untersucht. Dieser Injektionszeitraum ist von hoher Bedeutung für die resultierende Speicherkapazität und die Risikobewertung. Alle Langzeitprozesse, wie z.B. geochemische Reaktionen, hängen von diesem anfänglichen Ausbreitungszeitraum ab, da nur in den Teilen der Formation weitere Reaktionen stattfinden können, die auch vom CO_2 erreicht werden. Ebenso ist das Risiko für ein Austreten des CO_2 aus der Formation während des Injektionszeitraumes am höchsten, da hier der entstehende Überdruck am größten ist und sich die CO_2 Fahne stetig ausbreitet. Nach Injektionsende sinkt der entstandene Überdruck wieder ab und sekundäre Einschlussmechanismen, wie z.B. der Einschluss des CO_2 im Porenraum als nicht mehr verdrängbare Phase aufgrund von Mehrphasen-Gesetzmäßigkeiten, die Lösung des CO_2 im Formationswasser sowie die geochemische Bindung des CO_2 in Mineralen, führen zu einem beträchtlichen Sicherheitszuwachs. Zudem ist nach Abgleich gemessener Daten mit berechneten Simulationswerten (und Anpassung der Simulationsparameter) das Vertrauen in die Ergebnisse numerischer Prognoserechnungen hoch.

Das numerische Modell zur Beschreibung der CO_2 Speicherung

Die Entwicklung eines numerischen Modells, welches es ermöglicht die relevanten physikalischen und thermodynamischen Prozesse während einer CO_2 Injektion in geologische Formationen zu simulieren, war nicht Bestandteil dieser Arbeit. Es wurde ein am Institut für Wasserbau bereits entwickeltes Modell verwendet, weshalb die Leistungsfähigkeit hier nur kurz beschrieben wird.
Die Strömung und der Transport von CO_2 in einer porösen, starren Gesteinsmatrix werden je nach Fragestellung entweder mit einem 2-Phasen oder einem komplexeren 2-Komponenten-2-Phasen Ansatz beschrieben. Bei beiden Ansätzen existiert eine CO_2-Phase sowie eine Wasserphase. Im 2-Komponenten-2-Phasen Ansatz finden Lösungsprozesse der Komponenten (also CO_2 oder Wasser) in der jeweils anderen Phase statt und der diffusive Transport wird über einen Fickschen Ansatz beschrieben. Die Beschreibung der advektiven Flüsse erfolgt durch das Darcy-Gesetz. Die Eigenschaften der beiden Fluidphasen sowie der eventuelle Massentransfer der Komponenten zwischen den beiden Phasen werden in Abhängigkeit von Druck und Temperatur beschrieben. Die entstehenden Temperaturänderungen werden im 2-Komponenten-2-Phasen Ansatz ebenfalls berechnet. Die beschriebenen konzeptionellen Modelle, bzw. ihre mathematischen und numerischen Realisationen, sind in das Simulationsprogramm MUFTE-UG (**MU**ltiphase **F**low **T**ransport and **E**nergy Model on **U**nstructured **G**rids) implementiert. Das Modell

bewies in internationalen Vergleichsstudien die Fähigkeit zur adäquaten Beschreibung eines solchen Systems mit guter Übereinstimmung der Ergebnisse zu anderen kommerziellen und nicht-kommerziellen Simulationsprogrammen.

Analyse einer umfangreichen Datenbank

Die Eigenschaften potentieller geologischen Formationen wurden in einer Datenbankanalyse untersucht. Die öffentlich zugängliche Datenbank des "National Petroleum Council" der Vereinigten Staaten mit den Werten von über 1200 eingetragenen Reservoiren wurde hierfür verwendet. In dieser Datenbank sind zahlreiche Eigenschaften wie z.B. die Durchlässigkeit, die Porosität, die Tiefe und die durchschnittliche Temperatur von Ölreservoiren in den U.S.A. verzeichnet. Die Annahme ist hierbei, dass sich die Eigenschaften dieser Ölreservoire nicht wesentlich von den Eigenschaften potentieller, salzwasserführender Formationen unterscheiden. In statistischen Testverfahren hat sich gezeigt, dass die Parameterverteilungen keinen statistischen Standardverteilungen folgen. Aus dem Zusammenhang zwischen der Tiefe und der Temperatur wurde eine Verteilung für den geothermalen Gradienten entwickelt. Zwischen der absoluten Permeabilität und der Porosität kann ein Zusammenhang vermutet werden, wie z.B. eine Carman-Kozeny Beziehung. Die Korrelationskoeffizienten zwischen den anderen Parameterverteilungen sind gering. Die Bandbreiten und Verteilungen der relevanten Parameter wurden ermittelt um daraus typische Speicherformationen zu definieren, wie z.B. eine Formation mit Medianwerten, eine warme Formation, eine kalte Formation, eine tiefe Formation usw. Zusätzlich wurden typische Formationen definiert durch z.B. Rekombination der Formation mit Medianwerten mit gemessenen relativen Permeabilitäts-Sättigungs Beziehungen. Die ermittelten Parameterverteilungen wurden ebenfalls verwendet um zufällige Kombinationen von Formationseigenschaften zu generieren, die dennoch die statistischen Verteilungen berücksichtigen.

Dimensionsanalyse

In einem ersten Schritt wurden die dominierenden Kräfte und relevanten Prozesse in einer Dimensionsanalyse identifiziert und bewertet. Die geltenden Mehrphasen-Bilanz-Gleichungen wurden durch die Einführung so genannter *charakteristischer Größen* entdimensionalisiert. D.h. die physikalischen Einheiten der Gleichungen werden entfernt, indem die einheitenbehafteten Variablen relativ zu den charakteristischer Größen dargestellt werden. Um das zu erreichen, müssen charakteristische Größen für die Länge, die Zeit, die Geschwindigkeit und den Druck gefunden werden. Hierbei sind die Größen Geschwindigkeit, Länge und Zeit voneinander abhängig. Die entdimensionalisierten Bilanzgleichungen wurden so umgeformt, dass dimensionslose Kennzahlen darin zu finden sind. Diese Kennzahlen stellen Kräfteverhältnisse im porösen Medium dar. Die Kapillarzahl stellt hierbei das Verhältnis von Kapillarkräften zu viskosen Kräften dar und die Gravitationszahl stellt das Verhältnis

von Gravitationskräften zu viskosen Kräften dar. Letztendlich bestehen die so umgeformten Bilanzgleichungen aus dimensionslosen Kennzahlen, dimensionlosen Gradienten und sättigungsabhängigen, dimensionslosen Funktionen. Die einzelnen Terme sowie das Verhältnis der Terme zueinander, welches ausschlaggebend ist für das Ausbreitungsverhalten des CO_2 im Untergrund, konnte nun elegant durch die Wahl der charakteristischen Größen untersucht werden.
Zunächst wurden die charakteristischen Größen unabhängig voneinander und über eine große Bandbreite variiert um ein mathematisches Verständnis für das Systemverhalten zu entwickeln. Um dann ein physikalisches Systemverständnis zu erlangen, mussten die charakteristischen Größen in Abhängigkeit voneinander variiert werden. So konnte im vorliegenden Fall der CO_2-Ausbreitung im porösen Medium z.B. die charakteristische Länge durch eine typische Frontbreite abgeschätzt werden. Wobei sich die charakteristische Zeit dann herleitete aus der Dauer, die eine solche Front benötigt um einen gewählten Punkt in der Formation zu passieren. Da diese Abschätzungen durch die komplexen gegenseitigen Abhängigkeiten äußerst schwierig sind, wurden numerische 1-D und 3-D Experimente durchgeführt. Als Basis der Untersuchungen wurden die bereits definierten typischen Speicherformationen gewählt. Ziel war es nun, aus der Analyse der dimensionslosen Kennzahlen, qualitative Abschätzungen treffen zu können über die Speicherkapazität einer Formation und der Eignung, das CO_2 über lange Zeiträume sicher verwahren zu können. Dazu wurden zunächst vereinfachte Definitionen dieser beiden Kriterien getroffen. Es konnte dann gezeigt werden, dass eine kleine Gravitationszahl, d.h. schwache Gravitationskräfte im Verhältnis zu den viskosen Kräften, und zum Teil auch eine hohe Kapillarzahl, d.h. starke Kapillarkräfte im Verhältnis zu den viskosen Kräften, von Vorteil sind, d.h. dies führte zu hohen Speicherkapazitäten und einer sichereren Verwahrung. Die quantitativen Auswirkungen der simultanen Variation beider Kennzahlen müssen jedoch noch weiter Untersucht werden.

Analyse der Speicherkapazität einer geologischen Formation

Damit in einem nächsten Schritt die Speicherkapazität einer geologischen Formation in Abhängigkeit der geologischen Parameter abgeschätzt werden konnte, musste zunächst die Definition der Speicherkapazität festgelegt werden. Es gibt bis dato keine allgemein akzeptierte Definition der Speicherkapazität und verschiedene Forschergruppen und Institutionen nutzen verschiedene Ansätze, was teilweise zu widersprüchlichen Ergebnissen führt wenn es um die Abschätzung lokaler, regionaler oder globaler Speicherkapazitäten geht. In dieser Arbeit wurde ein Konzept weiterentwickelt, welches von der *Task Force for Review and Identification of Standards for CO_2 Storage Capacity Estimation* zur Nutzung vorgeschlagen wird. Dieses Konzept der sog. *Resource-Reserve Pyramids* berücksichtigt verschiedene Aspekte der CO_2-Speicherung wie z.B. verschiedene prozessabhängige Zeitskalen, verschiedene räumliche Bewertungsskalen und verschiedene Speichermöglichkeiten. In der sog. *Techno-Economic Resource-Reserve Pyramid* werden die Kapazitätsabschätzungen in verschiedene

Ebenen eingeteilt, je nach immanenter Unsicherheit der Schätzung und nach den Kosten der Speicherung. Auf der untersten Ebene steht die theoretische Kapazität einer Formation, dies ist der verfügbare Porenraum abzüglich der aufgrund von Mehrphasengesetzmäßigkeiten nicht verdrängbaren Wasseranteile. Auf der nächst höheren Ebene steht die effektive Kapazität. Sie ist eine Untermenge der theoretischen Kapazität. Teile der theoretischen Kapazität welche durch geologische oder ingenieurstechnische Gründe nicht erschlossen werden können, werden hier nicht berücksichtigt. Auf den höheren Ebenen werden dann legislatorische und Genemigungsaspekte sowie Aspekte der Infrastruktur usw. integriert. In dieser Arbeit interessiert die Relation der theoretischen zur effektiven Kapazitätsebene. Hier wurde ein volumenbasierter Speicherkoeffizient C definiert, der die theoretische in die effektive Kapazität überführt. Der Speicherkoeffizient C kann noch in weitere Einzelfaktoren zerlegt werden. Auf dieses Detail soll in dieser Zusammenfassung aber nicht weiter eingegangen werden. In der effektiven Kapzität, welche ein Speichervolumen darstellt, kann eine bestimmte Masse CO_2 gespeichert werden, hier als M_{eff} bezeichnet. Der Koeffizient C und die Masse M_{eff} wurden nun mit Hilfe numerischer 1-D und 3-D Simulationen der definierten typischen Speicherformationen berechnet und diskutiert. Es konnten vielerlei Aspekte der Speicherung gezeigt werden, so z.B. der Einfluss der relativen Permeabilitäten, des Kapillardrucks oder der Injektionsrate. In der Literatur gibt es bislang keine belastbaren Abschätzungen von C und M_{eff} für die vorhandene Bandbreite möglicher Formationsparameter, so dass diese Arbeit einen entscheidenden Fortschritt in dieser Richtung darstellt. Es wurde weiterhin gezeigt, dass es möglich ist die berechneten Koeffizienten C und die Massen M_{eff} mit Hilfe der entwickelten (dimensionslosen) Kennzahlen abzuschätzen. Die in dem vorangegangenen Kapitel bereits vermutete Vorteilhaftigkeit kleiner Gravitationszahlen sowie zum Teil hoher Kapillarzahlen konnte nun quantitativ bestätigt werden. Die berechneten Speicherkoeffizienten aller betrachteten Fälle sind kleiner als 18%, d.h. weniger als 18% des vorhandenen Porenraums kann zur CO_2 Speicherung genutzt werden. Überträgt man den höchsten berechneten Speicherkapazitätskoeffizienten auf die Jahresproduktion eines typischen kohlebefeuerten Kraftwerks (Ausstoß $1\,\text{MtCO}_2$ pro Jahr) über einen Zeitraum von 25 Jahren, so erhält man eine CO_2-Fahne mit einem Radius von 1.83 km (weitere Annahmen hierbei sind eine Formationsdicke von 100 m und eine CO_2-Dichte von $660.7\,\text{kg/m}^3$).

Sensitivitätsanalyse

Die Frage nach dem Einfluss einzelner Formationsparameter auf das Modellergebnis wurde in einer Sensitivtätsanalyse beantwortet. Als Modellergebnis dienten hier wieder Kriterien, welche repräsentativ sind für die Abschätzung der Speicherkapazität einer Formation sowie Kriterien zur Risikobewertung einer möglichen CO_2-Leckage. Die sog. Morris Methode wurde hier angewandt um auf eine sehr effiziente Weise eine Rangfolge der qualitativen Parametereinflüsse zu entwickeln. Diese Methode untersucht den gesamten definierten Parameterraum, wobei jeweils ein Parameter variiert wird. Somit wird an jedem untersuchten Punkt im Parameterraum ein lokales Sensitivitätsmaß ermittelt.

Gemittelt über alle untersuchten Punkte ergibt sich daraus eine qualitative Abschätzung des Parametereinflusses welcher in Relation zu den Einflüssen der anderen Parameter zu bewerten ist. Betrachtet man die Standardabweichung der lokalen Sensitivitäten lässt sich, in Relation zu den Standardabweichungen der lokalen Sensitivitäten der anderen Parameter, eine Parameterinteraktion oder ein nicht-lineares Parameterverhalten ermitteln. Es wurden 15 Formationsparameter ausgewählt und zufällig über den gesamten, jeweils physikalisch sinnvollen Bereich untersucht. Insgesamt wurden 64 individuelle Parameterkombinationen erstellt und simuliert. Diese 64 Fälle zufällig generierter Parameterkombinationen bilden die Grundlage für die Sensitivitätsanalyse. Als einflussreichste Parameter wurden die absolute Permeabilität, das Injektionsintervall, und die Formationstiefe identifiziert. Hingegen waren die CO_2 Injektionstemperatur und der Fallwinkel der Formation eher vernachlässigbar.

Risikoanalyse

In einer abschließenden Risikoanalyse wurde das Risiko bezüglich einer CO_2-Leckage an einem Brunnen in einiger Entfernung zum Injektionsbrunnen untersucht. Dabei wurden vier einflussreiche Formationsparameter bezüglich ihres Einflusses auf das potentielle Risiko einer Leckage statistisch untersucht.
Diese Untersuchung hatte verschiedene Ziele. Zum ersten soll sie die Möglichkeit bieten, verschiedene Formationen in Abhängigkeit ihrer Eigenschaften bezüglich des potentiellen Risikos miteinander zu vergleichen. Dies soll bei der Entscheidungsfindung helfen, für welche Formationen weitere Untersuchungen vielversprechend sind. Zum zweiten soll sie bei der Positionierung des Injektionsbrunnens helfen, der von mehreren potentiellen Leckage-Brunnen umgeben sein könnte.
Die unabhängigen Formationsparameter sind hierbei die Porosität, der geothermale Gradient, die Tiefe der Formation und die Anisotropie zwischen horizontaler und vertikaler absoluter Permeabilität. Diese Parameter wurden als unabhängig ausgewählt da sie einerseits in der Sensitivitätsanlyse als einflussreiche Parameter identifiziert wurden und andererseits eine Parameterverteilung für die statistische Untersuchung vorhanden war. Die Beschränkung auf vier unabhängige Parameter war aufgrund des hohen Rechenaufwandes nötig den eine Betrachtung aller einflussreichen Parameter verursacht hätte. Die weiteren Formationsparameter wurden durch Funktionalitäten der unabhängigen Parameter ausgedrückt. Diese Funktionalitäten beruhen auf einer umfassenden Literaturrecherche.
Das Risiko wurde durch die Wahrscheinlichkeit mit der eine solche Leckage auftreten könnte berechnet, multipliziert mit der entwichenen CO_2-Masse in Abhängigkeit von der Zeit seit Injektionsbeginn und in Abhängigkeit von der Distanz zwischen Injektionsbrunnen und Leckage-Brunnen. Das Risiko hat somit die Einheit einer Masse. Zahlreiche Simulationen wurden durchgeführt mit jeweils unterschiedlichen Formationseigenschaften. Die Formationseigenschaften wurden dabei so festgelegt, dass jeweils drei der vier unabhängigen Parameter zufällig aus der Parameterdatenbank generiert wurden. Der vierte unabhängige Parameter, die Anisotropie der absoluten Permeabilität, wurde zufällig aus einer Parameterverteilung

generiert die auf einem theoretischen Modell basiert. Die statistischen Verteilungen der Parameter wurden somit berücksichtigt. Die umfangreichen numerischen Simulationen wurden mit Hilfe des "CO2 Community Grid" durchgeführt, einer virtuellen Forschungsumgebung die es ermöglicht örtlich getrennte Supercomputer (Parallelrechner) in den Ländern Dänemark, Finnland und Norwegen über ein zentrales Zugangsportal einfach und einheitlich zu nutzen.
Aus dem berechneten Risiko wurde dann eine analytische Gleichung entwickelt. Mit dieser Gleichung ist es möglich schnell und einfach eine quantitative Abschätzung für das durchschnittliche, potentielle Risiko einer Leckage zu erhalten in Abhängigkeit der Zeit und der Distanz zum Leckage-Brunnen. Dies ist generell auch für mehrere Brunnen möglich, sofern die Brunnen sich nicht gegenseitig beeinflussen. Des Weiteren konnten die vier unabhängigen Formationsparameter bezüglich ihres Einflusses auf das Risiko untersucht werden. Den höchsten Einfluss hatte dabei der geothermale Gradient und die Tiefe der Formation. Ein steigender geothermaler Gradient und eine geringere Formationstiefe verursachten ein größer werdendes Risiko zu einem gewählten Zeitpunkt, d.h. das Risiko stieg früher an. Die Anisotropie der absoluten Permeabilität hatte einen gewissen Einfluss in einiger Distanz des Leckage-Brunnens zum Injektionsbrunnen. Hier führte eine größer werdende Anisotropie zu jedem gewählten Zeitpunkt zu einem größeren Risiko. Interessanterweise hatte die Porosität keinen Einfluss auf das potentielle Risiko. Dieses Verhalten ist begründet in der Abhängigkeit der absoluten Permeabilität von der Porosität. Mit größer werdender Porosität, und somit erwarteter langsamerer Ausbreitung der CO_2-Fahne, verursacht durch den vergrößerten verfügbaren Porenraum, steigt auch die absolute Permeabilität, was eine schnellerer Ausbreitung der CO_2-Fahne vor allem in den Bereichen direkt unterhalb des Caprocks verursacht. Diese beiden Effekte heben sich gegenseitig auf und das Risiko war hier nahezu unabhängig von Variationen der Porosität.
Abschließend wurde eine umfassende Diskussion über die Sensitivität der getroffenen Annahmen in Bezug auf das potentielle Risiko geführt. Dabei waren wichtige Diskussionspunkte die Bedeutung der Berücksichtigung weiterer unabhängiger Parameter, die Wahl unterschiedlicher Funktionalitäten für die Berechnung der abhängigen Parameter, die Bedeutung der Berücksichtigung zusätzlicher Prozesse (wie z.B. geochemische Prozesse) sowie der Einfluss realer geologischer Formationsgeometrien und Strukturen.

Zusammenfassend kann diese Arbeit zu einem verbesserten Prozessverständniss von CO_2-Injektionen in geologische Formationen beitragen. Die anfängliche Standortauswahl für ein CO_2 Speicherprojekt innerhalb einer Region kann durch einfach anzuwendende Abschätzungen maßgeblich unterstützt werden. Die Abschätzungen berücksichtigen dabei die wichtigsten Faktoren eines Speichervorhabens; dies sind die Speicherkapazität einer Formation und das potentielle Risiko, welches durch Leckage-Brunnen in der Umgebung der Injektionsstelle entstehen könnte.

1 Introduction

The climate on Earth has been subject to various changes in the past for various reasons. The main reasons include dynamic processes of Earth itself, variations in solar radiation, variation in the Earth's orbit, and variations in the concentration of greenhouse gases. Solar radiation is partly received by the Earth's surface as heat. Due its temperature, the Earth's surface emits energy in the form of infrared radiation. This infrared radiation is partly absorbed by the greenhouse gases naturally present in the atmosphere. The absorption causes a warming of the lower atmosphere and again of the Earth's surface. This process is referred to as the Greenhouse Effect (Arrhenius, 1896). With an increasing concentration of greenhouse gases, the temperature on the Earth's surface may rise. IPCC (2005) states that "most of the observed increase in globally averaged temperatures since the mid-20^{th} century is very likely due to the observed increase in anthropogenic greenhouse gas concentrations". The panel defines "very likely" as indicating probabilities greater than 90 %. Greenhouse gases include water vapour, carbon dioxide (CO_2), methane (CH_4), and nitrous oxide (N_2O). In the past 160 years, human fossil fuel use increased tremendously (see Figure 1.1). As a result, the global atmospheric CO_2 concentration has been increasing from a pre-industrial value of about 280 ppm* to 379 ppm in 2005 (IPCC, 2005).

The severe effects that nature and mankind are facing due to increasing temperature and changing climate include a rise in sea level, failing crop yields in many developing countries, and the extinction of animal and plant species. This ecological and economic interest led to the United Nations Framework Convention on Climate Change (1997), which has been accepted by 189 nations, and whose main objective is to achieve "... stabilisation of greenhouse gas concentrations in the atmosphere at a level that would prevent dangerous anthropogenic interference with the climate system. Such a level should be achieved within a time-frame sufficient to allow ecosystems to adapt naturally to climate change ...". In 2005, a number of nations approved an addition to this treaty which also includes some legally binding measures, known as the Kyoto Protocol. Nevertheless, due to the complexity of the problem, it is not clear to date what a sustainable level of greenhouse gas concentrations is and what emission reductions are necessary. From model runs, it has become clear that emission reductions in the range of 55–90 % by 2100, compared to the emissions of 2001, might be necessary to stabilise the atmospheric CO_2 concentration at a value of 450 ppm (IPCC, 2005). Beside the ecological interest, there is an economic interest. Stern (2007) states that

*parts per million, i.e. ratio of the number of molecules of the considered gas compared to the total number of molecules of dry air.

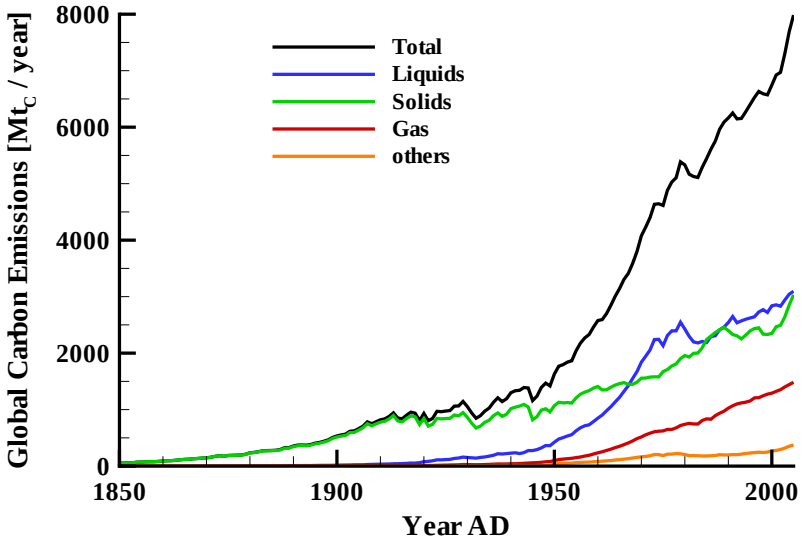

Figure 1.1: Variation of global annual carbon emissions from burning solids (e.g. coal), liquids (e.g. petroleum), natural gas, and others (i.e. cement production and natural gas lost during oil and gas mining) from 1850 to 2005 (after Marland et al. (2008)). One tonne of carbon compares to $3.\overline{6}$ tonnes of CO_2.

"the benefits of strong, early action on climate change outweigh the costs". "Costs" refers here to a global reduction of the gross domestic product.

The options for reducing global CO_2 emissions are manifold, although, considering the magnitude of the problem, one single option is not sufficient. Pacala and Socolow (2004) estimate the magnitude of the problem, discuss possible options for solving it, and state that viable techniques already exist. These authors assume that the current carbon emissions will continue to grow linearly and reach a value of 14000 Mt C/year by 2054. To stabilise the CO_2 concentration at 500 ppm, it is assumed sufficient to maintain current emissions ($\sim$7000 Mt C/year) for the next 50 years and reduce them significantly afterwards. Thus, the total mass of future emissions that need to be avoided in the next 50 years accumulates to 175 Gt C. The authors then discuss 15 options for activities that reduce emissions to the atmosphere. All necessary technologies are currently deployed on an industrial scale, but need to be upscaled. In their concept, activities start in 2004 at zero prevented emissions and reach a value of 1000 Mt C/year prevented emissions in 2054. If seven of those 15 activities could be scaled up to such a magnitude, this would solve the problem. Options are grouped in different sectors, i.e. energy efficiency and conservation, fuel shift, carbon dioxide capture and storage, nuclear fission, forests and agricultural soils. In conclusion, no single activity can prevent future emissions sufficiently, but there are a number of options which can be scaled up and simultaneously need to be expanded. The focus of this study lies on CO_2 capture and storage (CCS). The special attribute of CCS is the possibility of a fast and large-scale deployment that could outweight time delays in the development of other technologies. The long-term

goal, however, should be to achieve a sustainable energy generation and consumption.

Carbon dioxide capture and storage is a process that captures CO_2 from the burning of fossil and/or renewable fuels and from processing industries and then stores the CO_2 away from the atmosphere for geological periods of time. Carbon dioxide is primarily captured at point sources such as power plants and other large-scale industrial processes.

To capture the CO_2, there are different approaches, i.e. pre-combustion, post-combustion, and oxyfuel combustion. The process conditions for operation determine the approach to be selected. Each approach requires at some point a separation of CO_2, water, or oxygen from a bulk gas stream. Efficiencies of 80–90 % of captured CO_2 can be reached whereas about 10–40 % more energy is required for the additional operations (IPCC, 2005).

It is preferable to transport the captured CO_2 to feasible storage options in pipelines, but transportation by ship, rail, or road tankers is also possible. Challenges at the transport stage include costs, design, and safety, although experience with the current practice suggests that these problems can be solved.

Carbon dioxide storage can occur in geological formations, in the ocean, or by industrial fixation in inorganic carbonates. In the following, the focus is on storage in geological formations. Feasible reservoir types include deep saline aquifers, oil and gas fields and unminable coal seams. Accordingly, one can distinguish between the exclusive purpose of storing the CO_2 and the use of injected CO_2 to enhance oil recovery (EOR), natural gas (EGR) or methane from coal beds (ECBM). The latter three options are likely to be implemented in the near future because of cost benefits and presumably good knowledge about the site-specific geology as well as the existing infrastructure. However, in the following, the focus of this study is on storage in deep saline aquifers since estimates of the available storage capacity necessary to store the immense amounts of human CO_2 production are promising. In Figure 1.2, the technology is schematically sketched, including processes occurring in the sub-surface, monitoring devices, and potential leakage pathways.
Carbon dioxide is injected into a saline formation at a depth preferably greater than 800 m below the surface. The CO_2 plume spreads laterally in the aquifer, displacing the resident brine, which results in pressure increase. At the same time, due to the lower CO_2 density than the brine density at these pressures and temperatures, it migrates in an upward direction. To prevent CO_2 from leaving the formation a confining layer above the storage reservoir is necessary. This confining layer is usually called caprock and should provide low permeability, considerable thickness, and no geological weaknesses such as e.g. fractures or faults. However, the risk remains that CO_2 might leak out of the storage reservoir through these natural or man-made pathways. This issue needs to be addressed carefully in every storage attempt. Carbon dioxide leakage is illustrated in Figure 1.2 through a leaky well (e.g. poorly plugged abandoned well or old oil well) and through a fault. It may then mi-

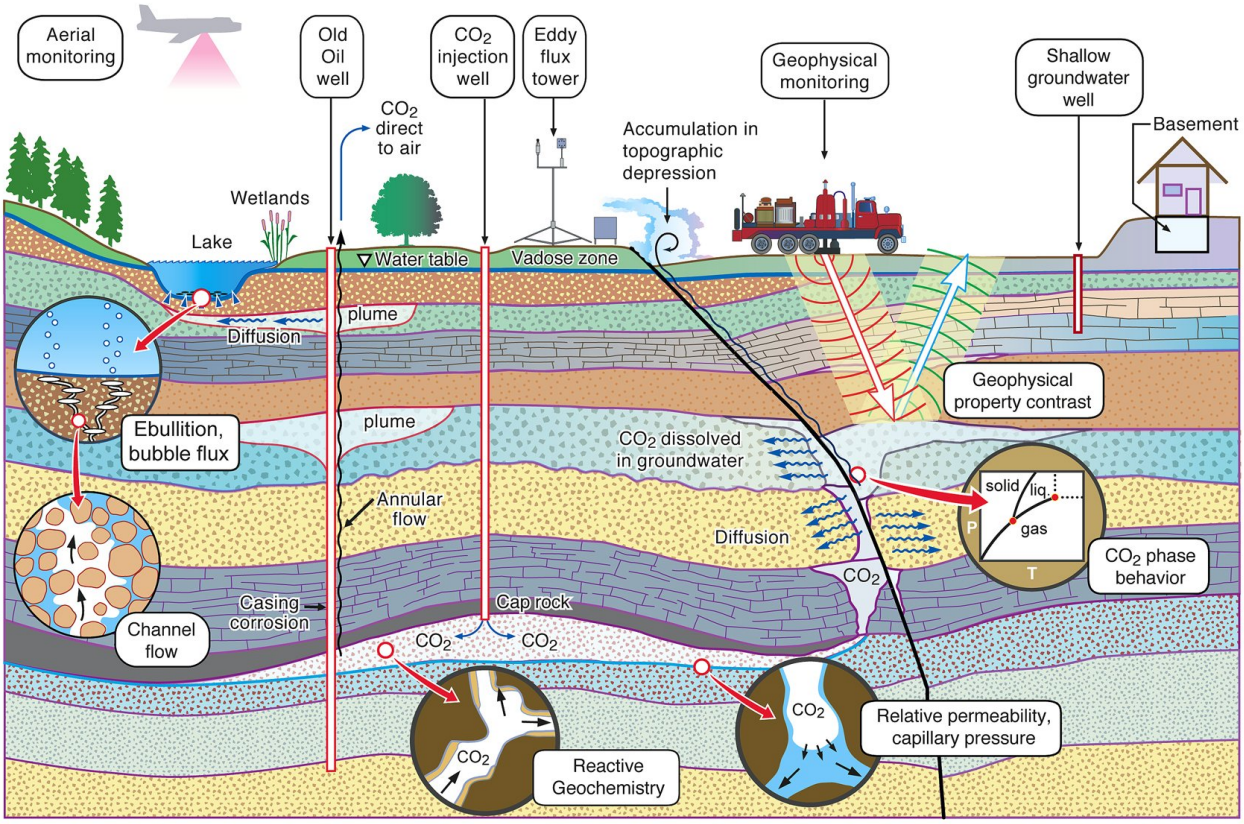

Figure 1.2: Principal processes, leakage risks, and monitoring techniques associated with CO_2 storage in geological formations (Figure courtesy of Lawrence Berkeley National Laboratory).

grate into shallower aquifers (harming potable groundwater) or migrate back to the surface (leading to risk directly associated with exposure to leaked CO_2). To prevent harm to the health of humans and animals as well as to the environment, an efficient and reliable monitoring network is essential. Monitoring leaked CO_2 on the land surface, geophysical (seismic) monitoring, and monitoring from aeroplanes is also sketched in Figure 1.2.

Currently, several projects all over the world are injecting CO_2 into saline aquifers for either socio-economic reasons or for research purposes. The first commercial attempt is being made by the Statoil-operated Sleipner project (Torp and Gale, 2004). Since 1996, approximately 1 Mt CO_2/year has been injected into the 50–250 m-thick Utsira formation in the North Sea at ∼1100 m depth. The CO_2 is extracted from natural gas (containing about 9% CO_2) that is captured from another field and then processed to the supercritical conditions of 80 bar pressure and 40 °C temperature before being re-injected. At another site in Norway, CO_2 has been injected since May 2008 - the Snøhvit field in the Barent Sea. The CO_2 content of the natural gas extracted there is decreased from 5–8 % to less than 50 ppm before the gas can be further processed (converted to liquefied natural gas). The ∼0.75 Mt CO_2 produced per

year are re-injected into a deeper formation. Another commercial example is the In-Salah project in the southern Sahara (Algeria), where CO_2 has been injected since 2004. Similar to the Norwegian projects, the natural gas produced initially has a CO_2 content of ∼10 %, which has to be decreased to ∼0.3 % to meet European market standards. The annually produced ∼1.2 Mt CO_2 are re-injected into a 1800 m-deep sandstone reservoir. The next commercial project in operation may be the Gorgon Joint Venture project (Australia). The natural gas produced there has a CO_2 content of up to 14 %, which is to be reduced. The ∼2.7–3.2 Mt CO_2 produced annually are to be re-injected into a saline formation at ∼2300 m depth (International Energy Agency Greenhouse Gas R&D Programme, 2008).

Beside that, several pilot sites are currently being investigated for experimental research purposes.
In the Nagaoka project, 10400 t CO_2 were injected in 2003 and 2004 in a ∼1100 m deep saline aquifer at the Iwanohara base near Nagaoka (Japan). The purpose of the project was the investigation of the behaviour of CO_2 during and after injection, the long-term stability of CO_2 in the reservoir, and the potential and costs of CO_2 storage (Nagaoka project consortium, 2009).
In 2004, the Frio project injected 1600 t CO_2 and 320 t CO_2 in two stages in two saline aquifers at the Frio site, north-east of Houston in the U.S.A. in ∼1600 m depth. Extensive monitoring techniques have been tested (Hovorka et al., 2006).
In the CO2SINK project, 8450 t CO_2 were injected until February 8th 2009 into a saline aquifer in the Ketzin anticline close to Berlin (Germany) at a depth of ∼500 m–700 m. It is planned to inject up to 60000 t CO_2 and sophisticated monitoring techniques are to be tested. The project provides an in-situ laboratory for CO_2 storage to fill the gap between the numerous conceptual engineering and scientific studies on geological storage and a fully-fledged on-shore storage demonstration (CO2SINK project consortium, 2009).
The Department of Energy in the U.S.A. has initiated a national network of seven regional partnerships to investigate the best approaches for capturing and storing gases that can contribute to global climate change (NETL, 2009). The partnerships aim at injecting CO_2 into 14 formations in the U.S.A. in 2009 and 2010. Injection rates at the sites vary between 3 kt and 10.8 Mt CO_2.

Having outlined the motivation for this study and the current state of the CSS technology, the principle trapping mechanisms of CO_2 injected in geological formations are explained in the following since they are essential comprehending of this study's objectives.

1.1 Trapping Mechanisms

The effectiveness and the security of CO_2 storage in geological formations depends on a combination of several physical and geochemical trapping mechanisms that are active on

very different time scales with varying contributions to the total trapping. The trapping mechanisms are a result of fundamental processes occurring in a reservoir after CO_2 has been injected.

Structural and Stratigraphic Trapping
After CO_2 is injected into a geological formation typically strong buoyancy forces act due to the density difference between the CO_2 and the naturally resident brine. Thus, the CO_2 plume migrates upwards to shallower depths. To impede a further rise, the CO_2 needs to be physically trapped below a caprock (seal of low permeability); this mechanism is called structural and stratigraphic trapping.

Common structural traps are distorted geological layers, forming e.g. folds or anticlines. Even closed faults can act as structural traps. Stratigraphic traps are referred to if the permeability changes to much lower values within the respective reservoir, thus forming a seal. The storage security, especially in the early stages after the start of the injection, is largely influenced by the caprock integrity. A fracturing of the caprock or fault re-activation due to over-pressurisation should be prevented by all means.

Residual Trapping
The minimum saturation that is attainable for a fluid when displaced by another (immiscible) fluid from a porous medium is called the residual saturation. The residual saturation cannot be further reduced by viscous forces. Thus, the fraction of the CO_2 plume below residual saturation is residually trapped. This is of special importance in regions where the CO_2 plume is displaced again by brine. The CO_2 in residual saturation may then dissolve in brine and eventually CO_2 as a separate phase disappears. The effect of hysteresis (discussed in Section 2.2.4) is also of importance here, since residual saturations may change, possibly increase, with every drainage-imbibition cycle. Such a drainage-imbibition cycle could be induced by non-continuous or varying CO_2 injection rates.

Solubility Trapping
When CO_2 comes into contact with resident brine, it immediately begins to dissolve up to a solubility limit. Thus, considerable amounts of CO_2 dissolve over time and by contact with fresh brine as the CO_2 plume expands. Since a de-pressurisation of the brine with CO_2 load is not to be expected, CO_2 is safely stored. This mechanism is referred to as solubility trapping. Since brine with dissolved CO_2 has a higher density than fresh brine, it slowly migrates to deeper regions and fresh brine may be available for further dissolution.

Mineral Trapping
When CO_2 is dissolved in brine, it may form ionic species as the rock dissolves, accompanied by an increase in pH. Finally, some fraction may be converted to stable carbonate minerals. This process is called mineral trapping (IPCC, 2005). Significant amounts of CO_2

mass trapped in minerals is expected only after some hundreds to thousands of years. However, chemical reactions are not included in this study due to the focus on the injection stage.

Time Scales

On a short time scale, structural and stratigraphic trapping are the dominant trapping mechanisms. Over time, the contribution of residual, solubility and mineral-trapping mechanisms increases, as does the storage security, since these mechanisms represent a long-term fixation of CO_2 (IPCC, 2005). The mineral-trapping mechanism is presumably negligible here since its contribution to trapping may only become significant after centuries. The different importance of the different trapping mechanisms over time is due to changes of the dominant processes. The advection-dominated multiphase flow regime occurs on the short to medium time scale. With declining pressure gradients and density differences, these processes lose their driving forces. Inter-phase mass-transfer processes, like the dissolution of CO_2 in brine gain importance on a large time scale. Geochemical reactions eventually lead to a very secure mineral trapping of CO_2. Figure 1.3 schematically shows the contribution of the individual trapping mechanisms to the total trapping versus time and variation of the dominant processes.

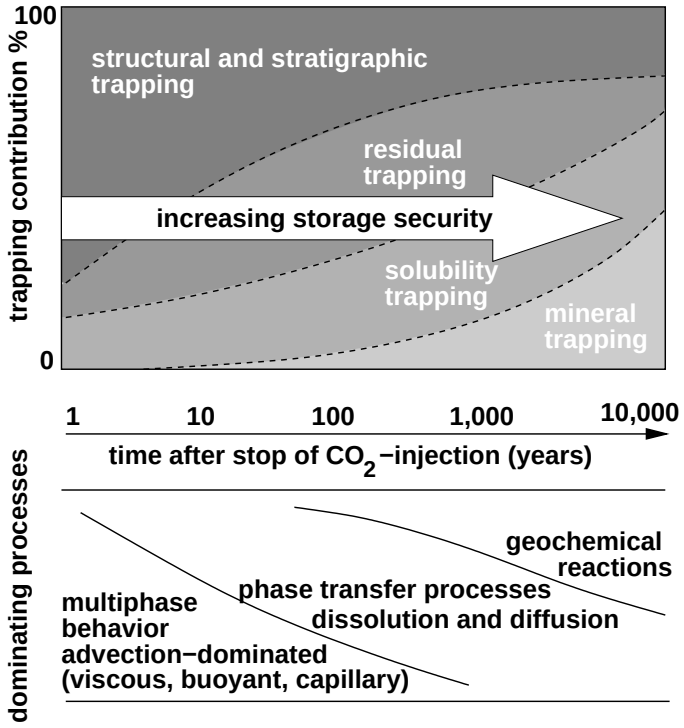

Figure 1.3: Storage security depending on different trapping mechanisms and dominant processes over time (modified after IPCC (2005), Class (2008)).

1.2 Objective of the Study

A conception of the life cycle of a CO_2 storage project is shown in Figure 1.4. Typical steps include the initial estimation of the magnitude of emissions from large stationary sources and the screening of regional storage opportunities for potential reservoirs (sites). A subsequent step includes the site-specific characterisation and assessment of the reservoir by developing a geological model, performing numerical simulations and performing a risk assessment. Then, a proposal is sent to the regulator and, if approved, CO_2 is injected and monitored for up to several decades. Finally, the site is properly closed.

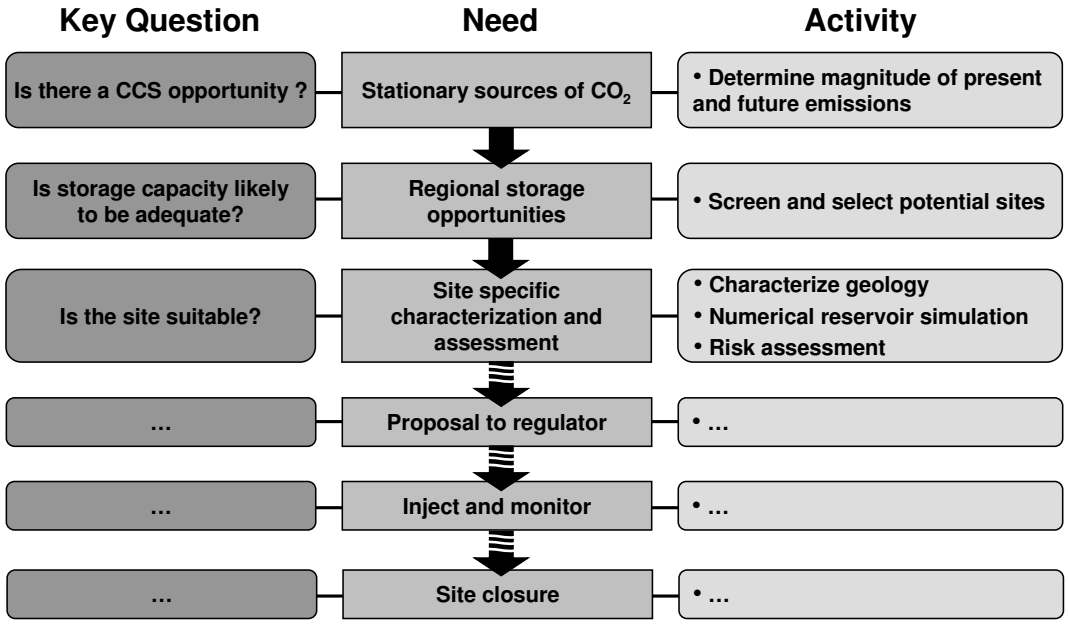

Figure 1.4: Life cycle of a CO_2 storage project (modified after IPCC (2005)).

This study refers to the key questions in the early phase of site screening and characterisation, i.e. "Is storage capacity likely to be adequate?" and "Is the site suitable?". Site screening is the initial step in site characterisation and is aimed towards a pre-selection of potential storage reservoirs. Usually, little information is available on the reservoir properties and geology at this stage of a project. Consequently, the entire range of parameters is considered in this study. At a later stage, further investigations on the properties of the identified reservoirs will lead to good data availability, which can then be fed into detailed investigation methods, e.g. site-specific numerical models. This study does not aim at developing a comprehensive framework which can be applied by regulators or operators. Rather, fundamental research is conducted and the underlying processes of CO_2 injection in geological formations are investigated. This is done by keeping the focus on the key questions, i.e. estimating storage capacity and evaluating risk. In site screening, operators usually try to identify sites with an anticlinal shape, high porosity, and high permeability, at a depth

of around 1000–2000 m. Such a site is potentially of low risk (since CO_2 spreading is limited by the anticlinal structure), provides good injectivity to inject CO_2 economically, and the estimated storage capacity is high. However, these sites are limited in number and will therefore not be available for a large-scale deployment of this technology after some time. Hence, the aquifers investigated here have a horizontal caprock and are limited by a defined leakage point at some distance to the injection point.

Following this argumentation, the outline of this study is to introduce the conceptual, mathematical, and numerical model to investigate the processes of interest and then to investigate the statistical characteristics of the relevant parameter distributions as a basis for analytical and numerical investigations. A dimensional analysis of the governing equations is subsequently conducted to identify and assess the dominant forces and processes. The carbon dioxide storage capacity is then defined and evaluated, based on the identified typical reservoir properties. It is analysed by using the dimensionless indicators developed. In a sensitivity analysis the influence of various reservoir parameters on the model results is assessed with respect to storage capacity and risk. Subsequently, a risk analysis investigates the effect of the parameters with the greatest influence on the risk of CO_2 leakage through a pre-existing well. A risk surface is calculated to estimate average risk quickly depending on the distance between the leaky well and the injection well and time.

The time scale considered here covers the injection stage. Processes in the early stages are presumably of higher relevance to storage capacity. All long-term processes, like geochemical reactions etc., depend on these early events since they only occur where CO_2 is present. Similarly, the risk of leakage is highest during the injection stage due to increasing reservoir over-pressure and growing CO_2 plume size. After shut-in, pressure recovers, secondary CO_2 trapping mechanisms contribute significantly to storing the injected CO_2 safely and confidence in history-matched numerical models is high (see Figure 1.5[†]). One exception to this reasoning is geochemical reactions, which could reduce caprock sealing efficiency. These processes can lead to increased risk in the long term.

1.3 State of the Art

The current state of the art of the relevant research fields is discussed in the following:

Multi-phase multi-component flow and transport simulation
The oil industry developed the first numerical models to describe multi-phase flow in porous media in the 1960s (Aziz and Settari, 1979). Nowadays, the technique is widely used for research and commercial purposes in many fields of application. Since the late 1990s, CO_2

[†]after Benson, S.M., Geological Storage of CO_2: Analogues and Risk Management, presentation given to Carbon Sequestration Leadership Forum, Pittsburgh, U.S.A., May 7^{th} 2007

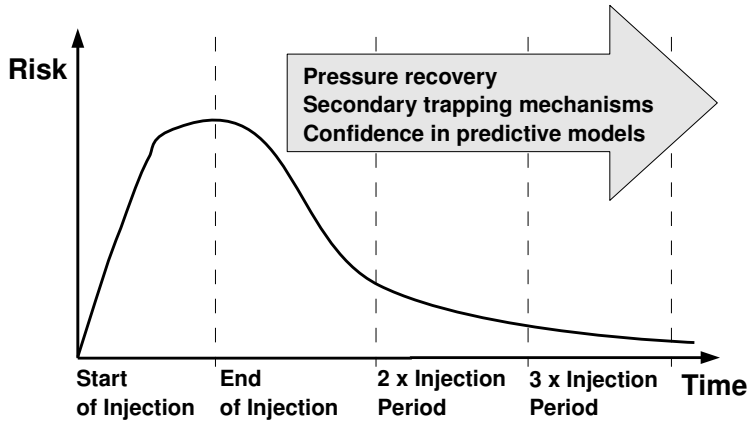

Figure 1.5: Hypothetical risk profile during the life cycle of a CCS project. Risk of leakage increases due to increasing reservoir over-pressure and growing CO_2 plume size. After shut-in, pressure recovers and secondary CO_2 trapping mechanisms contribute significantly to storing injected CO_2 safely.

storage in saline aquifers has been simulated. Numerical simulation is used to answer manifold questions related to the description of the processes occurring in the reservoir, e.g. storage capacity estimation, design of the injection site, design of the injection strategy, design of the monitoring network, assisting risk assessment by quantification of possible leakage rates, estimation of over-pressures, etc. Current fields of research include the coupling of multiphase flow and transport with other simulators describing geomechanical and geochemical processes and the proper description of the fluid properties of complex gas mixtures (e.g. CO_2 with some impurities like H_2S) (International Energy Agency Greenhouse Gas R&D Programme, 2008). Code comparison studies have been conducted to test consistency between different approaches (Pruess et al., 2003).

Development of semi-analytical solutions to describe CO_2 storage

Semi-analytical solutions describing plume evolution in aquifers have been developed by Nordbotten et al. (2004). The approach has been constantly further developed and is applied to estimate leakage through multiple abandoned wells in complex systems approximated by a sequence of homogeneous aquifers and aquitards with infinite extent. Fundamental approximations include essentially non-existent or vertical flow in aquitards whereas flow in aquifers is essentially horizontal away from wells. This approach, based on strong geometric simplifications, provides an interesting alternative to traditional numerical simulations in areas where the high density of existing wells is the major concern as regards leakage risk, surpassing all other concerns.

Geochemical processes

Numerical models have been developed to describe chemical reactions occurring in CO_2 storage by e.g. Gunter et al. (1997), Xu and Pruess (1998), and Clauser (2003). Questions

of interest include long term storage capacity contribution by mineral trapping (Kühn and Clauser (2006), Xu et al. (2007), Mito et al. (2008)), caprock alterations as a result of chemical reactions (Gherardi et al., 2007), and possible injectivity reduction. Fields of current research include the collection of basic thermodynamic and kinetic data at elevated pressure and temperature conditions and the modelling of reactions assuming impurities in the CO_2 stream (Gaus et al., 2008).

Geomechanical processes
The description of geomechanical processes occurring as a result of the injection of CO_2 into saline aquifers is undertaken by coupling geomechanical models to flow and transport models (Le Gallo et al. (2006), Rutqvist et al. (2008)). Various approaches have been followed for the coupling strategy, either a close coupling (feedback of geomechanical effects on porosity and permeability and thus on the flow and transport processes) or a loose coupling (no feedback effects and sole description of stresses and possible effects thereof). Questions of interest in geomechanical models are concerned with the reactivation of existing faults and hence the estimation of a maximum sustainable injection pressure, and the estimation of porosity and permeability changes and hence the influence on the flow and transport processes.

Natural and Industrial Analogues
Benson et al. (2005) studied natural and industrial analogues that could provide valuable information for CO_2 storage in terms of assessing, managing and mitigating risks. With respect to natural analogues, CO_2 reservoirs (e.g. from magmatic sources) have been investigated to demonstrate that safe long-term containment is possible on the one hand and there are potential risks from leakage on the other hand. Industrial analogues investigated include the disposal of industrial waste in deep geological formations, the storage of natural gas, and the storage of radioactive waste. The study is supplemented with a review of the response of human health and ecosystems to elevated CO_2 concentrations. Maul et al. (2007) compared the long-term performance assessment of radioactive waste disposal and CO_2 storage.

Reservoir properties databases - Experimental data
Data which are available to the public and which are relevant for the study conducted here are rather sparse. A single database could be found with the properties of oil reservoirs in the U.S.A. (NPC, 1984). In the conditions of interest, Plug and Bruining (2007) measured capillary pressure-saturation relations for CO_2-water systems and Bennion and Bachu (2008) measured relative permeability-saturation relations for CO_2-water and H_2S-water systems. This indicates a great demand for further investigations. Only if comprehensive databases are accessible can developed methods be tested and verified.

Dimensional Analysis
Dimensional analysis is a mathematical procedure for describing complex system behaviour in an elegant way. All physically meaningful equations can be converted into a dimen-

sionless form, consisting only of dimensionless parameters and dimensionless constants. In experiments, the dimensionless parameters can be varied over their physically meaningful range and, by determining the unknown dimensionless constants, a system understanding can be developed in a very efficient way, even for complex systems. One key theorem is stated by Buckingham (1914), who gives a procedure for deriving dimensionless parameter sets. However, for complex systems influenced by many unknowns, numerous possibilities arise and the selection of the most physically meaningful dimensionless parameter set is left to the investigator. The dimensional analysis in this study is based on the studies of Hilfer and Øren (1996) and Manthey et al. (2008). The basic two-phase flow equations are non-dimensionalised by introducing characteristic values. Selecting physically meaningful characteristic values which depend on the problem of interest means that the complex system can be analysed by interpreting the variation of the dimensionless parameters.

Storage-capacity assessment

As outlined by Bachu et al. (2007), a variety of approaches and methodologies for assessing CO_2 storage capacity has led to conflicting results for local, regional and global estimates. At present, two major methodologies are proposed. Bachu et al. (2007) propose the concept of so-called "Resource-Reserve Pyramids" in which several aspects of CO_2 storage are considered, e.g. time scales, assessment scales, and various storage options (in saline aquifers, in enhanced gas recovery, etc.). For example the "Techno-Economic Resource-Reserve" pyramid consists of theoretical, effective, practical, and matched storage-capacity estimates, having the units of a volume. The uncertainty of the estimates is reflected by its place in the pyramid. The theoretical capacity is the entire pore space of a formation, reduced by the residual (irreducible) water fraction. Effective storage capacity is the estimate of interest in this study, since it is a subset of the theoretical capacity estimate, which satisfies a range of geological and engineering constraints and which can be estimated by numerical simulation. This corresponds to the term "resources". Computationally, the effective capacity can be estimated by multiplying the theoretical capacity by a capacity coefficient. Estimations of this capacity coefficient are, however, not given by the authors. The practical storage capacity is defined as the reserves, considering economic, legal and regulatory, infrastructure, and general economic aspects. The matched capacity then results from detailed source–sink matching. To obtain an estimate related to the mass of CO_2 that can be stored, the volume estimates are multiplied by the average in-situ CO_2 density. The concept proposed by NETL (2007) is computationally equivalent to the effective capacity estimate of Bachu et al. (2007) for saline formations if the residual (irreducible) water fraction is included in the capacity coefficient and if the average CO_2 density is used in the equation rather than minimum and maximum values (International Energy Agency Greenhouse Gas R&D Programme, 2008). As an advancement, the NETL (2007) approach provides estimates for the capacity coefficient. The estimates were gained by assuming minimum and maximum values for the relevant reservoir properties and processes (e.g. porosity, height of the reservoir, areal displacement efficiency, vertical displacement efficiency, etc.), with normal distributions of these proper-

ties and after Monte Carlo simulations (no numerical multi-phase flow simulations). The resulting capacity coefficient ranges between 1 and 4 % for the 15 – 85 % confidence interval. As an assumption, the CO_2 injection wells are placed regularly throughout the basin/region to maximise storage.

Sensitivity analysis
Sensitivity analysis in general is the study of how a variation in the model input translates into a variation in the model output. As such, it is a method that is widely applied in various fields. Saltelli et al. (2000) review various methodologies and evaluate the trade-off between the computational cost and the possible information to be gained. In this study, the method proposed by Morris (1991) and extensions thereof are applied. Campolongo et al. (2004) tested the Morris Method and stated that the method is efficient in identifying irrelevant model input factors.

Risk analysis
Risk analysis is in general the systematic study of how uncertainties propagate into risks encountered and the estimation of the impact. It assists in developing mitigation options for minimising or preventing harm. With respect to CO_2 storage, there is considerable uncertainty involved in the knowledge about the subsurface. Consequently, the risk of CO_2 leaking out of the storage formation is a major concern which needs to be taken care of. Celia and Bachu (2003) state that in North America, due to the large number of existing wells and due to the sparse knowledge about the state of those wells, the leakage of CO_2 does not seem to be avoidable, given the large spatial and temporal scales associated with CCS. Subsequently, Gasda et al. (2004) analysed the spatial characteristics of existing well locations in the Alberta basin (Canada) and state that a typical CO_2 plume can encounter up to several hundreds of wells in high-density areas. Nordbotten et al. (2004) developed the already mentioned semi-analytical solutions to efficiently describe plume evolution and leakage in these complex aquifer systems. This yields a useful tool for estimating risk for systems where risk is mainly associated with the existing wells and their largely unknown state. A more general and comprehensive screening and ranking framework is presented by Oldenburg (2007) for evaluating potential storage sites on the basis of risk to health, safety and the environment arising from possible CO_2 leakage. The framework is based on expert judgement on e.g. the relative importance, relative risk, and certainty of an assessment attribute. However, up to now, there is no consistent risk-assessment methodology for CCS projects.

Site screening and characterisation
Chadwick et al. (2008) suggest screening potential sites in a region for CO_2 storage by deriving key indicators. Such key indicators are related to the estimated storage capacity (e.g. reservoir height, porosity, etc.) and caprock properties (e.g. lateral continuity, thickness, capillary entry pressure). The indicators are evaluated in a positive/negative approach

and the outcome just serves as a guideline. International Energy Agency Greenhouse Gas R&D Programme (2008) extended this set by indicators like injectivity, site logistics (e.g. distance from CO_2 source), and potentially compromised natural resources (e.g. groundwater, coal, etc.). Site screening can be seen as the initial step to site characterisation, leading ultimately to site selection. After Friedmann (2007) it includes the characterisation of injectivity, storage capacity, and effectiveness (long-term ability to store CO_2). It involves detailed geological characterisation, numerical flow and transport modelling, geochemical and geomechanical assessment, risk assessment, monitoring programme design, and transport (International Energy Agency Greenhouse Gas R&D Programme, 2008). The approach by Oldenburg (2007) already mentioned may be considered as a site screening tool, based on risk. Site screening and in particular site characterisation depend heavily on data availability (e.g. maps, seismic data, well logs, etc.).

2 Conceptual, Mathematical and Numerical Model

One important step in numerical simulation is the development of a conceptual model, the translation of the conceptual model into a mathematical model, and the implementation into a numerical model. The conceptual model describes the essential features and principal processes of the system of interest, but simplifies or neglects minor features and processes so that the resulting computational cost of the simulation can be handled. The degree of abstraction of the real world system is therefore dependent on the scope of the investigation, but also on other constraints, like the level of knowledge about the system, the spatial and temporal scale of interest, and the availability of computational power. Nevertheless, it is most important not to over-simplify the system and to guarantee the essential features and principal processes. As previously stated, the focus of this study is the investigation of CO_2 injection processes in geological formations for site screening. The temporal scale of interest covers the injection stage. The advection dominated multi-phase flow and transport processes are of importance on this scale, together with diffusion, and dissolution of CO_2 into the resident brine. In site screening, it is assumed that only very few data about the geological formations are available. Hence, chemical reactions, contributing significant amounts to the overall CO_2 trapping only after some decades and requiring knowledge about the mineral composition of the reservoir rock, are not considered. Furthermore, geo-mechanical processes are neglected, since it is assumed that appropriate measures to prevent caprock fracturing can be applied when designing the injection facility. For such a system the conceptual model is defined in the following. The mathematical and numerical model is briefly introduced. The interested reader is however referred to Appendix A, since a detailed discussion may detract the readers attention from the focus of this study (and the model development was not part of this study).

2.1 Basic Definitions

2.1.1 Phases and Components

The term “phase” describes a well-defined region of matter, having a relatively homogeneous chemical composition and physical state. Two phases are separated by an interface. Across

this interface, mass transfer can occur from one phase to the other. Generally, one can distinguish between solid, liquid and gaseous phases. Several solid or liquid phases may coexist, whereas only one gas phase may occur. Each phase can be composed of one or several components. A component relates here to either a pure chemical substance or a mixture of chemical substances. To consider a mixture of substances, different components are lumped into a so-called pseudo-component. A pseudo-component employs (fraction-weighted) average properties of the pure substances and considers the interaction effects between the substances as well.

2.1.2 State of Aggregation

Any chemical substance can occur in a solid, liquid, and gaseous state of aggregation. A transition from one state of aggregation to another is possible by change of the so-called state variables. State variables are, for instance, temperature, pressure, mass, volume. The state variables characterise the thermodynamic state of the system and are independent of any previous state of the system. Generally, one can distinguish between intensive and extensive state variables. Intensive state variables are independent of the size of the system, hence temperature and pressure are intensive state variables. Extensive state variables, however, vary with system size, e.g. mass and volume. When dividing two extensive state variables, a specific intensive state variable is the result, e.g. specific volume$=\frac{\text{volume}}{\text{mass}}$. If the state of aggregation changes from one state to another, a phase-coexistence curve (also known as phase boundary) is crossed. At this curve, defined by a specific set of state variable values, the substance forms two stable phases. One example is the phase-coexistence curve that separates the gaseous from the liquid state of aggregation, the so-called vapour-pressure curve. When crossing the phase-coexistence curves, fluid properties usually change discontinuously. In Figure 2.1, a schematic diagram shows the different states of aggregation for CO_2.

Three phases coexist at the end points of a phase-coexistence curve. In Figure 2.1, this occurs at the critical point and at the triple point. At temperatures and pressures above the critical values ($p_{crit,CO2} = 7.38\,\text{MPa} = 73.8\,\text{bar}$, $T_{crit,CO2} = 304.1\,\text{K} = 30.95\,^{\circ}\text{C}$), the fluid is in a supercritical state of aggregation. This state of aggregation is of special interest for CO_2 in storage scenarios, since the resulting high fluid density allows an efficient utilisation of the available pore volume.

In a multi-phase system, the states of aggregation of the individual phases may change independently. Hence, different combinations of states of aggregation for the phases may occur.

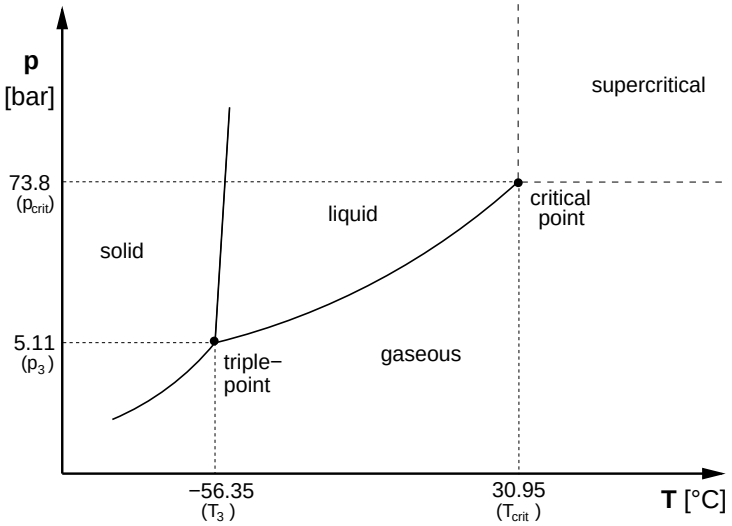

Figure 2.1: Schematic phase diagram of carbon dioxide, depending on pressure (p) and temperature (T). The liquid-gas phase boundary between the triple point and the critical point is known as the vapour-pressure curve (Lüdecke and Lüdecke, 2000).

2.1.3 Phase Change

In a multi-phase system, it is possible that fluid phases appear or disappear, e.g. due to displacement or due to mass transfer processes. A change in the number of locally present phases present is called a phase change. In the system investigated here, two fluid phases are considered, CO_2 and water. In each point in space, both fluid phases may occur, or only one of them.

To be more specific, two models are used in this study:
In the first (simpler) model (cf. Section A.1), one solid phase, one liquid water phase and one either liquid or gaseous CO_2 phase is considered. Whether the CO_2 phase is in a liquid or gaseous state of aggregation depends on the conditions at the considered (macroscopic) point of the system. The water phase is the water pseudo-component brine (cf. Section 2.1.1), taking into account the properties of pure water influenced by dissolved salt. The CO_2 phase assumes a pure CO_2 component.

In the second, more complex model (cf. Section A.2), one solid phase, one liquid water-component-rich phase (called water-rich phase in the following) and one either liquid or gaseous CO_2-component-rich phase (called CO_2-rich phase in the following) are considered. The water-rich phase can consist of the pseudo-component brine and a pure CO_2 component. The CO_2-rich phase consists of a CO_2 component only.

2.1.4 Equation of State

The equation of state (EOS) for a pure substance is a mathematical formulation describing the equilibrium relationship between pressure, temperature, and volume. Figure 2.2 shows a schematic diagram of such a relationship. Figure 2.1 is a projection of the pVT-surface onto the pT-plane. Van Der Waals (1873) proposed the first EOS as a polynomial of third order. Peng and Robinson (1976) extended this approach by modifying the original equation and introducing additional parameters. By parameter fitting, a good match can be obtained for most substances between the EOS given by Peng and Robinson (1976) and experimental results.

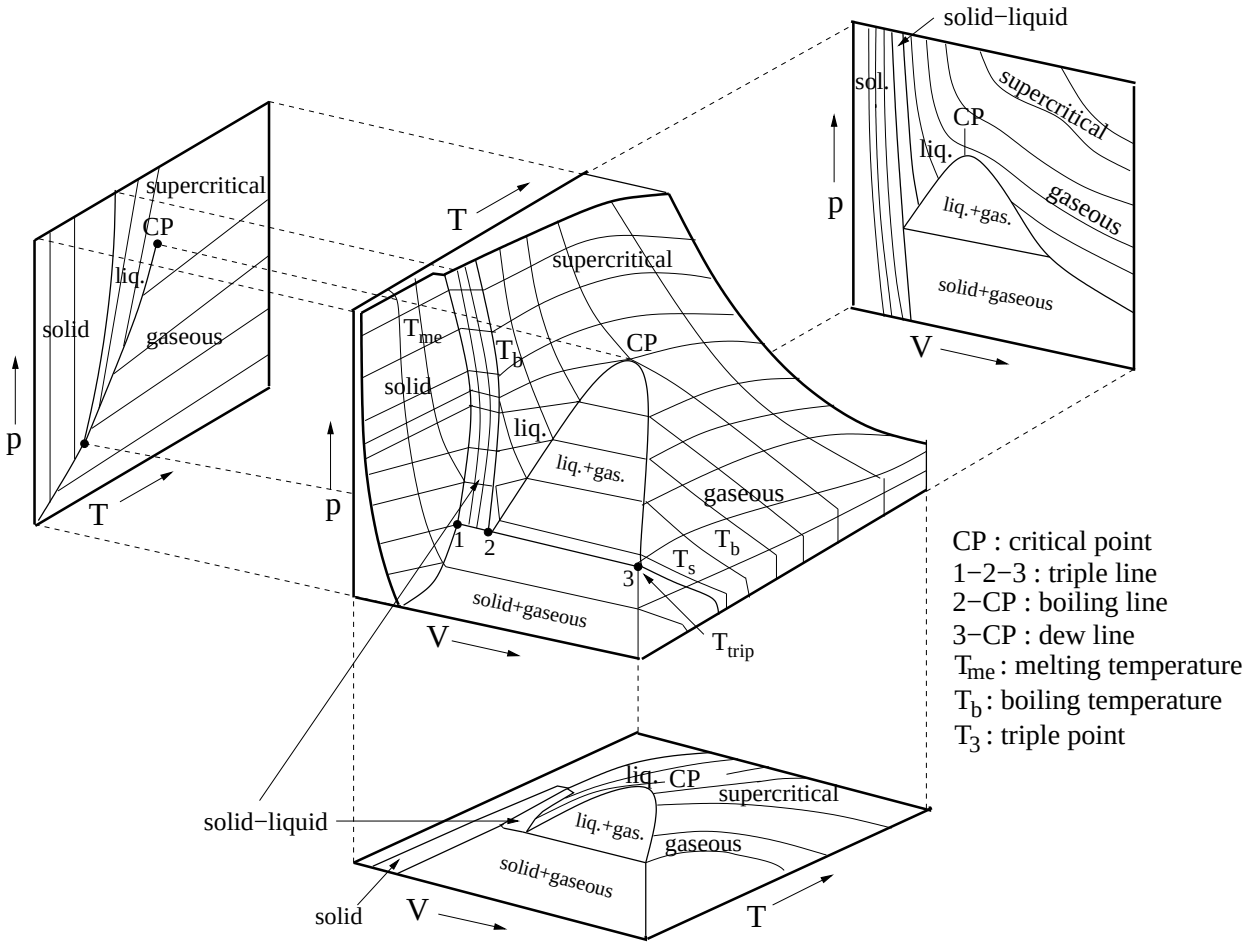

Figure 2.2: Schematic diagram of the equilibrium relationship between pressure (p), volume (V), and temperature (T) (known as the pVT-surface) of a pure substance which contracts upon freezing and projections onto the pT-, pV-, and VT-diagrams (Bielinski, 2006).

Mixtures of substances can also be described by an EOS by setting up mixing rules, taking into account the properties of the pure substances and the interaction effects between them.

2.1.5 Mole- and Mass Fraction

In a multi-component system, the properties of an individual phase generally depend on its composition. The composition can be described by mole or mass fractions. The mole fraction x of a component C in phase α is given by

$$x_\alpha^{\mathrm{C}} = \frac{n_\alpha^{\mathrm{C}}}{\sum_{\mathrm{C}} n_\alpha^{\mathrm{C}}}, \tag{2.1}$$

where n_α^{C} is the number of moles of component C in phase α. Similarly, the mass fraction X of component C in phase α is defined as

$$X_\alpha^{\mathrm{C}} = \frac{m_\alpha^{\mathrm{C}}}{\sum_{\mathrm{C}} m_\alpha^{\mathrm{C}}}, \tag{2.2}$$

where m_α^{C} is the mass of component C in phase α.

Mole and mass fractions add up to unity for each phase by definition:

$$\sum_{\mathrm{C}} x_\alpha^{\mathrm{C}} = \sum_{\mathrm{C}} X_\alpha^{\mathrm{C}} = 1. \tag{2.3}$$

The molecular weight M^{c} is the relation between these mass and mole fractions:

$$M^{\mathrm{c}} = m_\alpha^{\mathrm{C}} / n_\alpha^{\mathrm{C}}. \tag{2.4}$$

In the following, only mass fractions are used. In this study, the mass fractions of CO_2 in the water-rich phase $X_{\mathrm{w}}^{\mathrm{CO2}}$, and the mass fraction of water in the CO_2-rich phase $X_{\mathrm{CO2}}^{\mathrm{w}}$ are of importance.

2.1.6 Salinity

In deep geological formations, considerable amounts of salt are dissolved in the formation water. It is therefore often referred to as brine. To describe the amount of salt dissolved in the water-rich phase, the term "salinity" is introduced. Different definitions of salinity exist. In this study, salinity is defined as the mass fraction of salt related to the total mass of the solution [kg salt/kg solution]:

$$S = \frac{m_{\mathrm{salt}}}{m_{\mathrm{salt}} + m_{\mathrm{w}}}, \tag{2.5}$$

where S is salinity, m_{salt} is salt mass, and m_{w} is water mass.

2.2 System Properties

2.2.1 Spatial Scales

When investigating multi-phase flow and transport in porous media, the spatial and temporal scales of interest need to be defined. The description of processes may change depending on the scales and thus the influence of those processes on the model behaviour may change. Spatial scales of interest are discussed in the following:

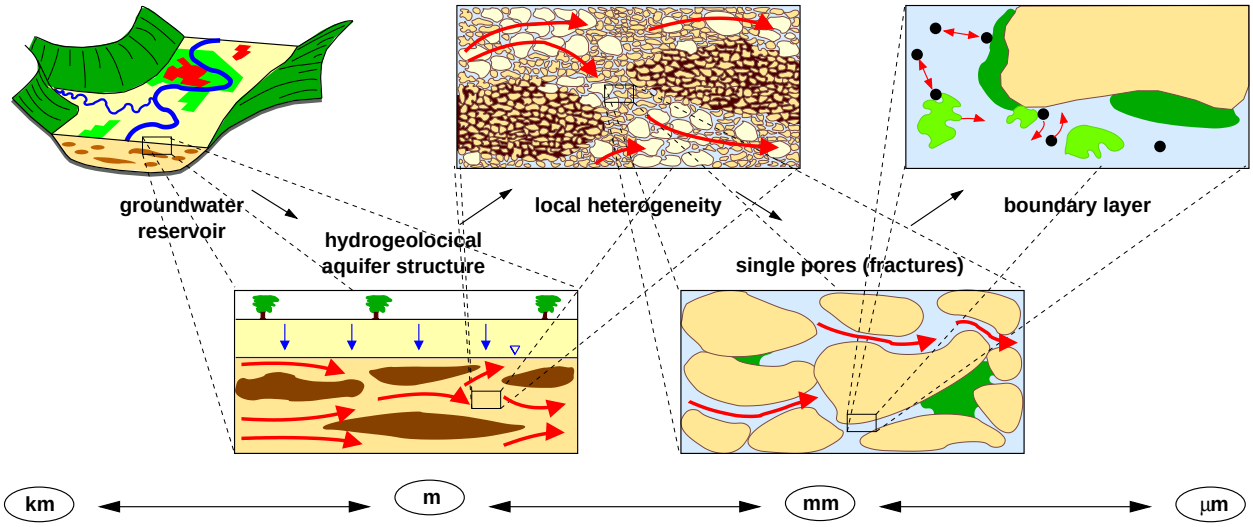

Figure 2.3: Different scales for fluid flow in porous media (modified after Kobus et al. (1996)).

On the molecular scale [$\sim 10^{-10}$m] the movement of individual molecules and the interaction with other molecules can be described. When such a system is modelled (e.g. in biochemistry), the computational cost is extremely high, even for small systems due to the large number of molecules ($6.0221 \cdot 10^{23}$) per mole of any substance.

On the microscale [$\sim 10^{-3}$m] an averaging is applied over individual molecules and their interactions. The "continuum approach" describes this averaging procedure over a sufficiently large number of molecules, consequently they can be assumed to be continuously distributed in space. Thus, new variables appear, e.g. density and viscosity. By solving the Navier-Stokes equations, multi-phase fluid flow can be described over a volume of several pores. Due to a lack of knowledge about realistic pore structures or the high cost of implementing these structures, simplified pore-network models are often used.

On the macroscale [$\sim 10^{-1}$m] the microscopic properties of the system are averaged within a defined volume. This volume is called the "representative elementary volume (REV)". It has to meet the requirement that the averaged properties are independent of minor

changes in volume size. Figure 2.4 shows schematically the definition of a REV for the volume fraction of the pore space within the respective volume, known as porosity on the macroscale. For small volume sizes, the pore space fraction fluctuates. When the volume is increased up to a certain minimum REV size, indicated by V_0, the pore space fraction (porosity) remains constant. When the volume is further increased, there is a limit where heterogeneities start to influence the averaging procedure; this represents the maximum REV size. As already indicated, new variables appear as a result of the averaging on the macroscale, these are e.g. porosity and saturations of the individual phases. This means that the distribution of the fluids in the pore space is not described exactly any more, but expressed by the volume fraction S_α the fluid occupies within the pore space of the respective volume. This is expressed in Equation 2.6:

$$S_\alpha = \frac{\text{volume occupied by phase}\,\alpha}{\text{total volume of pores}}, \tag{2.6}$$

where the sum of all fluid phase volume fractions has to be unity, i.e. the pore space is filled by the considered fluids:

$$\sum_\alpha S_\alpha = 1. \tag{2.7}$$

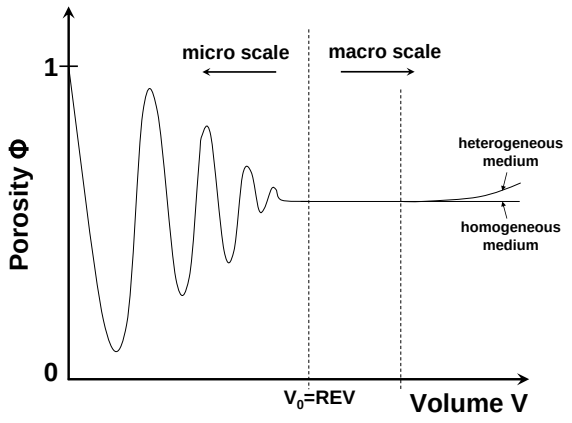

Figure 2.4: Definition of a representative elementary volume modified after Bear (1972).

On the field scale [$\sim 10^2$m] no additional averaging procedure occurs. The properties of this scale result from the averaging procedure described previously on the macroscale and the occurring heterogeneities are described by the REV properties. The field scale describes the scale of interest in this study. A typical geological formation considered for CO_2 storage extends laterally up to several kilometers. In a vertical direction, the scale of interest ranges from a few meters (for a thin injection formation only) up to some hundred meters (by considering several formations).

2.2.2 Fluid Properties

Density

One can distinguish between molar and mass density. Molar density is defined as the number of moles n per volume V

$$\varrho_{\mathrm{mol}} = \frac{n}{V}. \tag{2.8}$$

Similarly, mass density is defined as mass m per volume

$$\varrho_{\mathrm{mass}} = \frac{m}{V}. \tag{2.9}$$

In this study, only mass density is used. Generally, the density of a fluid depends on pressure, temperature, and its composition. The density of (pure) gases is often described by the ideal gas law

$$p\,V = n\,R\,T, \tag{2.10}$$

where R is the ideal gas constant (8.31447 J/(mol K)). With the identities given in Equations 2.4 and 2.9, the ideal gas law can be reformulated to

$$\varrho_{\mathrm{mass}} = \frac{p\,M}{R\,T}. \tag{2.11}$$

Thus, the density of an ideal gas increases with increasing pressure and decreasing temperature. The ideal gas law represents an equation of state (cf. Section 2.1.4) which neglects the size of the molecules and the intermolecular attractions. Thus, it is most accurate at at low pressures (i.e. large volumes) and at high temperatures (i.e. high thermal kinetic energy). The density of carbon dioxide and water at the conditions of interest here, i.e. high pressures and temperatures, cannot be described by the ideal gas law. In the following, the approaches for calculating the phase densities are given as used in the model.

Carbon-dioxide-rich phase density

A high-precision EOS given by Span and Wagner (1996) is used to calculate pure CO_2 density including the discontinuities at the phase-coexistence curve (i.e. when CO_2 changes from a gaseous to a liquid state of aggregation or vice versa). The influence of water dissolved in the CO_2-rich phase is neglected, since only very small amounts of water dissolve in CO_2. In Figure 2.5, the variation of CO_2 density with the depth of the reservoir and thus with increasing pressure is shown for three geothermal gradient conditions (the geothermal gradients reflect typical values (high, median, low) derived in a database analysis given in Chapter 3). The geothermal gradient indicates temperature increase with depth below surface.

For the high geothermal gradient case, CO_2 density increases gradually with depth. The vapour-pressure curve is not crossed when conditions change from the gaseous state to supercritical. For low and median geothermal gradients, however, the vapour-pressure curve

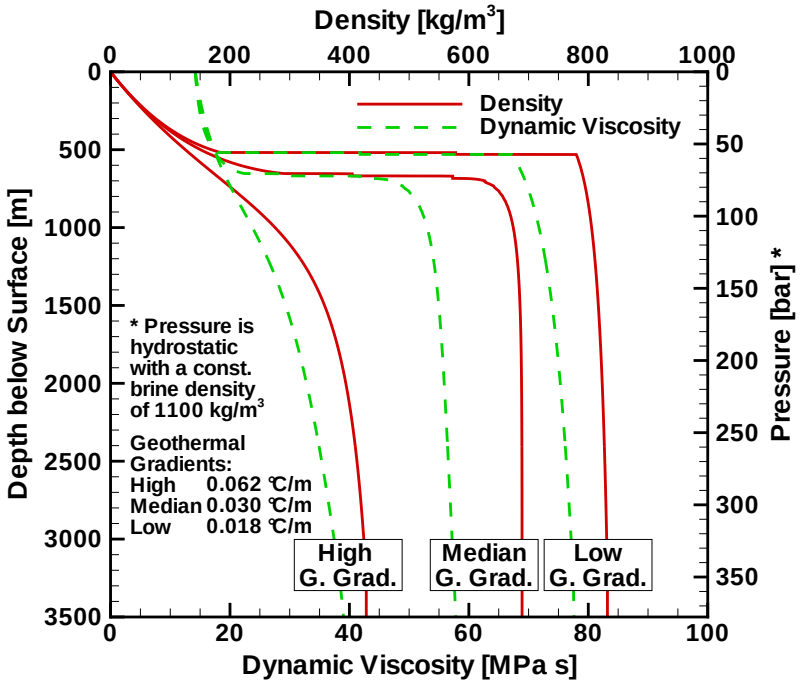

Figure 2.5: Variation of carbon-dioxide density and dynamic viscosity with depth for various geothermal gradients (high geothermal gradient = 0.062 °C/m, median geothermal gradient = 0.03 °C/m, low geothermal gradient = 0.018 °C/m). A surface temperature of 10 °C and a hydrostatic pressure distribution corresponding to a water-rich phase with density of 1100 kg/m^3 are assumed.

is crossed, as indicated by the discontinuous increase in density at a depth of around 520 metres for the low geothermal gradient and 650 metres for the median geothermal gradient.

Water-rich phase density

In the conditions of interest here, pure water always occurs in a liquid state of aggregation. The IAPWS (1997) formulation is used to calculate (pure) water density. However, since the water-rich phase consists of a water/salt pseudo-component and a pure CO_2 component, these influences need to be accounted for. Batzle and Wang (1992) present an approach for taking into account the density increase due to dissolved salt $\Delta\varrho(S)$ and the approach given by Garcia (2001) accounts for the density increase due to dissolved CO_2 $\Delta\varrho(T, p, X_{\mathrm{w}}^{\mathrm{CO2}})$. Hence, the water-rich phase density ϱ_{w} is calculated as (Bielinski, 2006)

$$\varrho_{\mathrm{w}} = \varrho_{\text{pure water}}(T, p) + \Delta\varrho(S) + \Delta\varrho(T, p, X_{\mathrm{w}}^{\mathrm{CO2}}). \tag{2.12}$$

Figure 2.6 shows variations in the water density as a result of varying pressure, temperature, and salinity. Density decreases with pressure and salinity, and increases with temperature.

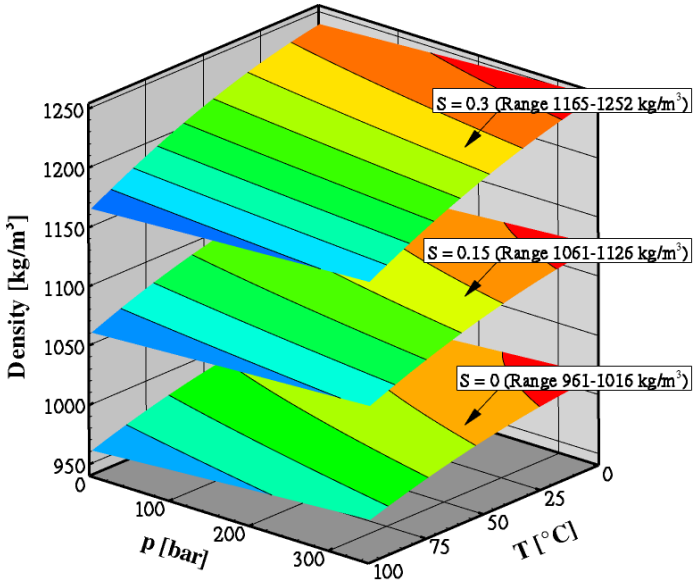

Figure 2.6: Variation of water density with pressure p and temperature T for salinity values of 0.0 (bottom plane), 0.15 (centre plane), and 0.3 (top plane).

Viscosity

Viscosity is a fluid's internal resistance to flow. The dynamic viscosity μ is the relation of the fluid's shear stress τ and the velocity gradient in the direction perpendicular to the direction of flow dv/dn

$$\mu = \frac{\tau}{dv/dn}. \tag{2.13}$$

For some cases, it may be advantageous to use the kinematic viscosity ν, which is dynamic viscosity divided by the fluid's density ($\nu = \mu/\varrho$). Generally, the viscosity of a fluid is a function of pressure, temperature, and its composition.

Carbon-dioxide-rich phase viscosity

The approach given by Fenghour et al. (1998) is used to calculate the dynamic viscosity of (pure) CO_2. In Figure 2.5, the variation of CO_2 dynamic viscosity with the depth of the reservoir and thus with increasing pressure is shown for three geothermal gradients. For the conditions of interest here, viscosity increases with pressure and decreases with temperature. One can observe the same behaviour as already seen for CO_2 density, i.e. a continuous increase of viscosity with depth for the high geothermal gradient case (here the vapour-pressure curve is not crossed when conditions change from the gaseous state to supercritical); for the low and median geothermal gradient cases, however, the vapour-pressure curve is crossed, and a discontinuous increase of viscosity is observed.

Water-rich phase viscosity

The dynamic viscosity of the water-rich phase is calculated after an approach given by Batzle and Wang (1992). The equations take into account temperature and salinity. The influence of pressure is small and can thus be neglected. Figure 2.7 shows the variation of water viscosity with temperature and salinity.

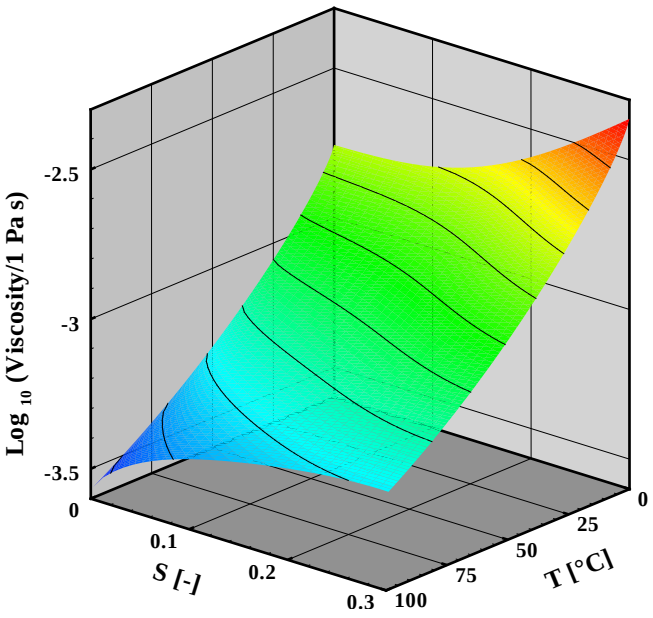

Figure 2.7: Variation of water dynamic viscosity with temperature T and salinity S.

Enthalpy

To describe non-isothermal processes occurring during the injection of CO_2 into porous media, the caloric state variables enthalpy and internal energy are introduced. Internal energy is related to the molecular structure and the degree of molecular activity in a system. For a gaseous fluid, the internal energy is mainly composed of kinetic energy due to motion of the molecules. For a solid or liquid fluid, considerable contributions are also made by the potential energy of attraction or repulsion in between individual molecules. The extensive state variable enthalpy (H) can be described by adding volume-changing work to the extensive internal energy (U):

$$H = U + p\,V. \tag{2.14}$$

Intensive state variables can be calculated by dividing the system by mass:

$$h = u + p\,v = u + \frac{p}{\varrho}, \tag{2.15}$$

where h is specific enthalpy, u specific internal energy, and v specific volume. For gases, the volume-changing work influences enthalpy considerably, since compressibility is usually high

and density variations with pressure are high. For liquids having only a low compressibility, the influence may be of minor importance. For mixtures of substances, the individual contributions of the components need to be considered as well as the heat of dissolution of the components.

Carbon-dioxide-rich phase enthalpy

The enthalpy of (pure) CO_2 is calculated after an approach given by Span and Wagner (1996) as a function of pressure and temperature. Figure 2.8 shows the specific enthalpy of CO_2 with respect to the reference state, i.e. $h = 0\,\mathrm{kJ/kg}$ at $p_{CO2} = 1.013\,\mathrm{bar}$ and $T = 0\,^{\circ}\mathrm{C}$.

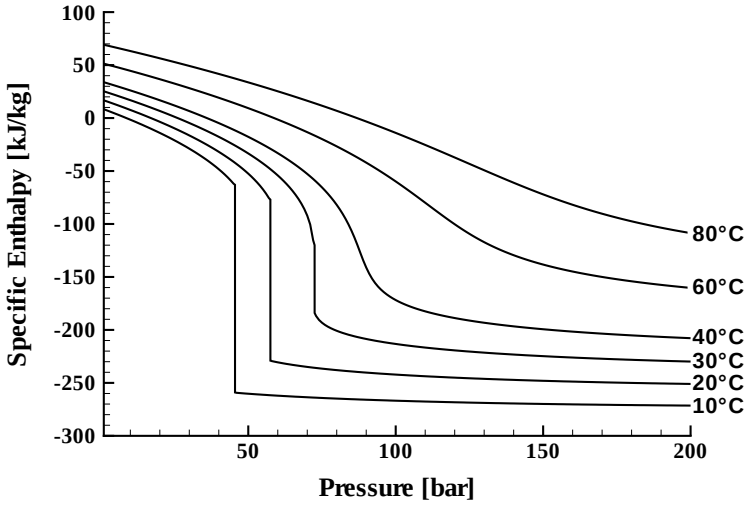

Figure 2.8: Variation of specific enthalpy of CO_2 with pressure for various temperature levels (after Bielinski (2006)).

The reference states of the CO_2-rich phase and the water-rich phase have to be identical to quantify enthalpy changes correctly. Span and Wagner (1996) use a reference state of $p_{CO2} = 1.013\,\mathrm{bar}$ and $T = 25\,^{\circ}\mathrm{C}$, resulting in a constant difference in specific enthalpy of $21.91\,\mathrm{kJ/kg}$. However, differences in specific enthalpy are not affected by this selection of the reference state (Bielinski, 2006). If the vapour-pressure curve is crossed, e.g. for the $10\,^{\circ}\mathrm{C}$ curve at a pressure of $45.5\,\mathrm{bar}$, there is a discontinuous decrease in specific enthalpy. For supercritical temperatures (or pressures), this is not observed.

Water-rich phase enthalpy

Water-rich phase enthalpy is calculated dependent on pressure, temperature and on the amount of the dissolved components salt and CO_2, as

$$\begin{aligned} h_{\text{water-rich phase}} = & \underbrace{(1 - X_{\text{w}}^{\text{NaCl}} - X_{\text{w}}^{\text{CO2}}) \cdot h_{\text{pure water}}(T,p)}_{\text{enthalpy of pure water}} \\ & + \underbrace{X_{\text{w}}^{\text{NaCl}} \cdot h_{\text{NaCl}}(T) + X_{\text{w}}^{\text{NaCl}} \cdot (\Delta h_{\text{L}}(T))_{\text{NaCl}}}_{\text{enthalpy change due to dissolved salt}} \\ & + \underbrace{X_{\text{w}}^{\text{CO2}} \cdot h_{\text{CO2}}(T,p) + X_{\text{w}}^{\text{CO2}} \cdot (\Delta h_{\text{L}}(T))_{\text{CO2}}}_{\text{enthalpy change due to dissolved } CO_2}, \end{aligned} \tag{2.16}$$

where $h_{\text{pure water}}$ is the enthalpy of pure water (dependent on pressure and temperature), h_{NaCl} is the enthalpy of salt (dependent on temperature), and h_{L} indicates heat of dissolution (dependent on temperature) (Garcia, 2003). Figure 2.9 shows the variation of specific enthalpy of water, salt, and CO_2 and variation of the heat of dissolution of CO_2 in the water-rich phase with temperature at a constant pressure of 100 bar. The specific enthalpy of pure water is calculated after IAPWS (1997) and the specific enthalpy of CO_2 follows the approach of Span and Wagner (1996). The specific enthalpy of NaCl is calculated by

$$h = u = \int c(T)\, dT, \tag{2.17}$$

where c is the specific heat capacity of salt, taken from Daubert and Danner (1989). The volume-changing work is neglected here, i.e salt is assumed to be incompressible.
The heat of dissolution of CO_2 in water $\Delta h_{\text{L}}(T)_{\text{CO2}}$ is calculated after Duan and Sun (2003) and is negative in the temperature range of interest; thus, the dissolution causes a warming of the water-rich phase (exothermic reaction) and overall water-rich phase enthalpy is reduced. The heat of dissolution of salt in water $\Delta h_{\text{L}}(T)_{\text{NaCl}}$ (after Michaelides (1981), including the corrections after Gudmundsson and Thrainsson (1989)) is positive for the entire temperature range considered here; hence, the dissolution causes a cooling of the water (endothermic reaction).

To summarise, Table 2.1 gives on overview of the fluid-property dependencies and literature sources used.

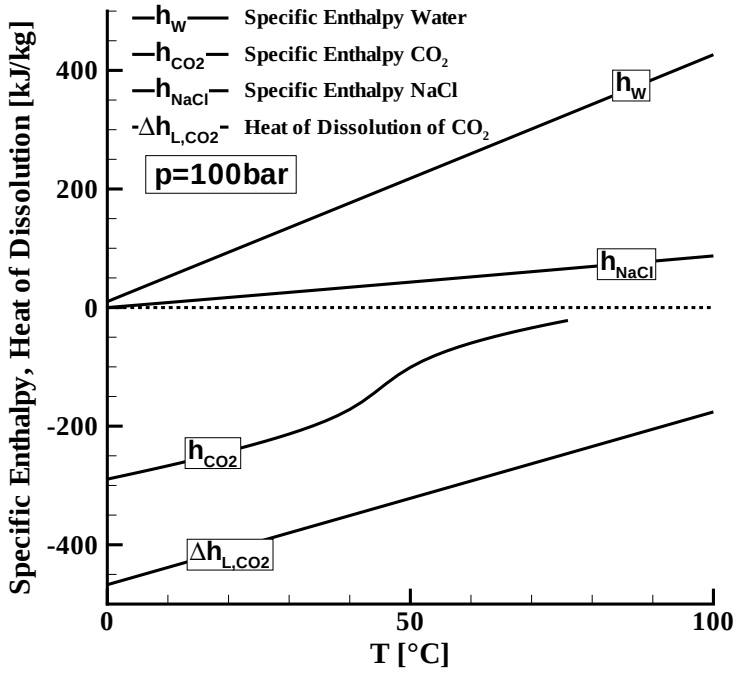

Figure 2.9: Variation of specific enthalpy and heat of dissolution of CO_2 in the water-rich phase with temperature at a constant pressure of 100 bar.

Fluid property	Dependency	Literature Source
CO_2-rich phase density ϱ_{CO2}	$f(T,p)$	Span and Wagner (1996)
CO_2-rich phase enthalpy h_{CO2}	$f(T,p)$	Span and Wagner (1996)
CO_2-rich phase viscosity μ_{CO2}	$f(T,p)$	Fenghour et al. (1998)
Water-rich phase density ϱ_w	$f(T,p,S,X_w^{CO2})$	IAPWS (1997), Batzle and Wang (1992), Garcia (2001),
Water-rich phase enthalpy h_w	$f(T,p,S,X_w^{CO2})$	IAPWS (1997), Michaelides (1981), Daubert and Danner (1989), Duan and Sun (2003)
Water-rich phase viscosity μ_w	$f(T,S)$	Batzle and Wang (1992)

Table 2.1: Fluid properties of CO_2-rich- and water-rich phase and dependencies on temperature (T), pressure (p), salinity (S), and mass fraction of CO_2 in the water-rich phase (X_w^{CO2}) (Bielinski, 2006).

2.2.3 Matrix Properties

In this study, the matrix properties are considered on the macroscale (cf. Section 2.2.1). The matrix properties described in this section are sole properties of the porous medium, thus independent of the fluid properties and the matrix is assumed to be rigid, immobile, and inert.

Porosity

Porosity has already been introduced exemplarily as a soil property on the macroscale. Total porosity describes the volume fraction of the pore space compared to the entire volume of the representative elementary volume (REV):

$$\phi = \frac{V_{\text{pore space}}}{V}. \tag{2.18}$$

This study always refers to effective porosity, i.e. the fraction of total porosity that is accessible to fluid flow. In comparison to the total porosity (as described above), effective porosity excludes e.g. pore fractions occupied by water bound to soil particles or isolated pores that are not connected.

Permeability

The absolute (intrinsic) permeability $\mathbf{k}$ is a measure of the resistance of a porous medium to transmitting fluids. Generally, the absolute permeability is dependent on the properties of the pore space, such as the porosity and several structural parameters of the porous medium (e.g. tortuosity of the flow channels). However, there is no exact method of calculating permeability and in practice it needs to be measured, e.g. by pumping tests (using Darcy's law, cf. Section 2.3.1), or to be estimated using empirically derived dependencies (e.g. on grain-size distribution). Approaches to estimating the absolute permeability, e.g. depending on the pore space geometry, have been made by Pape et al. (1999). Absolute permeability may vary over several orders of magnitude, even for a single rock type such as sandstone (Clauser, 1992). The related hydraulic permeability $\mathbf{k}_\text{f}$ is dependent on both the properties of the porous medium and the properties of the fluid of interest:

$$\mathbf{k}_\text{f} = \mathbf{k}\,\frac{\varrho\, g}{\mu}, \tag{2.19}$$

where g is gravity. Absolute and hydraulic permeability are tensorial quantities and in the typical geological formations of interest here, they may also vary by orders of magnitude depending on the direction of flow.

Heat Capacity

Heat capacity is a measure of the heat energy required to increase the temperature of a substance or system. It is an extensive state variable. With respect to this study, specific

heat capacity is more relevant. It is defined as the heat energy required to increase the temperature of a unit mass of a substance or system by a certain temperature interval. Here it is always referred to kJ/(kg K). For substances or systems with considerable compressibility, it may be necessary to distinguish between specific heat capacity at constant pressure or at constant volume. In this study, however, the porous medium is assumed to be incompressible, which leads to identical specific heat capacity at constant pressure and at constant volume, referred to as the specific heat capacity of the soil grains c_s. Moreover, the energy content of the fluid phases is described using the specific internal energy (u) (see Section 2.2.2).

2.2.4 Fluid-Matrix Interaction Properties

Besides the sole properties of the porous medium and the fluids flowing inside the pores, interaction properties exist which depend on both individual properties and which influence the multi-phase flow processes considerably. The interaction properties are described here on the macroscale; however, a description of the underlying process on the microscale is given as well.

Residual Saturation

The residual saturation defines the minimum saturation that is attainable for a fluid when displaced from a porous medium by another immiscible fluid. It is a measure of the fluid which cannot be displaced, due to viscous forces. On the microscale, the wetting phase (in this study, always the water-rich phase) residual saturation is caused by strong capillary forces that prevent further fluid displacement. For the non-wetting phase (in this study, always the CO_2-rich phase), this is caused by entrapped fluid bubbles in larger pores. It is also possible that a fluid phase is trapped in several pores if it is entirely surrounded by the other phase. The residual saturation is not only dependent on the properties of the porous medium and the fluids, but also on the history of displacement processes that occurred in the system. This is discussed further in Section 2.2.4 (Hysteresis). If the fluids are considered to be miscible, however, saturations smaller than the residual saturation can be attained for the displaced fluid (e.g. due to dissolution or evaporation).

Capillary Pressure

The effect of capillarity is caused by intermolecular forces in a multi-phase system. Two types of forces can be distinguished: adhesive forces caused by the interaction of different molecules (e.g. water and CO_2) and cohesive forces caused by interaction of molecules of the same substance. Cohesion is the driving force causing a fluid to diminish the interface area to another fluid and is thus the cause for interfacial tension (also named surface tension). Interfacial tension is the amount of work necessary to increase this interface area by one unit, usually written in J/m^2 or as N/m. Figure 2.10 illustrates the interfacial tension between CO_2 and water in the conditions of interest here.

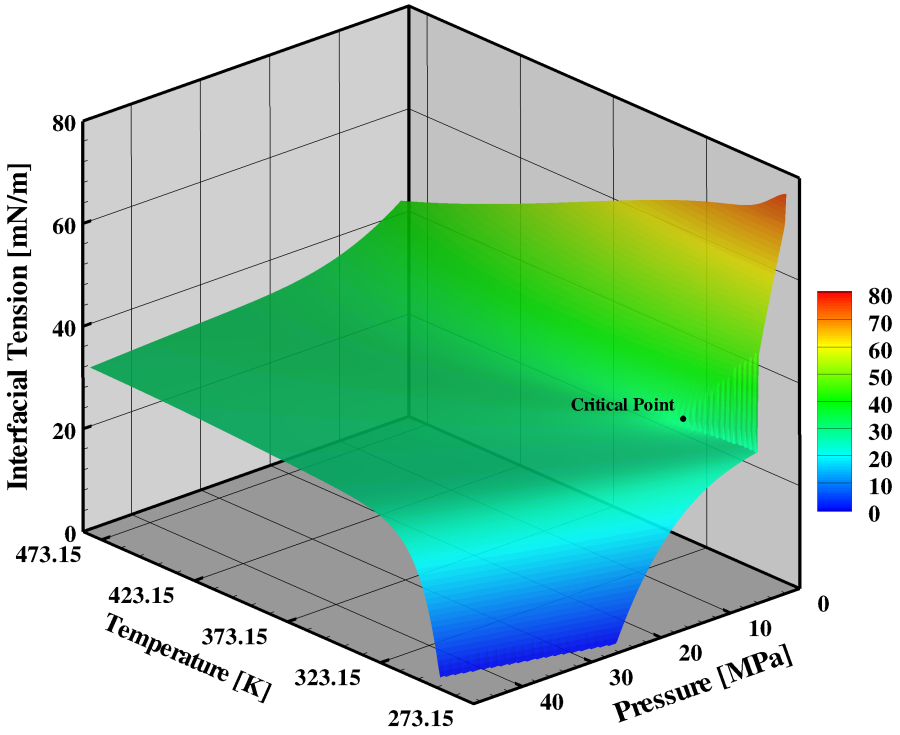

Figure 2.10: Interfacial tension between CO_2 and water dependent on pressure and temperature after an equation given by Kvamme et al. (2007). Accuracy is reported to be greater than 95 % within the experimental range. The experimental range includes temperatures between 278 K and 335 K and pressures between 0.1 MPa and 20 MPa. The range included in this study (cf. Chapter 7) is expanded beyond the experimental range; however, interfacial tension does not vary significantly at high pressures and temperatures (corresponding to great depth). At shallower depth, pressure and temperature conditions are covered by the experimental range.

In Figure 2.11, a sketch of the effect of interfacial tensions in a porous medium is shown. The contact angle Θ is dependent on the interfacial tensions after Youngs's equation (Helmig, 1997). Contact angles smaller than 90 degrees indicate the wetting fluid. At the equilibrium level h, the surface tension σ of the free liquid surface causes capillary forces F_{cap} that are in equilibrium with the gravitational forces F_{grav} of the wetting-phase (w) column,

$$2\pi\, r\, \sigma\, cos(\Theta) = \pi\, r^2\, \mathrm{h}\, g\, \varrho_\mathrm{w}, \tag{2.20}$$

where r is the radius of the capillary tube. Hence, the equilibrium level h can be formulated as

$$\mathrm{h} = \frac{2\,\sigma\, cos(\Theta)}{r\, g\, \varrho_\mathrm{w}}. \tag{2.21}$$

Reformulating Equation 2.21 ($\mathrm{h} = \frac{p}{\varrho\, g} + z$) yields the capillary pressure p_c

$$p_\mathrm{c} = \frac{2\,\sigma\, cos(\Theta)}{r}. \tag{2.22}$$

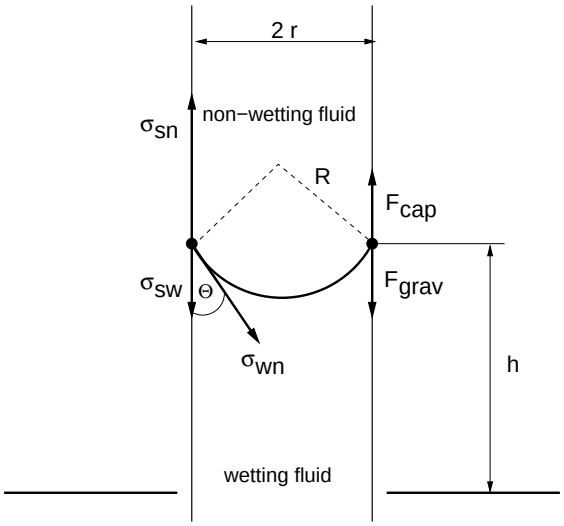

Figure 2.11: Single capillary tube with interfacial tensions between solid and non-wetting fluid σ_{sn}, between solid and wetting fluid σ_{sw}, and between wetting and non-wetting fluid σ_{wn}. Capillary forces $\mathrm{F_{cap}}$ cause a rise of the wetting fluid in the capillary tube until equilibrium is reached with gravitational forces $\mathrm{F_{grav}}$, indicated here at level h. Between the fluid interface and the solid wall, the so-called contact angle Θ is defined (after Ochs (2006)).

At the interface, the continuity of pressure is valid as

$$p_{\mathrm{c}} = p_{\mathrm{n}} - p_{\mathrm{w}}, \tag{2.23}$$

where p_{n} is the pressure of the non-wetting phase. Since the microscopic properties of the system are averaged within a defined volume on the macroscale, the capillary pressure cannot be described as outlined above. On the macroscale, capillary pressure is hence either measured or described by semi-empirical formulations. Two very common formulations for describing capillary pressure on the macroscale are given by Brooks and Corey (1964) and Van Genuchten (1980). The authors describe capillary pressure as a function of the wetting phase saturation by introducing additional fitting parameters to match laboratory experiments. The so-called "capillary pressure-saturation relation" after Brooks and Corey (1964) is given as

$$p_{\mathrm{c}} = p_{\mathrm{d}}\, S_{\mathrm{e}}^{\ -\frac{1}{\lambda_{\mathrm{BC}}}} \tag{2.24}$$

where p_{d} describes the capillary entry pressure, necessary to drain the biggest pore of a initially fully wetting-phase saturated porous medium, λ_{BC} is used as a fitting parameter to adapt the formulation to different grain-size distributions of porous media, and S_{e} is the effective saturation that accounts for the residual wetting-phase saturation (c.f Section 2.2.4). It is calculated after

$$S_{\mathrm{e}} = \frac{S_{\mathrm{w}} - S_{\mathrm{w,r}}}{1 - S_{\mathrm{w,r}}}. \tag{2.25}$$

Little information is available in the literature on capillary pressure-saturation relations for CO_2-brine systems. Plug and Bruining (2007) measured and discussed capillary pressure-saturation relations for CO_2-water systems. Bennion and Bachu (2006) measured capillary pressure-saturation relations at reservoir conditions for potential CO_2 storage reservoirs in the Alberta basin in Canada. Figure 2.12 (left) shows measured data along with a Brooks and Corey model employing parameter settings as given in Table 2.2.

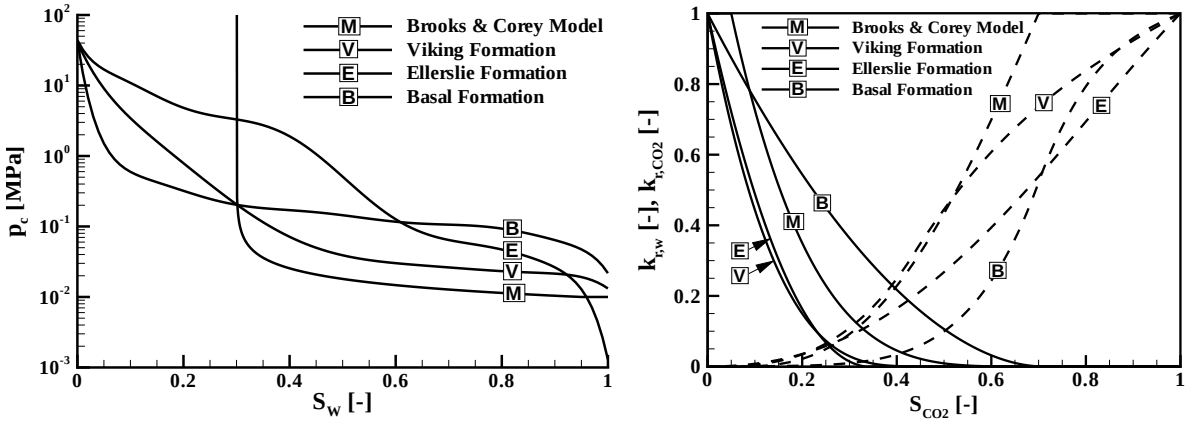

Figure 2.12: Capillary pressure-saturation relations (left) after Bennion and Bachu (2006) measured for CO_2-brine systems in cores of the Alberta basin in Canada (Viking, Ellerslie, and Basal Formations) and for a Brooks and Corey model (Brooks and Corey, 1964) employing input parameter settings as given in Table 2.2. Relative permeability-saturation relations (right) modified after Bennion and Bachu (2008) for the same reservoirs described above and for the same Brooks and Corey model. Letter coding according to Section 3.4, where these relations are used to define typical reservoir cases (full lines: brine; broken lines: CO_2).

Relative Permeability

Relative permeability accounts for the fact, that, if multiple fluids share the same pore space of a porous medium to flow, they interfere with each other. This can be explained by reduced pore throats available to each fluid to flow and by the increased tortuosity of the flow paths (since e.g. small pores might be fully saturated by the wetting-phase and the non-wetting phase has to circumvent these pores). However, due to the complexity of the pore geometry, these microscale considerations can only be represented qualitatively on the macroscale (Helmig, 1997).

On the macroscale, the effect of relative permeability is accounted for by multiplying the absolute permeability $\mathbf{k}$ by a dimensionless value $k_{\mathrm{r},\alpha}$, called the relative permeability, that is specific for each phase. Since $k_{\mathrm{r},\alpha}$ ranges between zero and one, $\mathbf{k}$ is always reduced. As

Case	$S_{w,r}$	$S_{CO_2,r}$	$\lambda_{BC,w}$	$\lambda_{BC,CO2}$	p_d [Pa]
Brooks-Corey Model	0.3	0.05	2.0	2.0	10000
Viking Formation	0.558	0.044	2.9	3.2	-
Ellerslie Formation	0.659	0.034	2.1	2.2	-
Basal Formation	0.294	0.035	1.8	5.0	-

Table 2.2: Residual saturations for water ($S_{w,r}$) and CO_2 ($S_{CO_2,r}$) and Brooks and Corey (1964) model parameters (λ_{BC} and p_d) for measured relative permeability-saturation relations (Bennion and Bachu, 2008) and for a synthetic model. The Brooks and Corey model parameters (λ_{BC}) for the measured relative permeability relations were obtained by optimisation in a regression analysis (Bennion and Bachu, 2008).

for the capillary pressure, relative permeability is either measured or described by semi-empirical formulations as a function of the wetting-phase saturation. For saturations below the residual saturations, $k_{r,\alpha}$ is zero for this phase, which means the phase is immobile.
The Brooks & Corey model introduced to describe capillary pressure on the macroscale (Section 2.2.4) can be used to derive a relative permeability-saturation relation (Burdine, 1953) as:

$$\begin{aligned} k_{r,w} &= S_e^{\frac{2+3\lambda_{BC}}{\lambda_{BC}}}, \\ k_{r,n} &= (1-S_e)^2 \cdot \left(1 - S_e^{\frac{2+\lambda_{BC}}{\lambda_{BC}}}\right). \end{aligned} \tag{2.26}$$

In this approach, the effective saturation used is $S_e = \frac{S_w - S_{w,r}}{1 - S_{w,r} - S_{n,r}}$.

As for the capillary pressure relations, little information is available on measured relative permeability relations for CO_2-brine systems. Figure 2.12 (right) shows measured relations for the formations in Canada already mentioned together with a Brooks and Corey model with parameter settings as discussed before. The relative permeabilities for CO_2 have been extrapolated to a value of one for water saturations lower than the residual water saturations. This makes the relations useful for simulations involving evaporation of water into the CO_2 phase, in which case the water saturation could be lower than the residual value.

Hysteresis

In general, hysteresis is a property of a system that exhibits path-dependence to arrive at a state of the system. With respect to this study, hysteresis is observed in the capillary pressure- and relative permeability-saturation relations, which means that the actual value of p_c and k_r is dependent on the history of the displacement processes that occurred in the system. Several reasons are considered to be responsible for this effect (on the microscale), i.e. a difference in the contact angle Θ for drainage (displacement of the wetting-fluid by

the non-wetting fluid) and imbibition (displacement of the non-wetting-fluid by the wetting fluid) processes (cf. Section 2.2.4), varying pore-throat diameters relevant for the drainage and imbibition process, and the already discussed effect of entrapped, non-wetting phase fluid bubbles (cf. Section 2.2.4) causing a change in the residual saturation. In recent years, various authors (Flett et al. (2005), Spiteri et al. (2005), Juanes et al. (2006), Doughty (2007), Leicht (2007), Spiteri et al. (2008)) studied hysteretic behaviour by experiments or numerical investigations and described its effect on various questions of interest related to CO_2 storage in geological formations. However, hysteresis is not included in this study since literature data on the underlying capillary pressure- and relative permeability-saturation relations is still sparse.

Thermal Conductivity

Thermal conductivity λ_{i} is a measure of the ability of a material to conduct heat. It varies by a factor of 2–3 for any given rock type and depends on fluid saturation, porosity, dominant mineral phase, temperature, pressure, and the pore space filling fluid (Clauser and Huenges (1995), Clauser (2006)). Generally, thermal conductivity is a tensor. Especially for sedimentary rocks, thermal conductivity might be anisotropic. Clauser and Huenges (1995) and (Clauser, 2006) review thermal-conductivity measurement techniques, correlation with other physical parameters (e.g. porosity) depending on the type of rock (sedimentary, metamorphic, volcanic, and plutonic) and discuss rock-type specific dependency on various factors. The authors conclude that literature data (even rock-type specific) might not provide site-specific information. This is due to the large variability in thermal conductivity depending on the factors mentioned above.

However, since λ_{i} is mostly measured in a vertical direction, it is assumed here to be isotropic. Furthermore, thermal conductivity is dependent on fluid saturation only. The thermal conductivity of the fluid-filled porous medium λ_{pm} is described using an approach proposed by Somerton et al. (1974)

$$\lambda_{\mathrm{pm}} = \lambda_{\mathrm{pm}}(S_{\mathrm{w}} = 0) + \sqrt{S_{\mathrm{w}}} \left(\lambda_{\mathrm{pm}}(S_{\mathrm{w}} = 1) - \lambda_{\mathrm{pm}}(S_{\mathrm{w}} = 0) \right), \tag{2.27}$$

where $\lambda_{\mathrm{pm}}(S_{\mathrm{w}} = 0)$ is the thermal conductivity of the dry porous medium and $\lambda_{\mathrm{pm}}(S_{\mathrm{w}} = 1)$ is the thermal conductivity in fully water-saturated conditions.

2.2.5 Equilibrium Assumptions

Local thermodynamic equilibrium is assumed in this study, i.e. local thermal, mechanical, and chemical equilibrium. Thermal equilibrium is valid if the temperatures in all phases (including the solid phase) are identical. Mechanical equilibrium is valid here as the capillary pressure difference between the phases on the macroscale is assumed. Chemical equilibrium

is valid if the chemical potential of a component is identical in all phases. The implications of this assumption on the mathematical and numerical model will be discussed in Sections A.1.3 and A.2.4. Local thermodynamic equilibrium can be justified by assuming slow flow velocities.

2.3 Flow and Transport Processes

To describe flow and transport in a multi-phase system, several processes need to be considered. These processes might show a highly non-linear behaviour and usually occur simultaneously.

2.3.1 Advection

The movement of a fluid phase due to a piezometric head gradient is called advection. The velocity of a phase in a porous medium can be described by Darcy's law (Darcy (1856), Bear (1972)):

$$\mathbf{v} = -\mathbf{k}\,\frac{\varrho\,\mathrm{g}}{\mu}\cdot\nabla\mathrm{h}, \tag{2.28}$$

where $\mathbf{v}$ is the Darcy velocity, and h is the piezometric head as $\mathrm{h} = \frac{p}{\varrho\,g} + z$. Darcy's law is valid for laminar flow indicated by Reynolds numbers smaller than one. The dimensionless Reynolds number relates inertial to viscous forces and can be calculated for a porous medium by

$$\mathrm{Re} = \frac{\mathrm{v\,d}}{\nu}, \tag{2.29}$$

where v is the fluid flow velocity and d is the mean pore diameter.

Darcy conducted his experiments for fully water-saturated conditions. To describe the phase velocity in a multi-phase system, Darcy's law is extended to (Helmig, 1997)

$$\mathbf{v}_\alpha = -\mathbf{k}\,\lambda_\alpha\Big(\nabla p_\alpha - \varrho_\alpha\,\mathrm{g}\,\nabla z\Big), \tag{2.30}$$

where λ_α is phase mobility, p_α is phase pressure, and z is elevation. The mobility is calculated as

$$\lambda_\alpha = \frac{k_{\mathrm{r},\alpha}}{\mu_\alpha}. \tag{2.31}$$

The Darcy velocity describes the flow velocity on the macroscale; thus, it neglects the pore geometry. To obtain the particle velocity, the Darcy velocity is divided by porosity.

The advective mass flux $\mathbf{q}^{\mathrm{C}}_{\alpha\mathrm{a}}$ of component C in phase α can be calculated by multiplying the Darcy velocity with the density of the phase, the mass fraction of the component in the phase, and the cross-sectional area A.

$$\mathbf{q}^{\mathrm{C}}_{\alpha,\mathrm{a}} = \varrho_\alpha \, X^{\mathrm{C}}_\alpha \, \mathbf{v} \, A. \tag{2.32}$$

2.3.2 Buoyancy

Fluid flow due to buoyancy forces is already described by the Darcy velocity. It is caused by density differences within one phase or between different phases. It is an important process in CO_2 storage in geological formations, since the CO_2-rich phase typically has a much lower density than the water-rich phase (cf. Section 2.2.2), causing the CO_2-rich phase to migrate upwards (against gravity). To prevent CO_2 from rising further, appropriate trapping mechanisms are required. This is discussed in Section 1.1.

Assuming hydrostatic conditions, the pressure gradient in z-direction is:

$$\nabla p_\alpha = \varrho_{\mathrm{w}} \, \mathrm{g}. \tag{2.33}$$

Inserting Equation 2.33 into Equation 2.30 yields the CO_2-rich phase flow velocity due to buoyancy forces, $\mathbf{v}_{\mathrm{CO2,b}}$:

$$\mathbf{v}_{\mathrm{CO2,b}} = -\mathbf{k} \, \lambda_{\mathrm{CO2}} (\varrho_{\mathrm{w}} - \varrho_{\mathrm{CO2}}) \, \mathrm{g} \, \nabla z. \tag{2.34}$$

Multiplying Equation 2.34 with the CO_2-rich phase density, the mass fraction of the component in the CO_2-rich phase, and the cross-sectional area A yields the mass flux of component C in the CO_2-rich phase due to buoyancy forces

$$\mathbf{q}^{\mathrm{C}}_{\mathrm{CO2,b}} = \varrho_{\mathrm{CO2}} \, X^{\mathrm{C}}_{\mathrm{CO2}} \, A \, \mathbf{v}_{\mathrm{CO2,b}}. \tag{2.35}$$

2.3.3 Molecular Diffusion

Molecular diffusion is a transport process that equilibrates differences in the density or velocity of molecules due to Brownian molecular movement. The net transport always occurs against the gradient of molecule density or velocity. Translated to the macroscale, the molecule density or velocity corresponds to quantities like concentration, pressure, and temperature. The mass flux due to molecular diffusion $\mathbf{q}^{\mathrm{C}}_{\alpha,\mathrm{d}}$ can thus be expressed as (Fick's first law)

$$\mathbf{q}^{\mathrm{C}}_{\alpha,\mathrm{d}} = -\varrho_\alpha \, \mathrm{D}^{\mathrm{C}}_{\mathrm{pm}} \, \nabla X^{\mathrm{C}}_\alpha \, A, \tag{2.36}$$

where $\mathrm{D}^{\mathrm{C}}_{\mathrm{pm}}$ is the diffusion coefficient of component C dissolved in phase α in the porous medium. Class (2001) suggested describing $\mathrm{D}^{\mathrm{C}}_{\mathrm{pm}}$ depending on the binary diffusion coefficient of component C in water $\mathrm{D}^{\mathrm{C}}_\alpha$ as

$$\mathrm{D}^{\mathrm{C}}_{\mathrm{pm}} = \tau \, \phi \, S_\alpha \, \mathrm{D}^{\mathrm{C}}_\alpha. \tag{2.37}$$

where τ is the tortuosity of the pore channels.

2.3.4 Mechanical Dispersion

The term mechanical dispersion is referred to as a transport process due to fluctuations in the velocity profile of the fluid. Micro- and macrodispersion can be distinguished. Microdispersion occurs on the microscale due to the parabolic shape of the velocity profile inside the pore channels. Macrodispersion occurs on the macroscale due to the heterogeneous properties of the porous medium, resulting in macroscale velocity fluctuations. Mechanical dispersion can be described similarly to diffusion, allowing the combination of the diffusion coefficient $\mathrm{D}^{\mathrm{C}}_{\mathrm{pm}}$ with a dispersion coefficient. However, knowledge about values of such dispersion coefficients is sparse in general and not available for the system of interest here (it also depends on the distribution of the phases); for these reasons mechanical dispersion is not included.

2.3.5 Heat Conduction

Similar to molecular diffusion, heat conduction describes the transfer of heat which equilibrates differences in temperature. The heat flux always occurs in the opposite direction to the temperature gradient. The heat flux $\mathbf{q}_{\mathrm{h}}$ through a cross-sectional area A using Fourier's law (e.g. Baehr and Stephan (1998)) is expressed as

$$\mathbf{q}_{\mathrm{h}} = -\lambda_{\mathrm{i}} \nabla T \, A, \tag{2.38}$$

where λ_{i} is the heat conductivity of a material.

In a multi-phase system, the temperatures of each phase (including the solid phase) may be different; hence, heat conduction needs to be described separately for each phase. However, due to small flow velocities in the problem of interest here which allows enough time for temperature equilibration among the phases, a single temperature value can be assumed for all phases. Consequently, a single thermal-conductivity value λ_{pm} is used in this study, as defined in Section 2.2.4.

2.3.6 Heat Convection

Heat convection is the heat transport due to the movement of fluid. It is possible to distinguish between heat convection due to temperature induced density differences, called free convection, and heat convection due to externally imposed pressure gradients, e.g. due to mass injection or withdrawal through a well, called forced convection. Heat convection is taken into account here by the advective term in the energy balance equation (cf. Section A.2.3). Heat transport due to radiation is neglected here.

2.3.7 Inter-Phase Mass and Energy Transfer

For the model taking into account the mutual dissolution of the component CO_2 and water into the water-rich phase or the CO_2-rich phase respectively (cf. Section 2.1.3), a mass and energy transfer between the phases can occur if both phases occur locally. Figure 2.13 shows a sketch of this model concept.

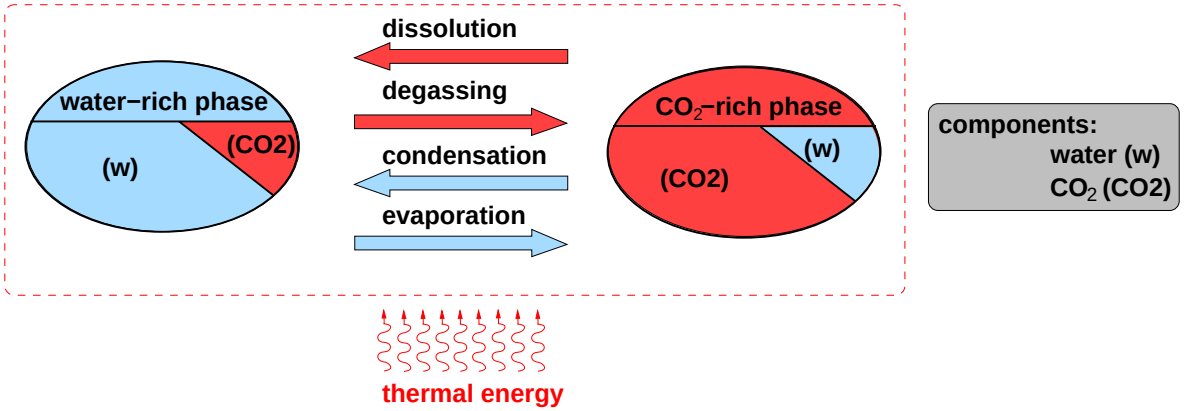

Figure 2.13: Non-isothermal two-phase two-component model concept for the CO_2-water system.

The water-mass fraction in the CO_2-rich phase is however is considered constant in this concept since it is at least one order of magnitude smaller than the CO_2-mass fraction in the water-rich phase in the conditions of interest here. Moreover, only few approaches exist in the literature which describe the change of the CO_2-rich phase properties due to the evaporation/dissolution of water (Bielinski, 2006).

The mass transfer of the CO_2 component between the phases is of importance here. Carbon dioxide dissolves in water, producing a weak acid according to the chemical reaction

$$CO_2 + H_2O \;\rightarrow\; H_2CO_3 \;\rightarrow\; HCO_3^- + H^+ \;\rightarrow\; CO_3^{2-} + 2H^+, \tag{2.39}$$

where in common notation H_2CO_3 is carbonic acid, HCO_3^- is hydrogen carbonate, and CO_3^{2-} is carbonate. The change of the pH-value and chemical reactions with the rock (porous medium) or other chemicals (e.g. impurities of the injected CO_2) are not considered here. Kinetic effects are also neglected and the resulting mass fraction of CO_2 in the water-rich phase in equilibrium conditions is dependent on the pressure, temperature, and salt content. Bielinski (2006) compared various approaches by different authors describing an EOS to quantify the amount of dissolved CO_2. Accordingly, the proposed approach by Duan and Sun (2003) is used in the following. Figure 2.14 shows the resulting variation of the CO_2 mass fraction in brine with pressure and salinity at different temperatures.
The energy transfer between the phases is included in the model concept by calculating the water-rich phase enthalpy depending on the CO_2 mass fraction (cf. Section 2.2.2).

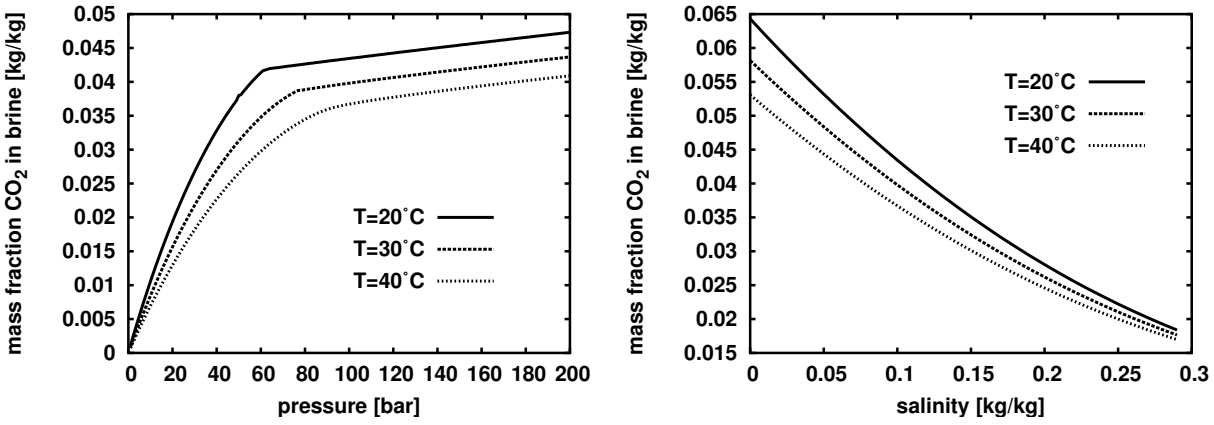

Figure 2.14: Variation of the CO_2 mass fraction in brine with pressure at a constant salinity of 0.1 kg/kg (left) and with salinity at a constant pressure of 100 bar (Bielinski, 2006).

2.4 Mathematical and Numerical Model - Overview

The mathematical and numerical model is given in detail in Appendix A since the development was not part of this study and the detailed discussion may detract the reader's attention from the focus of this study. In this Section a short overview is given.

The model follows an Eulerian approach where a set of balance equations is derived for a fixed control volume. In order to solve this set of balance equations, a number of closure relations are defined. The set of balance equations is solved numerically for the independent unknowns, the so-called "primary variables". Since two levels of complexity are considered to describe the relevant processes, consequently two types of mathematical and numerical models are derived in this study. These types of models are called "modules" in the following. The first module, called 2p-module, considers (only) isothermal multi-phase processes in porous media (cf. Section A.1). The second module, called 2p2cni-module, considers non-isothermal multi-phase multi-component processes in porous media (cf. Section A.2). The sections describing the initial and boundary conditions (Section A.3) and the linearisation and solution (Section A.5) apply to both modules. The section describing the discretisation of the differential equations in space and time (Section A.4) is shown exemplarily for the 2p2cni-module. The 2p- and 2p2cni-modules are implemented in the simulation platform MUFTE-UG, described in the follwing Section.

2.5 The Simulation Platform MUFTE-UG

The numerical simulator used for this study is the research code MUFTE-UG, jointly developed by the Universities Stuttgart and Heidelberg. MUFTE stands for **Mu**ltiphase **F**low, **T**ransport and **E**nergy model. This software package mainly contains the physical

model concepts and discretisation methods for isothermal and non-isothermal multi-phase multi-component flow and transport processes in porous and fractured-porous media (Helmig (1997), Helmig et al. (1998), Class et al. (2002), Assteerawatt et al. (2005)). UG is the abbreviation for **U**nstructured **G**rid. This toolbox provides the data structures and fast solvers for the discretisation of partial differential equations based on parallel, adaptive multigrid methods (Bastian et al., 1997). MUFTE-UG's special advantages also include the data structures for unstructured grids, functional parallelisation, especially designed for MIMD (**M**ultiple **I**nstruction stream, **M**ultiple **D**ata stream) parallel computers and adaptive local grid refinement.

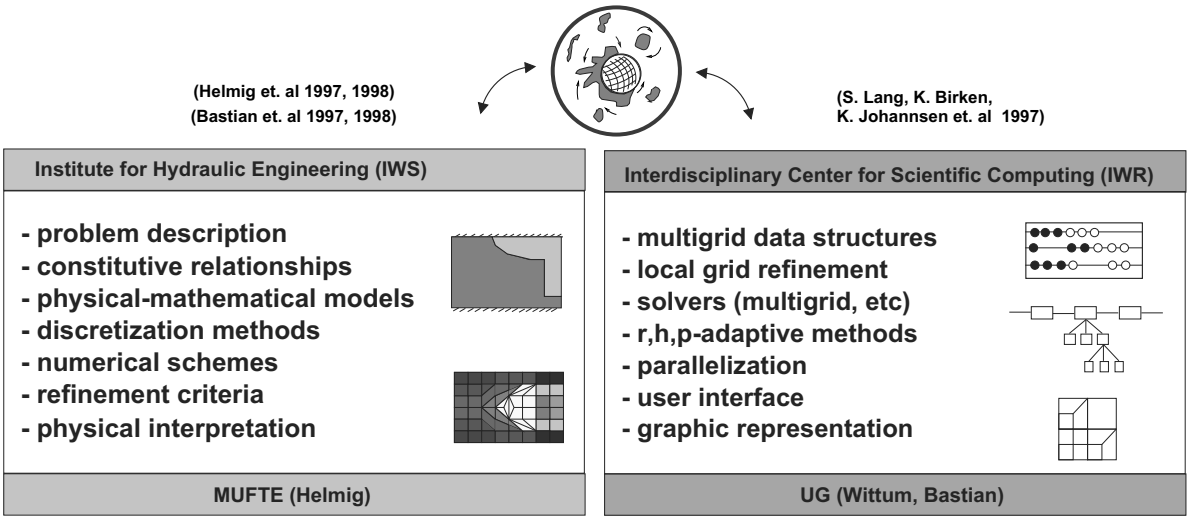

Figure 2.15: The simulation platform MUFTE-UG.

The simulation platform MUFTE-UG, especially the 2p- and 2p2cni-modules referred to here (Sections A.1 and A.2), has been extensively tested in code intercomparison studies and provides results in good agreement with other commercial and non-commercial codes (Pruess et al. (2003)). Detailed information on the capabilities of MUFTE-UG to simulate CO_2 storage in geological formations is given in Bielinski (2006).

3 Properties of Potential Geological Formations*

To investigate CO_2 injection processes in geological formations it is of importance to have a good knowledge of the range and distribution of the relevant reservoir parameters. These parameter ranges and distributions form the basis for setting up e.g. typical reservoirs allowing the definition of a number of random reservoir parameter setups respecting the statistical characteristics of parameter distributions. Statistical characteristics of reservoir parameters relevant for CO_2 storage on the reservoir scale can be calculated from the U.S. National Petroleum Council public database (NPC, 1984). The database was developed for the assessment of the United States' enhanced oil recovery potential in 1984. Today, it is part of the very comprehensive TORIS (**T**otal **O**il **R**ecovery **I**nformation **S**ystem) database. In this database, 2540 oil reservoirs are listed, accounting for over 64 % of the original oil-in-place estimated to exist in discovered crude oil reservoirs in the U.S.A.. The entire TORIS database is unfortunately not available for analysis. Nevertheless, the available public part comprises about half the total number of reservoirs listed in TORIS.

3.1 Calculated Statistical Characteristics

The collected data are suitable for an analysis of parameters of potential CO_2 storage reservoirs, as oil reservoirs are found within sedimentary basins. Sedimentary basins contain geological formations generally suitable for CO_2 storage if they exhibit both high porosity to store significant amounts of CO_2 and high injectivity (permeability) to economically inject CO_2 (Bachu, 2003). Moreover, (depleted) oil and gas reservoirs are especially favourable for CO_2 storage because they have proven their capability to store buoyant oil or gas for geological periods of time. Additionally, economic benefits of enhanced oil and gas recovery make use of those reservoirs likely. But again, the intent of this study is the analysis of CO_2 injection and storage processes in saline formations. Other geological formations are also suitable for CO_2 storage, but unfortunately no comprehensive database is known to the author. Therefore, one assumption is made here: statistical characteristics of parameters of

*This Chapter is published in Kopp, A., Class, H. and Helmig, R., Investigations on CO_2 storage capacity in saline aquifers - Part 1: Dimensional analysis of flow processes and reservoir characteristics, Int. J. Greenhouse Gas Control, 3(3), 263–276, DOI:10.1016/j.ijggc.2008.10.002, 2009.

saline formations do not differ fundamentally from those shown in the following for oil and gas reservoirs derived from the NPC database. Consequently the statistical characteristics can be used to evaluate CO_2 injection and storage in aquifers. The NPC database gives average parameter values for the entire reservoir. The histograms of porosity, logarithm of the intrinsic permeability, geothermal gradient, and mean reservoir depth below the surface are shown in Figure 3.1.

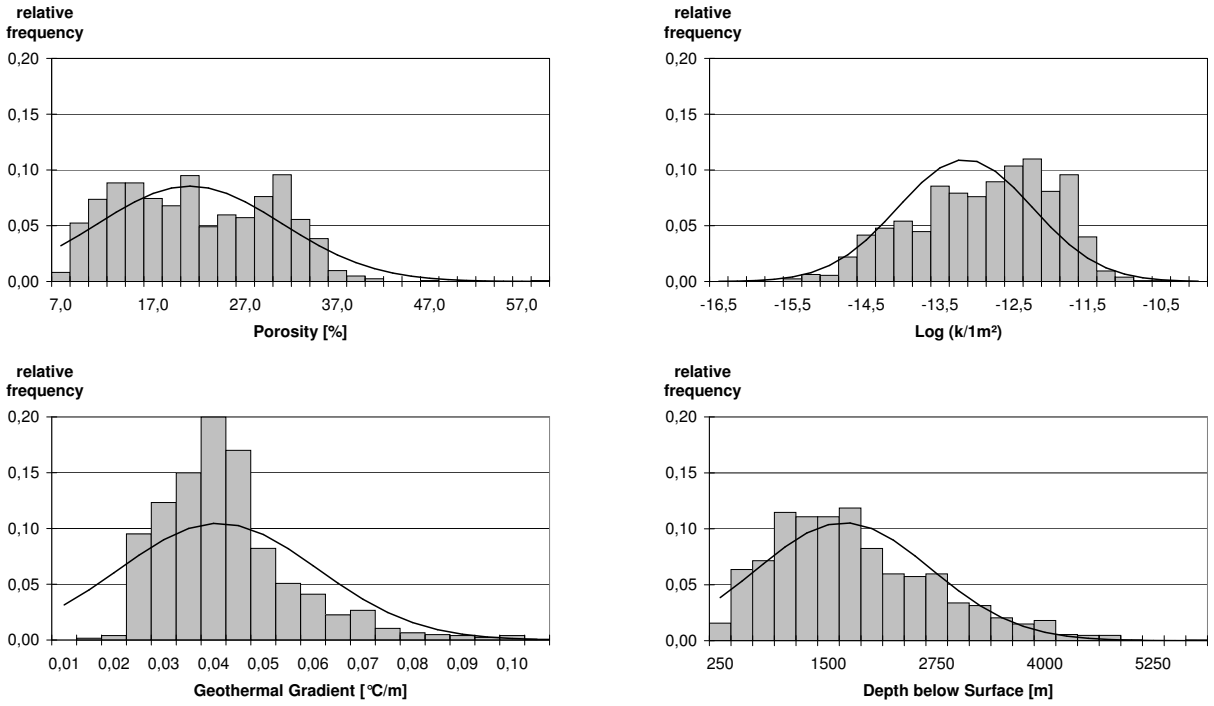

Figure 3.1: Histograms data show relative frequency of porosity [%] (top-left), absolute permeability [m^2] (top-right), geothermal gradient [$\frac{^\circ C}{m}$] (bottom-left), and reservoir depth below surface [m] (bottom-right) derived from the NPC database. Lines indicate normal or log-normal distributions having the same statistical characteristics as the respective histogram data sets.

Statistical characteristics are given in Table 3.1. Due to data errors in the records, only a portion of the reservoir data are used in the analysis. A typical error are negative data entries, e.g. negative porosity. The number of data values used (n) is given for each parameter in Table 3.1.

3.2 Test on Hypothesised Statistical Distributions

All data sets were tested by the Kolmogorov-Smirnov test (e.g. Laha and Chakravarti (1967)) to determine whether they differ significantly from a hypothesised distribution. The test statistics are calculated according to the sample size (n) and the maximum difference (a)

Parameter	n	Min	Max	A. Mean	Median	5^{th} Percentile	95^{th} Percentile
Log (k/1m^2)	1275	-16.00 0.1mD	-10.57 26.9D	-13.03 93mD	-12.91 123mD	-14.64 2.29mD	-11.71 1.95D
G.grad [°C/m]	1250	0.009	0.298	0.036	0.03	0.018	0.062
ϕ [%]	1222	7	58	21	20	9	34
Depth [m]	1273	17	5502	1680	1524	386	3495
Salinity [kg/kg]	924	0.000	0.231	0.068	0.048	0.001	0.185
Dip. A. [°]	441	0.0	25.0	7.6	4.0	0.5	25.0

Table 3.1: Statistical characteristics for reservoir parameters in the NPC-database: logarithm of total absolute permeability (Log (k/1m^2)), geothermal gradient (G.grad), porosity (ϕ), depth below surface, salinity and dip angle. Stated are the number of values in data sets (n), minimum (Min), maximum (Max), arithmetic mean (A. Mean), median, 5^{th} and 95^{th} percentile of the data. Maximum values for absolute permeability, geothermal gradient, and porosity seem to be unrealistic. However, in the further course of the study only median, 5^{th}, and 95^{th} percentile values are used (cf. definition of typical reservoirs in Section 3.4).

between the cumulative probability of the data and the cumulative probability of the hypothesised distribution (e.g. a normal distribution). The test statistics are calculated according to Equation 3.1.

$$a = \sup_x |\,\widetilde{F}(x) - F(x)\,| \tag{3.1}$$

where $\widetilde{F}(x)$ denotes the cumulative probability of the data and $F(x)$ the cumulative probability of the hypothesised distribution. The test statistics (multiplied by $\sqrt{n}$) are compared to a threshold. The threshold depends on a level of significance to be specified. The tested hypothesised distributions are a normal distribution and a log-normal distribution for all parameter data sets. See Figure 3.2 for cumulative probability plots of the permeability and geothermal gradient data sets, the hypothesised distributions and the test statistic (a).
The (null) hypothesis, i.e. that the data sets investigated follow either a normal or log-normal distribution, was rejected for all reasonable thresholds. Consequently, standard probability distributions cannot be used further in this study.

3.3 Test on Mutual Parameter Interrelations

All parameters given in the NPC database are tested for mutual interrelations. Figure 3.3 shows variation of absolute permeability with porosity, variation of absolute permeability

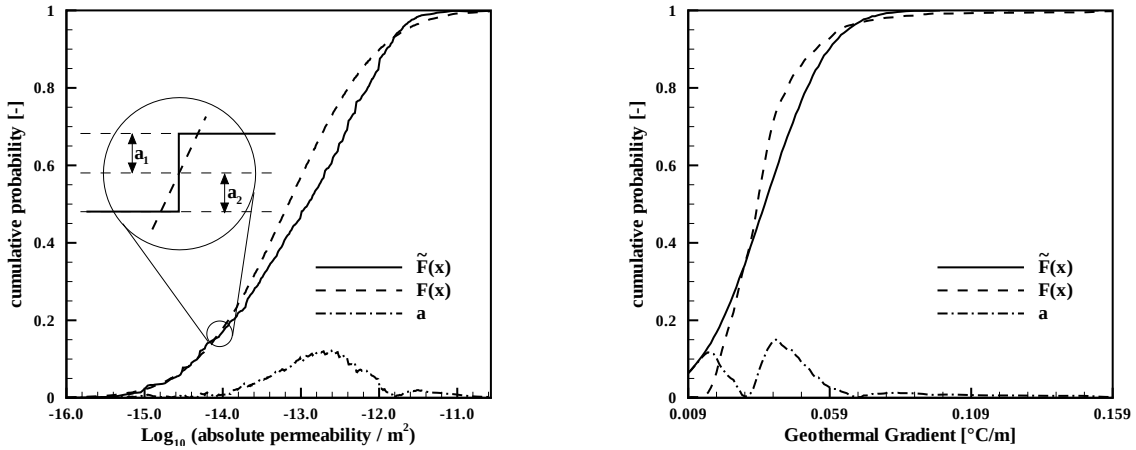

Figure 3.2: Kolmogorov-Smirnov test on absolute permeability and geothermal gradient. The cumulative probability of a log-normal distribution is shown, having absolute permeability parameters ($F(x)$, left) and a normal distribution having geothermal gradient parameters ($F(x)$, right), the cumulative probability of the data ($\widetilde{F}(x)$) and the difference between those two (a). Inset: Since the data are a piecewise constant function and the hypothesised distribution is continuous, a difference can be calculated to the left (a_1) and to the right (a_2) of the considered position x. The larger one is selected as a.

with depth, and variation of porosity with depth. The correlation coefficients are shown in the boxes.
Due to the low correlation coefficients, mutual interrelation of investigated parameters can be rejected. The hypothesized interrelation between absolute permeability and porosity will be further investigated in Chapter 7.

3.4 Definition of Typical Reservoirs

Typical reservoirs are defined employing parameters given in Table 3.1, except for the dip angle which is set to zero.

Case M The median reservoir case assumes median parameters for absolute permeability (123 mD†), geothermal gradient (0.03 °C/m), porosity (20 %), depth below surface (1524 m) and salinity (0.048 kg/kg). A Brooks and Corey model (Brooks and Corey, 1964) capillary pressure-saturation relation and relative permeability-saturation relation is assumed employing the input parameter set as given in Table 2.2.

Cases W and C The warm (W) and cold (C) reservoir cases have the same median parameters, except for the geothermal gradient; here the 5$^{\text{th}}$ and 95$^{\text{th}}$ percentile values are

†1D=$9.86932 \cdot 10^{-13}\text{m}^2 \approx 10^{-12}\text{m}^2$

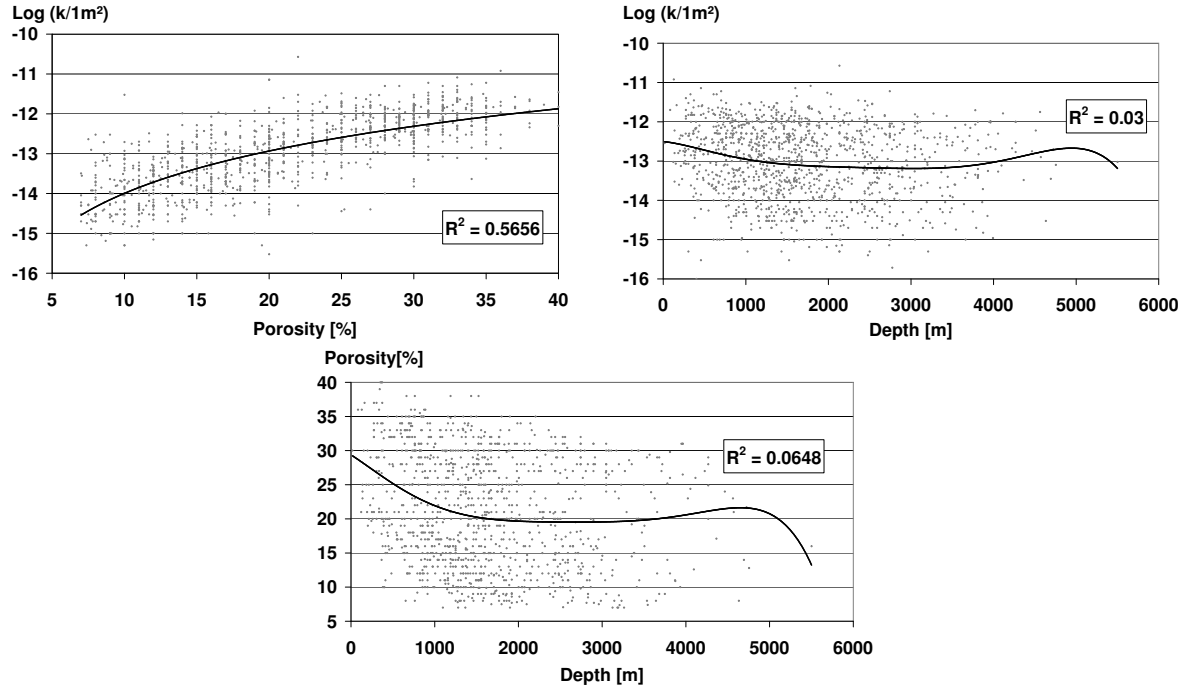

Figure 3.3: Variation of absolute permeability with porosity, variation of absolute permeability with depth, and variation of porosity with depth. Interpolated functions of the respective dataset are shown as red lines and correlation coefficients R are given in the boxes. Correlation coefficients are all rather low, however, an interrelation between permeability and porosity can be hypothesized.

used (0.018 °C/m and 0.062 °C/m, respectively). This means that these reservoirs are at the same depth as the median reservoir, but have a higher or lower temperature compared to the median reservoir.

Cases S and D The shallow (S) and deep (D) reservoir cases have the same median parameters, except for depth; here the 5^{th} and 95^{th} percentile values are used (386 m and 3495 m, respectively). The shallow case reservoir is located at a depth of only 386 m and thus at sub-critical conditions for CO_2. This case might be unrealistic for a large scale storage attempt. However, I do not want to manipulate the statistical characteristic of the parameters and moreover consider this case to be important to show the sensitivity of the results.

Cases V, E, and B The median reservoir parameter setup is combined with measured relative permeability relations of CO_2-brine systems in the Alberta basin in Canada (Viking (V)-, Ellerslie (E)-, and Basal (B) Formations) as introduced in Section 2.2.4 and shown in Figure 2.12.

Case P The median reservoir parameter setup is combined with a three times higher capillary entry pressure (p_{d}=30 kPa) in the Brooks and Corey models (Brooks and Corey,

1964). This results in a different capillary pressure-saturation relation.

Case Q The Median reservoir parameter setup is combined with a half the CO_2 injection rate compared to the other cases (the actual value depends on the model setup (1-D or 3-D) and is given in the relevant sections).

Case K Finally, a combination of the median reservoir parameter setup and an absolute permeability reduced by one order of magnitude (12.3 mD) yields Case K.

If the system is considered to be in hydrostatic and thermal equilibrium, this allows to calculate pressure and temperature at the depth of interest. With the pressure and temperature estimated at the depth of interest, the density and viscosity of the fluid phases can be calculated (cf. Section 2.2.2). The case setups are summarised in Table 3.2.

3.5 Summary and Conclusion

Ranges and distributions of properties of geological formations relevant for CO_2 storage were obtained from a large database of the U.S. National Petroleum Council. It could be shown that the distributions of various parameters of interest do not follow standard probability distributions. Mutual parameter interrelations have been investigated and discussed. Typical reservoirs were defined by classifying a "median reservoir" and "cold", "warm", "shallow", and "deep reservoirs". One characteristic property of each reservoir class was assigned a value corresponding to the 5^{th} and 95^{th} percentile of the distribution. Additional reservoirs were defined by assigning measured relative permeability-saturations relations to the median reservoir and by modification of the capillary entry pressure, the injection rate and the absolute permeability.

Cases	Letter Coding	Depth[m]	Press.[MPa]	Temp.[°C]	$S_{w,r}$[-]	$S_{CO2,r}$[-]	ϱ_w[kg/m^3]	ϱ_{CO2}[kg/m^3]	$\frac{\mu_{CO2}}{\mu_w}$
Median Reservoir	M	1524	15.47	55.13	0.30	0.05	1025.5	660.7	0.084
Warm Reservoir	W	1524	14.95	104.49	0.30	0.05	994.5	316.8	0.078
Cold Reservoir	C	1524	15.51	37.43	0.30	0.05	1031.7	805.5	0.088
Shallow Reservoir	S	386	4.06	21.58	0.30	0.05	1032.9	98.3	0.015
Deep Reservoir	D	3495	35.31	115.00	0.30	0.05	995.2	666.1	0.174
Median Reservoir+V.-kr	V	1524	15.47	55.13	0.56	0.044	1025.5	660.7	0.084
Median Reservoir+E.-kr	E	1524	15.47	55.13	0.66	0.034	1025.5	660.7	0.084
Median Reservoir+B.-kr	B	1524	15.47	55.13	0.29	0.035	1025.5	660.7	0.084
Median Reservoir+3p_d	P	1524	15.47	55.13	0.30	0.05	1025.5	660.7	0.084
Median Reservoir+$\frac{q}{2}$	Q	1524	15.47	55.13	0.30	0.05	1025.5	660.7	0.084
Median Reservoir+$\frac{k}{10}$	K	1524	15.47	55.13	0.30	0.05	1025.5	660.7	0.084

Table 3.2: Parameter settings for typical reservoirs. The three rightmost columns show calculated parameters based on pressure, temperature, and salinity. Cases V, E and B, use median reservoir properties in addition to measured relative permeability data for the Viking (V), Ellerslie (E) and Basal (B) formations from Alberta, Canada (Bennion and Bachu, 2008). For the case with index P a tripled entry pressure for the Brooks and Corey capillary pressure-saturation model is used. In Case Q, CO_2 is injected at half rate compared to the others. In Case K, the permeability is reduced by one order of magnitude.

4 Dimensional Analysis*

To identify and assess the dominant forces and processes relevant in CO_2 storage in geological formations, a dimensional analysis of the governing equations is performed. Characteristic values for length, time, velocity, and pressure are introduced in the balance equations in fractional flow formulation. These characteristic values represent typical length scales, typical timespans, typical flow velocities, and typical pressures which can be found when analysing the processes of interest, e.g. the CO_2 plume evolution. Furthermore, dimensionless numbers are defined, representing relations of forces in the system, i.e. capillary, viscous, and buoyancy forces. The resulting set of equations consists only of dimensionless gradients, dimensionless numbers and dimensionless functions which depend on phase saturations, relative permeability relations and fluid property relations. Thus, it is possible to investigate the individual dimensionless terms of the equations independently of each other by selecting the characteristic values or dependent on each other by calculating the characteristic values in numerical simulation experiments. As a basis for investigating the dimensionless terms, the typical reservoirs are considered as defined in Chapter 3. Two types of reservoirs are considered, i.e. a 1-D gravitation-free reservoir and a radially symmetric 3-D reservoir. The aim is to obtain a better qualitative understanding of the influence of the relations of forces and the selection of the characteristic values on the CO_2 plume evolution behaviour, the resulting storage capacity, and risk.

4.1 Derivation of Dimensionless Formulation

4.1.1 Fractional Flow Formulation

The system of fully coupled equations which describe flow in an isothermal two-phase system without mass transfer processes between the phases (Equation A.4) can be decoupled to give a pressure equation and a saturation equation. This decoupled form of Equation A.4 is called the fractional flow formulation (Chen and Ewing, 1997). The fractional flow function f for

*This Chapter is published in Kopp, A., Class, H. and Helmig, R., Investigations on CO_2 storage capacity in saline aquifers - Part 1: Dimensional analysis of flow processes and reservoir characteristics, Int. J. Greenhouse Gas Control, 3(3), 263–276, DOI:10.1016/j.ijggc.2008.10.002, 2009.

phase α is defined as

$$f_\alpha = \frac{\lambda_\alpha}{\lambda}, \tag{4.1}$$

where the total mobility λ can be calculated according to

$$\lambda = \sum_\alpha \lambda_\alpha. \tag{4.2}$$

The fractional flow functions add up to unity

$$\sum_\alpha f_\alpha = 1. \tag{4.3}$$

Summing up Equation A.4 over the phases and defining the total velocity $\mathbf{v}_{\mathrm{tot}}$ as the sum of the phase velocities (Equation 2.30), the pressure equation can be stated as (Chen and Ewing, 1997)

$$\nabla \cdot \mathbf{v}_{\mathrm{tot}} = -\frac{\partial \phi}{\partial t} - \sum_\alpha \frac{1}{\varrho_\alpha}\Big(\phi\, S_\alpha \frac{\partial \varrho_\alpha}{\partial t} + \mathbf{v}_\alpha \nabla \varrho_\alpha - \varrho_\alpha\, q_\alpha\Big), \tag{4.4}$$

$$\mathbf{v}_{\mathrm{tot}} = -\lambda\, \mathbf{k}\left(\nabla p_\alpha + f_\beta \nabla(p_\beta - p_\alpha) - \mathrm{g}\, \nabla z \sum_\alpha f_\alpha\, \varrho_\alpha\right), \tag{4.5}$$

with phases $\alpha, \beta \in$ (w,CO2) and $\alpha \neq \beta$. Resolving the phase velocities (Equation 2.30) for $\mathbf{k}\nabla p_\alpha$, then equating and solving again for the phase velocity yields

$$\mathbf{v}_\alpha = f_\alpha\, \mathbf{v}_{\mathrm{tot}} + f_\alpha\, \lambda_\beta\, (\varrho_\alpha - \varrho_\beta)\, \mathbf{k}\, \mathrm{g}\, \nabla z + \lambda_\beta\, f_\alpha\, \mathbf{k}\, \nabla(p_\beta - p_\alpha). \tag{4.6}$$

The saturation equation is obtained by inserting Equation 4.6 into Equation A.4:

$$\begin{aligned} \phi \frac{\partial S_\alpha}{\partial t} + \nabla \cdot \Big(f_\alpha\, \mathbf{v}_{\mathrm{tot}}\Big) + \nabla \cdot \Big(f_\alpha\, \lambda_\beta\, (\varrho_\alpha - \varrho_\beta)\, \mathbf{k}\, \mathrm{g}\, \nabla z\Big) + \nabla \cdot \Big(f_\alpha\, \lambda_\beta\, \mathbf{k}\, \nabla(p_\beta - p_\alpha)\Big) \\ = -S_\alpha \frac{\partial \phi}{\partial t} - \frac{1}{\varrho_\alpha}\Big(\phi\, S_\alpha \frac{\partial \varrho_\alpha}{\partial t} + \mathbf{v}_\alpha \cdot \nabla \varrho_\alpha + q_\alpha\Big). \end{aligned} \tag{4.7}$$

Equations 4.4, 4.5, and 4.7 are the fractional flow formulation for two-phase flow in porous media. Some assumptions can be made to simplify these equations for further analysis. The assumption of a rigid rock matrix leads to $\frac{\partial \phi}{\partial t} = 0$. Both fluid phases are assumed to be incompressible, leading to $\frac{\partial \varrho_\alpha}{\partial t} = 0$ and $\nabla \varrho_\alpha = 0$. This assumption is not valid for the CO_2-rich phase in reservoirs at shallow depth, however it is necessary at this point to simplify the equations. Sources or sinks are not considered; consequently, the right-hand side terms in Equations 4.4 and 4.7 vanish. In the following, the dynamic viscosity is also assumed to be constant.

Finally, using p_w as the independent pressure variable, one is left with a simplified set of pressure equations

$$\nabla \cdot \mathbf{v}_\mathrm{tot} = 0, \tag{4.8}$$

$$\mathbf{v}_\mathrm{tot} = -\lambda\,\mathbf{k}\left(\nabla p_\mathrm{w} + f_\mathrm{CO2}\,\nabla p_\mathrm{c} - \mathrm{g}\,\nabla z \sum_\alpha f_\alpha\,\varrho_\alpha\right), \tag{4.9}$$

and one saturation equation each for the water and CO_2 phases

$$\begin{aligned}\phi\,\frac{\partial S_\mathrm{w}}{\partial t} &+ \nabla\cdot\left(f_\mathrm{w}\,\mathbf{v}_\mathrm{tot}\right) \\ &+\nabla\cdot\left(f_\mathrm{w}\,\lambda_\mathrm{CO2}(\varrho_\mathrm{w}-\varrho_\mathrm{CO2})\,\mathbf{k}\,\mathrm{g}\,\nabla z\right) \\ &+\nabla\cdot\left(f_\mathrm{w}\,\lambda_\mathrm{CO2}\,\mathbf{k}\,\nabla p_\mathrm{c}\right) = 0,\end{aligned} \tag{4.10}$$

$$\begin{aligned}\phi\,\frac{\partial S_\mathrm{CO2}}{\partial t} &+ \nabla\cdot\left(f_\mathrm{CO2}\,\mathbf{v}_\mathrm{tot}\right) \\ &+\nabla\cdot\left(f_\mathrm{CO2}\,\lambda_\mathrm{w}(\varrho_\mathrm{CO2}-\varrho_\mathrm{w})\,\mathbf{k}\,\mathrm{g}\,\nabla z\right) \\ &-\nabla\cdot\left(f_\mathrm{CO2}\,\lambda_\mathrm{w}\,\mathbf{k}\,\nabla p_\mathrm{c}\right) = 0.\end{aligned} \tag{4.11}$$

The first term in Equations 4.10 and 4.11 is the accumulation term, the second term has (viscous) advective character, the third term has (gravitational) advective character, while the fourth term is of (capillary) diffusive nature.

4.1.2 Characteristic Values

Equations 4.8 to 4.11 can be non-dimensionalised by introducing the following definitions derived by Hilfer and Øren (1996) and extended by Manthey et al. (2008) for application to standard two-phase flow equations. Dimensionless quantities are marked by a hat.

$$\hat{z} = \frac{z}{l_\mathrm{cr}}, \tag{4.12}$$

$$\widehat{\nabla} = l_\mathrm{cr}\nabla, \tag{4.13}$$

$$\hat{t} = \frac{t}{t_\mathrm{cr}}, \tag{4.14}$$

$$\widehat{p_\alpha} = \frac{p_\alpha}{p_\mathrm{cr}}, \tag{4.15}$$

$$\widehat{p_\mathrm{c}} = \frac{p_\mathrm{c}}{p_\mathrm{cr}}, \tag{4.16}$$

$$\hat{\mathbf{v}}_\mathrm{tot} = \frac{\mathbf{v}_\mathrm{tot}}{\mathrm{v}_\mathrm{cr}}. \tag{4.17}$$

The subscript "cr" denotes a characteristic value. The choice of characteristic values requires a good understanding of the system being analysed and can influence the dimensionless quantities by orders of magnitudes.

The characteristic length (l_{cr}) is used to non-dimensionalise the elevation head (Equation 4.12) and the spatial derivatives (Equation 4.13). When applying l_{cr} to non-dimensionalise the spatial derivatives, it relates to a length over which a characteristic gradient occurs. Therefore, this length is alternatively chosen as the system length or the length (width) of a saturation front. In the first case, the characteristic gradient indicates a saturation or pressure drop over the system length; in the latter case, it refers to a saturation or pressure drop over the front length (width). The characteristic time (t_{cr}) is chosen as the time over which a characteristic saturation change occurs, and is thus related to the front propagation velocity. This means that the characteristic total velocity (v_{cr}) is coupled to the characteristic time and the characteristic length by $\mathrm{v}_{\mathrm{cr}} = \frac{\phi\, l_{\mathrm{cr}}}{t_{\mathrm{cr}}}$. Hence, one of these characteristic values t_{cr}, l_{cr}, v_{cr} is always dependent of the other two. The characteristic pressure p_{cr} is used to non-dimensionalise phase pressures and capillary pressure (Equations 4.15 and 4.16). This procedure is in agreement with the definition of capillary pressure (Equation 2.23). Hence, the characteristic pressure is chosen as a measure related to either capillary pressure, e.g. a capillary pressure drop over the system length or the front length (width), or to phase pressure, e.g. a phase pressure drop over the system length or the front length (width). The definitions of characteristic values are summarised in Table 4.1.

Characteristic value	Definition
Characteristic length l_{cr}	System length, or length (width) of a saturation front
Characteristic time t_{cr}	Time over which a characteristic saturation change occurs
Characteristic velocity v_{cr}	Front propagation (Darcy) velocity, coupled via $\mathrm{v}_{\mathrm{cr}} = \frac{\phi\, l_{\mathrm{cr}}}{t_{\mathrm{cr}}}$
Characteristic pressure p_{cr}	Capillary pressure drop over the system length or front length (width)

Table 4.1: Definition of characteristic values.

The choice of characteristic values is further discussed and illustrated in Sections 4.3 and 4.4.

4.1.3 Dimensionless Numbers

Additionally, the following dimensionless numbers are defined. The Capillary Number (Ca) is defined as

$$\mathrm{Ca} = \frac{\mathrm{k}\, p_{\mathrm{cr}}}{\mu_{\mathrm{CO2}}\, \mathrm{v}_{\mathrm{cr}}\, l_{\mathrm{cr}}} = \frac{\text{capillary forces}}{\text{viscous forces}}. \tag{4.18}$$

The Gravitational Number (Gr) is defined as

$$\mathrm{Gr} = \frac{(\varrho_{\mathrm{w}} - \varrho_{\mathrm{CO2}})\, \mathrm{g}\, \mathrm{k}}{\mu_{\mathrm{CO2}}\, \mathrm{v}_{\mathrm{cr}}} = \frac{\text{gravitational forces}}{\text{viscous forces}}. \tag{4.19}$$

The dimensionless Capillary and Gravitational Numbers relate forces acting on the system, where Ca relates forces (M·L)/T^2 and Gr relates forces per unit length M/T^2 (M is mass, L is length, and T is time). Note that absolute permeability in the dimensionless numbers is a scalar, which means that permeability is assumed to be isotropic.

A formal relation of capillary forces to gravitational forces can be defined, when dividing the Capillary Number Ca by the Gravitational Number Gr, this is the Bond number (Bo).

$$\mathrm{Bo} = \frac{p_{\mathrm{cr}}}{(\varrho_{\mathrm{w}} - \varrho_{\mathrm{CO2}})\,\mathrm{g}\,l_{\mathrm{cr}}} = \frac{\text{capillary forces}}{\text{gravitational forces}}. \tag{4.20}$$

However, the Bond Number is not found in the balance equations (as will be shown in the following section), therefore it is not discussed any further here.

4.1.4 Dimensionless Pressure and Saturation Equations

Finally, the dimensionless pressure equations can be formulated as

$$\widehat{\nabla}\cdot\hat{\mathbf{v}}_{\mathrm{tot}} = 0, \tag{4.21}$$

$$\hat{\mathbf{v}}_{\mathrm{tot}} = -\,\mathrm{Ca}\,\mathrm{A}\,\widehat{\nabla}\hat{p}_{\mathrm{w}} - \mathrm{Ca}\;k_{\mathrm{r,CO2}}\,\widehat{\nabla}\hat{p}_{\mathrm{c}} + \mathrm{Gr}\,\mathrm{A}\,\mathrm{B}\,\widehat{\nabla}\hat{z}, \tag{4.22}$$

where

$$\mathrm{A} = \frac{\mu_{\mathrm{CO2}}}{\mu_{\mathrm{w}}}\,k_{\mathrm{r,w}} + k_{\mathrm{r,CO2}}, \tag{4.23}$$

$$\mathrm{B} = (f_{\mathrm{w}} - f_{\mathrm{CO2}}) + \frac{\varrho_{\mathrm{w}}\,f_{\mathrm{CO2}}}{\varrho_{\mathrm{w}} - \varrho_{\mathrm{CO2}}} + \frac{\varrho_{\mathrm{CO2}}\,f_{\mathrm{w}}}{\varrho_{\mathrm{w}} - \varrho_{\mathrm{CO2}}}. \tag{4.24}$$

The water-phase saturation equation (Equation 4.10) is reformulated as

$$\frac{\partial S_{\mathrm{w}}}{\partial\hat{t}} + \widehat{\nabla}\cdot\left(f_{\mathrm{w}}\,\hat{\mathbf{v}}_{\mathrm{tot}}\right) + \widehat{\nabla}\cdot\left(\mathrm{Ca}\,\mathrm{C}\,\widehat{\nabla}\hat{p}_{\mathrm{c}}\right) + \widehat{\nabla}\cdot\left(\mathrm{Gr}\,\mathrm{C}\,\widehat{\nabla}\hat{z}\right) = 0, \tag{4.25}$$

where

$$\mathrm{C} = k_{\mathrm{r,CO2}}\,f_{\mathrm{w}}. \tag{4.26}$$

Using the closure relation $\sum_\alpha S_\alpha = 1$, the saturation equation for the CO_2 phase can simply be derived out of Equation 4.25 as

$$\frac{\partial S_{\mathrm{CO2}}}{\partial\hat{t}} - \widehat{\nabla}\cdot(\ldots) - \widehat{\nabla}\cdot(\ldots) - \widehat{\nabla}\cdot(\ldots) = 0. \tag{4.27}$$

The detailed derivation of Equations 4.21, 4.22, and 4.25 is given in Appendix B.

4.2 Preliminary Definitions of Risk and Storage Capacity

It is necessary to give at least a simplified definition of "risk" and "CO_2 storage capacity in geological formations" at this point. This is necessary in order to be able to discuss and investigate the effects on these "measures of performance" of a CO_2 storage attempt, dependent on the selection of the characteristic values. I do not want to give more complex definitions of these measures at this point, since it is not necessary for the understanding and could confuse the reader. A more complex definition of "CO_2 storage capacity" is given in Chapter 5, for "risk" the complex definition is given in Chapter 7.
When defining risk, the general approach is to define failure scenarios, attribute a likelihood to these failure scenarios, and quantify the consequences of the failures. At this point, I combine these three parts of risk analysis into one single idea. The failure scenario of interest here, is failure by CO_2 leakage through fractures, leaky wells or other geological weaknesses located at some distance from the CO_2 injection well. The sooner CO_2 arrives at such a feature, the larger risk since more time is left for leakage during the lifetime of a CO_2 storage project. This is equivalent to stating that reservoirs with larger CO_2 bodies are more risky than reservoirs with a compact CO_2 volume, since CO_2 arrives later at a fracture (having the same distance to the injection well) in the latter case and the probability to encounter additional fractures etc. is lower. Moreover, a reservoir is judged to be more risky if a larger fraction of the injected CO_2 accumulates in the upper parts of the reservoir, that is below the caprock, since this is where the leakage mainly occurs.

Storage capacity is, at this point, simply defined as the volume fraction of the reservoir available for CO_2 storage. Hence, it is a dimensionless quantity. Theoretically it ranges between zero (no storage is possible) to the volume fraction of the entire pore space of the reservoir, that is average porosity.

4.3 Analytical Investigations

With the derived set of equations (Equations 4.21 to 4.27), a subdivision of the balance equations could be obtained in dimensionless numbers Ca and Gr (relating forces), functions A, B and C (depending solely on phase saturations and fluid properties) and dimensionless gradients of dimensionless phase pressures, capillary pressure and elevation head. The properties of the homogeneous and isotropic porous medium are predefined for these investigations, that is considering properties of typical reservoirs as defined in Section 3.4. They are assumed to be constant on all length scales. Characteristic length, pressure and velocity are considered to be independent of each other. This assumption neglects the physical interactions. However, within this section, the discussion of the influence of the individual characteristic values is restricted to a mathematical point of view. An interpretation from a physical point of view follows later on.

4.3.1 Dimensionless Numbers Dependent on Selections of Characteristic Values

Dimensionless numbers Gr and Ca are analysed as functions of characteristic velocity, pressure, length and time. Figure 4.1 (left) shows the variation of Gr versus v_{cr}.

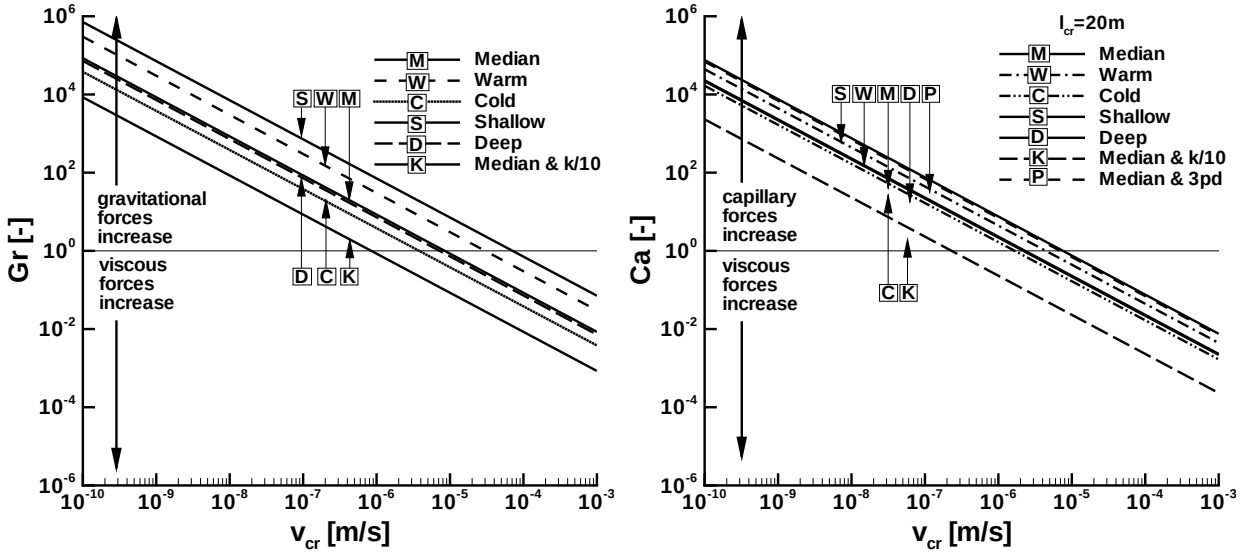

Figure 4.1: Variation of Gravitational Number Gr versus the characteristic velocity (left) and variation of the Capillary Number Ca versus the characteristic velocity (right). Letter coding according to Table 3.2.

As apparent from the definition of Gr, gravitational forces increase with increasing difference in fluid densities and increasing permeability. Viscous forces increase with increasing characteristic velocity or increasing dynamic viscosity. For the median case reservoir, a reference equilibrium state between gravitational and viscous forces, as indicated by Gr = 1, is given for $v_{cr} = 8.5 \cdot 10^{-6}$ m/s. If Gr becomes significantly larger than one, gravitational forces tend to dominate over viscous forces and vice versa. The number Gr is very sensitive to variations in reservoir depth. When comparing Gr calculated from median and from shallow reservoir properties, an increase in Gr by one order of magnitude for a presumably constant characteristic velocity is observed (the assumption of constant characteristic velocity is discussed in the following paragraph). This means that gravitational forces increase by a factor of ten in relation to viscous forces. For the Deep reservoir, fluid property changes are smaller and Gr decreases by a factor of 2.3 with respect to the Median case value. A similar behaviour is observed for a warmer / colder reservoir, a large increase in Gr for a warmer reservoir and a small decrease for a cooler reservoir. This is related to the non-linear behaviour of CO_2 density depending on pressure and temperature. With increasing depth (increasing pressure and temperature) changes in density become smaller (Bachu, 2003). A change in absolute permeability has a strong influence on Gr. As permeability may vary by several orders of

magnitude, this implies a variation in Gr by the same magnitude. However, with a different permeability, characteristic velocity will change simultaneously since both are closely coupled (Equation 2.30), or, depending on the boundary conditions, the pressure gradient will change.

Figure 4.1 (right) shows the variation of Ca versus v_{cr}. It is obvious from the definition of Ca that capillary forces increase with increasing characteristic capillary pressure or permeability. Viscous forces increase with increasing characteristic velocity, dynamic viscosity, or characteristic length. When varying v_{cr}, an assumption has to be made for the characteristic length l_{cr} in order to calculate Ca. Here l_{cr} is taken to be 20 metres which corresponds to the intermediate front width observed in the simulations (see Section 4.4). For the Median case, the reference equilibrium state between the forces, indicated by Ca = 1, is given for $v_{cr} = 1.18 \cdot 10^{-6}$ m/s. This is a significantly lower velocity than for the reference equilibrium state between gravitational and viscous forces (Gr = 1). This means that for the Median case, where capillary forces are at (reference) equilibrium state with viscous forces, the gravitational forces dominate over the viscous forces, indicated by Gr = 7.2. This is further analysed in the discussion of Figure 4.2. The Ca number is less sensitive to variations in reservoir temperature and depth than Gr. The ratio of capillary forces to viscous forces increases by a factor of two for the Warm reservoir and by factor of 3.6 for the Shallow reservoir compared with the Median reservoir at a given characteristic velocity. The same strong influence of permeability on Gr is found on Ca. The influence of p_{cr} on Ca is strong. As previously discussed, the characteristic pressure p_{cr} is used to non-dimensionalise capillary pressure and phase pressures. Very little information is available in the literature on capillary pressure-saturation relations relations for CO_2-brine systems (cf. Section 2.2.4). Capillary pressures vary over a range of four orders of magnitude for water saturations ranging from zero to one. In CO_2 storage scenarios, however, capillary pressures may vary only by two orders of magnitude, since very low water saturations accompanied by very high capillary pressures occur only in the close vicinity of the injection well. When selecting a phase pressure as the characteristic pressure, the variation in pressure between a deep and a shallow reservoir is approximately one order of magnitude. Therefore, despite a strong influence of p_{cr} on Ca, the expected changes are not as large as these induced by variable permeability.

In Figure 4.2, Gr versus Ca is shown for various characteristic velocities.
With characteristic velocities ranging from 10^{-10} m/s to 10^{-3} m/s, one can distinguish four sectors (note that a characteristic velocity of 10^{-3} m/s is unrealistically high for consolidated porous media in sedimentary basins, but still falls within the definition of Darcy flow). For high characteristic velocities, viscous forces dominate over capillary and gravitational forces, represented by the lower left sector. For small characteristic velocities, viscous forces lose influence against gravitational and capillary forces, represented by the upper right sector. In the remaining sectors, viscous forces are either small compared to gravitational forces (upper left sector) or capillary forces (lower right sector). Most favourable for CO_2 storage is a scenario in which capillary forces dominate over viscous forces and viscous forces, in

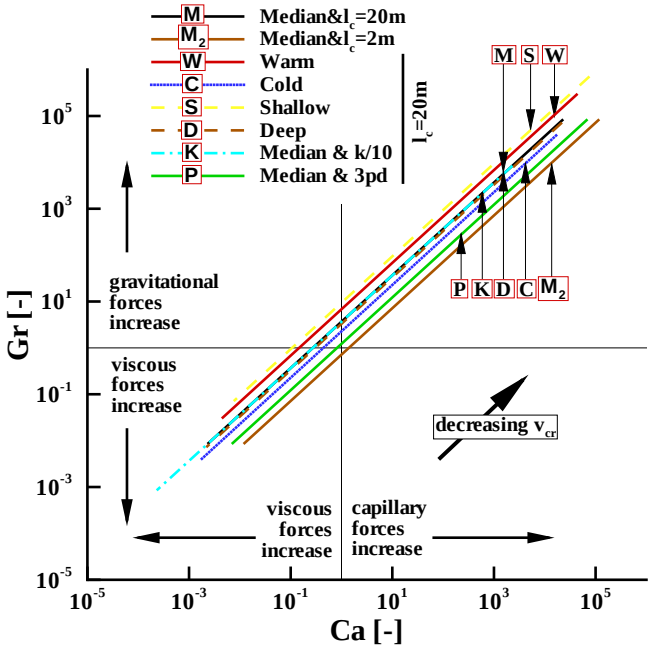

Figure 4.2: Gravitational Number Gr versus Capillary Number Ca for a varying characteristic velocity ranging from 10^{-10} m/s to 10^{-3} m/s. Letter coding according to Table 3.2.

turn, dominate over gravitational forces (lower right sector). In this case gravitational forces are rather weak, leading to a low buoyancy-induced upward CO_2 flow. Viscous forces ideally should be high, resulting in a cylindrically shaped plume. The stronger the capillary forces, the more diffuse the displacement front is. Values of both Gr and Ca around unity indicate a situation in which none of the three forces dominates. Comparing, for example, the Shallow reservoir to the Median reservoir, the effect of an increase in Gr and an increase in Ca results in a shift to the top/right. Reducing the permeability of the Median reservoir by a factor of 10 (Case Median & k/10), results in a shift in the bottom left direction, i.e. in direction of increasing viscous forces. A reduction of p_{cr} results in a parallel shift to the left, i.e. decreasing Ca.

Discussing changes in Ca or Gr based on changes in fluid properties or reservoir properties like permeability, and at the same time assuming a constant characteristic velocity, might lead to a mis-interpretation. As CO_2 density varies strongly between, for example, a super-critical (Median reservoir) and a sub-critical (Shallow reservoir) case, the characteristic velocity presumably changes as well. Here, a CO_2 density decrease by a factor of 6.7 leads to an increase in characteristic velocity of the same factor when applying a simple volume balance and assuming a constant cross-sectional area. Due to the decrease in CO_2 viscosity, viscous forces increase only moderately. Consequently, the actual ratio $\frac{\mathrm{Gr}^{\mathrm{Shallow}}}{\mathrm{Gr}^{\mathrm{Median}}}$ is only 1.2 (versus 10 when not considering a corresponding increase in characteristic velocity). Similarly, when reducing the permeability by a factor of 10 and comparing Gravitational Numbers, the influence of a changing characteristic velocity has to be accounted for.

4.3.2 Dimensionless Functions A,B, and C

As it can be seen in the dimensionless pressure equations (Equation 4.21 and 4.22) and the (water-phase) saturation equation (Equation 4.25), the combination of Ca and Gr with dimensionless gradients and saturation-dependent functions A, B, C yields the resulting total velocity and saturation change with time. The dimensionless functions A, B, C therein are dependent on fluid properties and relative permeability-saturation relations (cf. Section 2.2.4). Consequently, functions A, B, and C can be calculated using Equations 4.23, 4.24, and 4.26 as shown in Figure 4.3 for the Median reservoir.

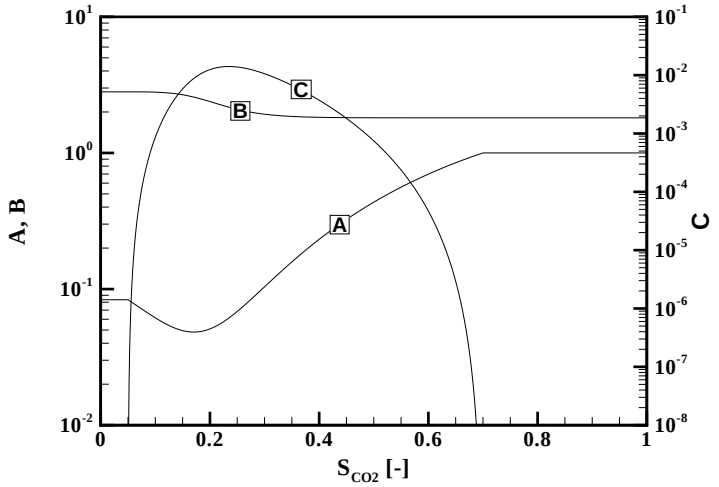

Figure 4.3: Functions A, B, and C for a relative permeability-saturation relation model after Brooks and Corey (1964) (employing input parameter setting of $\lambda = 2.0$, $p_\mathrm{d} = 10\,\mathrm{kPa}$, $S_\mathrm{w,r} = 0.3$ and $S_\mathrm{CO2,r} = 0.05$) and fluid property relations for the Median reservoir.

The magnitude of these functions, dependent on CO_2 saturation, can now be discussed. Note that the relative permeability endpoints (i.e. relative permeability at residual saturations) equal one in the Brooks and Corey model assumed here. A CO_2 saturation close to zero refers to the very initial phase of injection or to locations in a (homogeneous) reservoir far away from the injection well. A high CO_2 saturation relates to regions close to the injection well at later times or to a region below the caprock, where CO_2 presumably accumulates. For CO_2 saturations lower than $S_\mathrm{CO2,r}$, function A equals the dynamic viscosity ratio of the two fluids ($\frac{\mu_\mathrm{CO2}}{\mu_\mathrm{w}}$). With increasing CO_2 saturation, A decreases to a minimum and increases thereafter up to unity at the residual water saturation. Function B is always greater than one for $\varrho_\mathrm{CO2} > \frac{\varrho_\mathrm{w}}{2}$. It ranges between $-1 + \frac{\varrho_\mathrm{w}}{\varrho_\mathrm{w} - \varrho_\mathrm{CO2}}$ at residual water saturation and $1 + \frac{\varrho_\mathrm{CO2}}{\varrho_\mathrm{w} - \varrho_\mathrm{CO2}}$ for residual CO_2 saturation (as can be derived from Equation 4.24). Function C varies by

several orders of magnitude with a maximum at intermediate saturations.

4.3.3 Dimensionless Gradients

Dimensionless gradients should be ideally scaled to unity to allow for estimates of dominant forces. Characteristic values l_{cr} and p_{cr} have to be found to non-dimensionalise pressure and elevation head gradients. At different locations within a reservoir, ∇p_α, ∇p_{c}, and ∇z can vary. Pressure gradients vary also with time. But at various points in time or locations within the reservoir, e.g. right at the CO_2 front, these gradients can be estimated. In the vicinity of the injection well, phase pressure gradients are high, especially at the beginning of the injection process when relative permeabilities are low. At later times, pressure gradients are low. As capillary pressure is dependent on saturation, significant capillary pressure gradients (∇p_{c}) occur where significant gradients in saturation are found. This is the case right at the front of the CO_2 plume. In Section 4.4, it will be shown that it is possible to set either $\widehat{\nabla}\hat{p}_{\mathrm{w}}$ or $\widehat{\nabla}\hat{p}_{\mathrm{c}}$ equal to unity over either the front width or the system length. The gradient in elevation is obvious. In the horizontal plane, ∇z is zero and in vertical direction, ∇z is one. According to the NPC database (see Table 3.1), average reservoir dip angles of up to 25 degrees are possible, which correspond to $\nabla z = 0.466$.

4.4 Numerical Investigations

In the dimensional analysis so far, a mathematical understanding of the system behaviour, dependent on the pre-selection of characteristic values has been developed by investigating the behaviour of the dimensionless numbers, by investigating the magnitude of dimensionless functions A,B, and C dependent on CO_2 saturation, and by discussing the dimensionless gradients. However, the definition of characteristic length, pressure, and velocity, independent of each other, is not physically consistent. Moreover, the complex interplay of saturations, gradients, and ratios of forces can only by answered by simulation experiments. This is to investigate the mutual dependence of characteristic values and the resulting dimensionless numbers, i.e. relation of forces. Simulation experiments are conducted with the model for isothermal multi-phase processes without mass transfer between the phases, i.e. the 2p-module implemented in MUFTE-UG (cf. Section A.1). Although, mass transfer and non-isothermal processes could have been easily considered in the numerical simulations, the 2p-module is chosen to conduct the numerical experiments in order to be in accordance with the dimensional analysis. Typical reservoirs as previously defined are considered (cf. Table 3.2).

4.4.1 Plume evolution in a 1-D gravitation-free reservoir

Carbon dioxide is injected into a 1-D reservoir at the left boundary at a specified constant rate. At the right boundary, constant pressure is applied and water saturation is assumed to be unity. The model domain has a total length of 4000 m. In the 1-D horizontal model domain, gravitational forces cannot be considered (g = 0), thus the focus is on the analysis of the relation between capillary and viscous forces (Ca).
Figure 4.4 shows the resulting CO_2 saturation after 4 years model time. The saturation profiles are plotted over a velocity-type horizontal axis. Saturation profiles display the typical shape. Initially (i.e. infinite $\frac{x}{t}$), CO_2 saturation is zero. Later, the front arrives and CO_2 saturation increases. A diffusive front is observed due to the assumed non-linear capillary pressure-saturation relation and due to inevitable dispersion. Following the front, a rarefaction wave extends back to the injection point due to the non-linear relation between relative permeability and saturation. Note that the area below the saturation profiles multiplied by CO_2 density is the same for all cases because it represents the amount of injected CO_2 (except for Case Q in which the injection rate is halved).

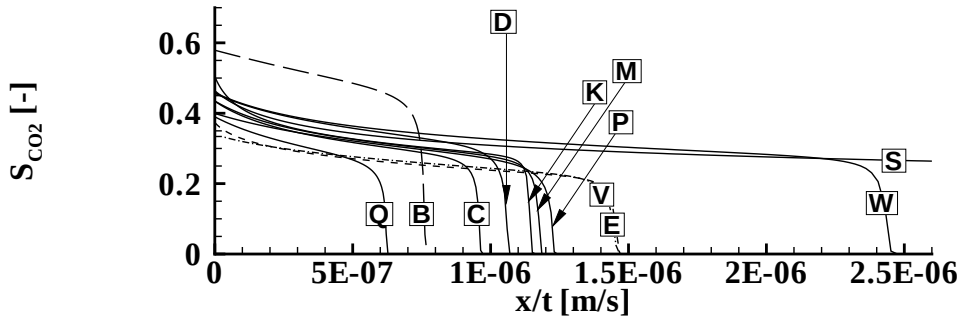

Figure 4.4: Carbon dioxide saturations versus similarity variable (distance from injection point divided by model time) in a horizontal 1-D reservoir after 4 years modeltime for all cases. Parameter settings and letter coding as shown in Table 3.2.

The fastest plume evolution is observed for the Shallow reservoir because of low CO_2 density. The front evolves with a velocity of $v_{CO2} = 1.05 \cdot 10^{-5}$ m/s (not shown in Figure 4.4). Similarly, the plume evolution in the Warm reservoir occurs faster than in the Median reservoir for the same reason. In contrast, plume evolution is slower in the Deep and Cold reservoir cases. The slowest plume evolution is observed for Case Q, where the injection rate is halved. The tripled entry pressure (Case P) causes a more diffusive front. A lower absolute permeability (Case K) causes a slightly slower plume evolution. This is due to the higher pressure gradient ∇p_w necessary to maintain the mass injection rate and at the same time quasi-constant ∇p_c, thus the front is less diffusive (more compact). For Case B (Basal reservoir relative permeability relation), plume evolution is also markedly slower, with at the same time much higher CO_2 saturations. In this case carbon dioxide relative permeability is significantly lower than for the Median case for CO_2 saturations lower than 0.7. Viking and

Ellerslie reservoir relative permeability relations produce almost identical results, a faster plume evolution with lower CO_2 saturations.
To calculate Ca, characteristic values v_{cr}, l_{cr}, and p_{cr} have to be defined. The characteristic velocity v_{cr} is estimated from the analytical solution of the Buckley-Leverett problem (Buckley and Leverett, 1942), analysing solely the fractional flow functions. This procedure is depicted in Figure 4.5. Note that capillary effects are neglected, and a hyperbolic problem is assumed for the determination of v_{cr}.

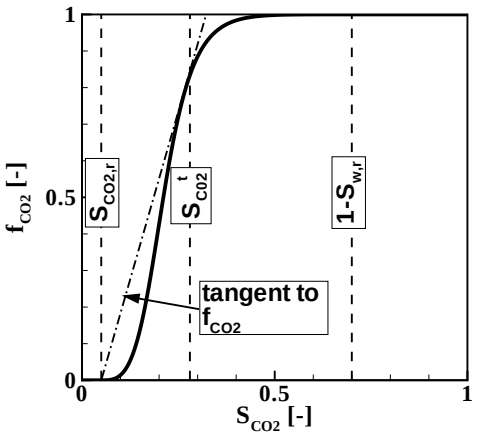

Figure 4.5: Construction of a sharp front (modified after LeVeque (1992) and Helmig (1997)) by taking the Brooks and Corey model fractional flow function as an example. The front is reported to travel with a speed v_t proportional to the derivative of a linear function starting at ($S_{CO2} = S_{CO2,r}$ and $f_{CO2} = 0$) and being tangential to the fractional flow function f_{CO2}. The saturation of the tangential point is called S^t_{CO2} further on.

The linear correlation coefficient (Pearson r, reflecting the degree of linear relationship between two variables) is r = 0.9998, obtained from the evolution velocity of the front with a saturation of S^t_{CO2} observed in the simulation experiments and from the analytically derived v_t times the injection rate q divided by porosity ϕ and CO_2 density ϱ_{CO2}, i.e. $v_t \frac{q}{\phi\, \varrho_{CO2}}$. This means that there is an almost perfect positive linear relationship between the two variables. This allows an estimation of the characteristic velocity without using model results. As outlined in Section 4.3.3, dimensionless gradients $\widehat{\nabla}\hat{p}_w$ and $\widehat{\nabla}\hat{p}_c$ should ideally be scaled to unity. This can either be obtained for the front or for the entire system. When considering a front approach, l_{cr} refers to the front width and p_{cr} refers to the pressure drop over this front width (water pressure or capillary pressure). The front width l_{cr} is defined as the distance between the farthest point the front has travelled and the point where S^t_{CO2} is observed. When considering a system approach, l_{cr} refers to the system length (in this case the model domain) and p_{cr} refers to the pressure (water/capillary) drop over the system length. Consequently, four options arise:

1. $\widehat{\nabla}\hat{p}_c \stackrel{!}{=} 1$ over the front width. See Figure 4.6 for the Median case construction sketch.

- l_{cr} is defined as the front width, i.e. distance between the point where CO_2 saturation is zero and the point where CO_2 saturation is equal to $S^{\mathrm{t}}_{\mathrm{CO2}}$.
- p_{cr} is defined as the capillary pressure drop over this front width: $p_{\mathrm{cr}} = p_{\mathrm{c},S^{\mathrm{t}}_{\mathrm{CO2}}} - p_{\mathrm{c,front}}$.

Equations 4.13 and 4.15 yield:
$\widehat{\nabla}\hat{p}_{\mathrm{w}} = \frac{p_{\mathrm{w},S^{\mathrm{t}}_{\mathrm{CO2}}} - p_{\mathrm{w,front}}}{l_{\mathrm{cr}}} \cdot \frac{l_{\mathrm{cr}}}{p_{\mathrm{cr}}} = \frac{p_{\mathrm{w},S^{\mathrm{t}}_{\mathrm{CO2}}} - p_{\mathrm{w,front}}}{p_{\mathrm{cr}}}$.

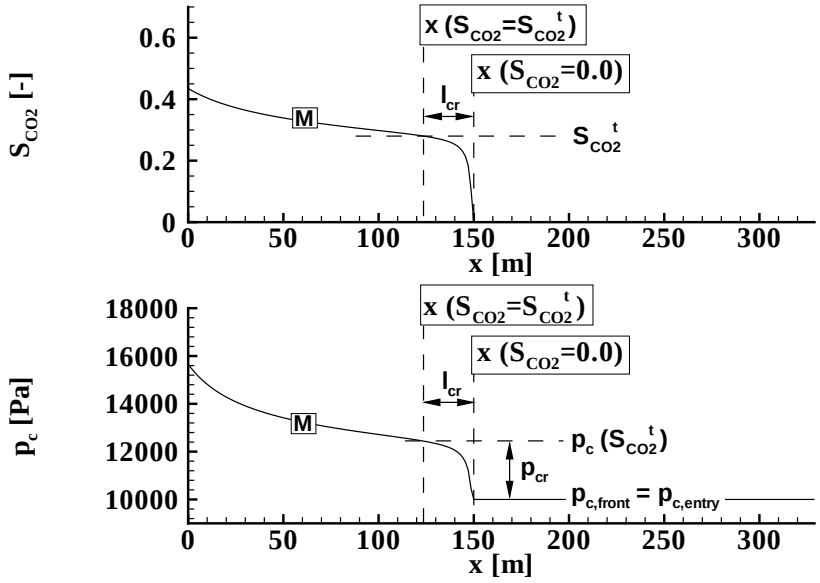

Figure 4.6: Selection of characteristic values to obtain $\widehat{\nabla}\hat{p}_{\mathrm{c}} \stackrel{!}{=} 1$ over the front width for the Median case.

The dimensionless gradients below are constructed analogously.

2. $\widehat{\nabla}\hat{p}_{\mathrm{w}} \stackrel{!}{=} 1$ over the front width.
   - l_{cr} is defined as the front width.
   - p_{cr} is defined as the water pressure drop over this front width: $p_{\mathrm{cr}} = p_{\mathrm{w},S^{\mathrm{t}}_{\mathrm{CO2}}} - p_{\mathrm{w,front}}$.

   Equations 4.13 and 4.16 yield:
   $\widehat{\nabla}\hat{p}_{\mathrm{c}} = \frac{p_{\mathrm{c},S^{\mathrm{t}}_{\mathrm{CO2}}} - p_{\mathrm{c,front}}}{p_{\mathrm{cr}}}$.

3. $\widehat{\nabla}\hat{p}_{\mathrm{c}} \stackrel{!}{=} 1$ over the system length.
   - l_{cr} is defined as the system length.
   - p_{cr} is defined as the capillary pressure drop over the system length: $p_{\mathrm{cr}} = p_{\mathrm{c,well}} - p_{\mathrm{c,front}}$.

Equations 4.13 and 4.15 yield:
$\widehat{\nabla}\hat{p}_{\mathrm{w}} = \frac{p_{\mathrm{w,well}} - p_{\mathrm{w,init}}}{p_{\mathrm{cr}}}$.

4. $\widehat{\nabla}\hat{p}_{\mathrm{w}} \stackrel{!}{=} 1$ over the system length.
   - l_{cr} is defined as the system length.
   - p_{cr} is defined as the water pressure drop over the system length: $p_{\mathrm{cr}} = p_{\mathrm{w,well}} - p_{\mathrm{w,init}}$.

   Equations 4.13 and 4.16 yield:
   $\widehat{\nabla}\hat{p}_{\mathrm{c}} = \frac{p_{\mathrm{c,well}} - p_{\mathrm{c,front}}}{p_{\mathrm{cr}}}$.

Since phase pressure and capillary pressure are strongly coupled via Equation 2.23, it is possible to scale gradients $\widehat{\nabla}\hat{p}_{\mathrm{c}}$ and $\widehat{\nabla}\hat{p}_{\mathrm{w}}$ in options 1 and 2 (front approach) simultaneously to unity.
To calculate $\hat{\mathbf{v}}_{\mathrm{tot}}$ from Equation 4.22, A, B and $k_{\mathrm{r,CO2}}$ are additionally evaluated at the saturation $S^{\mathrm{t}}_{\mathrm{CO2}}$. When comparing the resulting CO_2 phase velocity with the numerically calculated CO_2 (Darcy) velocity, the linear correlation coefficient (Pearson r) for the front approach is r = 0.9871 and r = 0.9779 for the system approach. Note that the results are identical when either capillary pressure drop or water pressure drop is chosen to be p_{cr}. They differ depending on the definition of l_{cr}. When looking at the Capillary Numbers calculated by the front approach with $\widehat{\nabla}\hat{p}_{\mathrm{c}} \stackrel{!}{=} 1$, the order for the cases in Table 3.2 is as follows:

$$\begin{aligned}\mathrm{Ca^B} = 0.80 > \mathrm{Ca^Q} = 0.45 > \mathrm{Ca^P} = 0.38 > \mathrm{Ca^D} = 0.29 > \mathrm{Ca^C} = 0.19 > \mathrm{Ca^M} = 0.18 \\ > \mathrm{Ca^W} = 0.10 > \mathrm{Ca^V} = 0.10 > \mathrm{Ca^E} = 0.09 > \mathrm{Ca^K} = 0.03 > \mathrm{Ca^S} = 0.02\end{aligned}$$

The order of Capillary Numbers closely follows the observed order of evolution velocities except for the lower permeability case and the tripled capillary pressure. Modification of permeability k and capillary entry pressure p_{d} alters Ca by orders of magnitude, although the plume evolution velocities do not change much in the 1-D model approach. The left boundary condition assumes a constant injection rate, therefore the pressure increase is high for reduced permeability (k) and diffusive spreading loses influence. In three dimensions, the pressure increase would be much smaller and rapidly decline with distance from the injection well. The influence of modified relative permeability, temperature, depth and injection rate is represented well by Ca.
In conclusion, for this 1-D gravitation-free reservoir, $S^{\mathrm{t}}_{\mathrm{CO2}}$ (the saturation of the tangential point of the fractional flow function) is used as an estimate for average CO_2 saturation. The evolution velocity of the CO_2 front is estimated by dimensional analysis. This is a prerequisite for the estimation of storage capacity and risk. The 1-D gravitation-free reservoir shows that relative permeability plays an important role in plume evolution behaviour. Nevertheless, knowledge of phase pressure increase and the capillary pressure-saturation relation is necessary, which is difficult to obtain without simulations and further investigations on reservoir properties.

4.4.2 Plume evolution in a radially symmetric 3-D reservoir

The concept can now be extended to a 3-D radially symmetric reservoir assuming the same typical reservoir properties as before. The domain has a constant height of 100 m and a radius of 4000 m. Carbon dioxide is injected at the centre with a constant rate of 1 Mt CO_2 per year. This is the amount that a medium-sized coal-fired power plant discharges annually. The domain is closed at the top and bottom boundaries. At the lateral boundary, hydrostatic pressure and fully water saturated conditions are assumed. Due to buoyancy forces, CO_2 is flowing towards the caprock at the top and gravity segregation occurs, which results in generally in an "S"-shaped front as shown in Figure 4.7.

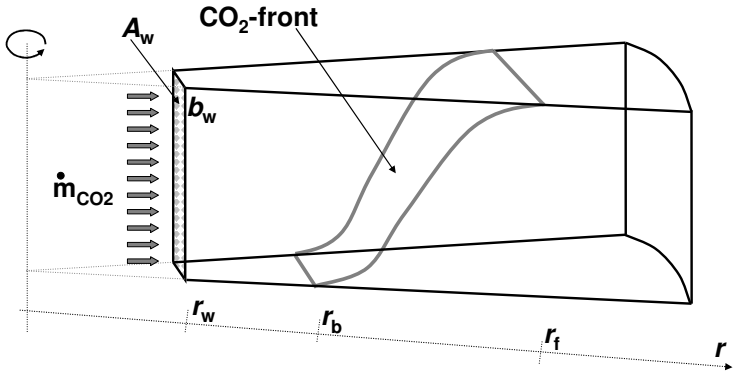

Figure 4.7: Sketch of a radially symmetric domain. The front velocity at the top of the domain (at distance r_f) is higher than the velocity at the bottom of the domain (at distance r_b) due to gravity segregation. Symbols: r_w indicates injection well radius, b_w width of injection well sector and A_w the injection well surface.

Due to gravity segregation, the front velocity at the top of the domain (at distance r_f) is higher than at the bottom (at distance r_b) of the domain. This behaviour cannot be approximated by a simple volume balance approach. Roughly, the squares of the radial distances are linearly proportional to time (Barenblatt et al., 1990). For example in the Median case, the front at the bottom of the domain even stops entirely after 3.7 years. This means that under these circumstances, regions at the bottom of the domain that are further away than approximately 150 m from the injection well cannot be accessed for storage. Figure 4.8 shows CO_2 saturation iso-lines for all reservoir setups after 3.85 years of injection and consequently an injected total CO_2 mass of 3.85 Mt CO_2 (1.925 Mt CO_2 for Case Q).
Here, the focus is on the evaluation of forces acting in the reservoir, and thus on the assessment of dimensionless numbers. To non-dimensionalise the equations and calculate the dimensionless numbers Ca and Gr, characteristic values v_{cr}, l_{cr} and p_{cr} have to be defined once again. These values change with time and location in the reservoir. Characteristic velocity v_{cr} is defined by averaging CO_2 Darcy velocities at every timestep in the simulations. Performing mass averaging, the element value (e.g. euclidian norm of the velocity) is weighted by the CO_2 phase mass fraction of the element with respect to the total CO_2 phase

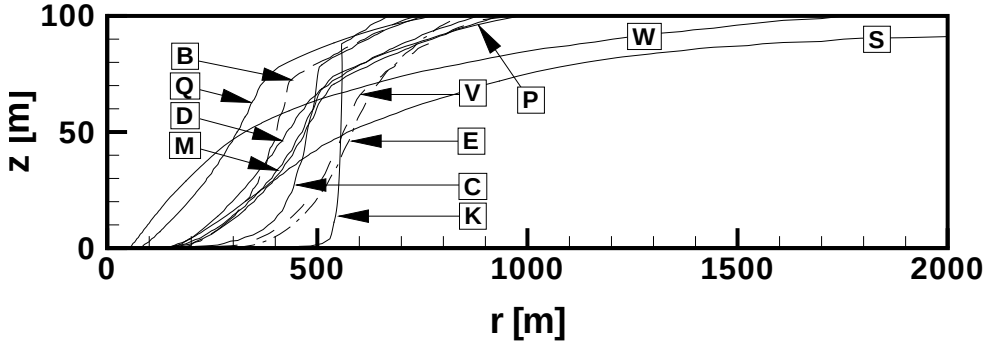

Figure 4.8: Carbon dioxide saturation 10% iso-lines developing for relative permeability-saturation relations given in Figure 2.12 and reservoir cases shown in Table 3.2 after 3.85 years model time. Letter coding according to Table 3.2.

mass in the reservoir:

$$\mathrm{v_{cr}} = \sum_{\mathrm{j=1}}^{\mathrm{elements}} \frac{\mathrm{mass_{CO2,j}} \cdot || \, \mathbf{v}_{\mathrm{CO2,j}} \, ||_e}{\sum_{\mathrm{i=1}}^{\mathrm{elements}} \mathrm{mass_{CO2,i}}}. \tag{4.28}$$

Two options are examined, $\widehat{\nabla}\hat{p}_\mathrm{c} \stackrel{!}{=} 1$ over the front width and $\widehat{\nabla}\hat{p}_\mathrm{c} \stackrel{!}{=} 1$ over the system length. Figure 4.9 shows the resulting Capillary Numbers Ca versus Gravitational Numbers Gr. For each case, the start of injection is marked by a square. Time is reflected by the length of the curves in Figure 4.9 (however, curve length is not a scale for time). The lengths of the curves vary, since injection is stopped when the CO_2 plume spreads a radial distance of 1 kilometer from the injection well. For example, the curve for Case K (Median & k/10) describes a timespan of 7.48 years whereas Case S represents only a timespan of 0.37 years. The Median case timespan is 3.85 years.

For the estimate, where $\widehat{\nabla}\hat{p}_\mathrm{c} \stackrel{!}{=} 1$ over the front width (Figure 4.9, left), Gr is increasing with increasing time, whereas Ca is rather constant. The Gravitational Number Gr is increasing with time since $\mathrm{v_{cr}}$ is decreasing and all other values in Gr are constant. The Capillary Number Ca varies only marginally since l_cr (selected here as the front width at $\frac{2}{3}$ of the reservoir height) is increasing with time due to capillary diffusion and $\mathrm{v_{cr}}$ is decreasing at the same rate; these effects cancel each other out. The small oscillations in Ca are due to l_cr being a step function due to numerical discretisation. Note that the characteristic pressure p_cr is constant in time for both options; i.e. capillary pressure drop over front width or system length. With increasing time, the gravitational forces become more and more important and finally dominate.

For the estimate where $\widehat{\nabla}\hat{p}_\mathrm{c} \stackrel{!}{=} 1$ over the system length (Figure 4.9, right), both Gr and Ca are increasing with time. This is due to the fact that $\mathrm{v_{cr}}$ is decreasing whereas l_cr (selected as the system length) is constant. The characteristic pressure p_cr is slowly increasing here.

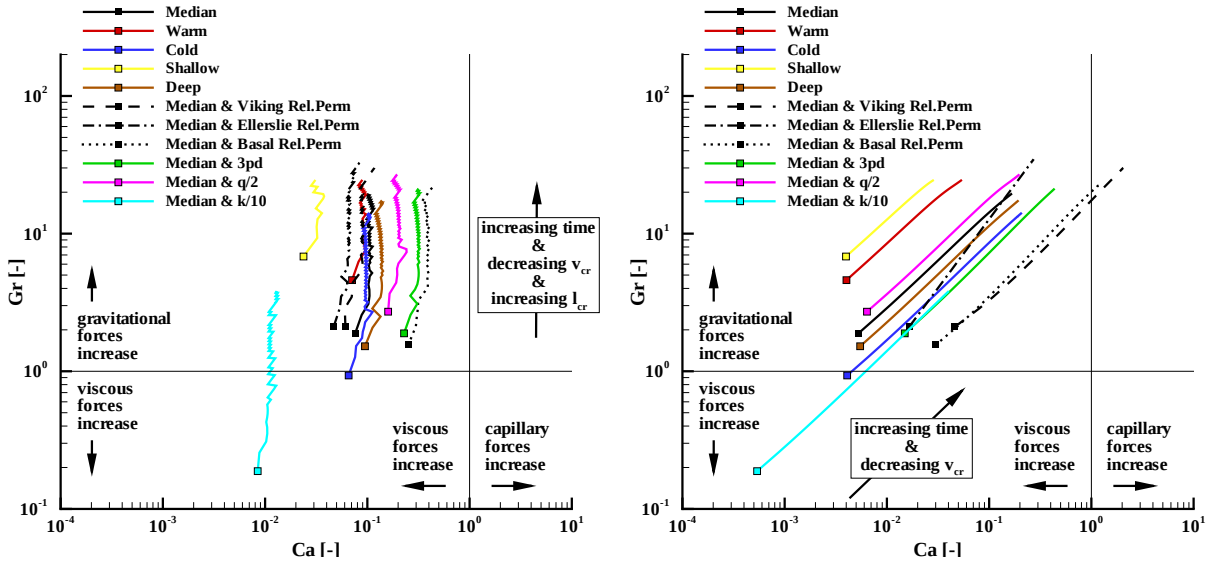

Figure 4.9: Variation of the Gravitational Number Gr versus Capillary Number Ca for a radially symmetric domain derived from simulation experiments. Left: Gr versus Ca where $\widehat{\nabla}\hat{p}_c \stackrel{!}{=} 1$ over the front width. Right: Gr versus Ca where $\widehat{\nabla}\hat{p}_c \stackrel{!}{=} 1$ over the system length.

This means that, with increasing time, and according to this definition of Ca under the given assumption that $\widehat{\nabla}\hat{p}_c \stackrel{!}{=} 1$ over the system length, both gravitational and capillary forces become more and more important and finally dominate over the viscous forces.

When looking at Figure 4.9, it might be confusing that, depending on the choice for characteristic values, the importance of capillary forces varies in time. This behaviour relates to the scale on which the problem is considered. When looking at the system at a reservoir scale (l_{cr} = system length), capillary forces are initially weak and viscous forces dominate. Over time, viscous forces become weaker (due to a reduction of v_{cr}) and capillary forces gain importance. Due to this reasoning, reservoir engineers, mostly interested in average reservoir pressures and production rates, often neglect capillary forces when viscous forces are strong (field in production). When looking at the system on a process dependent scale (l_{cr} = front width), capillary pressure is of equal importance during the entire process, since the process dependent length scale increases at the same rate as the velocity decreases, leading to constant viscous forces. Considering the system on a process-dependent scale allows for more detailed and physically motivated interpretations, but requires better knowledge of the system.

The choice of characteristic values leading to estimates of Ca and Gr as shown in Figure 4.9 has now been physically justified by the processes in the reservoir and the dimensionless numbers are interdependent now. In the initial analytical investigation (Figure 4.2), this was not the case because the analysis of Ca and Gr was mathematically motivated and the characteristic values were independent of each other.

4.4.3 Qualitative Dependencies of Risk and Storage Capacity on Dimensionless Numbers

The qualitative effect on risk and on storage capacity, as defined in Section 4.2, is now investigated depending on the numerically calculated Dimensionless Numbers Gr and Ca. A larger Gr, that is stronger gravitational forces in relation to viscous forces, is expected to result in a reduction of storage capacity since an increase of gravitational forces leads to enhanced gravity segregation, and thus to more pore space that cannot be utilised for storage in the lower parts of the reservoir. Accordingly, a lower Gr stands for a higher capacity due to an increase of viscous forces leading to a more cylindrically shaped plume evolution, and thus CO_2 reaches also deeper parts of the reservoir at greater distance to the injection point. This holds for both options of characteristic values ($\widehat{\nabla}\hat{p}_c \stackrel{!}{=} 1$ over the front width and $\widehat{\nabla}\hat{p}_c \stackrel{!}{=} 1$ over the system length, cf. Section 4.4.1) since Gr is the same for both options. The number Ca can be used to investigate the average CO_2 saturation S_{CO2} behind the front. A higher Ca is expected to result in a decrease of S_{CO2} since stronger capillary forces lead to a smoother front where the non-wetting phase saturation is lower. Hence, high capillary forces, i.e. large Ca numbers, improve the storage capacity of a reservoir. The dependency of storage capacity on the Dimensionless Numbers is investigated in more detail in Chapter 5.

Similarly, the effect of the dimensionless numbers on risk can be described. A higher Gr is expected to result in an increase of risk, since an increase of gravitational forces leads to enhanced gravity segregation. Hence, a larger fraction of the injected CO_2 accumulates in the upper part of the aquifers, i.e. below the caprock, which is potentially risky. Accordingly, a lower Gr stands for a lower risk due to an increase of viscous forces, leading to a more compact plume, and thus larger portions of the injected CO_2 are found in deeper parts of the reservoir. A higher Ca describes an increase in capillary forces in relation to viscous forces. This results in lower CO_2 saturations behind the front due to increased capillary dispersion. Lower CO_2 saturations result in lower risk, since potential leakage rates are lower, if a fault etc. is encountered. Counteracting on the lower risk estimate is the simultaneously larger plume extent (at constant density), which increases the risk. However, a stronger influence of (capillary) diffusive or dispersive processes is expected to result in lower risk since this generally results in higher fractions of total injected CO_2 mass dissolved in brine and thus leads to less potential leakage of free-phase CO_2.

4.5 Summary and Conclusion

A dimensional analysis was conducted to improve the understanding of processes occurring in a geological reservoir during the injection of CO_2.
A fractional flow formulation was chosen in order to derive a dimensionless form of the governing equations. This could be achieved by defining the dimensionless Capillary Number Ca and the Gravitational Number Gr, and choosing appropriate characteristic values for length, time, pressure, and velocity. These were supplemented by further dimensionless terms A, B, and C, which depend via relative permeability relations on phase saturations and on fluid properties.
The relationships between forces in a reservoir influencing storage capacity and risk estimates were evaluated using a two-step approach. First, dimensional analysis based on the dimensionless form of the equations was carried out, which aimed at showing the influence of capillary, viscous, and gravitational forces for the different reservoirs classes. In the second step, 1-D and 3-D simulation experiments were carried out, in which the evolution of a CO_2 plume in a reservoir was simulated. The results of these simulations and their interpretation, using the characteristic numbers Ca and Gr, were discussed in detail.
The basic conclusions and findings are summarised as follows:

- The 1-D simulation study neglects gravity effects and thus reflects the influence of the Ca number on plume evolution velocities. It was shown that the order (ranking) of the Ca numbers resembles the order of plume evolution velocities and that the average CO_2 saturation can be estimated by analysing the fractional flow function. This is a prerequisite when estimating storage capacity. However, particularly the influence of varying injection rate, capillary pressure and permeability is quantitatively less significant. The reason for this is that gravity segregation is neglected due to the 1-D assumption.

- In the 3-D simulation study, the influence of gravity segregation is included and the development of both the Ca and the Gr numbers was shown. It is possible to order geological reservoirs qualitatively according to their plume evolution behaviour using the dimensionless numbers Ca and Gr. The Gravitational Number Gr appears to have a stronger influence than the Capillary Number Ca. However, it is not clear how the simultaneous variations of Gr and Ca quantitatively affects storage capacities and risk estimates. One should expect that Ca numbers further lose influence when the system dimensions become larger. Nevertheless, a low ratio of gravitational to viscous forces (low Gr) - and to some extent also a high ratio of capillary to viscous forces (high Ca)- possibly leads to high CO_2 storage capacity and low risk.

- The relative permeability-saturation relations have proven to be of great influence for plume evolution velocity and average CO_2 saturation. Therefore, they have a great influence on storage capacity and risk.

5 Analysis of Storage Capacity*

In Chapter 4, a dimensional analysis was performed to assess the dominant forces and processes relevant in CO_2 storage in geological formations. This was done by introducing characteristic values and defining dimensionless numbers. Different options for the selection of the characteristic values were investigated and a qualitative understanding of the influence of the relation of forces on the CO_2 plume evolution behaviour and on a simplified measure of storage capacity was developed. This idea is further extended here by developing a more sophisticated method for estimating storage capacity. The more sophisticated method respects the physical trapping mechanisms introduced in Section 1.1, which interact on very different time scales with varying contribution to the total trapping. Detailed time-dependent storage-capacity estimates are calculated by numerical simulations for the previously used 1-D and 3-D reservoirs employing typical reservoir parameter setups. The detailed estimates of storage capacity are interpreted using the calculated dimensionless numbers.

5.1 Discussion of Storage Capacity

As outlined by the *Task Force for Review and Identification of Standards for CO_2 Storage Capacity Estimation* for the Technical Group of the Carbon Sequestration Leadership Forum (CSLF) and published in Bachu et al. (2007), different authors employ a variety of approaches and methodologies to assess CO_2 storage capacity. The widely varying estimates are thus difficult to compare and evaluate. Bachu et al. (2007) propose using the concept of "Resource-Reserve Pyramids".

5.1.1 Resource-Reserve Pyramids

This concept considers several aspects of CO_2 storage, i.e. various process-dependent time scales, different assessment scales (basin, regional, local, or site scale), different assessment types, and different geological storage options (Bachu et al., 2007). Several resource-reserve

*This Chapter is published in Kopp, A., Class, H. and Helmig, R., Investigations on CO_2 storage capacity in saline aquifers - Part 2: Estimation of storage capacity coefficients, Int. J. Greenhouse Gas Control, 3(3), 277–287, DOI:10.1016/j.ijggc.2008.10.001, 2009.

pyramids have been proposed, reflecting the multi-faceted aspects of CO_2 storage. This study always refers to the Techno-Economic Resource-Reserve pyramid.

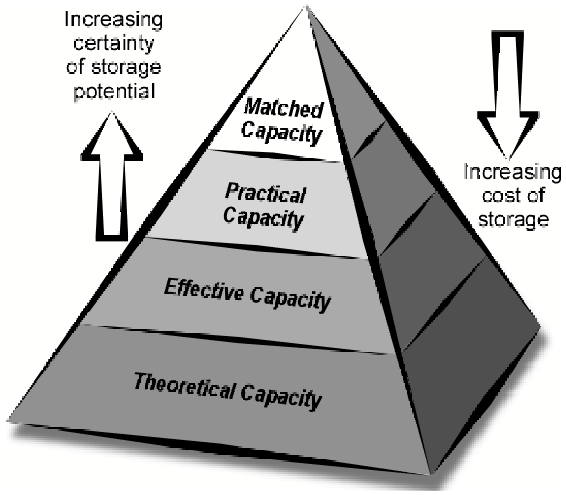

Figure 5.1: Techno-Economic Resource-Reserve pyramid for CO_2 storage capacity in geological media after Bachu et al. (2007).

This pyramid consists of four levels of capacity estimates. The theoretical capacity $V_{\mathrm{CO2,t}}$ [m^3] represents the first level and assumes that the entire pore volume of a formation minus the residual water-rich phase saturation is accessible to store CO_2.

$$V_{\mathrm{CO2,t}} = \iiint \phi(1 - S_{w,r})\, dxdydz, \tag{5.1}$$

where $S_{w,r}$ is residual water-rich phase saturation. The theoretical capacity, which is a volume, represents the size of the resource pyramid. The second level, the effective capacity, excludes portions of the theoretical capacity which are not accessible for storage due to geological and engineering reasons. The third level, the practical capacity, is a subset of the effective capacity which also considers economic, legal and regulatory, infrastructural, and general economic aspects. The top level of the pyramid, the matched capacity, is a subset of the practical capacity. It is obtained by detailed matching of large stationary CO_2 sources with adequate geological storage sites.
To calculate the mass of CO_2 that can effectively be stored, M_{eff}, effective capacity is multiplied by CO_2 density. This can be a delicate task, since pressure and temperature vary during the CO_2 injection phase depending on many reservoir and process controlled parameters (i.e. absolute and relative permeability, reservoir boundaries, injection strategy, etc.). Note that the effective capacity, CO_2 density, and consequently M_{eff} are generally time dependent.
The aim of this section is to provide more insight into the effective capacity estimates and the effective CO_2 mass that can be stored (M_{eff}), based on investigations on reservoir properties of potential formations (Section 3). No reference to a specific reservoir, basin, or region is

made. Instead, the general range of effective storage capacity and the mass which can be stored therein are investigated, together with processes and parameters which may increase or decrease them. Several attempts have been made in the literature to estimate effective storage capacity and M_{eff}, which include the models described in the following.

5.1.2 Doughty Model

Doughty et al. (2001) propose a methodology to estimate effective capacity as a volume fraction of the reservoir available for CO_2 storage. Theoretically, the effective capacity coefficient C [-] ranges between zero (no storage is possible) and the volume fraction of the entire pore space of the reservoir, i.e. average porosity ϕ_{avg}. The coefficient C is constructed as a product of four factors.

$$C = C_{\text{i}} \cdot C_{\text{g}} \cdot C_{\text{h}} \cdot \phi_{\text{avg}}, \quad C \in \{0, \phi_{\text{avg}}\}, \tag{5.2}$$

where C_{i} is the intrinsic capacity coefficient [-], C_{g} is the geometric capacity coefficient [-], C_{h} is the heterogeneity capacity coefficient [-] and ϕ_{avg} is average formation porosity [-]. Figure 5.2 illustrates the definition of the capacity coefficients. The intrinsic capacity coefficient C_{i} has contributions from the fraction of pore space that is occupied by the CO_2-rich phase ($C_{\text{i,CO2}}$) and the fraction of the pore space that CO_2, dissolved in the water-rich phase, would occupy if it was converted to the CO_2-rich phase ($C_{\text{i,w}}$). The coefficients $C_{\text{i,CO2}}$ and $C_{\text{i,w}}$ add up to C_{i}.
Doughty et al. (2001) estimate $C_{\text{i,CO2}}$ by a Buckley-Leverett type analysis (Buckley and Leverett, 1942) as

$$C_{\text{i,CO2}} \cong S_{\text{CO2}}, \tag{5.3}$$

where S_{CO2} is the average CO_2-rich phase saturation [-]. The coefficient $C_{\text{i,w}}$ is estimated by

$$C_{\text{i,w}} \cong S_{\text{w}} \cdot X_{\text{w}}^{\text{CO2}} \cdot \frac{\varrho_{\text{w}}}{\varrho_{\text{CO2}}}, \tag{5.4}$$

where S_{w} is the average water-rich phase saturation, $X_{\text{w}}^{\text{CO2}}$ the average mass fraction of CO_2 dissolved in the water-rich phase. Parameters and variables S_{w}, $X_{\text{w}}^{\text{CO2}}$, and ϱ are averaged behind the CO_2 front.
The geometric capacity coefficient C_{g} accounts for partially penetrating wells, gravity segregation and dipping aquifers which reduce the theoretical storage capacity. It is defined here as the volume fraction of the entire pore space, occupied by the CO_2-rich phase, divided by the entire available pore space (limited by the reservoir size, for example a spill point, etc.).
The heterogeneity capacity coefficient C_{h} accounts for heterogeneities in absolute permeability, leading to a further reduction or increase in accessible storage capacity. Note that

these capacity coefficients cannot always be estimated individually. For example, in a three-dimensional, heterogeneous reservoir, only the product of C_g and C_h can be estimated. For simplified problems, for example, in one dimensional gravitation-free reservoirs, $C_{i,CO2}$ and $C_{i,w}$ can be estimated individually and C_g and C_h are unity by definition.

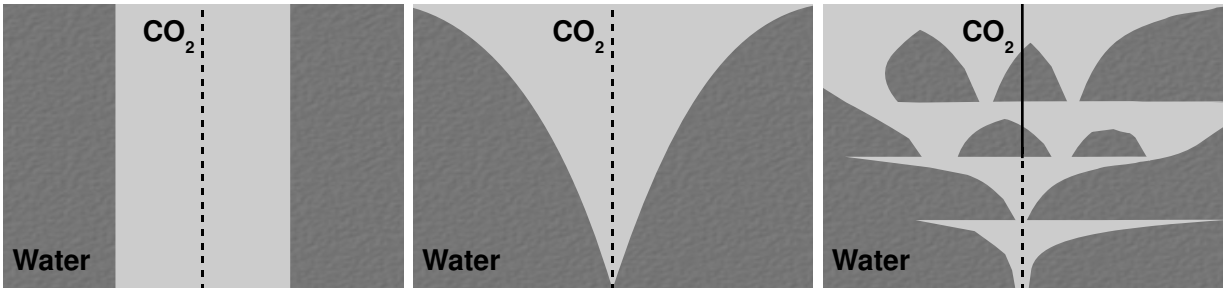

Figure 5.2: Sketch showing estimation of storage capacity coefficients depending on model complexity (after Doughty et al. (2001)); dark-grey colour indicates water-rich phase and light-grey colour CO_2-rich phase. Left: Estimation of intrinsic storage capacity coefficient (C_i) in a gravitation free, homogeneous reservoir ($C_g = C_h = 1$). Saturations etc. are averaged within the light-grey area. Centre: Estimation of the intrinsic (C_i) and geometric (C_g) storage capacity coefficients in a homogeneous reservoir ($C_h = 1$). Coefficient C_g is equivalent to the ratio of the light-grey area to the dark-grey area. Right: Estimation of the intrinsic (C_i), geometric (C_g), and heterogeneity (C_h) storage capacity coefficients in a heterogeneous reservoir. Note that in the latter case, only the product of C_g and C_h can be estimated (that is the ratio of the light-grey area to the dark-grey area), since individual contributions can not be identified.

Doughty et al. (2001) do not give further insight into calculation of the effective CO_2 mass that can be stored in this volume fraction of the reservoir (M_{eff}).

5.1.3 CSLF Model

Bachu et al. (2007) propose a methodology in which the effective capacity, the so-called effective storage volume, is obtained by reduction of the theoretical capacity $V_{CO2,t}$ (cf. Equation 5.1) by the capacity coefficient C_c.

$$V_{CO2,e} = C_c \cdot V_{CO2,t}, \qquad C_c \in \{0,1\}, \tag{5.5}$$

where $V_{CO2,e}$ is the effective storage volume [m^3] and C_c is the capacity coefficient [-]. Here, the porosity ϕ is already included in the calculation of $V_{CO2,t}$. The capacity coefficient C_c ranges between zero and one, i.e. between no storage capacity and usability of the entire theoretical capacity. Bachu et al. (2007) state that C_c incorporates the cumulative effects of heterogeneities in absolute permeability, CO_2 buoyancy and sweep efficiency.

To calculate M_{eff}, Bachu et al. (2007) define two limits for the pressure to calculate an upper and a lower estimate of the CO_2 density. The lower estimate of the CO_2 density is calculated by considering initial reservoir pressure conditions, p_{i}. The upper estimate of the CO_2 density is calculated by considering a maximum pressure, p_{max}, which is the lowest of the maximum pressure allowed by regulatory agencies in order to avoid rock fracturing, and the threshold entry pressure of the caprock. For temperature, the authors define initial reservoir temperature. These definitions lead to a range of M_{eff} as given in Equation 5.6.

$$M_{\text{eff,min}} = \varrho_{\text{CO2}}(p_{\text{i}}, T_{\text{i}}) \cdot V_{\text{CO2,t}} \cdot C_{\text{c}} \leq M_{\text{eff}} \leq \varrho_{\text{CO2}}(p_{\text{max}}, T_{\text{i}}) \cdot V_{\text{CO2,t}} \cdot C_{\text{c}} = M_{\text{CO2,max}}. \quad (5.6)$$

Bachu et al. (2007) state that currently no values for the site-specific capacity coefficient C_{c} are provided in the literature.

5.1.4 Proposed model

The model proposed here considers Doughty's model to calculate the effective capacity coefficient C, as given in Equation 5.2. In case that the pore volume containing dissolved CO_2 is considerably larger than the pore volume containing CO_2-rich phase (e.g. in long-term investigations after injection stop, see (see Figure 5.3), Equation 5.2 needs to be reformulated. The geometric capacity coefficient C_{g} is split into two coefficients, $C_{\text{g,CO2}}$ and $C_{\text{g,w}}$, and the intrinsic capacity coefficients $C_{\text{i,CO2}}$ and $C_{\text{i,w}}$ are averaged over the respective pore volume fraction. This is, $C_{\text{i,CO2}}$ is averaged over the pore volume occupied by the CO_2-rich phase ($C_{\text{g,CO2}}$), whereas $C_{\text{i,w}}$ is averaged over the pore volume occupied by brine with dissolved CO_2 load ($C_{\text{g,w}}$). Since in a complex heterogeneous reservoir no individual estimation on C_{g} and C_{h} can be made, the capacity coefficient C_{h} is also split into two new coefficients, $C_{\text{h,CO2}}$ and $C_{\text{h,w}}$. This leads to the following extended definition of storage capacity coefficient C

$$C = \underbrace{C_{\text{i,CO2}} \cdot (C_{\text{g,CO2}} \cdot C_{\text{h,CO2}}) \cdot \phi_{\text{avg}}}_{\text{Volumetic share}} + \underbrace{C_{\text{i,w}} \cdot (C_{\text{g,w}} \cdot C_{\text{h,w}}) \cdot \phi_{\text{avg}}}_{\text{Dissolved share}} \quad (5.7)$$

In this case, the geometric capacity coefficients $C_{\text{g,CO2}}$ and $C_{\text{g,w}}$ for the CO_2-rich phase and the water-rich phase differ. Consequently, CO_2-rich phase saturation in Equation 5.3 ($C_{\text{i,CO2}}$) is averaged behind the CO_2-rich phase front, whereas the properties S_{w}, $X_{\text{w}}^{\text{CO2}}$ and ϱ in Equation 5.4 ($C_{\text{i,w}}$) are averaged behind the dissolved CO_2 front. Probst (2008) investigates storage capacity by using this approach for multiple realisations of heterogeneous permeability fields in a realistic reservoir at shallow depth.
However, in this study a continuous injection into a homogeneous reservoir is considered and it is not necessary to split C_{g} and C_{h}, hence the effective storage capacity coefficients C are identical using either definition.
To calculate M_{eff}, based on Doughty's model, the effective capacity coefficient C is multiplied by CO_2 density and the total geometric reservoir volume (bulk volume) V_{total}. It is necessary

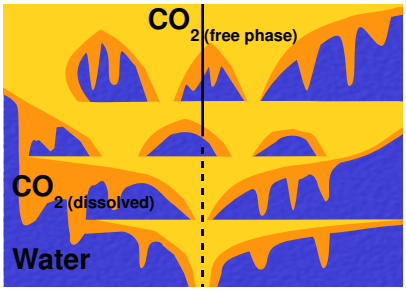

Figure 5.3: Estimation of storage capacity coefficients according to Equation 5.7 for long-term investigations, that is when the pore volume containing dissolved CO_2 (dissolved share indicated by orange plus yellow coloured area) is considerably larger than the pore volume containing CO_2-rich phase (volumetric share indicated by yellow coloured area).

to multiply by the total geometric reservoir volume because average reservoir porosity and residual water-rich phase saturation (inherently) are included in the coefficient C. The effective CO_2 mass stored M_{eff} is calculated according to Equation 5.8.

$$M_{\text{eff}} = C \cdot V_{\text{total}} \cdot \varrho_{\text{CO2}}(T, p), \tag{5.8}$$

where CO_2 density is a function of reservoir temperature and pressure.
As a clarification of the difference between the capacity coefficient C in the Doughty Model (used in the following) and C_{c} in the CSLF Model: The porosity ϕ is already included in Doughty's capacity coefficient C, therefore C represents the fraction of the total (bulk) aquifer volume that can be used for storage (C thus varies between zero and (average) porosity ϕ). On the other hand, in the CSLF formulation, ϕ is included in the pore-space volume calculations, so that C_{c} represents the fraction of the pore space that can be used for storage (C_{c} thus varies between zero and one). The relation between the two is

$$C_{\text{Doughty/Kopp}} = \phi_{\text{avg}} \cdot C_{\text{c,CSLF}}. \tag{5.9}$$

This relationship allows portability and comparison of results obtained by the different models.

5.2 Numerical Investigations

To determine the storage capacity for typical reservoirs based on the proposed concept, a series of numerical experiments was conducted. The numerical experiments are conducted with the model for isothermal multi-phase processes without mass transfer between the phases, i.e. the 2p-module implemented in MUFTE-UG (cf. Section A.1). Detailed storage capacity coefficients are given for an idealised 1-D gravitation-free reservoir and for a 3-D

radially symmetric domain. The parameter setups for the various cases are identical to those previously defined (cf. Table 3.2).
To derive capacity estimates, it is necessary to limit the reservoir volume at some point. This serves to calculate the total geometric reservoir volume V_{total} (cf. Equation 5.8). The capacity estimates in the following are given at the point in time when the CO_2 phase reaches a spill point and leakage occurs. This "virtual spill point" is defined at one kilometre distance from the injection well. The model domain extends beyond the leaky well distance to limit unwanted influence of boundary conditions on model results.

5.2.1 Plume evolution in a 1-D gravitation-free reservoir

In Section 4.4.1, CO_2 injection into a 1-D reservoir is analysed. The resulting CO_2-rich phase saturation is shown in Figure 4.4 after 4 years model time. Results have been discussed with respect to the relation between capillary and viscous forces as given by the Capillary Number Ca. The qualitative dependency of storage capacity on dimensionless numbers was introduced in Section 4.4.3. In the following, the focus is on the quantitative analysis of the storage capacity. In this 1-D horizontal model domain, gravitational forces cannot be considered (g = 0). Thus, this example problem focuses on the analysis of the intrinsic capacity coefficient C_{i}. It has been stated and discussed that it is possible to estimate the average CO_2-rich phase saturation by $S^{\mathrm{t}}_{\mathrm{CO2}}$, i.e. the CO_2-rich phase saturation of the tangential point of the fractional flow function. The average saturation is an estimator for the intrinsic capacity coefficient C_{i}. Since $C_{\mathrm{i,w}}$ is neglected here, and C_{g} and C_{h} are equal to one for a homogeneous gravitation-free reservoir, the storage coefficient C can be easily calculated.
Table 5.1 lists the resulting capacity coefficients as calculated from Equations 5.2 to 5.4. The mass fraction of dissolved CO_2 in the water-rich phase $X_{\mathrm{w}}^{\mathrm{CO2}}$ required to calculate $C_{\mathrm{i,w}}$, follows the solubility model of Duan and Sun (2003), taking into account pressure, temperature and brine salinity. Dissolution of CO_2 in the water-rich phase is, however, not included in the numerical simulations of this study and $C_{\mathrm{i,w}}$ is therefore marked by brackets in Table 5.1 and not included in the calculation of C.
Note that values shown for $C_{\mathrm{i,w}}$ in Table 5.1 indicate upper limits. They are calculated at full water-rich phase saturation ($S_{\mathrm{w}} = 1$), which is, however, time-dependent. To obtain comparable capacity estimates, the virtual spill point of the reservoir has to be equal for all reservoirs. The virtual spill point is reached by the front at different points in time for the different cases. This means that the amount of injected CO_2 differs. The effective mass M_{eff} [-] in Table 5.1 (according to Equation 5.8) indicates this amount normalised to the Median case. The effective capacity coefficient for the Median reservoir is $C_{\mathrm{Median}} = 0.065$, which means that 6.5 % of the total geometric reservoir volume is used for storage. Since the Median reservoir has a porosity of 0.2, this volume accounts for 32.5 % of the pore space. In this volume the (normalised) mass (1.0) can be stored. In comparison, the Warm reservoir has an effective capacity coefficient of 0.064, which is similar to that of the Median reservoir

Cases	Letter Coding	C_i [-]		C [-]	M_eff [-]
		$C_\mathrm{i,CO2}$ [-]	$C_\mathrm{i,w}$ [-]		
Median Reservoir	M	0.323	(0.031)	0.065	1.00
Warm Reservoir	W	0.320	(0.052)	0.064	0.48
Cold Reservoir	C	0.324	(0.027)	0.065	1.23
Shallow Reservoir	S	0.245	(0.234)	0.049	0.11
Deep Reservoir	D	0.359	(0.028)	0.072	1.12
Median R.+V.-kr	V	0.256	(0.036)	0.051	0.80
Median R.+E.-kr	E	0.260	(0.033)	0.052	0.80
Median R.+B.-kr	B	0.505	(0.022)	0.101	1.57
Median R.+3p_d	P	0.311	(0.031)	0.062	0.97
Median R.+$\frac{q}{2}$	Q	0.316	(0.031)	0.063	0.98
Median R.+$\frac{k}{10}$	K	0.328	(0.030)	0.066	1.02

Table 5.1: Storage capacity coefficients for the 1-D gravitation-free reservoir. The coefficient $C_\mathrm{i,w}$ is calculated according to the solubility model of Duan and Sun (2003), but it is not included in the numerical simulations and consequently it is not included in the calculation of C. Coefficients C_g and C_h equal unity by definition here. Porosity ϕ, necessary to calculate the effective capacity C is 0.2. Note that C refers to the total geometric volume of the reservoir. To convert C to pore space volume utilised, one needs to divide C by porosity. The effective mass M_eff [-] indicates CO_2 mass injected when reaching the virtual spill point of the reservoir, normalised by the Median case mass.

and surprising at first sight. But only a normalised mass of 0.48 can be stored, since the CO_2 density is much lower. Thus, the effective capacity coefficient C as defined here, is not a sufficient measure when analysing different reservoirs. Instead, the resulting M_eff has to be considered.

The Cold and Deep reservoir cases have a high effective mass (M_eff) of CO_2 that can be stored due to high CO_2 density. The Median reservoir with Basal formation relative permeability relations has a higher M_eff than the Median reservoir case, since in this case the relative permeability to CO_2 is much lower and therefore average CO_2-rich phase saturation $C_\mathrm{i,CO2}$ is higher. The Median reservoir with either tripled entry pressure, halved injection rate, or reduced permeability yields similar M_eff as the reference case does.

Lower M_eff is achieved in the Warm and Shallow reservoir cases due to low CO_2 density. The high value of $C_\mathrm{i,w}$ in the Shallow reservoir case (0.234) is also due to the low CO_2 density at these pressure and temperature conditions. A value of 0.234 for $C_\mathrm{i,w}$ means that the amount of CO_2 that could be dissolved in brine would occupy a fraction of 0.234 of the pore space

when converted to the CO_2-rich phase. The amount of CO_2 that could be stored in the brine phase (dissolved), is almost identical to the amount that could be stored in the CO_2-rich phase (0.245).
The Median reservoir with Viking or Ellerslie relative permeability relations has a lower M_{eff} than the Median reservoir case due to lower average CO_2-rich phase saturation. In these cases the very high residual water-rich phase saturation together with a slightly higher relative permeability of CO_2 in the important range of S_{CO2} between zero and 0.3 lead to lower average CO_2-rich phase saturation. The lower relative permeability of the water-rich phase seems not to be of importance here.
The 1-D gravitation-free reservoir shows that relative permeability plays an important role for estimating storage capacity. It influences the capacity estimates to a similar extent as the entire range of reservoir properties like geothermal gradient and depth. Effects of density are nicely demonstrated. However, the 1-D approach reveals effects of changing entry pressure, injection rate and absolute permeability only to some extent. Particularly, a different absolute permeability is expected to have a huge influence on capacity estimates. This will be shown in the following section.

5.2.2 Plume evolution in a radially symmetric 3-D reservoir

A 3-D radially symmetric domain, briefly described in Section 4.4.2, with the parameter settings given in Table 3.2, is investigated. In Figure 4.8 CO_2-rich phase saturation iso-lines after 3.85 years of injection are shown. The results are discussed with respect to resulting storage capacity coefficients. For this 3-D radially symmetric domain, this is more complicated than for the 1-D domain, because C_{i} and C_{g} vary with time.
The Shallow and Warm reservoir setups show very strong gravity segregation due to lower CO_2 density, hence stronger buoyancy, leading to a fast plume evolution at the top of the reservoir (note that the r-axis in Figure 4.8 shows only the first 2000 m of the reservoir). This yields then a small geometric capacity coefficient (C_{g}). Cold reservoir setups and those with reduced permeability show a more cylindrical plume evolution, i.e. a larger geometric capacity coefficient, which is due to higher viscosity or lower permeability. The Median case setups with relative permeability relations from the Viking and Ellerslie formations show a faster plume evolution than the Median case. This is because of the generally lower CO_2-rich phase saturation in the reservoir (and thus lower $C_{\text{i,CO2}}$), as already seen in the 1-D reservoir simulation (see Section 5.2.1). In comparison, the Median case with the relative permeability relation from the Basal formation and the deep reservoir setup show a much slower plume evolution velocity (due to higher $C_{\text{i,CO2}}$). The tripled entry pressure does not have a great influence.
In Figure 5.4, the variation of the average capacity coefficient $C_{\text{i,CO2}}$ ($\cong S_{\text{CO2}}$) versus time is shown. The capacity coefficient $C_{\text{i,CO2}}$ is volume-averaged over the portion of the pore volume with non-zero CO_2-rich phase saturation. The capacity coefficient $C_{\text{i,CO2}}$ increases with time for all cases. The end-points of the lines indicate the points in time when the

virtual spill point of the reservoir is reached.

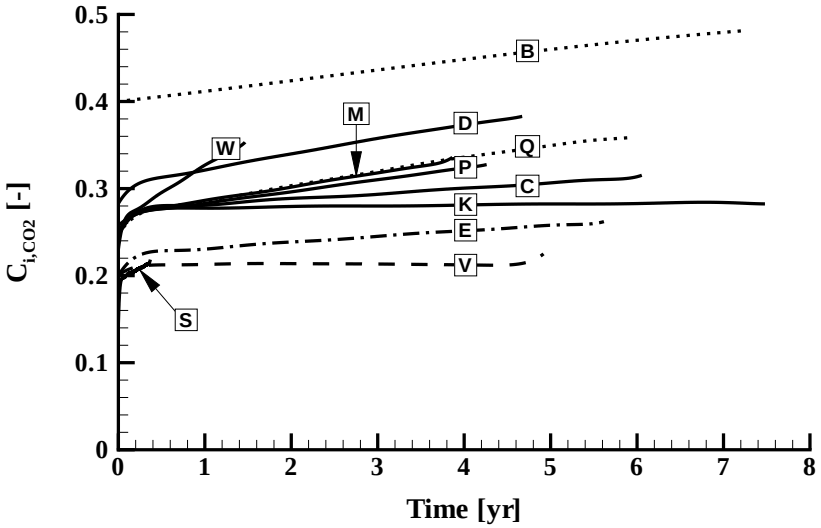

Figure 5.4: Variation of the intrinsic CO_2-rich phase capacity coefficient $C_{\mathrm{i,CO2}}$ ($\cong S_{\mathrm{CO2}}$) in time for various reservoirs. Letter coding according to Table 3.2.

Figure 5.5 shows the geometric capacity coefficient C_{g} versus time. Due to the virtual spill point, the reservoir size is fixed and therefore C_{g} increases until the spill point is reached by the CO_2 plume.
A projection of the curves in Figures 5.4 and 5.5 to the r-axis gives the time since the start of injection and the non-normalised M_{eff} (in Case M this is 3.85 Mt CO_2). Case Q is the only exception here. Since the injection rate is halved, the r-axis values need to be halved as well to represent M_{eff}.
To summarise, Table 5.2 shows capacity coefficients at the point in time when the virtual spill point is reached. The point in time when the virtual spill point is reached, varies for the different cases. Therefore, Table 5.2 requires a closer look to be comparable to Figure 4.8. Figure 4.8 shows CO_2-rich phase saturation iso-lines after 3.85 years of injection, i.e when the CO_2 plume reaches the virtual spill point in the Median reservoir case. The total geometric volume of the reservoir up to the virtual spill point is

$$V_{\mathrm{total}} = \pi \cdot r^2 \cdot \mathrm{height} = \pi \cdot 1000\ \mathrm{m}^2 \cdot 100\ \mathrm{m} = 0.314 \cdot 10^9\ \mathrm{m}^3 = 0.314\ \mathrm{km}^3. \tag{5.10}$$

According to Equation 5.8 and the definition of the C value from Table 5.2, the effective stored mass M_{eff} for the Median case is

$$M_{\mathrm{eff}} = 0.01855 \cdot 0.314 \cdot 10^9\ \mathrm{m}^3 \cdot 660.7\ \mathrm{kg/m}^3 = 3.85\ \mathrm{Mt\ CO_2}. \tag{5.11}$$

Since 1 Mt CO_2 per year is injected and the virtual spill point is reached after 3.85 years, the effective mass M_{eff} for the Median case must be 3.85 Mt CO_2.
In the Median reservoir case (M), a fraction of 0.279 of the pore space (C_{g}) is used for storage. Multiplying C_{g} with the average CO_2-rich phase saturation ($C_{\mathrm{i,CO2}}$) of 0.3325 and porosity

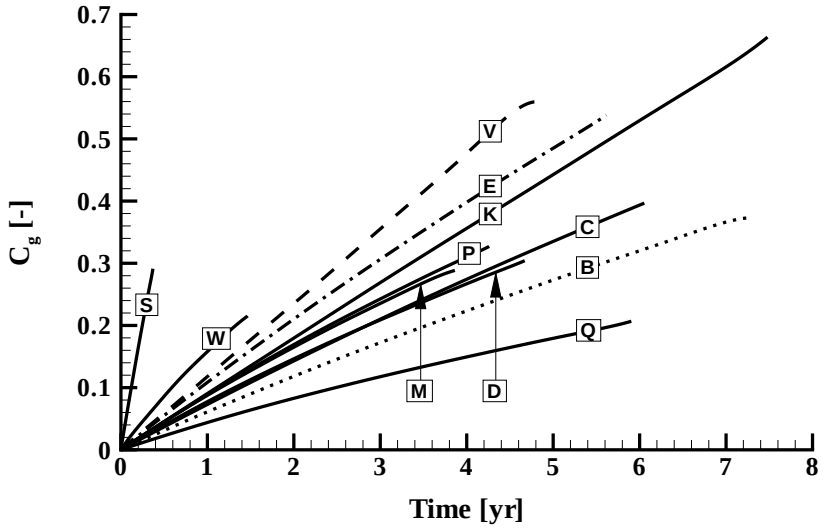

Figure 5.5: Variation in time of the geometric capacity coefficient C_g for various reservoirs. Letter coding according to Table 3.2.

gives an effective capacity coefficient of 0.01855. To convert the effective capacity coefficient C (which refers to total reservoir volume) to pore space volume, one needs to divide C by the porosity, yielding approximately 0.093. Generally, the range of effective capacity coefficients for the radially symmetric reservoir is larger than for the 1-D gravitation-free reservoir. The coefficient C ranges in this 3-D study from 0.0117 (Case S) up to 0.036 (Case K). The same cases also mark the smallest and largest value of M_{eff}; from 0.09 up to 1.94. This means that in a reservoir at Shallow case conditions (Case S) less than 5 % of CO_2 can be stored compared to an equally-sized reservoir having a smaller permeability (Case K). Note that the Shallow case assumes sub-critical conditions for the CO_2 phase.

The Median reservoir case with reduced permeability (Case K) shows a very high effective stored mass (M_{eff}) due to the high geometric capacity coefficient C_g. In other words, Case K refers to a more cylindrical plume evolution.

Median reservoir cases with relative permeability relations from the Viking (Case V), Ellerslie (Case E), or Basal (Case B) formations show all higher M_{eff} than the Median case. The average CO_2-rich phase saturation ($C_{\text{i,CO2}}$) in each case is comparable to the 1-D experiments and is presumably caused by the relative permeability of CO_2 (for Cases V and E, the average CO_2-rich phase saturation ($C_{\text{i,CO2}}$) is lower compared to the Median case, for Case B it is higher). However, the geometric capacity coefficients C_g are higher in all cases (V, E, and B) compared to the Median case, which is presumably due to the lower relative permeability of the water-rich phase at high water-rich phase saturations, i.e. $S_w > 0.85$ (at the front). Since cases V and E have even lower relative permeability of the water-rich phase in the considered range than Case B, these cases reach even higher C_g. As a result, when calculating M_{eff}, Case B stores 188 % of the mass that is stored in the Median reservoir. Cases V and E store 129 % and 145 % respectively. This shows that very different relative permeability relations (see

Cases	Letter Coding	C_i [-]		C_g [-]	C [-]	M_eff [-]
		$C_\mathrm{i,CO2}$ [-]	$C_\mathrm{i,w}$ [-]			
Median Reservoir	M	0.3325	(0.0301)	0.2790	0.01855	1.00
Warm Reservoir	W	0.3517	(0.0497)	0.2067	0.0145	0.38
Cold Reservoir	C	0.3129	(0.0279)	0.3820	0.0239	1.57
Shallow Reservoir	S	0.2150	(0.2432)	0.2723	0.0117	0.09
Deep Reservoir	D	0.3809	(0.0271)	0.2933	0.0224	1.21
Median R.+V.-kr	V	(0.2207)	(0.0351)	(0.5433)	(0.0240)	(1.29)
Median R.+E.-kr	E	0.2610	(0.0333)	0.5162	0.0270	1.45
Median R.+B.-kr	B	0.4868	(0.0231)	0.3587	0.0349	1.88
Median R.+3p_d	P	0.3264	(0.0304)	0.3147	0.0205	1.11
Median R.+$\frac{q}{2}$	Q	0.3592	(0.0289)	0.1978	0.0142	0.77
Median R.+$\frac{k}{10}$	K	0.2839	(0.0323)	0.6334	0.0360	1.94

Table 5.2: Storage capacity coefficients for a radially symmetric reservoir. The coefficient C_h equals unity by definition here. Porosity $\phi = 0.2$, necessary to calculate effective capacity C. The coefficient $C_\mathrm{i,w}$ is calculated according to the solubility model of Duan and Sun (2003), but not included in the numerical simulations and consequently not included in the calculation of C. The effective Mass M_eff [-] indicates CO_2 mass injected when reaching the virtual spill point of the reservoir, normalised to the Median case. A value M_eff of 1.0 equals 3.85 Mt CO_2, i.e. in the Median case this mass is injected before the virtual spill point is reached. Note that C refers to the total geometric volume of the reservoir. To convert C to pore space volume utilised, one needs to divide C by porosity (here 0.2).

Figure 2.12) can lead to high M_eff. This shows that not only the residual water- and CO_2-rich phase saturations are of importance when estimating storage capacity, but also the shape of both branches of the relative permeability relation (exponent λ in the Brooks-Corey model, cf. Table 2.2 for values for Cases V, E, and B). Case V is shown in brackets in Table 5.2 since fingering occurred here caused by an unstable front. This matter is not pursued further, since including dissolution of CO_2 in brine will reduce fingering. In a realistic heterogeneous permeability case, the distribution of permeability rather than hydrodynamic instability dominates fluid displacement (Garcia and Pruess (2003), Johannsen et al. (2006)).

Warm and Shallow reservoir cases show a capacity coefficient C lower than the Median case together with a low CO_2 density, leading to very low M_eff. In contrast, Cold and Deep reservoir cases show a capacity coefficient C higher than in the Median case along with a high CO_2 density, leading to high M_eff. In a radially symmetric domain, the tripled capillary entry pressure leads to an 11 % increase of effective stored mass. This is due to the increase

in the geometric capacity coefficient. The CO_2 plume is more spread out in this case. An effective stored mass of 0.77 for Case Q indicates that a high injection rate is advantageous. Low viscous forces lead here to stronger gravity segregation and a rather inefficient utilisation of the available pore volume (C_g).
The qualitative dependency of storage capacity on dimensionless numbers suggested in Section 4.4.3 can now be proven by comparison with calculated capacity coefficients.

5.2.3 Interpretation of storage capacity using dimensionless numbers

When comparing the capacity coefficient C and the effective stored mass M_{eff} for the different cases with the dimensionless numbers Ca and Gr shown in Figure 4.9 for the same reservoirs, a relation becomes apparent between the gravity number Gr and the effective stored mass M_{eff}. As already suggested in Section 4.4.3, increasing gravitational forces in relation to viscous forces (large Gr) result in lower effective stored mass. This holds for all cases that use the same relative permeability relations as in the Median case (M). The cases that apply different relations for the relative permeabilities do not fit nicely into this scheme. For example, Case B has the second highest M_{eff} while Gr is similar to Case D. The Capillary Number Ca in Case B is higher than Ca in Case D, which indicates that higher Ca values can partly outweigh higher Gr values with respect to M_{eff}, which is what one would expect. However, this is not the case for Cases V and E, as can be seen when comparing Figure 4.9 with the respective M_{eff} values. Apparently, there is an influence of the shape of the relative permeability relations causing a non-monotonic ordering of M_{eff} values with respect to Gr and Ca. This influence can be explained by the differences in the k_r-dependent functions A, B, and C (see Section 4.3.2) which influence the system behaviour. However, for this study, this aspect is not pursued further since the general trend of low Gr - and to some extent also high Ca - leading tentatively to high M_{eff} are already apparent.

Applying the upper estimate for the storage capacity coefficient C in this study of 0.036 (compare to Case K) to the lifetime emissions of a typical coal-fired power plant yields a CO_2 plume footprint area of 10.51 km^2. This is a plume with a radius of 1.83 km. Assumptions are a production of 1 Mt CO_2 per year over a 25 year period, CO_2 density of 660.7 kg/m^3 (i.e. density of the Median reservoir case) and 100 m formation thickness.

5.3 Summary and Conclusion

An approach to quantify storage capacities for CO_2 injected into geological formations during the early injection phase was presented. The present concepts to evaluate storage capacity in geological formations were discussed. For comparing storage capacities of different reservoirs, the quantities C and M_{eff} were introduced, where C represents a volume measure of storage efficiency and M_{eff} is the effective mass that can be stored in a reservoir. The latter was necessary in order to deal with CO_2 compressibility, i.e. the effect of different CO_2 densities at different reservoir conditions. A new method was proposed to quantify storage capacity in long-term investigations.
Numerical 1-D and 3-D experiments were carried out; CO_2 plume evolution in reservoirs was simulated with the numerical simulator MUFTE-UG. Detailed storage capacity measures were given for simulated cases.
For the 3-D numerical experiments, a radially symmetric domain with a horizontal cap was chosen, and storage capacities were calculated as function of time until a virtual spill point was reached at 1 km distance from the injection well. The results of these numerical simulations and their interpretation using the dimensionless numbers Ca and Gr were discussed.

The basic conclusions and findings are summarised as follows:

- The investigations show a clear tendency that deep, cold and/or low-permeability reservoirs are generally more favourable for the efficient utilisation of available storage volume than shallow, warm, and/or high-permeability reservoirs. This conclusion confirms the qualitative analysis of Bachu (2003) for screening and selecting sites for CO_2 storage. An increase in the injection rate also revealed some potential to increase storage capacity, since higher viscous forces allow for better spreading of the injected CO_2. In the 3-D simulations, the difference in storage capacity between the most favourable and least favourable reservoirs was larger than in the 1-D study. The result of the 3-D study identifies the Median reservoir with reduced permeability, the Median Reservoir with Basal formation relative permeability relations and the Cold reservoir (in this order) as the most favourable reservoirs for CO_2 storage. Least favourable for CO_2 storage are the Warm reservoir and the Shallow reservoir.

- In the 3-D simulations, the capacity coefficient C ranges from 0.0117 (Case S) to 0.036 (Case K). The same cases also have the smallest and largest value of M_{eff} (between 0.09 up to 1.94, normalised to the median case). This means a shallow reservoir can store less than 5 % of the CO_2 that can be stored in an equally-sized reservoir with a 10 times lower permeability at median depth. Note that the Shallow case assumes sub-critical conditions for the CO_2 phase.

- The relative permeability-saturation relations have proven to be of great influence for storage capacity. When estimating storage capacity for different relative permeability

relations, both branches $k_{r,CO2}$ and $k_{r,w}$, together with the residual water- and CO_2-rich phase saturations are of high importance. This study indicates that $k_{r,CO2}$ together with the residual water-rich phase saturation have a major influence on $C_{i,CO2}$, whereas $k_{r,w}$ has a major influence on C_g. As already indicated in Section 4.4, the relative permeability-saturation relations influence the capacity estimates to a similar extent as the entire range of reservoir properties like geothermal gradient and depth. Since few data are available on these relations, particularly for CO_2-brine mixtures, this indicates a great need for further research.

- The results have shown that in all 3-D cases less than 3.6 % of the total geometric reservoir volume could be used by the injected CO_2 before the spill point at one kilometre distance was reached. This is equivalent to less than 18 % of the pore volume. One should keep in mind that this result was achieved with a single vertical injection well and a reservoir height of 100 m. More wells, different setups, or different reservoir geometry obviously can lead to a more efficient or less efficient utilisation of the available pore space.

- The concept of calculating storage capacity for a model domain with a horizontal cap and one injection well is a conservative approach since structural-, solubility-, and chemical trapping mechanisms, which are not considered here, would lead to further increase in storage capacity. However, these mechanisms mainly contribute to total trapping at later times.

- High storage capacity of a given reservoir is typically achieved for low injectivities. This is in conflict with an economically feasible performance, and compromises have to be made in engineering practise.

6 Sensitivity Analysis

In the previous chapters, a sound understanding of the forces and processes influencing the plume evolution and the resulting storage capacity has been gained. Detailed storage-capacity estimates have been calculated by numerical simulations for reservoirs employing typical reservoir parameter setups. The question now arises, as to the influence of individual parameters like porosity, permeability, residual saturations, etc. on the model results, considering their full parameter range. The scope of this chapter is to determine the influence of various reservoir parameters on the model results with respect to storage capacity and risk and to order qualitatively the parameters depending on their influence. This is a prerequisite for the following Chapter 7, where a risk analysis is performed. Since in a risk analysis the computational cost is very high, only parameters with the strongest influence can be chosen to be independent, whereas the others (of less influence) are calculated by functional dependencies.

6.1 Discussion of Sensitivity Analysis

In every model, the question arises as to the confidence that can be placed in the results, or in the uncertainty inherent in all model results. The uncertainty in model results originates is a possibly poor or partial understanding of the active processes and poor or partial knowledge of input factors. Sensitivity Analysis can help to reduce this uncertainty. Saltelli et al. (2000) stated:

"*Sensitivity Analysis is the study of how the variation in the output of a model (numerical or otherwise) can be apportioned, quantitatively or qualitatively, to different sources of variation and how the given model depends upon the information fed into it.*"

Sensitivity Analysis methods can be grouped into three classes (Saltelli et al., 2000): "screening", "local" and "global".

- Screening sensitivity analysis methods can be performed when computationally expensive models are to be evaluated. The aim is to "screen" a large number of model input factors and to identify factors with high overall influence on the model results. These methods are quite economical, but tend to provide only qualitative sensitivity

measures, i.e. they provide a ranking of input factors, but do not provide quantitative sensitivity measures.

- Local sensitivity analysis methods give local quantitative measures of input factor influence. In other words, they often compute partial derivatives at one point in multidimensional parameter space. Thus, the sensitivity measure is only valid locally, and especially for highly non-linear models, this produces a limited applicability. With respect to the computational cost of the evaluation, they range between screening and global sensitivity analysis methods.

- Global sensitivity analysis methods apportion the output uncertainty to the uncertainty in the input factors. This approach usually varies all input factors simultaneously and sensitivity measures are given over the entire range of each input factor distribution. The computational cost for a global sensitivity analysis is high; more than a hundred model evaluations are necessary per input factors.

For all the sensitivity analysis methods considered, there is a clear trade-off between computational cost and possible information to be gained. With respect to the numerical experiments undertaken in this section for an analysis of CO_2 injection processes, the computational cost can be considered very high. The complexity of the model together with the highly non-linear fluid properties (cf. Section 2.2.2) and constitutive relations (cf. Sections A.1.3 and A.2.4) impose a highly non-linear model result behaviour. On the one hand, this non-linear behaviour would require choosing a global sensitivity analysis method; on the other hand, it precludes it (due to the high computational cost). A hint for solving the dilemma is given by Campolongo et al. (1999). They propose performing a screening analysis based on the so-called Morris Method. The Morris Method can be considered a "global screening analysis". It can be regarded "screening" because one input factor out of many is modified in each model evaluation. This is known as a one-at-a-time design. It is "global" because the methodology randomly selects points in the input factor space. Thus, a qualitative input factor ranking is produced with respect to the entire input factor space. One severe drawback, however, remains: no quantitative sensitivity measures are produced.

6.1.1 The Morris Method

The screening method proposed by Morris (1991) is composed of experiments based on randomised individual input parameter variations. The model output is evaluated in turn.

Consider a point $\mathbf{x} = (x_1, x_2, \ldots, x_\mathrm{k})$ in the k-dimensional input factor space. x_i is an individual input factor ($\forall \mathrm{i} \in \mathrm{k}$). For each input factor x_i, a number of values, called levels p can be selected. These levels are within the factor range of variation. The experimental region is therefore a k-dimensional p-level grid. In the study presented here, all input factors

x_i have been normalised to a range of variation of unity ($x_\mathrm{i} \cup (0,1)$). Thus, the p-level values of x_i can be written as $\{0, \frac{1}{p-1}, \frac{2}{p-1}, \ldots, 1\}$. To obtain the input factor for an experiment $\mathbf{x}$, one individual input factor x_i is varied by Δ, a predetermined level value, i.e. a multiple of $\frac{1}{p-1}$. The outcome of a (numerical) experiment is written as $y = y(x_1, \ldots, x_\mathrm{k})$.
The sensitivity measure proposed by Morris is based on so-called "Elementary Effects" (EE). For the i^{th} input factor EE_i is calculated to

$$EE_\mathrm{i}(x_1, \ldots, x_\mathrm{k}) = \frac{y(x_1, \ldots, x_\mathrm{i\text{-}1}, x_\mathrm{i} + \Delta, x_\mathrm{i+1}, \ldots, x_\mathrm{k}) - y(x_1, \ldots, x_\mathrm{k})}{\Delta}. \tag{6.1}$$

Note that EE_i is a local measure of sensitivity at point $\mathbf{x}$. To obtain a global measure of sensitivity, several randomly selected points $\mathbf{x}^r$ in the input parameter space are evaluated, where r is the number of local measures. In his original study, Morris proposes two measures of sensitivity for each input factor:

$$\mu(x_\mathrm{i}) = \overline{EE_\mathrm{i}^1, \ldots, EE_\mathrm{i}^\mathrm{r}}, \tag{6.2}$$

$$\sigma(x_\mathrm{i}) = stddev(EE_\mathrm{i}^1, \ldots, EE_\mathrm{i}^\mathrm{r}). \tag{6.3}$$

A high value of the mean of the distribution of the Elementary Effects ($\mu(x_\mathrm{i})$) (compared to μ of other input factors) indicates an overall high influence on the outcome of the experiment by input factor i. A high value of the standard deviation of the distribution of the Elementary Effects ($\sigma(x_\mathrm{i})$) (compared to σ of other input factors) indicates interaction effects of the considered factor with other factors, or a non-linear effect on the outcome of the experiment. To put it precisely, ($\sigma(x_\mathrm{i})$) does not provide estimates of individual interaction among different input factors, but it estimates whether any significant interaction exists.
Campolongo and Braddock (1999) realised that, when Elementary Effects EE_i have opposite signs, they may cancel each other out. They proposed a modified measure for the mean of the distribution of the Elementary Effects by only considering absolute values:

$$\mu^*(x_\mathrm{i}) = \overline{|EE_\mathrm{i}^r|, \ldots, |EE_\mathrm{i}^r|} \tag{6.4}$$

To save computational costs, so-called "trajectories" are constructed. This is the selection of the point $\mathbf{x}$ as a starting point to estimate the Elementary Effects of an input factor as the endpoint of the preceding estimation:

$$EE_1^1 = \frac{y(x_1 + \Delta, x_2) - y(x_1, x_2)}{\Delta} \tag{6.5}$$

$$EE_2^1 = \frac{y(x_1 + \Delta, x_2 + \Delta) - y(x_1 + \Delta, x_2)}{\Delta} \tag{6.6}$$

Thus, $\mathbf{x}^r$ is only selected randomly for each trajectory, not for every experiment. The overall cost of the method can be calculated as r $\cdot$ (k+1) where r $\sim$ 4–10.
The Morris Method in the version explained above has been tested by Campolongo et al. (2004); the authors state that the method is efficient in identifying irrelevant factors (i.e. low μ^* and σ). Cropp and Braddock (2002) demonstrated that analyses even using quite a

small number of trajectories (r) at coarse resolutions (low number of levels p) can provide very good estimates of model sensitivity to parameter perturbations and interactions of up to three parameters. They further state that the method is a powerful and efficient tool for global sensitivity analysis.
The software package SimLab (Joint Research Centre of the European Commission, 2004) is a development framework for uncertainty and sensitivity analysis and is used to generate the input parameter sets and is used for the analysis of the model output results.

6.2 Parameters

The reservoir parameters investigated in the sensitivity analysis are given in Table 6.1 along with the minimum and maximum values allowed and the literature source. For parameters k_h, ϕ, dip angle, S, dT/dz, and D, the 5th (Min) and 95th (Max) percentile values of the NPC-database statistics (cf. Table 3.1) are used to limit the range. The maximum capillary entry pressure value p_d and the maximum residual water-rich phase saturation $S_{w,r}$ are the maximum values measured by Bennion and Bachu (2008). The minimum CO_2-injection temperature (T_{CO2}) is selected as the critical temperature. The injection interval ranges from injection only in the lowest 10% of the reservoir height to a CO_2 injection over the entire reservoir height (100%). Other values are best-guess values.

Parameter type	Symbol	Unit	Min	Max	Literature Source / Remark
Horizontal permeability	$\log(k_h)$	m^2	-14.64	-11.71	NPC (1984)
Permeability anisotropy	$AnIso$	-	0.001	0.33	-
Porosity	ϕ	%	9	34	NPC (1984)
Reservoir height	H	m	30	60	-
Dip angle	α	°	0	20	NPC (1984)
Salinity	S	$\frac{kg}{kg}$	0.0	0.185	NPC (1984)
Res. water-rich phase sat.	$S_{w,r}$	-	0.10	0.66	Max: Bennion and Bachu (2008)
Res. CO_2-rich phase sat.	$S_{CO_2,r}$	-	0.01	0.20	-
CO_2 mass influx	$\log(q_{CO2})$	$\frac{kg}{s \cdot m}$	-3.22	-2.22	-
CO_2 injection temperature	T_{CO2}	°C	304.1	360.0	Min: Critical temperature
Geothermal gradient	dT/dz	$\frac{°C}{m}$	0.018	0.062	NPC (1984)
Depth	D	m	386	3495	NPC (1984)
Injection Interval	II	%	10	100	-
Sorting factor	λ_{BC}	-	0.50	4.00	-
Capillary entry pressure	p_d	Pa	0	217000	Max: Bennion and Bachu (2008)

Table 6.1: Parameters investigated in the sensitivity analysis, parameter range, and literature source.

When these 15 input parameters are considered in a Morris Method-type sensitivity investigation, the number of necessary model runs using four trajectories is 64. The parameter distribution within the range is assumed to be uniform. To avoid an influence of different

input parameter ranges on the sensitivity measures, all parameter ranges are normalised to a range of zero to one. Consequently, the results of the numerical simulations have also been normalised to a range of zero to one to calculate μ^* and σ.

6.3 Numerical Investigations

To reduce computational cost, the sensitivity investigations are performed as 2-D experiments. This allows the screening of a sufficiently large number of parameters. The simulation experiments are conducted with the model for non-isothermal multi-phase multi-component processes (including mass transfer between the phases), i.e. the 2p2cni-module implemented in MUFTE-UG (cf. Section A.2).

6.3.1 Model Set-up

A model setup as shown in Figure 6.1 is used to perform input parameter sensitivity investigations. The model domain has a length of 2000 meters and a variable height H. It is rotated by a dip angle α around the lower western corner. Carbon dioxide is injected at a constant rate q_{CO2} with temperature T_{CO2} at the western boundary along an injection interval II, ranging from the bottom up to between 10 % and 100 % of the height of the domain. The lower western corner is located at depth D below the surface. The domain is homogeneous, having a total horizontal permeability $\mathrm{k_h}$ and a vertical permeability $\mathrm{k_v}$ calculated in dependence on the horizontal permeability by the anisotropy ratio $AnIso$. Porosity ϕ and salinity S are constant throughout the domain. Residual water- and CO_2-rich phase saturations are given by $S_{\mathrm{w,r}}$ and $S_{\mathrm{CO_2,r}}$. Capillary pressure is calculated depending on water-rich phase saturation by a Brooks & Corey model employing parameters p_{d} (entry pressure), $S_{\mathrm{w,r}}$, $S_{\mathrm{CO_2,r}}$ and λ_{BC} (sorting factor). Top and bottom boundaries are closed to any flux (no-flow), as is the western boundary, except along the injection interval. The system is initially considered to be hydrostatic and in thermal equilibrium, which allows pressure and temperature calculations at the depth D of interest by using a constant brine density respectively the vertical geothermal gradient dT/dz. With the pressure and temperature estimated at the depth of interest, the density and viscosity of the fluid phases can be calculated. At the eastern boundary, identical equilibrium conditions apply.

6.3.2 Results

In Figure 6.2 (left), the centres of gravity of the CO_2 plumes of the individual model runs are shown as diamonds. A large variability of resulting CO_2 mass distributions within the reservoir is observed. There are combinations of input parameters, leading to a CO_2 plume spreading far into the reservoir (large centre of gravity x value), others lead to a CO_2 plume closely distributed around the injection boundary (small centre of gravity x value). Consequently, the information value of the derived sensitivity measures are representative

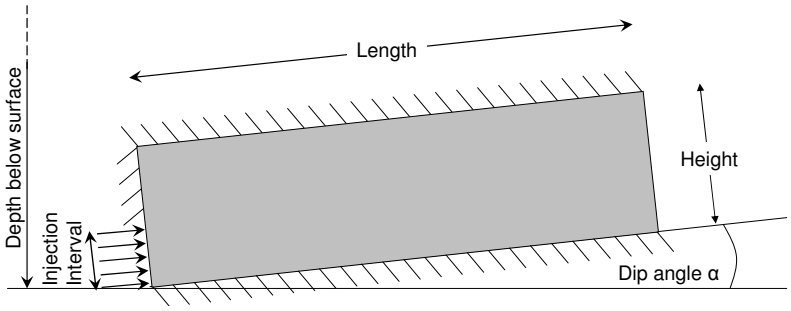

Figure 6.1: Model setup to test for input parameter sensitivity.

for a broad range of flow and transport conditions in the reservoir. The simulations are stopped before the CO_2 plume reaches the eastern boundary. This is to prevent unwanted influence of boundary conditions on the results.

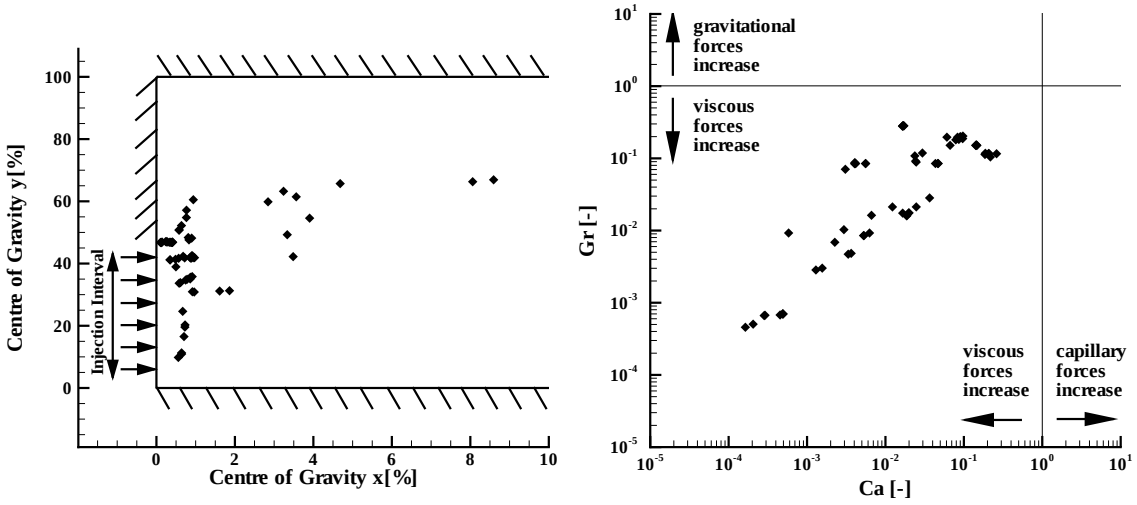

Figure 6.2: Centre of gravity of the CO_2 plume given in percent of the length of the domain (2000 m) versus percent of the height of the domain (H) (left). Capillary Number Ca versus Gravity Number Gr (right). Both figures are shown after a total of 22 t_{CO2}/m is injected. Each diamond indicates an individual model run.

Figure 6.2 (right) shows Capillary Number Ca versus Gravity Number Gr. The dimensionless numbers have been calculated by using CO_2-mass weighted averages over all discretisation cells for CO_2 density, viscosity, capillary pressure and velocity. Furthermore, k is represented by horizontal permeability. Characteristic length l_{cr} is represented by the height of the domain D. The actual front widths have not been considered, which might lead to an error in the range of less than one order of magnitude in Ca. The range of variation for Ca and Gr is three orders of magnitude, mainly due to a variation in absolute permeability k_h, changing by three orders of magnitude. A vague trend can be identified from high Gr / high

Ca to low Gr / low Ca. This behaviour is already observed in the analytical experiments in the dimensional analysis for varying characteristic velocities v_{cr} (cf. Figures 4.2 and 4.9 (right)). This relation of dimensionless numbers (balance of forces) represents a snapshot after 22 t_{CO2}/m have been injected. The numerical experiments here are rather dominated by viscous forces. For model runs with conditions leading to dimensionless numbers close to the equilibrium of forces (Gr and Ca close to one), gravitational and capillary forces gain importance. Hence, parameter sensitivities can only be derived and interpreted for this state of the system; i.e. parameter sensitivities might be different for a reservoir that is dominated by gravitational or capillary forces.

To perform a sensitivity analysis, the questions of interest need to be clearly defined. The focus here is to define questions which are important to answer in storage capacity studies and in risk assessment studies. Hence, the parameter sensitivities with respect to the answers to these questions enables the identification of parameter importance in these types of studies. The following questions are addressed:

- When does the CO_2 arrive at an observation point?
  One could imagine that the observation point represents a leakage pathway for CO_2 out of the reservoir. Then the storage capacity is limited due to this leakage point and risk assessment studies need to consider possible leakage along this pathway.

- Which fraction of the total injected CO_2 is in free-phase (not dissolved in brine) in the topmost region of the reservoir at a given point in time?
  The fraction of free-phase CO_2 mass in the topmost region of the reservoir is a measure of the strength of the buoyancy forces. As shown in Section 5, strong buoyancy forces reduce storage capacity. The mass fraction is also a measure of risk, since only the free-phase CO_2 in the topmost regions could potentially leak if a leakage pathway is present.

- What is the mass ratio between CO_2 occurring in free phase and CO_2 dissolved in brine at a given point in time?
  Here, the same reasoning holds with respect to risk as in the previous bullet, only the free-phase CO_2 could potentially leak if a leakage pathway is present. Carbon dioxide dissolved in brine can be considered as safely stored.

- What is the maximum overpressure developing below the caprock?
  The developing overpressure is a constraint in terms of possible injection rates, and thus a constraint to storage capacity over time. The overpressure always has to be limited to the fracturing pressure of the caprock to minimise risk.

To answer the first question, an observation point needs to be defined. A point at 20 metres distance from the western boundary and 20 metres above the bottom of the domain is selected. It is necessary here to select a point rather close to the western injection boundary

due to the broad parameter range considered. On the one hand, there are cases with parameter combinations, which lead to strong gravity segregation, i.e. quick upward movement of the CO_2 plume and fast lateral spreading below the caprock. On the other hand, there are cases with parameter combinations having e.g. small injection intervals and weak gravity segregation. In these cases, the CO_2 plume does not reach the caprock at all and CO_2 spreads only a small distance into the reservoir. Hence, the observation point selected is the most distant point from the injection boundary where the CO_2 arrival is observed for all cases.

To answer the second and third questions, a time needs to be defined. Here, the sensitivity measures are compared at the point in time when the same amount of CO_2 is stored in the reservoirs, i.e. $22\,t_{CO2}/m$.

The input parameter sensitivity measures μ^* and σ (cf. Section 6.1.1) for the questions stated are given in Figures 6.3 and 6.4.

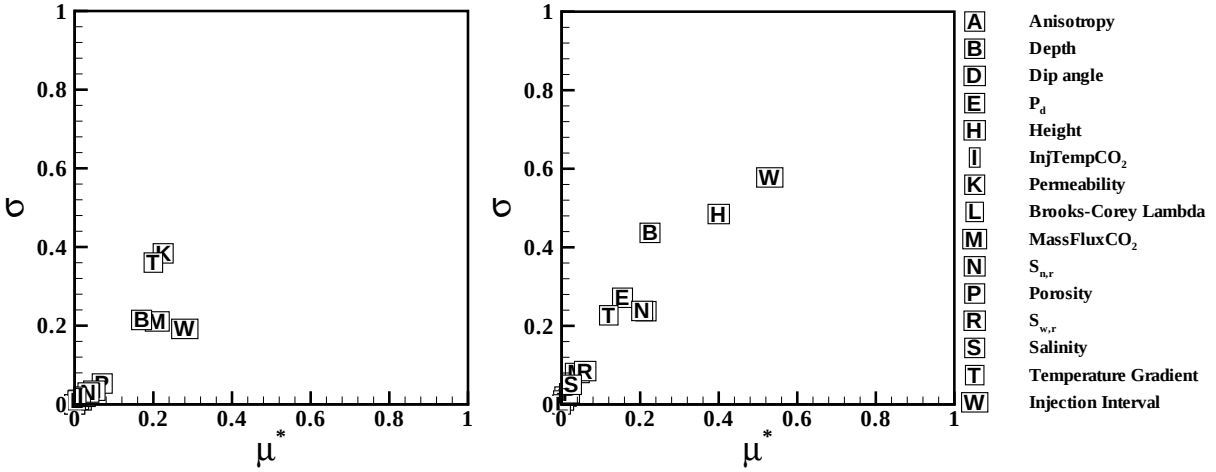

Figure 6.3: Input parameter sensitivity measures μ^* (e.g. Equation 6.4) and σ (e.g. Equation 6.3) with respect to CO_2 arrival time at an observation point (left) and with respect to the total CO_2 mass (free phase) in the upper 20 % of the reservoir (right). Low μ^* indicates little overall influence on model answers. Low σ indicates parameters with little interaction of the considered factor with others.

Figure 6.3 (left) shows sensitivity measures with respect to the arrival time of the CO_2 plume at the observation point. The arrival time at this point is sensitive to permeability, injection interval and injection rate, geothermal gradient and reservoir depth. Sensitivity to the first two parameters can be attributed to the developing overpressure, as will be shown later. The sensitivity of the injection interval is due to the close position of the observation point to the injection boundary. Geothermal gradient and reservoir depth are sensitive parameters since they account for the density of the CO_2, and therefore for the buoyancy forces. Other input parameters are negligible. All parameters mentioned show a comparable overall effect

on arrival time (μ^*).

Figure 6.3 (right) shows sensitivity measures with respect to the fraction of the total injected CO_2 in free phase located in the topmost 20 % pore space of the reservoir after 22 t_{CO2}/m have been injected. The injection interval has the highest overall effect on the model answers. This can be explained by a simple example. If the injection interval is 1.0, at least 20 % of the CO_2 mass are located in the topmost 20 % of the pore space of the reservoir just after the injection start. If the injection interval is less then 0.8, no CO_2 is located in the topmost 20 % of the pore space of the reservoir just after the injection start. The amount of CO_2 located in the topmost region after some time thus depends not only on the effects of buoyancy forces; especially at early times, it can largely be influenced by the injection interval. The strength of the buoyancy forces is largely influenced by the density difference between the water- and CO_2-rich phases, these depend on the depth, the geothermal gradient, and the permeability anisotropy. These parameters are shown to have a large effect on model answers. The model answers are also sensitive to the height of the reservoir, since it accounts for the distance the CO_2 has to migrate in order to reach the topmost 20 % of the pore space of the reservoir. Some influence is also found for the capillary entry pressure and the residual CO_2-rich phase saturation. The residual CO_2-rich phase saturation parameter accounts for the amount of CO_2 which is residually trapped, and therefore reduces the amount of CO_2 which may reach the topmost 20 % of the pore space of the reservoir.

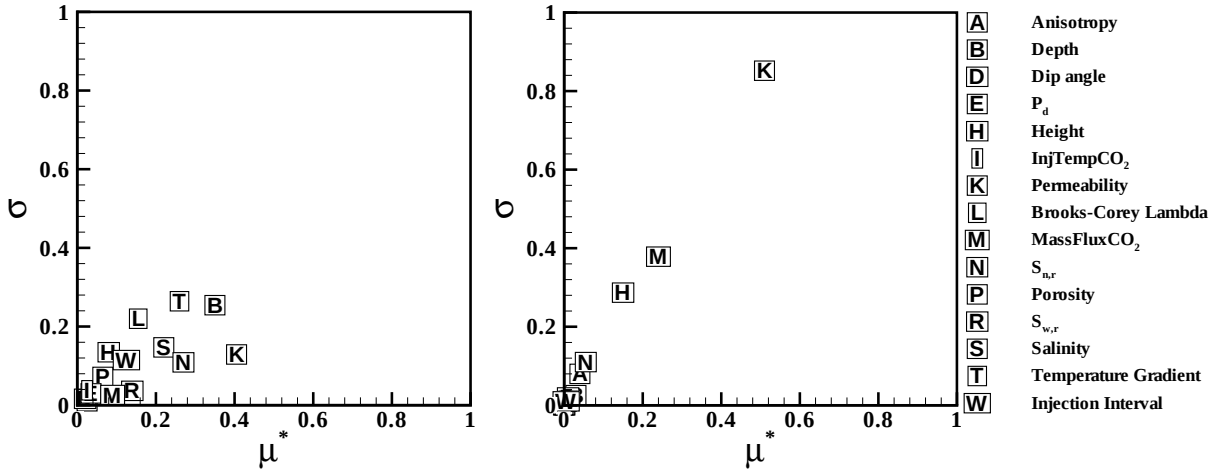

Figure 6.4: Input parameter sensitivity with respect to the mass fraction of CO_2 occurring in free phase in relation to the CO_2 dissolved in brine (left) and with respect to maximum overpressure developing below the caprock (right). Low μ^* indicates little overall influence on model answers. Low σ indicates parameters with little interaction of the considered factor with others.

Figure 6.4 (left) shows sensitivity measures with respect to the mass ratio of CO_2 occurring in free phase and CO_2 dissolved in brine when 22 t_{CO2}/m are injected. The mass ratio de-

scribed is not dominated by a single or few parameters. Rather five to ten parameters have some effect. Among these influencing parameters are permeability, depth, residual CO_2-rich phase saturation, geothermal gradient, salinity, sorting factor, residual water-rich phase saturation injection interval, and height of the reservoir. It is surprising that the mass injection rate has very little effect.

Figure 6.4 (right) shows sensitivity measures with respect to the maximum overpressure developing in the reservoir due to CO_2 injection. The maximum overpressure developing is sensitive to the absolute permeability, the CO_2 injection rate and the height of the domain, in this order of importance. Other input parameter influences are negligible here. The absolute permeability shows the highest overall influence (high μ^*) on the developing overpressure and has either a strong non-linear influence on the overpressure or interaction effects with other parameters (high σ), possibly CO_2 injection rate. The developing overpressure is sensitive to the height of the domain because it is comparable to the available pore space the CO_2 is injected into. One would expect some sensitivity of overpressure with respect to the CO_2 injection temperature or depth, since these parameters influence CO_2 density and thus CO_2 compressibility, but they seem to be negligible when compared to the influence of permeability, injection rate and domain height. This information is of practical use when the overpressure below a caprock is to be limited. Then it is most advisable to keep injection rates low and search for highly permeable reservoirs, which is what one would expect. Varying the CO_2 injection temperature and the injection interval does not have an effect.

Assuming that these questions are representative and allow for conclusions on parameter importance in storage capacity estimation and in risk assessment studies, a qualitative parameter ranking can be derived, as shown in Table 6.2. This is done by averaging the overall parameter effect in the four individual parameter sensitivity rankings.
According to Table 6.2, parameters like horizontal permeability, injection interval, reservoir depth, reservoir height, and geothermal gradient have the largest influence on the model results with respect to the questions stated here. On contrast, parameters like the salinity, residual water-rich phase saturation, entry pressure, porosity, sorting factor, CO_2 injection temperature and the dip angle can be neglected in further investigations in the fields of storage capacity estimation and risk assessment. However, this is only valid for the chosen setup. It was shown that the setup chosen here is strongly influenced by viscous forces. In other setups, which might be strongly influenced by gravitational or capillary forces, the parameters identified here as having little influence might become important. This has to be discussed when neglecting parameters.

Rank	Parameter	Name
1	k_h	Horizontal permeability
2	II	Injection Interval
3	D	Reservoir depth
4	H	Reservoir height
5	dT/dz	Geothermal gradient
6	q_{CO2}	CO_2 injection rate
7	$S_{CO_2,r}$	Residual CO_2-rich phase saturation
8	$AnIso$	Permeability anisotropy
9	S	Salinity
10	$S_{w,r}$	Residual water-rich phase saturation
11	p_d	Entry pressure
12	ϕ	Porosity
13	λ_{BC}	Sorting factor
14	T_{CO2}	CO_2 injection temperature
15	α	Dip angle

Table 6.2: Qualitative ranking of parameter effect as the average of individual overall parameter effects for the four stated questions of interest.

6.4 Summary and Conclusion

In this chapter, the principal attributes of sensitivity analysis methods have been described. Reasons leading to the selection of the presented Morris Method include an effective, reliable and robust screening of input parameter effects on the results, combined with a consideration of the entire input parameter space (global analysis). The extended Morris Method theory is described. Fifteen individual input parameters are tested for their effect on several questions of interest; the arrival of CO_2 at an observation point, free-phase CO_2 in the topmost region of the reservoir, etc. This is done in a numerical experiment with a 2-D reservoir setup employing parameter ranges derived from the NPC database, from literature, or best-guess values. The parameters are assumed to be independent of each other and no distribution has been assumed within the considered parameter ranges. A qualitative ranking of the average parameter influence with respect to the questions stated, associated with CO_2 storage capacity and risk, is finally given.

The main findings and conclusions are :

- Parameters like horizontal permeability, injection interval, reservoir depth, reservoir height, and geothermal gradient have proven to have the largest influence on the model results with respect to the questions stated here.
- Parameters like the salinity, residual water-rich phase saturation, entry pressure, porosity, sorting factor, CO_2 injection temperature and the dip angle have little influence on the model results with respect to the questions stated here and with respect to the setup chosen.
- For other setups than the one considered here, parameters identified here as having little influence might become important. For example in two-dimensional space, the increase of pore space with increasing distance r from the injection boundary is linear ($H \cdot r$). In three-dimensional space, an exponential increase of pore space with increasing distance from the injection boundary is observed ($H \cdot \pi \cdot r^2$). In the latter case, this results in a rapid decrease of total velocity and therefore a rapid decrease of viscous forces which dominate here. With an increasing influence of buoyancy and/or capillary forces, other parameters, which have been identified as being negligible here, could gain importance.

7 Risk Analysis*

In the previous Chapter 6, a sensitivity analysis was performed to order reservoir parameters qualitatively, depending on their influence on storage capacity and risk. In the following risk analysis, only the parameters with the strongest influence are chosen to be independent, whereas the others (with less influence) are calculated by functional dependencies. The reason for this simplification is the high computational cost that is generated by considering all parameters to be independent. The risk analysis investigates a scenario where CO_2 is leaking out of a storage reservoir through a pre-existing leaky well. Risk is expressed in this case as the likelihood of this leakage to occur times the leaked CO_2 mass at a given point in time and for a given distance between the leaky well and the injection well. Numerous simulation experiments are run, employing individual reservoir parameter setups. To set up an individual simulation experiment, three out of four independent parameters are randomly sampled from the database parameter distributions given in Chapter 3. The fourth independent parameter is randomly sampled from a parameter distribution calculated by a theoretical model. Thus, the risk analysis is performed with respect to the database reservoir parameter distributions, by considering a theoretical model, and by selected literature sources on functional dependencies of the dependent parameters.

While the concept of risk developed and applied in this study is straightforward, it is intended to provide

- a systematic framework for engineers for determining the ideal properties for a subsurface CO_2 storage reservoir,
- assistance in rating storage sites in terms of risk depending on their properties. This knowledge can assist experts when utilising more comprehensive screening and ranking frameworks,
- estimates of risk of a site which can be compared to the risk of other sites, possibly leading to the decision where to conduct further investigations,
- a selection of the most appropriate location for an injection well based on risk estimations depending on the number and distribution of surrounding leaky wells.

*This Chapter is submitted to Energy Conversion and Management with the title "Kopp, A., Binning, P.J., Johannsen, K., Class, H. and Helmig, R., Risk Analysis for Leakage through Abandoned Wells in Geological CO_2 Storage" by December, 17^{th} 2008.

7.1 Discussion of Risk

The design of a carbon dioxide storage system is subject to considerable uncertainty. For example, there is some chance that geological conditions will cause leakage from the CO_2 reservoir. But uncertainty is also involved in the engineering work, in possible leakage through man-made pathways back into the atmosphere and in the abandonment of the site. In order to select suitable geological formations for CO_2 storage and design these systems it is therefore important to develop a concept of risk. The management of risk is an inevitable part of every CO_2 storage attempt to mitigate potential harm to the health of humans and animals, and to the environment. Risk management has to be site specific to be successfull. Nevertheless, a general framework should be adopted on to serve as a basis for site specific risk management.

7.1.1 Risk Scenarios in CO_2 storage

A CO_2 reservoir may fail by leakage through wells or faults, or other geological "weak spots" located at some distance away from the CO_2 injection well. The focus is here on CO_2 leakage through abandoned wells, although the method can be generalised to other leakage pathways. Leakage through an abandoned well can occur by multiple pathways (Celia et al., 2004). Since information is limited on the state of such a well (material, condition and set-up of cement plugs, casings, etc.), uncertainty of potential leakage is large. The leakage through one well is then multiplied by the number of wells encountered by the CO_2 plume in the subsurface, yielding cumulative leakage out of the storage formation. Leakage rates have been investigated by Nordbotten et al. (2004), Nordbotten et al. (2005b), and Nordbotten et al. (2005a) by a semi-analytical approach. Gasda et al. (2004) analysed spatial characteristics of well locations in the Alberta basin (Canada) and state that a typical CO_2 plume can encounter up to several hundreds of wells in high-density areas. Here, leakage is judged to be significant if it occurs within a given time period. Such a failure can be evaluated by numerical simulation. The simulator is used to determine the distribution of CO_2 in the reservoir, and failure is defined to occur if leakage is produced. This is equivalent to stating that reservoirs where the CO_2 is spread over a greater lateral area are more risky than reservoirs with a compact CO_2 volume.

7.1.2 Time aspect

A characteristic of CO_2 storage in geologic formations is the varying contribution of several physical and geochemical trapping mechanisms on very different time scales (cf. Section 1.1). This varying contribution of trapping mechanisms on different time scales adds complication to risk assessments. Similarities can be found in radioactive waste disposal where performance assessment calculations must consider the return of radionuclides to the accessible environment over periods of longer than 10000 years (Maul et al., 2007). For CO_2 storage,

two time scales may be of interest, and these are directly related to the environmental impacts that might occur from leakage: local environmental effects or global effects. The scope of the risk assessment and the associated time scales are defined dependent on these impacts (IPCC, 2005). The medium to long timescale (∼20 years or longer) considers global effects, that is the return of the CO_2 back into the atmosphere. The short time scale considers local environmental impacts, leading to risk directly associated with exposure to leaked CO_2; that is local health, safety and environmental hazards. For example, Pruess (2008b) suggests a potential for self-enhancement of leakage rates, leading to a so-called "pneumatic eruption"; although the author says it is unlikely. Pacala (2003) states that local risks (together with economic considerations) are likely to constrain allowable leakage rates more tightly than global impacts. Hence, the focus of the risk assessment method developed here is on the short time scale, i.e. up to ∼20 years.

7.1.3 Screening and Ranking Frameworks

At present, geological CO_2 storage risk assessments rely on expert opinions to rate individual scenarios, which are then combined to an overall risk. For example, Oldenburg (2007) developed a screening and ranking framework to evaluate potential storage sites on the basis of risk arising from possible CO_2 leakage to health, safety and the environment. In the spreadsheed-type analysis, the investigator has to rate, for example, the lithology of the storage formation by giving it a "weight" (relative importance), an "assessment attribute relative to risk" and a "certainty factor" (judging how well the information is known). Estimates of the reliability and uncertainty are dependent on the level of knowledge of the investigator. The risk assessment outlined in the following, decreases subjectivity and therefore may increase confidence of investigators and experts using such comprehensive frameworks.

7.1.4 Risk Analysis Concept

There are many ways how risk can be defined. According to Kaplan (1997) it can be defined in terms of three questions:

- How can a system fail?
- What is the likelihood of failure?
- What are the consequences of failure?

Relating to the first question, there are many ways in which a CO_2 storage system can fail. For example the system can fail in providing the necessary injectivity with respect to the CO_2 mass delivered by the surface installations (power plant, pipe network, process engineering devices etc.). There are a number of engineering failures associated with the design of the installations and the injection process, for example well corrosion, untight well plugs, formation clogging due to halite precipitation in the close vicinity of the injection

well. There might be failure associated with the design of the CO_2 monitoring devices to measure CO_2 plume evolution and possible CO_2 leakage. The system can also fail to provide the necessary capacity to store the intended CO_2 production. Finally, the system can fail after injection due to CO_2 leakage, e.g. through the injection well.

The risk study conducted here focuses on CO_2 leakage out of the storage reservoir. IPCC (2005) summarised number of possible leakage pathways: (i) through the pore system in low-permeability caprocks such as shales, if the capillary entry pressure at which CO_2 may enter the caprock is exceeded; (ii) through openings in the caprock or fractures and faults; (iii) through anthropomorphic pathways, such as poorly completed or abandoned pre-existing wells. The focus is here on leakage through poorly completed or abandoned pre-existing wells. Abandoned wells have been identified as one of the most probable leakage pathways for CO_2 (Benson (2005), Gasda et al. (2004)). A pre-existing (leaky) well is assumed to exist at some distance from the injection well. It has a constant diameter of 1 m and is screened over the full reservoir thickness. Other (presumably smaller) well diameters can easily be considered, as will be shown later. The leakage pathway in the abandoned well is not of importance, as will be explained in the definition of the consequences of failure.

The likelihood of failure can be assessed by considering the potential range of reservoir parameters like porosity, geothermal gradient, depth, and anisotropy. The statistical characteristics of reservoir parameters were determined from a database including information from over 1200 reservoirs or by a model (permeability anisotropy). The parameter space of reservoir properties is randomly sampled and simulations are conducted to assess the distribution of CO_2 in the subsurface. For each simulation, failure is assessed by examining whether CO_2 has spread to a given radius within a given time. If CO_2 has spread beyond the leaky well radius, this case has failed. By simulation of many such cases, a likelihood of failure can be given by relating the number of cases that failed n_f (dependent on distance r from the injection well to the leaky well and time t) to the total number of cases simulated (N).

To determine the consequences of failure, the damage is defined as the amount of CO_2 mass that has spread beyond the leaky well distance (compare to Figure 7.1). The assumption is that damage (D_i) measures the mass that can potentially leak through the pre-existing well out of the system. This means that in this study the leakage process itself is not modelled. Consequently it is not necessary to be more specific about the leakage pathway in the abandoned well, as given in Gasda et al. (2004).

IPCC (2005) outline a "framework for assessing environmental risks". They define two categories of environmental impacts that might occur from geological CO_2 storage: local environmental effects and global effects. Global effects arise from CO_2 leakage to the atmosphere and relate to the uncertainty in the effectivity of CO_2 storage. Local effects arise from the direct exposure of surrounding plant and life species to CO_2 or other dangers associated with the leakage in the close surrounding of the site. This study partially addresses both impact categories. The CO_2 mass that has spread beyond the leaky well can potentially leak through the well. However, the impact of this CO_2 is not explicitly considered. The leaked

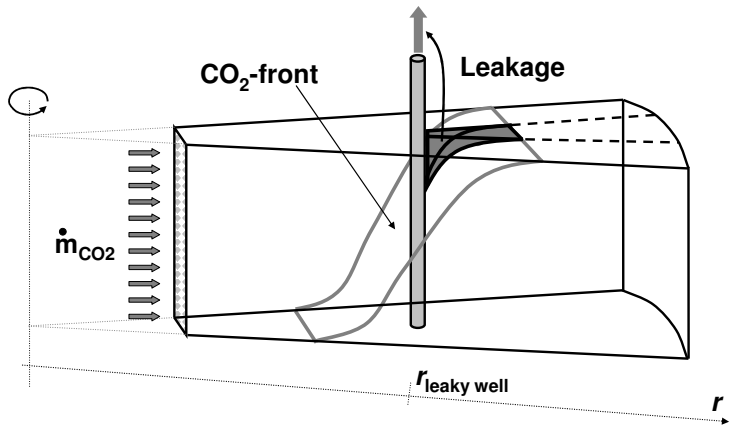

Figure 7.1: Sketch of the radially symmetric model domain and definition of the leakage that occurred after time t at a leaky well in distance $r_{\text{leaky well}}$ from the injection well. CO_2 is injected into the centre boundary and spreads laterally in the reservoir. Buoyancy forces drive the CO_2 upwards where it accumulates below the caprock. Consequently the CO_2 plume spreads faster at the top than at the bottom.

CO_2 could possibly leak (i) to the next shallower geological unit where it is safely stored, or (ii) leak to a fresh-water bearing aquifer and pollute drinking water, or (iii) leak back to the atmosphere. In cases (ii) and (iii) it is important to determine the rate at which the CO_2 leaks. If it leaks at considerable rate, local health, safety and environmental hazards may arise, yielding risk that is much higher and may not be proportional to the amount of CO_2 that has leaked (IPCC, 2005).
Since in this study a simple reservoir geometry is used together with a random sampling of statistical parameters distributions, this risk assessment does not refer to any specific site. Risk, as it is defined here, refers rather to a statistical leakage probability that might occur at a pre-existing well. Summarising, risk is defined by multiplying the likelihood of failure with the consequence of failure, which is expressed in Equation 7.1.

$$\text{Risk [kg]} = \underbrace{\frac{n_\text{f}}{\text{N}}}_{\text{likelihood of failure}} \cdot \underbrace{\sum_{\text{i}=1}^{\text{N}} \frac{D_\text{i}}{n_\text{f}}}_{\text{consequence of failure}}, \tag{7.1}$$

where n_f is the number of cases that failed [-] (dependent on distance r [m] from the injection well to the leaky well and time t [d]), N is the total number of cases simulated [-], and D_i is the damage [kg] of case i at time t.
Note that since a radially symmetric domain is assumed with a leaky well diameter of 1 m (as indicated in Figure 7.1), the damage D_i is calculated by simply multiplying it with $\frac{1\text{m}}{2\,\pi\,r}$, which represents the fraction of a full circle affected by the leaky well, where r is the distance of the leaky well from the injection point. To consider smaller leaky well diameters,

the resulting damage and risk values presented in the following just need to be multiplied by the leaky well radius (since results are given for a unit leaky well diameter, i.e. 1 m). Risk has the unit of mass (kg). Since leakage is not explicitly modeled (no leaky well is included in the simulations), a single model run can be used to calculate damage and risk for many leaky well radii r.

The concept outlined above, calculates risk as an average over the entire parameter space. This becomes apparent because n_f cancel out of Equation 7.1 and what is left is average risk $\sum_{\mathrm{i}=1}^{\mathrm{N}} \frac{D_\mathrm{i}}{N}$. The average risk, using the statistical distribution within the parameter space, can be used to draw some important conclusions (as given in Sections 7.3.3 and 7.5), but does not determine the risk of an individual case.

A procedure to calculate risk for an individual case, could be the following: Assume that each simulation has four independent input parameters, $p_1 \ldots p_4$, among the parameter distributions. When fixing p_2, p_3, and p_4, the probability of failure P_1 due to variation of parameter p_1 can be determined by varying p_1 and finding p_1^* that partitions between failure and no failure. The probability P_1 is then determined from the probability distribution to be the probability that $p_1 > p_1^*$, where $p_1 > p_1^*$ defines the range of parameters p_1 leading to failure. The total failure probability P of this case can then be calculated by $P = P_1 \cdot P_2 \cdot P_3 \cdot P_4$. The risk associated with this case would be the damage produced by this case times the failure probability, i.e. $\mathrm{risk_i} = D_\mathrm{i} \cdot P_1 \cdot P_2 \cdot P_3 \cdot P_4$. This individual risk is of course dependent on the distance r from the injection well to the leaky well and the time t. This study does not consider the risk of an individual case any further, but instead focuses on the average risk and the conclusions that can be drawn from it.

7.2 Parameters

To define parameter input sets for simulations, four independent parameter distributions are randomly sampled. These four parameters are porosity ϕ, depth D of the reservoir below surface, average geothermal gradient dT/dz at the site, and the anisotropy between vertical and horizontal absolute permeability $AnIso$. These are called primary parameters. All other parameters, called secondary parameters, are functions of primary parameters or constants. The primary parameters have been selected based on previous sensitivity investigations (cf. Section 6.3.2) where they have shown to be the parameters which are most influential on CO_2 plume evolution behaviour in a reservoir[†]. When comparing the qualitative ranking of parameter effects (cf. Table 6.2) determined in the sensitivity analysis, primary parameters rank on third, fifth, eighth and twelfth position. Other parameters are not selected as primary parameters for three reasons, (i) there is a lack of data, (ii) there is a mutual interrelation with primary parameters, (iii) computational effort would be too high. Detailed

[†]Kopp, A., Class, H. and Helmig, R., Sensitivity Analysis of CO_2 Injection Processes in Brine Aquifers, presentation given at European Geosciences Union (EGU) General Assembly, April 18$^{\mathrm{th}}$, Vienna, Austria, 2007

information on the selection, statistical characteristics of primary parameters, dependencies of secondary on primary parameters, mutual interrelation of parameters, parameter sources, etc. is given in the following and summarised in Table 7.1.

Parameter type	Symbol	Unit	Dependency/Type	Source/Remark
Primary parameters				
Porosity	ϕ	[-]	Statistical Dist.	NPC (1984)
G.grad	dT/dz	[°C/m]	Statistical Dist.	NPC (1984)
Depth	D	[m]	Statistical Dist.	NPC (1984)
Permeability anisotropy	$AnIso$	[-]	Statistical Dist.	Layered reservoir model
Secondary parameters (var.)				
Horizontal permeability	k_h	[m^2]	f(ϕ)	Kozeny-Carman model (Scheidegger (1960))
Vertical permeability	k_v	[m^2]	f(k_h,$AnIso$)	Definition
Temperature	$T_{BC+Init}$	[°C]	f(D,dT/dz]	Geothermal boundary and initial condition
Pressure	$p_{BC+Init}$	[Pa]	f(D,ϱ_b^*)	Hydrostatic boundary and initial condition
CO_2 solubility in brine	X_w^{CO2}	[kg/kg]	f(T,p)	Duan and Sun (2003)
CO_2 density	ϱ_{CO2}	[kg/m^3]	f(T,p)	Span and Wagner (1996)
CO_2 enthalpy	h_{CO2}	[J/kg]	f(T,p)	Span and Wagner (1996)
CO_2 viscosity	μ_{CO2}	[Pa·s]	f(T,p)	Fenghour et al. (1998)
Brine density	ϱ_b	[kg/m^3]	f(T,p,S,X_w^{CO2})	Batzle and Wang (1992), Garcia (2001), IAPWS (1997)
Brine enthalpy	h_b	[J/kg]	f(T,p,S,X_w^{CO2})	Daubert and Danner (1989), Duan and Sun (2003), IAPWS (1997), Michaelides (1981)
Brine viscosity	μ_b	[Pa·s]	f(T,S)	Batzle and Wang (1992)
CO_2-brine interfacial tension	σ	[N/m]	f(T,p)	Kvamme et al. (2007)
Capillary pressure	p_c	[Pa]	f(ϕ,σ,Θ,S_w)	scaled by a Leverett J-function, based on a p_c relation given in Plug and Bruining (2007)
Relative permeability	k_r	[-]	f($S_{w,r}$,$S_{CO2,r}$,λ_{BC},S_w)	Brooks and Corey (1964)
Secondary parameters (const.)			Value	
Salinity	S	[kg/kg]	0.048	NPC (1984) median value
Water solubility in CO_2	X_{CO2}^w	[kg/kg]	0.001	Negligible
Contact angle	Θ	[°]	49.46	Plug and Bruining (2007)
Res. water-rich phase sat.	$S_{w,r}$	[-]	0.3	-
Res. CO_2-rich phase sat.	$S_{CO2,r}$	[-]	0.05	-
Sorting factor	λ_{BC}	[-]	5.87	Plug and Bruining (2007) Brooks and Corey (1964)
Reservoir dip	α	[°]	0	-
Injection			Value/Dependency	
CO_2 injection rate	q_{CO2}	[Mt CO_2/yr]	1	Medium-sized coal fired power plant
Heat influx	q_h	[J/yr]	f(p,T,q^{CO2})	Resembles injection at actual reservoir conditions

* ϱ_b is constant for the calculation of initial and boundary conditions (1160 [kg/m^3]).

Table 7.1: Definition of primary and secondary model input parameters, dependencies, and sources.

7.2.1 Primary Parameters

Statistical characteristics of primary parameters ϕ, D, and dT/dz can be calculated from the U.S. National Petroleum Council public database (NPC, 1984) as shown in Section 3. Table 3.1 summarises the resulting statistical characteristics. In Figure 3.1 the histograms of the NPC parameter distributions employed in the following are shown.

To calculate statistical characteristics of the 4^{th} primary parameter, the absolute permeability anisotropy ($AnIso$), a layered reservoir is considered. Layers have varying thickness and an alternating constant absolute permeability of $3.24 \cdot 10^{-15}$ m^2 and $1451.85 \cdot 10^{-15}$ m^2. These permeabilities reflect the 5^{th} and 95^{th} percentiles of the absolute permeability distribution in the NPC database. When estimating upscaled or effective permeability for flow in a layered reservoir, the direction of the flow is of importance. The harmonic mean HM of the permeabilities is used to estimate effective permeability for flow perpendicular to the layers:

$$HM = \frac{\sum_{\mathrm{i}} \mathrm{m_i}}{\sum_{\mathrm{i}} \frac{\mathrm{m_i}}{\mathrm{k_i}}}, \tag{7.2}$$

where i is the layer index, $\mathrm{m_i}$ [m] is the thickness of the layer having permeability $\mathrm{k_i}$.
The arithmetic mean AM of the permeabilities is used to estimate effective permeability for flow parallel to the layers,

$$AM = \frac{\sum_{\mathrm{i}} \mathrm{m_i} \cdot \mathrm{k_i}}{\sum_{\mathrm{i}} \mathrm{m_i}}. \tag{7.3}$$

The anisotropy of effective flow permeability is calculated as the harmonic mean divided by the arithmetic mean. When varying the number and the thickness of the layers, the distribution as given in Figure 7.2 is the result.
Statistical characteristics of the distribution are: minimum = 0.0089, maximum = 1.0, arithmetic mean = 0.0283, median = 0.0118, 5^{th}percentile = 0.00891 and 95^{th}percentile = 0.0842.
Section 7.2.3 gives the procedure of sampling the primary parameter distributions in order to define a simulation case.

7.2.2 Secondary Parameters

Secondary parameters, for example absolute horizontal and vertical permeability, capillary pressure, residual phase saturations and relative permeabilities, are dependent on primary parameters. Functional dependencies are given in the following.

Absolute horizontal permeability $\mathrm{k_h}$ versus porosity is shown in Figure 7.3. Correlation functions taken from the literature (Kozeny-Carman type (Scheidegger, 1960), Pape et al. (1999), Holtz (2002)) along with NPC database values are also shown.

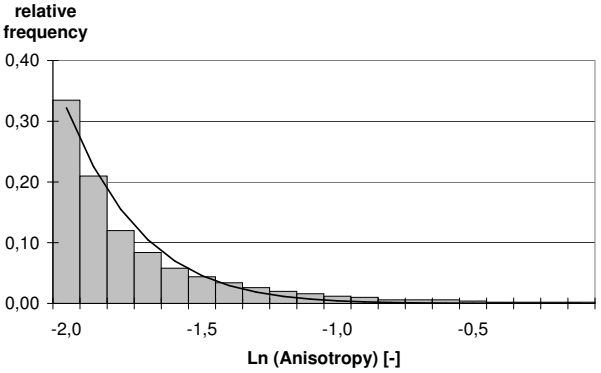

Figure 7.2: Histogram data show relative frequency of the natural logarithm of anisotropy between vertical and horizontal intrinsic permeability [-] derived from a anisotropy model. Line indicates a normal distribution having the same statistical characteristics as the histogram data set.

Correlation coefficients of functions and database values are rather poor. However, the Kozeny-Carman function given in Equation 7.4 with an average grain diameter of 35 μm fits the interpolated NPC database values reasonably well. The absolute horizontal permeability is therefore calculated from porosity by using:

$$k_h = \frac{1}{150} D_{50} \frac{\phi^3}{(1-\phi)^2}, \tag{7.4}$$

where D_{50} is average grain diameter [μm]. Hence, absolute permeability, which is the parameter with the highest effect in the sensitivity analysis (cf. Table 6.2), is considered by a dependency on porosity. Porosity was preferred as a primary parameter, since porosity measurements are more reliable than permeability measurements.

Injection Interval (II), CO_2 injection rate q_{CO2}, and reservoir height are assumed to be constant in this analysis, although they showed a high effect in the sensitivity analysis (rank two, four and six in Table 6.2). The reason for not choosing them as primary parameters is, that the injection interval and the CO_2 injection rate can easily be modified when drilling and screening one or more injection wells. They are not a reservoir property. The reservoir height is a reservoir property, here a lack of data prevents consideration as a primary parameter.

Absolute vertical permeability k_v is calculated by multiplying absolute horizontal permeability k_h with the anisotropy factor $AnIso$ (a primary parameter).

Residual water- and CO_2-rich phase saturations ($S_{w,r}$ and $S_{CO2,r}$) are defined as constant since no suitable correlation function is known to the author. Holtz (2002) gives a

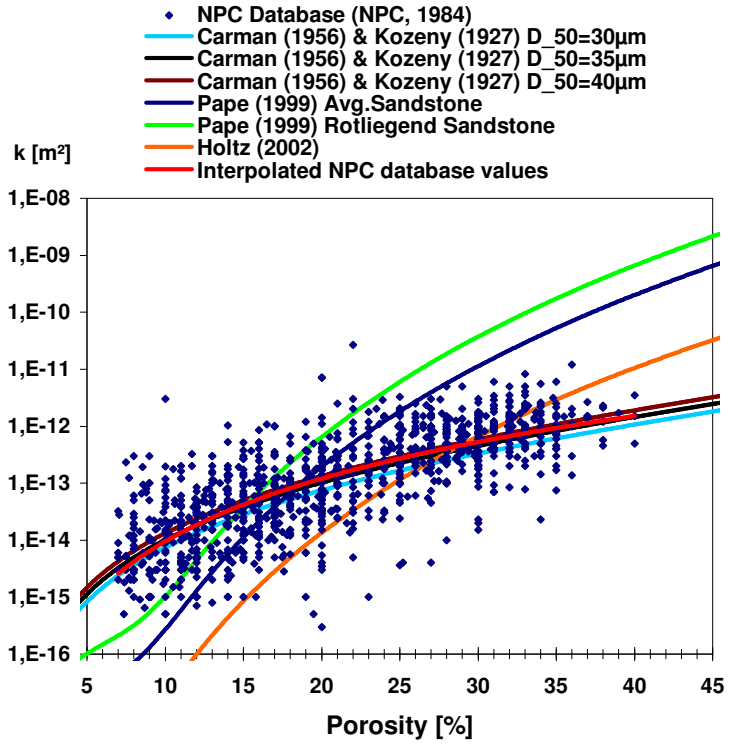

Figure 7.3: Correlation functions between porosity and absolute permeability and NPC database reservoir values. Given are correlations by a Kozeny-Carman model (Scheidegger (1960)) for different average grain diameters, correlations by Pape et al. (1999) for average sandstones and Rotliegend sandstone, a correlation given by Holtz (2002), and an interpolation of the NPC database values (k $[m^2]=2.046 \cdot 10^{-11}\,\phi^{3.6555}$).

correlation function for the residual water-rich phase saturation dependent on absolute permeability and porosity for a specific site. However, permeability and porosity ranges and distributions leading to the functionality given, are not identical to the data considered here. This results in unrealistic values for residual water-rich phase saturation $S_{w,r}$.

Relative permeability k_r is defined by a Brooks & Corey model (Brooks and Corey (1964)). Since Brooks & Corey input parameters $S_{w,r}$, $S_{CO2,r}$ together with the sorting factor λ_{BC} are constant, the relation is identical in all simulations. This is a simplification which is necessary due to lack of better knowledge (data). Only very few measured relative permeability relations of CO_2-brine systems are known, e.g. Bennion and Bachu (2005). But these sparse data do not allow the definition of dependencies on e.g. primary parameters. Relative permeability has a high influence on plume evolution behaviour, as will be discussed in Section 7.4.

Capillary pressure p_c is dependent on porosity, interfacial surface tension between the

water-rich and the CO_2-rich phase, water-rock contact angle, and water-rich phase saturation. A measured capillary pressure-saturation relation and the Leverett J-function (Lake, 1989) are used to determine a distribution of capillary pressure relations as a function of the primary parameters. The measured data are from Plug and Bruining (2007) experiment no. 12 where the sand column has a permeability of approx. $2 \cdot 10^{-10}\,\mathrm{m}^2$ and a porosity of 0.37. The experiment was conducted at a pressure of 8.5 MPa and at 300.15 K. The author also gives values for interfacial tension σ and contact angle Θ. These data allow to use a Leverett J-function to normalise the capillary pressure relation. This relation is representative for the investigated rock-type. The dimensionless Leverett J-function is given in Equation 7.5:

$$J(S_\mathrm{w}) = \frac{p_\mathrm{c}(S_\mathrm{w})}{\sigma \cdot cos\Theta}\sqrt{\frac{\mathrm{k_h}}{\phi}}. \tag{7.5}$$

The assumption, underlying Equation 7.5 is, that the porous medium can be modelled as a bundle of non-connecting capillaries. In this model, $\sqrt{\frac{\mathrm{k_h}}{\phi}}$ [m] is proportional to the typical pore throat radius. The Leverett J-function is used to scale the given capillary pressure relation to other permeability, porosity, temperature and pressure (since the interfacial tension σ changes with pressure and temperature). This is done by equating the J-function for two cases and solving for the capillary pressure of interest (cf. Equation 7.6).

$$p_{\mathrm{c},2}(S_\mathrm{w}) = p_{\mathrm{c},1}(S_\mathrm{w})\sqrt{\frac{\mathrm{k_{h,1}}}{\mathrm{k_{h,2}}}\frac{\phi_2}{\phi_1}}\frac{\sigma_2 cos\Theta_2}{\sigma_1 cos\Theta_1}. \tag{7.6}$$

Subscript "1" indicates reference capillary pressure relation and rock properties (here experiment 12 in (Plug and Bruining, 2007)), subscript "2" the capillary pressure relation for rock properties of interest. An equation for the interfacial tension σ for water and CO_2 systems, as a function of pressure and temperature, is given by (Kvamme et al., 2007) (see Figure 2.10). Examples of resulting capillary pressure relations are shown in Figure 7.4.

Salinity S is defined as a constant. This is because in a previous sensitivity study this parameter had little influence on plume evolution behaviour (Kopp et al., 2007). However, statistical characteristics could have been calculated from the NPC database.

Reservoir dip α is defined to be a constant at zero. Although, statistical characteristics could have been calculated from the NPC database, the computational effort required to include reservoir dip as a primary parameter would have been too high. In order to include reservoir dip in simulations, full 3-D simulations would have become necessary and the computational advantage of employing radial symmetry would have been lost. In the sensitivity investigations, reservoir dip has a negligible effect (rank 15). Nevertheless, reservoir dip is expected to strongly influence plume evolution in setups were buoyancy forces are strong

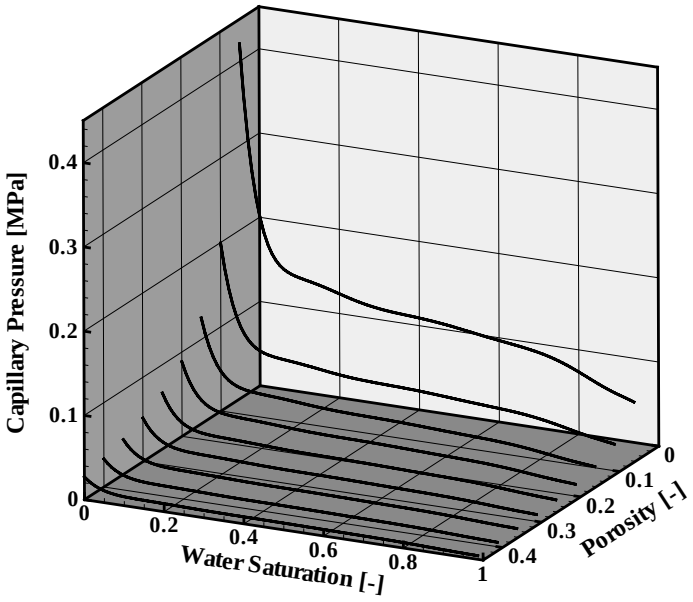

Figure 7.4: Capillary pressure dependence on water-rich phase saturation and porosity. Here $\sigma_1 = \sigma_2$, i.e. relations are at constant temperature and pressure.

and results will be discussed with respect to this simplification in Section 7.4.

CO_2 fluid properties (density and viscosity) are calculated dependent on temperature and pressure. Since in the risk analysis reservoir depth D is a primary paramater and its range includes depths where CO_2 occurs in gaseous, liquid and supercritical state of aggregation, the calculation of CO_2 fluid properties needs to cover a broad range of possible pressures and temperatures.

Other secondary parameters, like brine fluid properties, solubility of CO_2 in brine etc. are calculated by functions given in literature (as cited in Table 7.1) or are defined as constant values since results are insensitive to variation of these parameters.

All parameters given in the NPC database are tested for mutual interrelations (cf. Section 3.3). Apart from the considered dependencies (between porosity and absolute permeability and between depth and temperature, which is the geothermal gradient) no significant correlations have been found.

7.2.3 Procedure of Defining a Simulation Case

The four independent primary parameters are sampled by generating four random numbers between zero and one. These random numbers reflect percentiles of the parameter distributions, for example if the random number is 0.5, the median of the parameter distribution

is obtained. Primary parameters are constant throughout a simulation. Following the generation of four random primary parameters, the secondary parameters are calculated. All secondary parameters, which are dependent on the unknowns in the simulation, i.e. pressure, temperature, saturation or CO_2 mass fraction dissolved in brine, are continuously updated during model simulations. This means, for example, that the capillary pressure relation could be different in each box (cf. Section A.4) and that it changes with time. Other secondary parameters are fixed during the simulation.

7.3 Numerical Investigations

The simulation experiments are conducted with the model for non-isothermal multi-phase multi-component processes (including mass transfer between the phases), i.e. the 2p2cni-module implemented in MUFTE-UG (cf. Section A.2).

7.3.1 Model Set-up

CO_2 is injected in a radially symmetric model domain as shown in Figure 7.1. The reservoir has a lateral extent (radius) of 100 km and a height of 100 m. CO_2 is injected at the centre boundary at a constant rate of 1 Mt CO_2 per year. This rate resembles the CO_2 produced by a medium-sized coal-fired power plant. Since a heat balance is solved, a heat influx at the centre boundary also has to be defined. Carbon dioxide is assumed to be injected at reservoir conditions. Note that the reservoir conditions change with time and heat influx is adapted to these changing conditions. Top, bottom and side boundaries are closed to any flux (Neumann). At the lateral boundary, hydrostatic pressure, geothermal temperature and fully water-rich phase saturated conditions are assumed. This resembles a laterally infinite aquifer with impermeable cap- and baserock.

7.3.2 The "CO2 Community Grid"

To conduct the computationally very expensive simulations, the "CO2 Community Grid" was used (Johannsen et al., 2008). The "CO2 Community Grid" is a virtual research environment (VRE) for massively parallel simulations related to CO_2 storage in porous media. The VRE allows for the usage of a number of supercomputers located in the countries Denmark, Finland, and Norway. This is realised by means of a grid infrastructure, a kind of meta-computing system, based on the Nordugrid (NDGF, 2008) software ARC (Advanced resource connector (Ellert et al., 2007)), a middleware for lightweight computational grids, which provides a unified access to supercomputers. To ease the use of the system, the VRE is realised on a service computer. This computer gives access to users and provides them a simple, unified access to supercomputer platforms. The system allows the execution of multiple instances of parallel simulations simultaneously.

7.3.3 Results

In Figure 7.5 typical results are shown for two cases. The amount of injected CO_2 is in both cases 20 Mt CO_2. Randomly sampled primary parameters for Case 11 are $\phi_{11} = 0.19$, $dT/dz_{11} = 0.020\,°C/m$, $D_{11} = 1920.2\,m$, $AnIso_{11} = 0.009$ and for Case 48 are $\phi_{48} = 0.26$, $dT/dz_{48} = 0.053\,°C/m$, $D_{48} = 640.1\,m$, $AnIso_{11} = 0.023$. These settings lead to CO_2 density around $790\,kg/m^3$ in Case 11 and $330\,kg/m^3$ in Case 48. In Case 11 no leakage occurs up to the time represented by the figure, whereas for Case 48 leakage occurs.

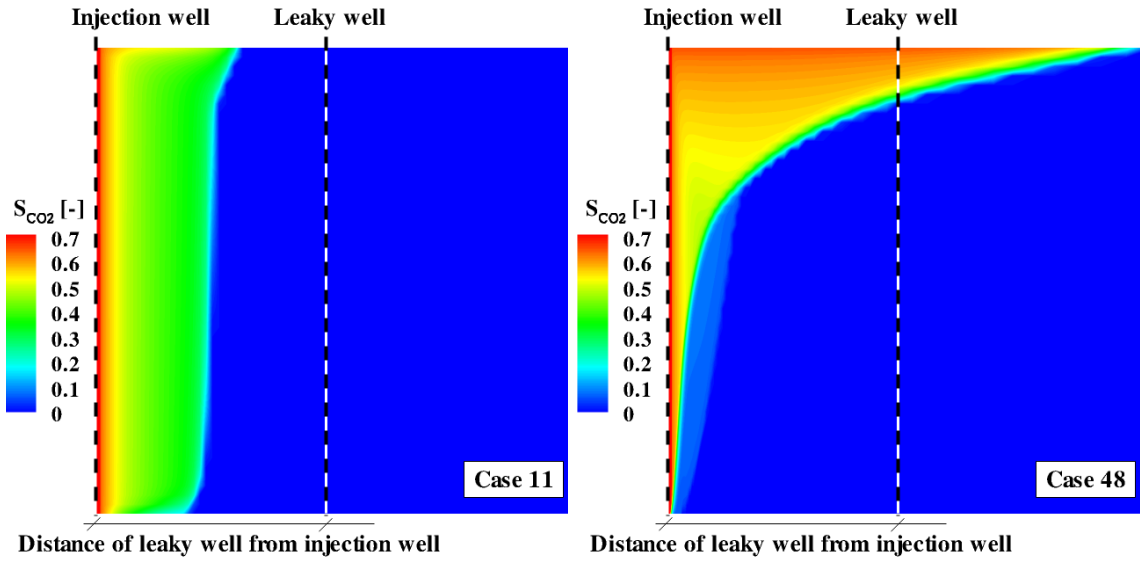

Figure 7.5: Slice of the radially symmetric domain showing CO_2-rich phase saturation after 20 years of continuous injection for Case 11 (left) and Case 48 (right). Shown is only the centre (inner) part of the domain where reservoir height is exaggerated. No leakage can occur in Case 11, whereas for Case 48 CO_2 has spread beyond leaky well distance and potential leakage is high.

Given the definition of risk in Equation 7.1, the two terms of the equation are examined separately before looking at the product of both terms, yielding risk.

In Figure 7.6 the likelihood of failure is shown. Each point on the surface resembles the combined results of all simulations conducted. Range of the likelihood of failure is between zero (no case has failed) and one (all cases have failed). Initially no CO_2 is injected and consequently no failure has occurred. After 7000 days all cases below $r_{\text{leaky well}} = 1100\,m$ have failed and the likelihood of failure is equal to one. For distances larger than $r_{\text{leaky well}} = 1100\,m$ the likelihood of failure is smaller, since less cases fail with increasing distance. For $r_{\text{leaky well}} = 2000\,m$ only 20 % of all cases fail after 7000 days of CO_2 injection. Generally the likelihood of failure increases with time and decreases with distance $r_{\text{leaky well}}$.
In Figure 7.7, the consequence of failure is shown. Each point on the surface resembles the combined results of all simulations conducted. Range of the consequence of failure is between

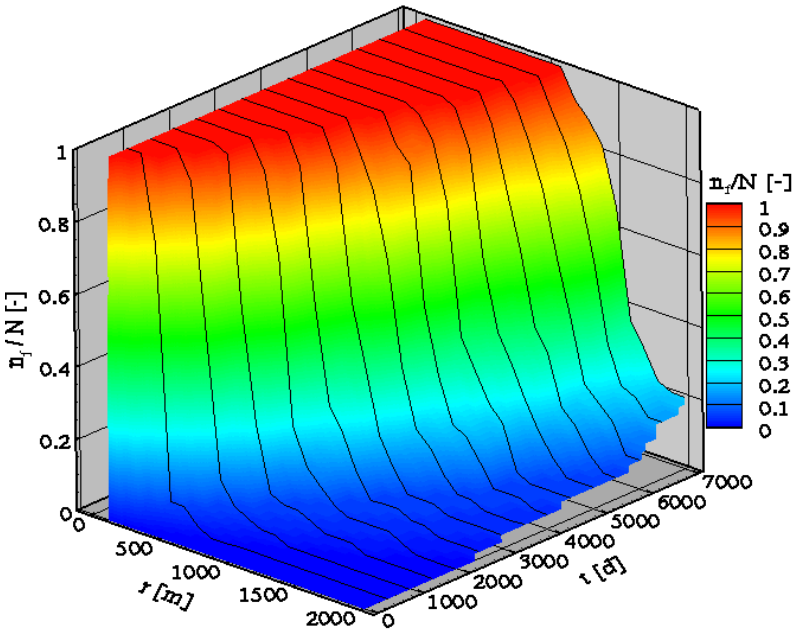

Figure 7.6: Likelihood of failure [-] calculated as n_f/N versus distance $r_{\text{leaky well}}$ between injection well and leaky well and time t.

zero (no leakage occurred in any case) and $2.72 \cdot 10^7$ kg, where all cases produced considerable damage after 7000 days at $r_{\text{leaky well}} = 100$ m. The consequence of failure increases with time and decreases with distance $r_{\text{leaky well}}$. For any given distance $r_{\text{leaky well}}$ the consequence of failure increases quickly once damage has started to occur. For example occurs a consequence of failure larger than zero for a leaky well in 200 m distance after 91 days of injection. It increases then to 10^6 kg at 792 days, and to 10^7 kg after 5401 days. Another example is a leaky well in 2000 m distance, a consequence of failure larger than zero occurs after 2409 days of injection. It increases then to 10^4 kg at 2806 days, and to 10^5 kg after 4819 days.

When looking at the product of both terms, risk as shown in Figure 7.8 is the result. Range of risk is identical to range of the consequence of failure. This is because the consequence of failure is multiplied with the likelihood of failure, which is between zero and one. Risk increases with time and decreases with distance $r_{\text{leaky well}}$, as one would expect.

The risk contour line (red line in Figure 7.8) identifies risk equal to 1 g fitted by a power-function as given in Equation 7.7.

$$t[\mathrm{d}] = e^{\mathrm{A} \cdot \log(r) + B}, \tag{7.7}$$

where r is leaky well distance and A and B are power-fitted coefficients given in Table C.1.

The time contour lines (black lines in Figure 7.8) can be used to calculate risk dependent on leaky well radii r. They are fitted by a exponential function to the risk surface as given in

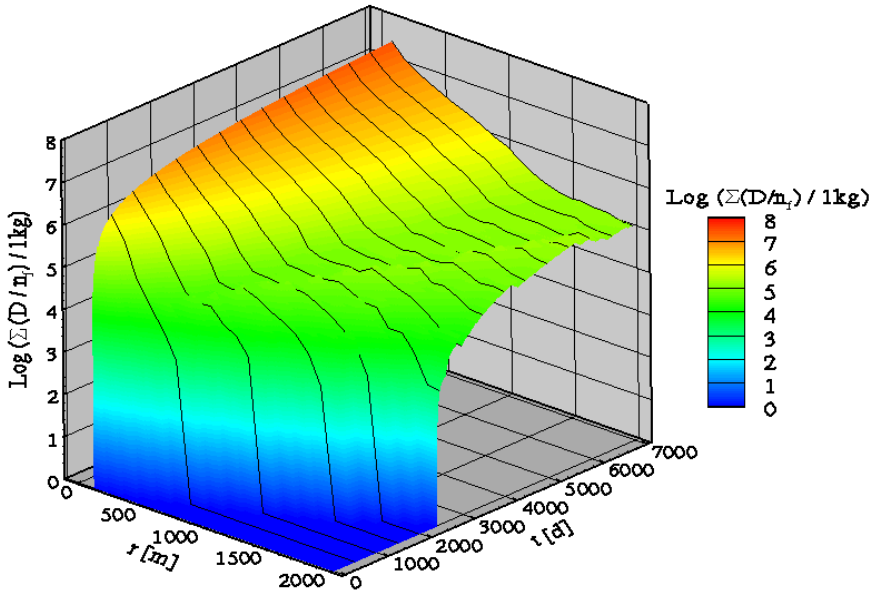

Figure 7.7: Consequence of failure [log kg] calculated as $\sum_{i=1}^{N} \frac{D_i}{n_f}$ versus distance $r_{\text{leaky well}}$ between injection well and leaky well and time t.

Equation 7.8.

$$\text{Log(Risk/1kg)} = \sum_{i=0}^{9} A_i \cdot r^i, \tag{7.8}$$

where r is leaky well distance and A_i are coefficients given in Table C.2.

In Figure 7.9 risk is shown for few selected leaky well distances and for various primary parameters. In general, risk for all cases increases with time of injection and with smaller leaky well radii. For a leaky well radius of 200 m, risk is basically identical in all cases. This result is expected given the short time and spatial scale, because the results are independent of the multiphase flow and transport regime in the reservoir and consequently independent of reservoir parameters. The effect and sensitivity of primary parameters is discussed in the following, where results are shown for clustered groups of cases having the same parameters (e.g. all cases with porosity of 0.106, 0.190, and 0.320 in Figure 7.9 (top-left)).

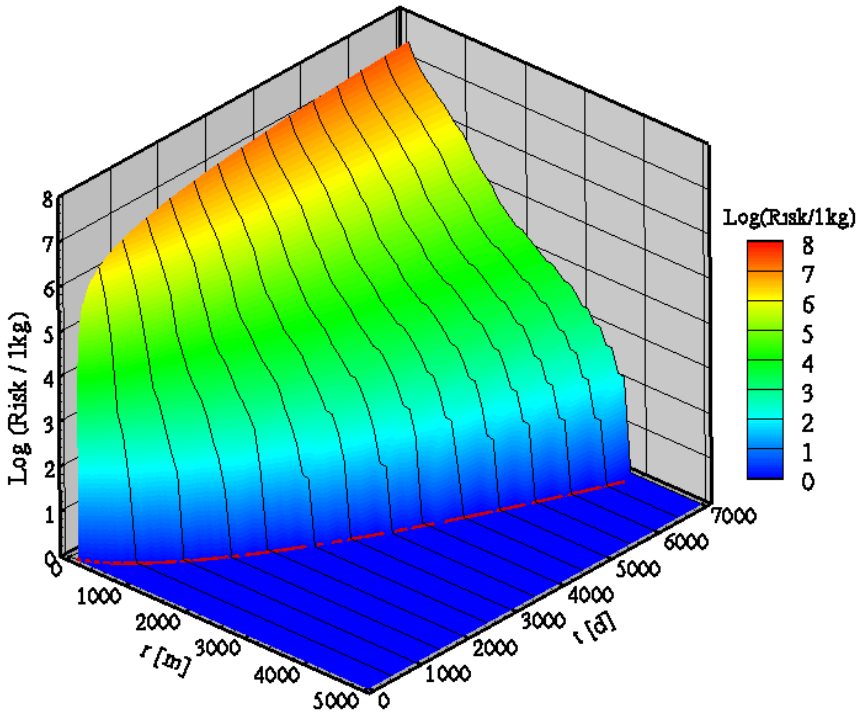

Figure 7.8: Log (Risk/1 kg) calculated as $\frac{n_f}{N} \cdot \sum_{i=1}^{N} \frac{D_i}{n_f}$ versus distance $r_{\text{leaky well}}$ between injection well and leaky well and time t.

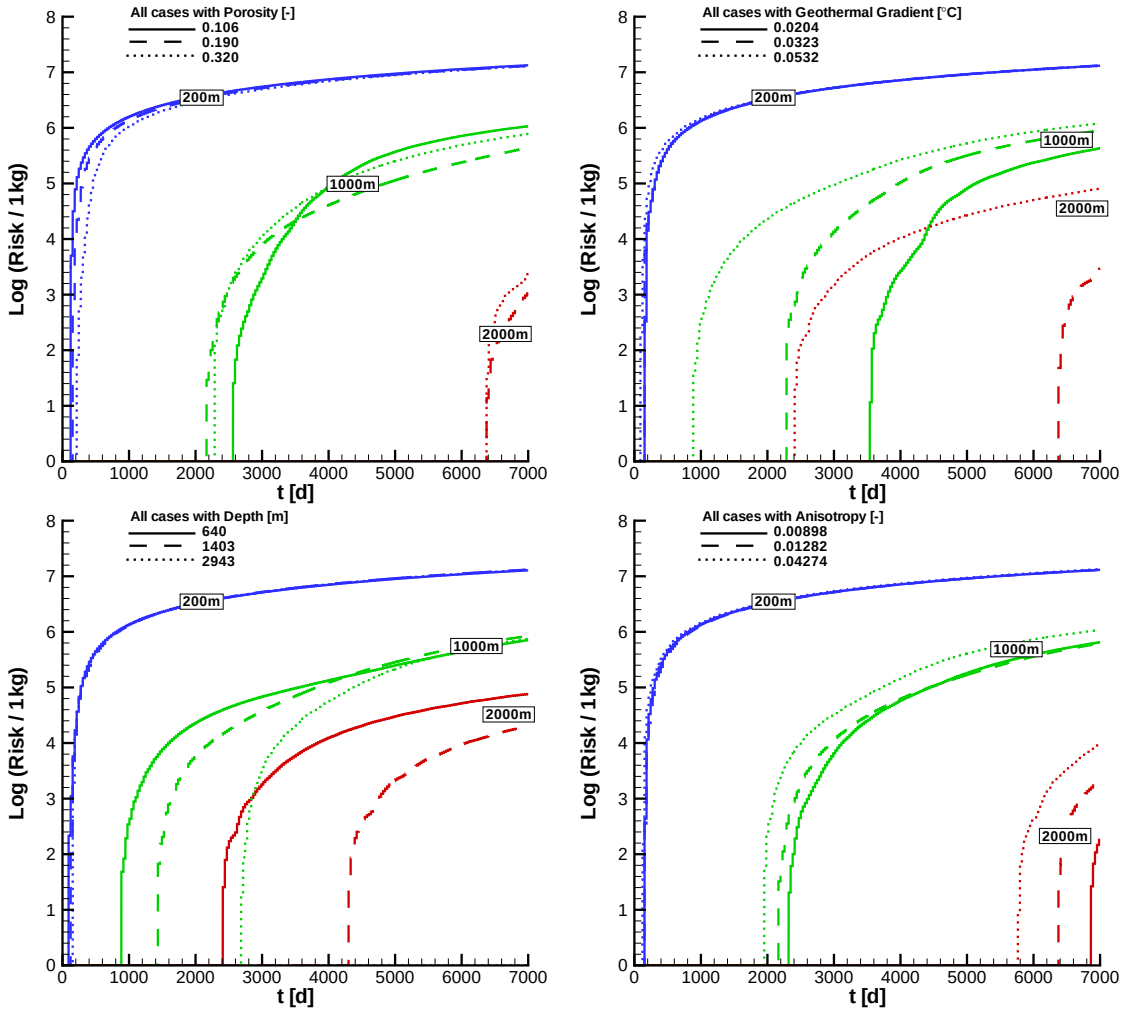

Figure 7.9: Log (Risk/1kg) versus time [d] for selected $r_{\text{leaky well}}$ distances (shown in the boxes). Shown are clustered groups of primary parameters including porosity (top-left), geothermal gradient (top-right), depth (bottom-left), and absolute permeability anisotropy (bottom-right).

Figure 7.9 (top-left) shows risk as a function of porosity. No clear trend of risk as a function of porosity can be seen. Cases with a porosity of 0.106 produce almost the same risk as the cases do with a porosity of 0.19, and 0.32 respectively. With increasing porosity one would expect a retardation of the plume evolution velocity, simply due to increased pore space, and consequently a later increase of risk, i.e. lower risk at any time. But the permeability also increases with porosity, since it is coupled by a Kozeny-Carman functionality (cf. Section 7.2.2). The increased permeability leads to stronger gravity segregation and hence to increased plume evolution velocity below the caprock. Note that vertical permeability is coupled to horizontal permeability via the Anisotropy parameter. The effects of the retarded plume evolution velocity due to increased porosity and stronger gravity segregation due to increased horizontal and vertical permeability cancel each other out, i.e. risk is independent of porosity. Small differences in risk are due to the other (random) primary parameters (e.g. depth).

Figure 7.9 (top-right) shows risk for a given geothermal gradient. It can be seen that risk increases earlier for higher geothermal gradients. This is because of the lower CO_2 density for a higher reservoir temperature. Gravity segregation is stronger at higher temperatures and fast lateral plume evolution occurs below the caprock. For $r_{\text{leaky well}} = 1000\,\text{m}$, risk increases after 884 days for a thermal gradient of $0.0532\,^\circ\text{C/m}$, after 2287 days for a thermal gradient of $0.0323\,^\circ\text{C/m}$, and after 3538 days for a thermal gradient of $0.0204\,^\circ\text{C/m}$. Risk is also quite different after 7000 days, i.e. $4.31 \cdot 10^5$ kg, $8.96 \cdot 10^5$ kg, and $1.2 \cdot 10^6$ kg, corresponding to a factor of 3.

Figure 7.9 (bottom-left) shows risk as a function of depth below ground surface and shows that risk increases earlier for shallower depth. This is also due to CO_2 density, because at lower density gravity segregation is stronger leading to fast lateral plume evolution below the caprock. For $r_{\text{leaky well}} = 1000\,\text{m}$, risk increases after 884 days for a depth of 640 m, after 1433 days for a depth of 1403 m, and after 2684 days for a depth of 2943 m. However, after 7000 days, risk can be viewed as being identical for all depths.

Figure 7.9 (bottom-right) shows risk as a function of permeability anisotropy. Risk increases earlier for larger anisotropy factors. The gravity segregation effect is stronger for a large anisotropy factor. Parameter sensitivity, however, is lower, compared to the sensitivities of geothermal gradient and depth. For $r_{\text{leaky well}} = 1000\,\text{m}$, risk increases after 1952 days for an anisotropy of 0.04274, after 2165 days for an anisotropy of 0.01282, and after 2318 days for an anisotropy of 0.00898. This difference in time grows with increasing $r_{\text{leaky well}}$.

Summarising, it can be concluded that high risk corresponds to short leaky well distances, long injection times, high geothermal gradients, high permeability anisotropy, and low depth. Risk, as it is defined here, does not depend on porosity.

7.4 Qualitative Sensitivity Considerations

The assumptions made for the secondary parameters, together with other simplifications, are discussed in the following with respect to their potential to lower (−) or increase (+) leakage (lead to later (−) or earlier (+) leakage):

Reservoir geometry +/−: An increased height of the reservoir, a negative dip angle towards the leaky well, and a sealing fracture in the reservoir in between the injection and the leaky well leads to lower or later leakage through the leaky well. For converse assumptions, i.e. decreased height, positive dip angle and a sealing fracture on the opposite side of the injection well, this would lead to higher or earlier leakage. Mosthaf (2007) studied the influence of varying dip angles (amongst others) and described the influence by dimensionless numbers. Hesse et al. (2008) suggest that an increasing slope of an aquifer accelerates residual trapping and that lateral migration of the injected CO_2 traps the CO_2 relatively quickly as residual saturation. The results were, however, obtained with simplified 2-D models neglecting (amongst other simplifications) density and viscosity changes.

Diffuse leakage through caprock +/−: Diffusive leakage into shallower reservoirs could reduce leakage at the leaky well. The effect on risk depends of course on the judgement whether this diffusive leakage is acceptable (e.g. because leaking CO_2 is trapped in the shallower aquifer) or is not acceptable (leads also to damage or risk). However, Li et al. (2006) showed, that if the sealing pressure of the caprock is not exceeded, leakage of CO_2 by molecular diffusion is negligible during the short-term injection stage. If the sealing pressure is exceeded though, leakage rates can become (very) large. Gherardi et al. (2007) shows that when the transport of chemicals primarily occurs by molecular diffusion in the water-rich phase, CO_2 leakage becomes self-limiting, i.e. pores become clogged after a very short time. In case of a fractured caprock, however, gaseous CO_2 penetrates into the caprock and induces some enhancement in porosity and permeability, which reduces the sealing efficiency of the caprock.

Permeability: +/−: A different functionality of permeability on porosity (e.g. Pape et al. (1999), Holtz (2002), or a Kozeny-Carman model with modified parameters), could lead to reduction or increase of leakage. Considering the concept of risk developed here, leakage is lower or occurs later at lower permeabilities, i.e. the CO_2 plume is more compact (Kopp et al., 2009a).

Heterogeneity +/−: Reservoir heterogeneity can lead to either increased or earlier, or to decreased or later leakage. For example, when assuming a high-permeability channel structure towards the leaky well, leakage occurs earlier and at higher rates. When assuming low-permeability structures in the reservoir, gravitational segregation is reduced, and consequently leakage is reduced or retarded. Flett et al. (2007) studied the impact of different net-sand-to-gross-shale ratios on the development of the CO_2

plume shape and on dissolved, residually trapped, and mobile CO_2 mass fractions. They conclude that with increasing amounts of shale in the reservoir, vertical movement of the plume is restricted and lateral movement aided. An increasing amount of shale and consequently a restricted vertical movement thus leads to reduced leakage. Consequently, it can be concluded that the assumption of homogeneity is a conservative approach on risk.

Relative Permeability +/–: Considering a different shape of the relative permeability relation or different residual saturations (and consequently different end-points) could lead to either increased or earlier, or to decreased or later leakage. Bennion and Bachu (2008) measured relative permeability relations for CO_2-brine systems in the Alberta basin in Canada, and these do influence the plume evolution behaviour (as shown by Kopp et al. (2009b)) to a similar degree as the reservoir properties considered here (depth, geothermal gradient, etc.).

Capillary Pressure +/–: The approach employed to scale a measured capillary pressure relation to actual reservoir conditions at a given pressure, temperature, and (constant) porosity is quite sophisticated. However, such a scaling assumes the same rock-type in all reservoirs. As this is not generally the case, a different capillary pressure relation might lead to an increase or decrease of leakage. Generally, stronger capillary forces lead to less leakage, since more CO_2 is stored by capillary trapping (Ide et al. (2007), Kopp et al. (2009b)). In a heterogeneous reservoir, the effect of high capillary entry pressures of low permeable shale structures amplifies the effects discussed earlier with respect to heterogeneity, i.e. CO_2 may not escape a high-permeability channel structure towards the leaky well, which leads to earlier leakage and to higher rates.

Hysteresis –: Hysteretic behaviour in either the relative permeability or capillary pressure relation (cf. Sections 1.1 and 2.2.4) influences plume evolution, and thus influences leakage. Incorporating hysteresis of any kind will lead to decreased or later leakage since additional CO_2 is trapped.

Anisotropy model +/–: A different anisotropy distribution (here a primary parameter derived by conceptual modeling) could lead to increased or earlier or to a decreased or later leakage. Generally, an increase in anisotropy leads to decreased or later leakage due to reduced gravity segregation.

Salinity +/–: As salinity influences brine density, viscosity and the solubility of CO_2 in brine, a higher or lower salinity than assumed influences leakage. Generally, lower salinity leads to an increase in CO_2 solubility in brine (Duan and Sun, 2003), hence leakage is decreased or occurs later.

Leakage simulation –: If leakage was actually simulated assuming low permeability well plugs etc. it would always be less than assumed here where leakage composes all the

CO_2 mass that passed by the leaky well. In practise, not all of the mass passing by the leakage point will flow out of the reservoir. Ebigbo et al. (2007) investigated CO_2 leakage rates through an abandoned well. The considered reservoir has an open leaky well (without well plugs etc.) at 100 m distance to the injection well which connects to a shallower aquifer. An additional simulation is conducted here, resembling the reservoir parameters and the setup presented by Ebigbo et al. (2007). Hence, the leakage rate of this additional simulation case derived by the methodology presented here, and the leakage rate given by Ebigbo et al. (2007) can be compared, as shown in Figure 7.10.

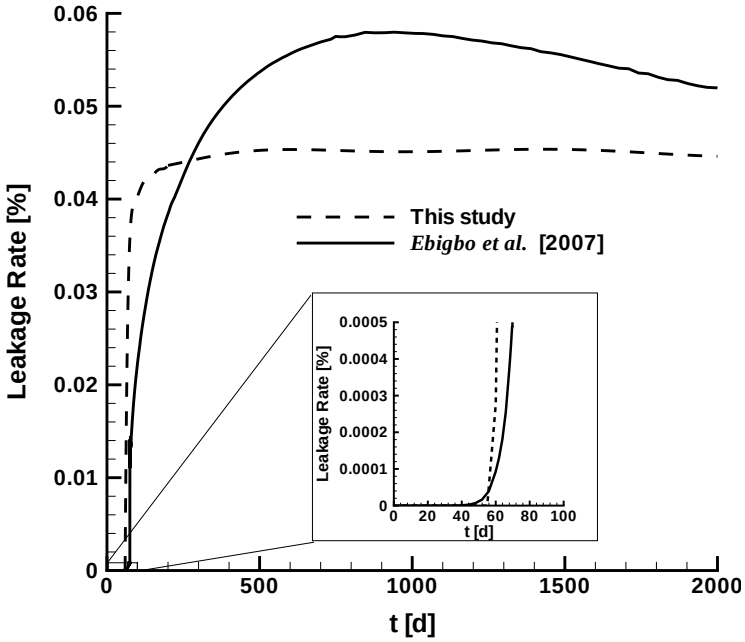

Figure 7.10: Comparison of leakage rates versus time obtained by Ebigbo et al. (2007) and calculated by the methodology presented in this study. Leakage rates are given as a fraction of the CO_2 rate injected.

The times when significant leakage commences are almost identical. The difference is due to slightly different boundary conditions and the different reservoir geometry (single radially symmetric reservoir in this study versus a fully 3-D simulation with two reservoirs, connected by the leaky well in the centre). Leakage rates then start to increase at a slower rate in the study of Ebigbo et al. (2007), reach a peak leakage rate, and decrease on the long term. The gradual increase of the leakage rate is explained by up-coning of the brine into the well (Nordbotten et al., 2005b). The higher peak rate and later decrease is explained by thermodynamic and hydraulic processes in the leaky well. Pruess (2008a) investigated physical and chemical processes in CO_2 leakage through a fault zone into a shallow reservoir, and eventually consecutive leakage to the atmosphere along another fault. He outlined some potential for self-enhancement of

leakage rates by factors of 2–3 relative to CO_2 flow rates at depth. This corresponds to three-phase conditions (water-rich phase – liquid CO_2-rich phase – gaseous CO_2-rich phase) at relatively shallow depth. But since (i) this happens only temporarily, (ii) the system was purposefully designed to facilitate such behaviour, and (iii) CO_2 was injected right into the fault, neglecting the processes occurring in the reservoir, the self-enhancement of leakage is not of importance here. Assuming any kind of (untight) well plugs etc., reduces leakage rates largely, so that the approach in this study can be considered a worst case.

Additional assumptions on leaky well properties −: Here the leaky well is assumed to penetrate the entire formation thickness and is assumed to be completely open to the atmosphere. In practise this is not the case. For example, partial penetration of the formation, well plugs, incorporation of detailed leakage pathways in the leaky well, knowledge about material behaviour etc. will always reduce leakage rates.

CO_2 injection scheme and rate +/−: In this study a continuous injection of CO_2 is assumed. By a modified injection scheme, i.e. alternating injection of gas and fresh brine, additional CO_2 could be trapped residually (Ide et al., 2007). Kopp et al. (2009b) showed that the injection rate also has an considerable influence on the shape of the plume and therefore on the potential leakage. High injection rates lead to rather cylindrical plume shapes, resulting in less lateral extent of the plume.

Injection well design −: By intelligent design of the injection well (horizontal setup, screening in lower regions, etc) leakage could be reduced or retarded.

Geochemistry −: Geochemical processes can lead to mineral trapping in the reservoir (Rosenbauer et al. (2005), Kühn and Clauser (2006), Xu et al. (2007), Mito et al. (2008)), which could lead to lower or later leakage. This influence is rather important on the long term, i.e. much later than 100 years, and is not included in this study. If the caprock is subject to chemical processes, this can lead to very large leakage rates as discussed under the heading “Diffuse leakage through caprock”.

7.5 Summary and Conclusion

The concept developed, utilises a well tested simulation code to derive risk of potential CO_2 leakage through pre-existing leaky wells, subject to multiphase transport processes occurring in a reservoir. Leakage is calculated as the accumulated CO_2 mass that has spread within the leaky well sector beyond the leaky well distance of interest at time t. The reservoir is assumed to have a simplified geometry and is homogeneous. The study takes into account four independent primary parameters randomly sampled from probability density functions derived from a large reservoir properties database and a model respectively. The risk surface derived is thus an average risk over the considered primary parameter ranges. Additional

leaky wells in the surrounding of the injection well can be easily incorporated by summing up the individual risk for each well. The additional assumption herein is, that the leaky wells do not influence each other, i.e. no leaky well is located in the radial share of a leaky well that is closer to the injection well (cf. Figure 7.1). Since other than primary reservoir properties are fixed or have certain dependencies on primary parameters, different assumptions made for these parameters or for the reservoir could lead to lower/higher or earlier/later leakage at the leaky well, and hence to lower/larger risk. This is discussed in Section 7.4.
Given the assumptions, this study adopts a conservative approach concerning the leakage of CO_2 through abandoned wells with regard to most reservoir parameters. However, risk is underestimated if reservoir geometry is very different (large dip, small height) or if the relative permeability relations show a high CO_2 permeability together with large residual water-rich phase saturation (significantly larger than 0.3).
Main findings and conclusions are :

- The presented study defines a quantitative method for the evaluation of risk with respect to CO_2 leakage through pre-existing wells based on comprehensive reservoir properties statistics.

- Within the given framework, a range of possible risks is defined. This can be used to determine whether an individual site is good or not in terms of potential leakage rate through a number of leaky wells with given distribution around the injection well. Hence, assistance is given to experts when rating storage sites with unknown/uncertain reservoir properties. The cumulative risk for any site with given leaky well distances can be calculated, and sites can be compared to each other. Thus, the relative risk might assist in making decisions on where to conduct further investigations or to help experts when utilising more comprehensive screening and ranking frameworks.

- The study identifies reservoir parameters of importance to risk assessment. Among the four selected independent primary parameters, the depth of the reservoir and the geothermal gradient are shown to have highest influence on risk. Anisotropy shows an influence only up to some distance from the injection well. In this study, risk is independent of porosity (due to coupling of permeability to porosity). An ideal reservoir should thus be located at great depth, should have a low geothermal gradient, and should have a high anisotropy.

- The placement of the injection well can be optimised with respect to risk arising from abandoned wells in the surroundings. For a given injection well location, the combined risk for any number of leaky wells in the surroundings can be calculated for the time of interest analytically. Thus, it is possible to compare risk for several injection well locations and pre-select the location yielding the lowest risk.

8 Final Remarks

8.1 Summary

Due to tremendous human fossil-fuel use in the past 160 years, the concentration of greenhouse gases in the atmosphere increased and is most likely the cause of an observed global increase of average temperature and of changing climate. It is expected that, with further global warming, there will be drastic ecological and economic impacts. No one single option or technology will be sufficient achieve the necessary emission reduction in a growing global economy.

Carbon dioxide capture and storage considers capturing CO_2 in large local sources, such as power plants etc., transportation to the storage site, and storing the CO_2 away from the atmosphere for geological periods of time. This study focuses on the latter part and considers storage in deep saline geological formations. Injected CO_2 spreads in the formation and is subject to strong buoyancy forces, driving it towards the top of the reservoir where it is usually kept from further ascent by a low permeable caprock. However, the caprock may show geological weaknesses or may be perforated by wells which are a potential leakage pathways for the injected CO_2 out of the formation causing risk to health, safety, and the environment. The careful selection, analysis, and evaluation of a storage site is therefore an indispensable part of a storage project.

The main objective of this study is the improvement of insight into CO_2 injection processes in geological formations to assist site screening. Site screening is defined as the very first steps in site selection, where usually little information is available about reservoir properties. Questions of interest in site screening include the estimation of the storage capacity, which should be sufficient to store the long-term production of the CO_2 source, and the long-term ability to store CO_2, which is related to the efficiency of the project and risk. These questions are investigated by the statistical analysis of a database, analytical, and numerical experiments.

In Chapter 2 the essential features and principal processes of CO_2 storage in geological formations are described and a conceptual model is set up. Based on the conceptual model, a mathematical and numerical model is formulated.

The properties of potential storage sites in geological formations are derived in Chapter 3 by

analysing a large database listing the properties of more than 1200 reservoirs. The parameter ranges and distributions are used to define typical reservoirs, e.g. a warm, a cold, a deep, and a shallow reservoir. Additional reservoirs are defined by re-combination of the median reservoir properties with measured relative permeability-saturations relations, modified capillary entry pressure, halved injection rate and reduced absolute permeability.

With dimensional analysis the dominant forces and relevant processes during the CO_2 injection stage are assessed in Chapter 4. This is done by non-dimensionalising the governing flow equations in the fractional flow formulation by introducing characteristic values for length, time, velocity, and pressure. The resulting set of balance equations consists only of dimensionless gradients, dimensionless numbers, and dimensionless saturation-dependent functions. The dimensionless numbers represent relations of forces in the system, i.e. capillary, viscous, and buoyancy forces. The individual dimensionless terms are then investigated by independent variation of the characteristic values. This yields a better mathematical understanding of the system behaviour. To develop a physical understanding of the system, the mutual dependence of characteristic values and the simultaneous variation of saturations, gradients, and ratios of forces is investigated in numerical 1-D and 3-D experiments. The typical reservoirs defined earlier are chosen as a basis.

In Chapter 5, a methodology for investigating the CO_2 storage capacity of geological formations during the injection stage is developed. This approach respects the physical trapping mechanisms. The storage capacity coefficient C and the effective mass that can be stored in a reservoir M_{eff} are introduced to compare the storage capacity of the typical reservoirs defined earlier. To estimate storage capacity, it is necessary to limit the reservoir volume at some point. This is done by defining a spill point at one kilometre distance from the injection well. Time-dependent storage capacity estimates are calculated in 1-D and 3-D numerical experiments. Finally, the results are interpreted using the simultaneously calculated ratios of forces (dimensionless numbers) in the experiments.

In Chapter 6, the influence of individual reservoir parameters on the model results is investigated in a sensitivity analysis. The reservoir parameters are varied over their full range assuming uniform distribution. Model results of interest include measures related to storage capacity (e.g. arrival time at a spill point) and risk (e.g. developing over-pressure). The robust, reliable, and efficient Morris Method is used to conduct the sensitivity analysis because the method is especially suited to screening a large number of model input parameters by randomly sampling the input parameter space. Qualitative measures are derived identifying irrelevant input parameters that result in an average input parameter ranking.

In Chapter 7, a risk analysis for potential CO_2 leakage through pre-existing leaky wells is performed. Risk is expressed as the likelihood of leakage occurring times the damage produced, which is defined here as the potentially leaking CO_2 mass at a point in time for arbitrary

distances between the leaky well and the injection well. The likelihood of leakage occurring is evaluated by running numerous numerical experiments. In each individual experiment, properties are randomly sampled from statistical distributions derived from the database analysis mentioned earlier. The independent parameters are porosity, depth of the reservoir below surface, average geothermal gradient, and the absolute permeability anisotropy. Other reservoir parameters are derived by a functional dependency from independent parameters, or are chosen as constants. In each individual numerical experiment, leakage is calculated as the accumulated CO_2 mass that has passed by the leaky well at a given distance to the injection well at a given time. Thus, leakage is here primarily subject to multiphase transport processes occurring in the reservoir. The risk surface derived, i.e. risk as a function of leaky well distance and time, represents average risk for any site with unknown reservoir properties. The result is discussed comprehensively with respect to the assumptions made.

8.2 Conclusions

The major conclusions and insights into CO_2 injection processes in geological formations are briefly reviewed.

Properties of Potential Geological Formations: Statistical characteristics of reservoir properties relevant for CO_2 storage are calculated from a database.

- It is shown that the distributions of analysed reservoir properties do not follow standard probability distributions.
- The correlation coefficients between investigated properties are low. Mutual parameter interrelations are rejected, except for the interrelation between absolute permeability and porosity; here, a Kozeny-Carman relation is assumed.

Dimensional Analysis: Dominant forces and relevant processes during the CO_2 injection stage are assessed by dimensional analysis.

- The dimensionless numbers Ca and Gr are basically able to characterise the plume evolution during the initial injection phase dominated by multiphase processes.
- The Capillary Number Ca generally reflects plume evolution velocities in 1-D numerical experiments. Cases with varying injection rate, capillary pressure and permeability do not fit into this scheme since gravity segregation is neglected as a result of the 1-D assumption.
- In 3-D numerical experiments, it is shown that geological formations can be qualitatively ordered according to their plume evolution behaviour using the dimensionless Capillary Number and Gravity Number, where Gr has the stronger influence. It is

not fully understood how the simultaneous variation of Gr and Ca affects estimates of storage capacity and risk. However, a low ratio of gravitational to viscous forces (low Gr) - and to some extent also a high ratio of capillary to viscous forces (high Ca)- possibly leads to high CO_2 storage capacity and low risk.

- The relative permeability-saturation relations are of great influence for plume evolution velocity and average CO_2 saturation. Therefore, they have a great influence on storage capacity and risk.
- The average CO_2 saturation can be estimated by analysing the fractional flow function.

Analysis of Storage Capacity: A sophisticated method for estimating storage capacity is developed and detailed time-dependent estimates are calculated for typical reservoirs.

- A clear tendency is evident that deep, cold and/or low-permeability reservoirs have a higher storage capacity than shallow, warm, and/or high-permeability reservoirs. An increased injection rate leads to an increase in storage capacity due to higher viscous forces.
- 3-D simulations considering gravity forces show a larger difference in maximum and minimum storage capacity estimates, than the 1-D simulations.
- In the 3-D simulations, the reservoir with median properties and reduced permeability, the reservoir with median properties and basal formation relative permeability-relations and the cold reservoir (in this order) show the highest storage capacity. The warm and the shallow reservoir shows the smallest storage capacity.
- The estimated storage capacity coefficient C in the 3-D simulations ranges from from 0.0117 (for the shallow reservoir) to 0.036 (for the reservoir with median properties and reduced permeability). By inclusion of the CO_2 density for these setups this translates to an effective mass that can be stored M_{eff} in a range between 0.09 and 1.94 (normalised to the reservoir with median properties).
- In all 3-D simulations, less than 3.6 % of the total geometric reservoir volume (equivalent to less than 18 % of the pore volume) can be used by the injected CO_2 before the spill point at one kilometre distance is reached.
- Storage capacity estimates are largely influenced by the relative permeability-saturation relations ($k_{\mathrm{r,CO2}}$ and $k_{\mathrm{r,w}}$, together with the residual water- and CO_2-rich phase saturations). They influence the capacity estimates to a similar extent as the entire range of reservoir properties investigated.
- This study indicates that $k_{\mathrm{r,CO2}}$ together with the residual water-rich phase saturation have a major influence on the intrinsic storage capacity coefficient $C_{\mathrm{i,CO2}}$, whereas $k_{\mathrm{r,w}}$ has a major influence on the geometric storage capacity coefficient C_{g}.

- A conservative approach to estimating storage capacity is presented, since all secondary trapping mechanisms (structural, solubility, and chemical trapping mechanisms) are neglected, which would lead to a further increase in the storage capacity at later times.

Sensitivity Analysis: The sensitivity of various reservoir parameters to the estimated storage capacity and risk is analysed and parameters are qualitatively ordered.

- Parameters like horizontal permeability, injection interval, reservoir depth, reservoir height, and geothermal gradient (in this order) show the largest sensitivity with respect to the questions of interest.
- Parameters like the salinity, residual water-rich phase saturation, entry pressure, porosity, sorting factor, CO_2 injection temperature and the dip angle show the smallest sensitivity with respect to the questions of interest.
- It is expected that for other setups, like in 3-D simulations, this ordering might be different due to different relations of the dominant forces in the course of time.

Risk analysis: The risk associated with CO_2 leakage through pre-existing wells is analysed based on comprehensive reservoir-property statistics and a quantitative average risk surface as a function of the distance of the leaky well distance to the injection well and of time has been calculated.

- Important reservoir properties with respect to risk are identified based on CO_2 plume evolution behaviour. The reservoir depth below the surface and the geothermal gradient show the highest influence on average risk estimations. Permeability anisotropy influences the risk estimates only up to some distance from the injection well.
- A large reservoir depth below the surface, a low geothermal gradient, and a large permeability anisotropy are advantageous for low risk estimates.
- In this study, risk is independent of porosity (due to the coupling of permeability to porosity).
- The quantitative average risk surface calculated allows the comparison of individual sites with respect to risk imposed by the potential leakage through a number of leaky wells with a given distribution around the injection well. This risk estimate can be used to decide where to conduct further investigations or help experts utilising more comprehensive screening and ranking frameworks.

In conclusion, a significant contribution has been made towards the evaluation and the understanding of CO_2 injection processes in geological formations with respect to storage capacity estimates and risk for leakage through pre-existing wells.

8.3 Outlook

In this relatively young, but complex field of research involving various scientific disciplines and often subject to highly uncertain (geological) data, additional aspects can be included with the aim of a comprehensive site screening methodology. However, the more aspects are included in site screening, the more data are necessary which might not be available.

- A dimensionless number related to the developing over-pressure during the injection stage could be included. The developing over-pressure should always be limited to the fracture pressure of the caprock to prevent damage leading to the loss of the long-term ability to store CO_2. If other formations used for CO_2 storage are present in the same region, the mutual pressure increase complicates the problem further. If the pressure increase is above certain limits, an active pressure management might become necessary, e.g. by brine discharge.

- The aspect of reservoir geometry and property distribution could be included in a dimensionless number. A anticlinal shape of the reservoir is advantageous due to limited spreading of the CO_2. Heterogeneity in the permeability can also be advantageous to plume spreading, if e.g. gravity segregation is increased. On the other hand, highly permeable flow paths towards a potential spill point are disadvantageous. The use of hypothetical sites or real-field project sites would be beneficial here. However, with the current computational power, it is hardly possible to conduct numerous simulations ($\sim$100s) of complex reservoir setups for research purposes. With access to computer clusters or grid environments, this might be different.

- A dimensionless number related to the properties of the caprock could be developed. Qualities of interest here include a large thickness, a low permeability, no fractures or other weaknesses, and lateral continuity.

- The aspect of an economical CO_2 injection into saline aquifers (high injectivity, lower drilling costs at shallow reservoir depth) could be included by adding another dimensionless number. The injectivity aspect relates to the developing over-pressure, but other economic aspects may produce a different ranking of the reservoirs here.

- This economic aspect could be further extended by including the aspect of the hydrocarbon potential of a site (by enhanced oil recovery, enhanced gas recovery, or enhanced coal bed methane). However, it would then also be necessary to include all costs (drilling costs, infrastructure, etc.) when comparing sites.

- Indicators related to geomechanical and geochemical processes expected to occur at a site could be included. Especially for the geochemical part, where the effects of many different combinations of minerals need to be evaluated and rated, this seems to be a challenging part. This could be further complicated when considering impurities in the CO_2 stream.

- More risk-related aspects could be included, e.g. brine displacement to shallower formations, tectonism, etc.
- The aspect of ambient water flow could be included in a screening methodology. A site could be advantageous for a CO_2 storage attempt if ambient water flow occurs in down-dip direction, thus slowing or even stopping the upward migration of the CO_2 plume and leading to increased solubility trapping.
- As the effects of hysteresis in the capillary pressure- and relative permeability-saturation relations are different for every rock type and lead to additional trapping, this could potentially be included in the site screening.

Most of these aspects could be investigated by numerical simulation. Finally, all aspects could be combined in a comprehensive site screening methodology, allowing for a preliminary, but quantitative comparison between sites.

At a later stage, in site characterisation, a general requirement would be the development of an accepted methodology to identify modeling needs depending on site specific requirements. One step towards such an methodology is the comparison of the entire process of model building by giving different groups access to field data and comparing the approaches and techniques used and the results gained.

Above all, there is a major need for data to develop, apply, and verify techniques and tools. For this study, more data on measured relative permeability- and capillary pressure-saturation relations (possibly including hysteresis) would yield great improvements, along with a global saline-aquifer-properties database to make detailed region-specific storage capacity estimates possible and to apply and verify developed techniques.

Bibliography

Arrhenius, S., 1896. On the Influence of Carbonic Acid in the Air upon the Temperature of the Ground. Philosophical Magazine and Journal of Science (5^{th} series) 41, 237–275.

Assteerawatt, A., Bastian, P., Bielinski, A., Breiting, T., Class, H., Ebigbo, A., Eichel, H., Freiboth, S., Helmig, R., Kopp, A., Niessner, J., Ochs, S., Papafotiou, A., Paul, M., Sheta, H., Werner, D., Ölmann, U., 2005. MUFTE-UG: Structure, Applications and Numerical Methods. Newsletter 23 (2), Colorado School of Mine, International Groundwater Modeling Centre, Golden, Colorado, U.S.A., http://igwmc.mines.edu/news/.

Aziz, K., Settari, A., 1979. Petroleum Reservoir Simulation. Elsevier, Amsterdam, The Netherlands.

Bachu, S., 2003. Screening and ranking of sedimentary basins for sequestration of CO2 in geological media in response to climate change. Environmental Geology 44 (3), 277–289.

Bachu, S., Bonijoly, D., Bradshaw, J., Burruss, R., Holloway, S., Christensen, N., Mathiassen, O., 2007. CO_2 storage capacity estimation: methodology and gaps. International Journal of Greenhouse Gas Control 1 (4), 430–443.

Baehr, H., Stephan, K., 1998. Wärme und Stoffübertragung. Springer, Berlin, Germany.

Barenblatt, G., Entov, V. M., Ryzhik, V. M., 1990. Theory of Fluid Flows Through Natural Rocks. Springer, Dordrecht, The Netherlands.

Bastian, P., Birken, K., Johannsen, K., Lang, S., Eckstein, K., Neuss, N., Rentz-Reichert, H., Wieners, C., 1997. UG - A Flexible Software Toolbox for Solving Partial Differential Equations. Computing and Visualization in Science, 1(1), 27–40.

Bastian, P., Helmig, R., 1999. Efficient Fully-Coupled Solution Techniques for Two Phase Flow in Porous Media. Parallel Multigrid Solution and Large Scale Computations. Advances in Water Resources 23, 199–216.

Batzle, M., Wang, Z., 1992. Seismic Properties of Pore Fluids. Geophysics 57, 1396–1408.

Bear, J., 1972. Dynamics of Fluids in Porous Media. Dover, New York, U.S.A.

Bennion, B., Bachu, S., 2005. Relative Permeability Characteristics for Supercritical CO_2 Displacing Water in a Variety of Potential Sequestration Zones in the Western Canada Sedimentary Basin. Society of Petroleum Engineers, SPE 95547, http://www.spe.org.

Bennion, B., Bachu, S., 2006. The Impact of Interfacial Tension and Pore Size Distribution/Capillary Pressure Character on CO_2 Relative Permeability at Reservoir Conditions in CO_2-Brine Systems. Society of Petroleum Engineers, SPE 99325, http://www.spe.org.

Bennion, B., Bachu, S., 2008. Drainage and Imbibition Relative Permeability Relationships for Supercritical CO_2/Brine and H_2S/Brine Systems in Intergranular Sandstone, Carbonate, Shale, and Anhydrite Rocks. SPE Reservoir Evaluation and Engineering 11 (3), 487–496.

Benson, S., 2005. Lessons learned from industrial and natural analogs for health, safety and environmental risk assessment for geologic storage of carbon dioxide. Carbon Dioxide Capture for Storage in Deep Geologic Formations - Results from the CO_2 Capture Project, Chapter 25, 1133–1141, Lawrence Berkeley National Laboratory, Berkeley, California, U.S.A.

Benson, S., Hepple, R., Apps, J., Tsang, C., Lippmann, M., 2005. Lessons Learned from Natural and Industrial Analogues for Storage of Carbon Dioxide in Deep Geological Formations. Energy Citations Database, Report Number LBNL–51170, Lawrence Berkeley National Laboratory, Berkeley, California, U.S.A., http://repositories.cdlib.org/lbnl/LBNL-51170/.

Bielinski, A., 2006. Numerical Simulation of CO_2 Sequestration in Geological Formations. Ph.D. thesis, Institut für Wasserbau, Universität Stuttgart, Germany, Mitteilungsheft Nr. 155, http://elib.uni-stuttgart.de/opus/frontdoor.php?source_opus=2953&la=de.

Brooks, A., Corey, A., 1964. Hydraulic Properties of Porous Media. Colorado State University Hydrology Paper No.3, Fort Collins, Colorado, U.S.A.

Buckingham, E., 1914. On Physically Similar Systems: Illustrations of the Use of Dimensional Analysis. Physical Review 4, 107–116.

Buckley, S., Leverett, M., 1942. Mechanism of Fluid Displacements in Sands. Transactions of the AIME 146, 107–116.

Burdine, N., 1953. Relative Permeability Calculations from Pore–Size Distribution Data. American Institute of Mining, Metallurgical and Petroleum Engineers, Petroleum Transactions 198, 71–77.

Campolongo, F., Braddock, R., 1999. The use of graph theory in the sensitivity analysis of the model output: a second order screening method. Reliability Engineering and System Safety 64, 1–12.

Campolongo, F., Cariboni, J., Saltelli, A., Schouters, W., 2004. Enhancing the Morris Method. Hanson, M.K. and Hemez, F.M. (Editors): 4^{th} International Conference on Sensitivity Analysis of Model Output, Los Alamos National

Laboratory, Santa Fe, New Mexico, U.S.A., 369–379, http://library.lanl.gov/cgi-bin/getdoc?event=SAMO2004&document=samo04-52.pdf.

Campolongo, F., Tarantola, S., Saltelli, A., 1999. Tackling quantitatively large dimensionality problems. Computer Physics Communications 117, 75–85.

Celia, M., Bachu, S., 2003. Geological Sequestration of CO_2: Is Leakage Unavoidable and Acceptable? Gale, J. and Kaya, Y. (Editors): 6^{th} International Conference on Greenhouse Gas Control Technologies (GHGT-6), Kyoto, Japan, Sept. 30^{st}–Oct. 4^{th}, 477–482.

Celia, M., Bachu, S., Nordbotten, J., Gasda, S., Dahle, H., 2004. Quantitative Estimation of CO_2 Leakage from Geological Storage: Analytical Models, Numerical Models, and Data Needs. Rubin, E.S. and Keith, D.W. and Gilboy, C.F. (Editors): 7^{th} International Conference on Greenhouse Gas Control Technologies (GHGT-7), Vancouver, Canada, Sept. 5^{th}–9^{th}, p. 9, http://www.ieagreen.org.uk/ghgt7.html.

Chadwick, A., Arts, R., Bernstone, C., May, F., Thibeau, S., Zweigel, P., 2008. Best Practice for the Storage of CO_2 in Saline Aquifers - Observations and Guidelines from the SACS and CO2STORE projects. British Geological Survey Occasional Publication, 14, Nottingham, U.K., http://www.bgs.ac.uk/.

Chen, Z., Ewing, R., 1997. Comparison of Various Formulatios of Three-Phase Flow in Porous Media. Journal of Computational Physics 132, 362–373.

Class, H., 2001. Theorie und numerische Modellierung nichtisothermer Mehrphasenprozesse in NAPL-kontaminierten porösen Medien. Ph.d. thesis, Institut für Wasserbau, Universität Stuttgart, Germany, Mitteilungsheft Nr. 105, http://elib.uni-stuttgart.de/opus/frontdoor.php?source_opus=2436&la=de.

Class, H., 2008. Models for Non-Isothermal Compositional Gas-Liquid Flow and Transport in Porous Media. Habilitation, Institut für Wasserbau, Universität Stuttgart, Germany, http://elib.uni-stuttgart.de/opus/frontdoor.php?source_opus=3847&la=de.

Class, H., Helmig, R., Bastian, P., 2002. Numerical simulation of non–isothermal multiphase multicomponent processes in porous media. - 1. An efficient solution technique. Advances in Water Resources 25, 533–550.

Clauser, C., 1992. Permeability of crystalline rocks. EOS Transactions 73, 233.

Clauser, C., 2003. Numerical Simulation of Reactive Flow in Hot Aquifers, SHEMAT and Processing SHEMAT. Springer, Berlin.

Clauser, C., 2006. Geothermal Energy, In: K. Heinloth (Editor), GroupVIII: Advanced Materials and Technologies, Vol. 3: Energy Technologies, Subvol. C: Renewable energies Edition. Landolt-Börnstein, Springer, Heidelberg.

Clauser, C., Huenges, E., 1995. Thermal Conductivity of Rocks and Minerals, In: T.J. Ahrens (Editor), Rock Physics and Phase Relations - a Handbook of Physical Constants, AGU Reference Shelf Edition. Vol. 3. American Geophysical Union, Washington.

CO2SINK project consortium, 2009. CO2SINK - In-situ R&D laboratory for geological storage of CO_2,
http://www.co2sink.org.

Cropp, R., Braddock, R., 2002. The New Morris Method: an efficient second-order screening method. Reliability Engineering and System Safety 78, 77–83.

Darcy, H., 1856. Les Fontaines Publiques de la Ville de Dijon. Dalmont, Paris, France.

Daubert, T., Danner, R., 1989. Physical and thermodynamic properties of pure chemicals: data compilation. Hemisphere, New York, U.S.A.

Doughty, C., 2007. Modeling geologic storage of carbon dioxide: Comparison of non-hysteretic and hysteretic characteristic curves. Energy Conversion and Management 48(6), 1768–1781.

Doughty, C., Pruess, K., Benson, S., Hovorka, S., Knox, P., Green, C., 2001. Capacity investigation of brine-bearing sands of the Frio-Formation for geological sequestration of CO_2. Paper LBNL-48176, Lawrence Berkeley National Laboratory, Berkeley, Ca, U.S.A., http://repositories.cdlib.org/lbnl/LBNL-48176.

Duan, Z., Sun, R., 2003. An Improved Model Calculating CO_2 Solubility in Pure Water and Aqueous NaCl Solutions from 273 to 533 K and from 0 to 2000 bar. Chem. Geol. 193, 257–271.

Ebigbo, A., Class, H., Helmig, R., 2007. CO_2 leakage through an abandoned well: problem-oriented benchmarks. Computational Geosciences 11(2), 103–115.

Ellert, M., Grønager, M., Konstantinov, A., Konya, B., Lindemann, J., Livenson, I., Nielsen, J. L., Niinimäki, M., Smirnova, O., Wäänänen, A., 2007. Advanced Resource Connector middleware for lightweight computational Grids. Future Generation Computer Systems 23, 219–240.

Fenghour, A., Wakeham, W., Vesovic, V., 1998. The Viscosity of Carbon Dioxide. Journal of Physical and Chemical Reference Data 27(1), 31–44.

Flett, M., Gurton, R., Taggart, I., 2005. The function of gas-water relative permeability hysteresis in the sequestration of carbon dioxide in saline formations. Society of Petroleum Engineers SPE 88485-MS, http://www.spe.org/.

Flett, M., Gurton, R., Weir, G., 2007. Heterogeneous saline formations for carbon dioxide disposal: Impact of varying heterogeneity on containment and trapping. Journal of Petroleum Science and Engineering 57(1-2), 106–118.

Friedmann, S., 2007. Site Characterization and Selection Guidelines for Geological Carbon Sequestration. Report for U.S. Department of Energy by Lawrence Livermore National Laboratory, Livermore, California, U.S.A., Contract No. W-7405-Eng-48, http://www.osti.gov/bridge//product.biblio.jsp?query_id=0&page=0&osti_id=915602.

Garcia, J., 2001. Density of Aqueous Solutions of CO_2. Tech. rep., LBNL Report 49023, Lawrence Berkeley National Laboratory, Berkeley, California, U.S.A., http://repositories.cdlib.org/lbnl/LBNL-49023/.

Garcia, J., Pruess, K., 2003. Flow Instabilities During Injection of CO_2 into Saline Aquifers. Tech. rep., Lawrence Berkeley National Laboratory, California, U.S.A., Paper LBNL-57973, http://repositories.cdlib.org/lbnl/LBNL-57973.

Garcia, J. E., 2003. Fluid Dynamics of Carbon Dioxide Disposal into Saline Aquifers. Ph.D. thesis, Lawrence Berkeley National Laboratory, California, U.S.A.

Gasda, S., Bachu, S., Celia, M., 2004. The potential for CO_2 leakage from storage sites in geological media: analysis of well distribution in mature sedimentary basins. Environmental Geology 46(6–7), 707—-720.

Gaus, I., Audigane, P., André, L., Lions, J., Jacquemet, N., Durst, P., Czernichowski-Lauriol, I., Azaroual, M., 2008. Geochemical and solute transport modelling for CO_2 storage, what to expect from it? International Journal of Greenhouse Gas Control 2(4), 605–625.

Gherardi, F., Xu, T., Pruess, K., 2007. Numerical modeling of self-limiting and self-enhancing caprock alteration induced by CO_2 storage in a depleted gas reservoir. Chemical Geology 244, 103–129.

Gudmundsson, J., Thrainsson, H., 1989. Power potential of two-phase geothermal wells. Geothermics 18(3), 357–366.

Gunter, W., Wiwchar, B., Perkins, E., 1997. Aquifer disposal of CO_2-rich greenhouse gases: extension of the time scale of experiments for CO_2-sequestering reactions by geochemical modelling. Mineralogy and Petrology 59, 121–140.

Helmig, R., 1997. Multiphase flow and transport processes in the subsurface. Springer, Berlin, Germany.

Helmig, R., Class, H., Huber, R., Sheta, H., Ewing, R., Hinkelmann, R., Jakobs, H., Bastian, P., 1998. Architecture of the Modular Program System MUFTE_UG for Simulating Multiphase Flow and Transport Processes in Heterogeneous Porous Media. Mathematische Geologie 2, 123–131.

Hesse, M., Orr, F., Tchelepi, H., 2008. Gravity Currents with Residual Trapping. Journal of Fluid Mechanics 611, 35–60.

Hilfer, R., Øren, P., 1996. Dimensional analysis of pore scale and field scale immiscible displacement. Transport in Porous Media 22, 53–72.

Holtz, M., 2002. Residual Gas Saturation to Aquifer Influx: A Calculation Method for 3-D Computer Reservoir Model Construction. SPE 75503, paper presented at the SPE Gas Technology Symposium held in Calgary, Alberta, Canada, April 30st–May 2nd, http://www.spe.org/.

Hovorka, S., Benson, S., Doughty, C., Freifeld, B., Sakurai, S., Daley, T., Kharaka, Y., Holtz, M., Trautz, R., Seay Nance, H., Myer, L., Knauss, K., 2006. Measuring Permanence of CO_2 Storage in Saline Formations: the Frio Experiment. Environmental Geosciences 13, 105–121.

Huber, R., Helmig, R., 1999. Multiphase Flow in Heterogeneous Porous Media: A Classical Finite Element Method versus an Implicit Pressure - Explicit Saturation-based Mixed Finite Element - Finite Volume Approach. International Journal for Numerical Methods in Fluids 29, 899–920.

IAPWS, 1997. Industrial Formulation 1997 for the Thermodynamic Properties of Water and Steam, International Association for the Properties of Water and Steam. http://www.iapws.org/.

Ide, S., Jessen, K., Orr, F., 2007. Storage of CO_2 in saline aquifers: Effects of gravity, viscous, and capillary forces on amount and timing of trapping. International Journal of Greenhouse Gas Control 1, 481–491.

International Energy Agency Greenhouse Gas R&D Programme, 2008. Aquifer Storage – Development Issues. Report No. 2008/12, Cheltenham, U.K.

IPCC, 2005. IPCC Special Report on Carbon Dioxide Capture and Storage. Metz, B., Davidson, O., de Coninck, H.C., Loos, M., Meyer, L.A. (Editors): Prepared by Working Group III of the Intergovernmental Panel on Climate Change, Cambridge University Press, Cambridge, U.K., http://www.ipcc.ch/ipccreports/special-reports.htm.

Johannsen, K., Oswald, S., Held, R., Kinzelbach, W., 2006. Numerical simulation of three-dimensional saltwater-freshwater fingering instabilities observed in a porous medium. Advances in Water Resources 29 (11), 1690–1704.

Johannsen, K., Tourunen, O., Kleist, J., 2008. The CO2-Community Grid. http://wiki.ndgf.org/display/ndgfwiki/CO2.

Joint Research Centre of the European Commission, 2004. SIMLAB package Version 2.2, a simulation environment for sensitivity analysis. Econometrics and Applied Statistics Unit (EAS), Ispra, Italy, http://simlab.jrc.ec.europa.eu.

Juanes, R., Spiteri, E., Orr, F., Blunt, M., 2006. Impact of relative permeability hysteresis on geological CO_2 storage. Water Resources Research 42 (12).

Kaplan, S., 1997. The Words of Risk Analysis. Risk Analysis 17 (4), 407–408.

Kobus, H., Barczewski, B., Koschitzky, H., 1996. Groundwater and Subsurface Remediation. Springer, Berlin.

Kopp, A., Class, H., Helmig, R., 2007. Sensitivity Analysis of CO_2 Injection Processes in Brine Aquifers. Presentation given at European Geosciences Union (EGU) General Assembly, April 18th, Vienna, Austria.

Kopp, A., Class, H., Helmig, R., 2009a. Investigations on CO_2 storage capacity in saline aquifers - Part 1: Dimensional analysis of flow processes and reservoir characteristics. International Journal of Greenhouse Gas Control, 3(3), 263–276.

Kopp, A., Class, H., Helmig, R., 2009b. Investigations on CO_2 storage capacity in saline aquifers - Part 2: Estimation of storage capacity coefficients. International Journal of Greenhouse Gas Control, 3(3), 277–287.

Kühn, M., Clauser, C., 2006. Mineralische Bindung von CO_2 bei der Speicherung im Untergrund in geothermischen Reservoiren. Chemie Ingenieur Technik 78(4), Special Issue: Kohlendioxid und Klimaschutz, 425–434.

Kvamme, B., Kuznetsova, T., Hebach, A., Oberhof, A., Lunde, E., 2007. Measurements and modelling of interfacial tension for water+carbon dioxide systems at elevated pressures. Journal of Computational Materials Science 38, 506–513.

Laha, I. M. R. G., Chakravarti, J. R., 1967. Handbook of Methods of Applied Statistics, Volume I. John Wiley and Sons, Hoboken, New York, U.S.A.

Lake, L., 1989. Enhanced Oil Recovery. Prentice Hall Inc., Old Tappan, New York, U.S.A.

Le Gallo, Y., Trenty, L., Michel, A., Vidal-Gilbert, S., Parra, T., Jeannin, L., 2006. Long-term flow simulations of CO_2 storage in saline aquifers. Gale, J. and Bolland, O. (Editors): 8th International Conference on Greenhouse Gas Control Technologies (GHGT-8), Trondheim, Norway, June 19th–22nd, p. 6, http://www.ieagreen.org.uk/ghgt8.html.

Leicht, F., 2007. Investigations of Carbon Dioxide Storage Capacity in Saline Aquifers. Diploma Thesis, Institute of Hydraulic Engineering, University Stuttgart, Stuttgart, Germany, http://www.hydrosys.uni-stuttgart.de/publikationen/ausgabe.php?diplom=1&betreuer=21.

LeVeque, R., 1992. Numerical Methods for Conservation Laws. Birkhäuser, Basel, Switzerland.

Li, Z., Dong, M., Li, S., Huang, S., 2006. CO_2 sequestration in depleted oil and gas reservoirs — caprock characterization and storage capacity. Energy and Conversion and Managment 47, 1372–1382.

Lüdecke, C., Lüdecke, D., 2000. Thermodynamik. Springer, Berlin, Germany.

Manthey, S., Hassanizadeh, S., Helmig, R., Hilfer, R., 2008. Dimensional analysis of two-phase flow including a rate-dependent capillary pressure–saturation relationship. Advances in Water Resources 31(9), 1137–1150.

Marland, G., Andres, B., Boden, T., 2008. Global CO_2 Emissions from Fossil-Fuel Burning, Cement Manufacture, and Gas Flaring: 1751-2005. The Carbon Dioxide Information Analysis Center (CDIAC), Oak Ridge National Laboratory, Oak Ridge, Tennessee, U.S.A., http://cdiac.ornl.gov.

Maul, P., Metcalf, R., Pearce, J., Savage, D., West, J., 2007. Performance assessment for the geologic storage of carbon dioxide: Learning from the radioactive waste disposal experience. International Journal of Greenhouse Gas Control 1, 444–455.

Michaelides, E., 1981. Thermodynamic properties of geothermal fluids. Geothermal Resources Council Transactions 5, 361–364.

Miller, C., Christakos, G., Imhoff, P., McBride, J., Pedit, J., Trangenstein, J., 1996. Multiphase flow and transport modeling in heterogeneous porous media: challenges and approaches. Advances in Water Resources 21(2), 77–120.

Mito, S., Xue, Z., Ohsumi, T., 2008. Case study of geochemical reactions at the Nagaoka CO_2 injection site, Japan. International Journal of Greenhouse Gas Control 2, 309–318.

Morris, M., 1991. Factorial Sampling Plans for Preliminary Computational Experiments. Technometrics 33(2), 161–174.

Mosthaf, K., 2007. CO_2 Storage into Dipped Saline Aquifers Including Ambient Water Flow. Diploma Thesis, Institute of Hydraulic Engineering, University Stuttgart, Stuttgart, Germany, http://www.iws.uni-stuttgart.de/publikationen/ausgabe.php?person=1&autor[0]=1195.

Nagaoka project consortium, 2009. Research Institute of Innovative Technogoly for the Earth, CO_2 Sequestration Research Group, Kizugawadai, Kizugawa-shi, Kyoto, Japan, http://www.rite.or.jp/English/lab/geological/geological.html.

NDGF, 2008. Nordic Data Grid Facility. Copenhagen, Denmark, http://www.ndgf.org.

NETL, 2007. Carbon Sequestration Atlas of the United States and Canada. U.S. Department of Energy - National Energy Technology Laboratory, Pittsburgh, Pennsylvania, U.S.A., http://www.netl.doe.gov/technologies/carbon_seq/refshelf/atlasII/index.html.

NETL, 2009. Regional Carbon Sequestration Partnerships. U.S. Department of Energy - National Energy Technology Laboratory, Pittsburgh, Pennsylvania, U.S.A., http://www.netl.doe.gov/technologies/carbon_seq/partnerships/partnerships.html.

Nordbotten, J., Celia, M., Bachu, S., 2004. Analytical Solutions for Leakage Rates through Abandoned Wells. Water Resources Research 40(4), W04204.

Nordbotten, J., Celia, M., Bachu, S., 2005a. Injection and Storage of CO_2 in Deep Saline Aquifers: Analytical Solution for CO_2 Plume Evolution During Injection. Transport in Porous Media 58(3), 339–360.

Nordbotten, J., Celia, M., Bachu, S., Dahle, H., 2005b. Semi-Analytical Solution for CO_2 Leakage through an Abandoned Well. Environmental Science and Technology 39(2), 602–611.

NPC, 1984. U.S. National Petroleum Council Public Database. Washington D.C., U.S.A., http://www.netl.doe.gov/technologies/oil-gas/Software/database.html.

Ochs, S., 2006. Steam injection into saturated porous media - process analysis including experimental and numerical investigations -. Ph.D. thesis, Universität Stuttgart, Stuttgart, Germany, Mitteilungsheft Nr. 159, http://elib.uni-stuttgart.de/opus/frontdoor.php?source_opus=2971&la=de,.

Oldenburg, C., 2007. Screening and ranking framework for geologic CO_2 storage site selection on the basis of health, safety, and environmental risk. Environmental Geology 54 (8), 1687–1694.

Pacala, S., 2003. Global constraints on reservoir leakage. Gale, J. and Kaya, Y. (Editors): 6^{th} International Conference on Greenhouse Gas Control Technologies (GHGT-6), Kyoto, Japan, Sept. 30^{st}–Oct. 4^{th}, 267–272.

Pacala, S., Socolow, R., 2004. Stabilization Wedges: Solving the Climate Problem for the Next 50 Years with Current Technologies. Science 305, 968–972.

Pape, H., Clauser, C., Iffland, J., 1999. Permeability prediction based on fractal pore-space geometry. Geophysics 64(5), 1447–1460.

Peng, D.-Y., Robinson, D. B., 1976. A New Two-Constant Equation of State. Industrial and Engineering Chemistry Fundamentals 15, 59–64.

Plug, W.-J., Bruining, J., 2007. Capillary pressure for the sand-CO_2-water system under various pressure conditions. Application to CO_2 sequestration. Advances in Water Resources 30 (11), 2339–2353.

Probst, P., 2008. Numerical Simulations of CO_2 Injection into Saline Aquifers: Estimation of Storage Capacity and Arrival Times using Multiple Realizations of Heterogeneous Permeability Fields. Diploma Thesis, Institute of Hydraulic Engineering, University Stuttgart, Stuttgart, Germany, http://www.iws.uni-stuttgart.de/publikationen/ausgabe.php?diplom=1&betreuer=484.

Pruess, K., 2008a. Leakage of CO_2 from geologic storage: Role of secondary accumulation at shallow depth. International Journal of Greenhouse Gas Control 2, 37–46.

Pruess, K., 2008b. On CO_2 fluid flow and heat transfer behavior in the subsurface, following leakage from a geologic storage reservoir. Environmental Geology 54, 1677–1686.

Pruess, K., Bielinski, A., Ennis-King, J., Fabriol, R., Le Gallo, Y., Garcia, J., Jessen, K., Kovscek, T., Law, D.-S., Lichtner, P., Oldenburg, C., Pawar, R., Rutqvist, J., Steefel, C., Travis, B., Tsang, C.-F., White, S., Xu, T., 2003. Code Intercomparison Builds Confidence in Numerical Models for Geologic Disposal of CO2. Gale, J. and Kaya, Y. (Editors): 6^{th} International Conference on Greenhouse Gas Control Technologies (GHGT-6), Kyoto, Japan, Sept. 30^{st}–Oct. 4^{th}, 463–470.

Rosenbauer, R., Koksalan, T., Palandri, J., 2005. Experimental investigation of CO_2–brine–rock interactions at elevated temperature and pressure: Implications for CO_2 sequestration in deep-saline aquifers. Fuel Processing Technology 86, 1581–1597.

Rutqvist, J., Birkholzer, J., Tsang, C.-F., 2008. Coupled reservoir–geomechanical analysis of the potential for tensile and shear failure associated with CO_2 injection in multilayered reservoir–caprock systems. International Journal of Rock Mechanics and Mining Sciences 45(2), 132–143.

Saltelli, A., Chan, K., Scott, E. M. (Eds.), 2000. Sensitivity Analysis. John Wiley & Sons, Chichester, U.K.

Scheidegger, A. E., 1960. The physics of flow through porous media. Macmillan Co., New York, U.S.A.

Somerton, W., El-Shaarani, A., Mobarak, S., 1974. High Temperature Behaviour of Rocks Associated with Geothermal Type Reservoirs. SPE-4897-MS, paper presented at the SPE California Regional Meeting, 4^{th}–5^{th} April, San Francisco, California, U.S.A., http://www.spe.org/.

Span, R., Wagner, W., 1996. A New Equation of State for Carbon Dioxide Covering the Fluid Region from the Triple–Point Temperature to 1100 K at Pressures up to 800 MPa. Journal of Physical and Chemical Reference Data 25(6), 1509–1596.

Spiteri, E., Juanes, R., Blunt, M., Orr, F., 2005. Relative-Permeability Hysteresis: Trapping Models and Application to Geological CO_2 Sequestration. SPE 96448-MS, paper presented at the Annual Technical Conference and Exhibition, 9^{th}–12^{th} October, Dallas, Texas, U.S.A., http://www.spe.org/.

Spiteri, E., Juanes, R., Blunt, M., Orr, F., 2008. A New Model of Trapping and Relative Permeability Hysteresis for All Wettability Characteristics. Society of Petroleum Engineers Journal 13(3), 277–288.

Stern, N., 2007. The Economics of Climate Change: The Stern Review. Cambridge University Press, Cambridge, U.K.

Torp, T., Gale, J., 2004. Demonstrating storage of CO_2 in geological reservoirs: The Sleipner and SACS projects. Energy 29 (9–10), 1361–1369.

United Nations Framework Convention on Climate Change, 1997. The Kyoto Protocol. The Climate Change Secretariat, Bonn, Germany, http://unfccc.int/kyoto_protocol/items/2830.php.

Van Der Waals, J. D., 1873. Over de continuiteit van den gas- en vloeistoftoestand. Ph.D. thesis, Universiteit Leiden, Leiden, The Netherlands.

Van Genuchten, M., 1980. A closed-form equation for predicting the hydraulic conductivity of unsaturated soils. Soil Science Society of America Journal 44, 892–898.

Xu, T., Apps, J., Pruess, K., Yamamoto, H., 2007. Numerical modeling of injection and mineral trapping of CO_2 with H_2S and SO_2 in a sandstone formation. Chemical Geology, 242, 319–346.

Xu, T., Pruess, K., 1998. Coupled modeling of nonisothermal multiphase flow, solute transport and reactive chemistry in porous and fractured media: 1. Model development and validation. Report Number LBNL–42050, Lawrence Berkeley National Laboratory, Berkeley, California, U.S.A., http://repositories.cdlib.org/lbnl/LBNL-42050/.

A Mathematical and Numerical Model

A.1 Mathematical Model for Multi-Phase Processes - the 2p-module

The Reynolds transport theorem is used to formulate the basic conservation laws of mass and momentum. The theorem states that the change of an extensive property E with time is equal to the change of quantity e (where e is the appropriate intensive property [E per mass]) within the control volume over time plus the net rate of change across the boundaries of the control volume

$$\frac{dE}{dt} = \int_{\Omega} \frac{\partial(\varrho\, e)}{\partial t}\, d\Omega + \int_{\Gamma} (\varrho\, e)(\mathbf{v}\cdot\mathbf{n})\, d\Gamma, \tag{A.1}$$

where Ω is the control volume domain and Γ is the control volume boundary. The vector $\mathbf{n}$ is normal to the boundary Γ of the control volume domain.

A.1.1 Conservation of Mass and Momentum

Conservation of Mass

Applying the Reynolds transport theorem for mass as the extensive property, i.e. $E = m$ and therefore $e = 1$, applying the Green-Gaussian integral rule $\int_\Gamma \varrho(\mathbf{v}\cdot\mathbf{n})\, d\Gamma = \int_\Omega \nabla\cdot(\varrho\mathbf{v})\, d\Omega$ (e.g Helmig (1997)) and considering an infinitesimally small control volume yields a formulation for the mass conservation in differential form:

$$\frac{\partial \varrho}{\partial t} + \nabla\cdot(\varrho\,\mathbf{v}) = 0. \tag{A.2}$$

Conservation of Momentum

The momentum conservation is set up by inserting $(m\mathbf{v})$ for the extensive property E (consequently $e = \mathbf{v}$). When applying Newton's second law, i.e. the rate of change of momentum $(\frac{dE}{dt})$ is equal to the external forces $(\sum F)$ exerted upon the system, and the Green-Gaussian integral rule $\int_\Gamma (\varrho\,\mathbf{v})(\mathbf{v}\cdot\mathbf{n})\, d\Gamma = \int_\Omega \nabla\cdot(\varrho\mathbf{v}\cdot\mathbf{v})\, d\Omega$ is applied, the momentum conservation reads in differential form:

$$\frac{d(\varrho\,\mathbf{v})}{dt} + \nabla\cdot(\varrho\,\mathbf{v}\cdot\mathbf{v}) = \frac{\sum F}{V}, \tag{A.3}$$

where V is the volume of the domain Ω. Equation A.3 is valid for describing the momentum conservation of any fluid on the microscale. On the macroscale however, the multi-phase extension of the empirically derived Darcy law (Equation 2.30) is used to calculate the phase velocity $\mathbf{v}_\alpha$. The advantage is that the phase velocity is explicitly given and can be inserted into the mass balance equation (Equation A.4).

A.1.2 Mass Balance Equations

In porous media, only the pore space is available for fluid flow. This pore space is occupied by several fluid phases α. Here, a water phase (w) and a CO_2 phase (CO_2) are considered. The storage term in Equation A.2 is extended by the porosity ϕ and the phase saturations S_α. A term q_α is included to account for sources and sinks and the multi-phase extension of the Darcy's law (Equation 2.30) is used to describe the phase velocities $\mathbf{v}_\alpha$, leading to:

$$\frac{\partial(\phi\, S_\alpha\, \varrho_\alpha)}{\partial t} + \nabla \cdot (\varrho_\alpha\, \mathbf{v}_\alpha) - q_\alpha = 0, \qquad \alpha \in \{\mathrm{w}, \mathrm{CO_2}\}. \tag{A.4}$$

A.1.3 Closure Relations

To solve the balance equations, it is necessary to consider a number of closure relations. According to Miller et al. (1996), closure relations include a number of simplifying assumptions, equations of state, constitutive relations, and auxiliary conditions.

Simplifying Assumptions
The accurate solution of any multi-phase system in a porous medium would result in a large system of balance equations. The computational cost of the solution of such a large system is very high and simplifying assumptions can be made to reduce the cost. It is of importance to make these assumptions without reducing the accuracy of the model considerably. In the context of this study, it can be assumed that the solid phase (the porous media) is rigid (thus $\frac{\partial \phi}{\partial t} = 0$), immobile, and inert.

Furthermore, different components are lumped to a pseudo-component with average properties. This is to reduce the total number of components and thus the number of balance equations. In the context of this study, it is assumed that only pure CO_2 is injected into the geological formation and impurities are of minor importance. The chemical substances of the water-rich phase (except CO_2) are lumped to a water pseudo component (water and salt, i.e. sodium chloride (NaCl) equivalent).

Local thermodynamic equilibrium is assumed, i.e. local thermal, mechanical, and chemical equilibrium (cf. Section 2.2.5). However, thermal and chemical equilibrium is not of importance in this module, since temperature effects are neglected (no energy balance is solved) and mass transfer between the phases is also neglected (mutual dissolution of components

is not considered). Thus, only mechanical equilibrium is valid here as the capillary pressure difference between the phases on the macroscale is considered. This will be different for the non-isothermal multi-phase multi-component model (Section A.2).

Equation of State
The equation of state for a pure substance is a mathematical formulation describing the equilibrium relationship between pressure, temperature, and volume. The equation of state for the system considered here is discussed in Section 2.1.4.

Constitutive Relations
Typical constitutive relations for multi-phase systems include the capillary pressure-saturation relations and the relative permeability-saturation relations (cf. Section 2.2.4). These relations are typically of empirical nature; thus, they are most often only approximate and uncertain.

Auxiliary Conditions
Auxiliary conditions are necessary to close the system of equations and result directly from the definitions of saturation (Equation 2.6) and of the capillary pressure relation on the macroscale (Equation 2.23) already known. This means phase saturations have to add up to one and the phase pressure of one phase can be calculated from the phase pressure of the respective other phase and the capillary pressure (which is a function of saturation on the macroscale).

A.1.4 Primary Variables

The set of balance equations (Equation A.4) and closure relations is solved for the independent unknowns, the so-called "primary variables". Knowing these primary variables allows the calculation of all other variables of the system. For the two-phase system considered here the solution of two independent primary variables is necessary. These variables are the water phase pressure p_{w} and the CO_2 phase saturation S_{CO2}.

A.2 Mathematical Model for Non-Isothermal Multi-Phase Multi-Component Processes - the 2p2cni-module

As for the multi-phase model (Section A.1), the Reynolds transport theorem (Equation A.1) is used to formulate the basic conservation laws for the non-isothermal multi-phase multi-component model. Here, it is also applied to the conservation of energy.

A.2.1 Conservation of Mass, Momentum, and Energy

The conservation laws for mass and momentum as derived in Section A.1.1 remain valid here.

Conservation of Energy
The first law of thermodynamics states that the energy in a closed system is conserved (Baehr and Stephan, 1998). Mathematically expressed, this means that the change in the internal energy (dU) is equal to the amount of energy added by heating (Q) plus the amount of energy added by doing work on the system (dW):

$$dU = dQ + dW. \tag{A.5}$$

Applying the Reynolds transport theorem (Equation A.1) for internal energy as the extensive property, i.e. $E = U$ and $e = u$, yields:

$$\frac{dU}{dt} = \int\limits_{\Omega} \frac{\partial(\varrho\, u)}{\partial t} d\Omega + \int\limits_{\Gamma} (\varrho\, u)(\mathbf{v} \cdot \mathbf{n})\, d\Gamma = \frac{dQ}{dt} + \frac{dW}{dt}. \tag{A.6}$$

A heat flux over the system boundaries may result from radiation and heat conduction only. However, when radiation due to small temperature gradients in the subsurface is neglected, the heat flux term reads as follows:

$$\frac{dQ}{dt} = -\int\limits_{\Gamma} (\mathbf{q}_{\mathrm{h}} \cdot \mathbf{n})\, d\Gamma. \tag{A.7}$$

Applying the Green-Gaussian integral rule $\int_\Gamma (\mathbf{q}_{\mathrm{h}} \cdot \mathbf{n})\, d\Gamma = \int_\Omega \nabla \cdot \mathbf{q}_{\mathrm{h}}\, d\Omega$ (Helmig, 1997) and inserting Fourier's law (Equation 2.38) for the heat conduction $\mathbf{q}_{\mathrm{h}}$ leads to:

$$\frac{dQ}{dt} = \int\limits_{\Omega} \nabla \cdot (\lambda_{\mathrm{i}}\, \nabla T)\, d\Omega. \tag{A.8}$$

The change of internal energy due to the amount of energy added by doing work can either result from dissipative work or from volume-changing work. Due to small flow velocities

dissipative work can be neglected and volume-changing work is then expressed as (Ochs, 2006):

$$\frac{dW}{dt} = -\int_{\Omega} \nabla \cdot (p\,\mathbf{v})\, d\Omega. \tag{A.9}$$

Following application of the Green-Gaussian integral rule $\int_{\Gamma}(\varrho\, u)(\mathbf{v}\cdot\mathbf{n})\, d\Gamma = \int_{\Omega} \nabla\cdot(\varrho\, u\, \mathbf{v})\, d\Omega$, and insertion of Equations A.8 and A.9 into Equation A.6, energy conservation is expressed as:

$$\frac{dU}{dt} = \int_{\Omega} \frac{\partial(\varrho\, u)}{\partial t}\, d\Omega + \int_{\Omega} \nabla \cdot (\varrho\, u\, \mathbf{v})\, d\Omega = \int_{\Omega} \nabla\cdot\big(\lambda_{\mathrm{i}}\, \nabla T\big)\, d\Omega - \int_{\Omega} \nabla \cdot (p\,\mathbf{v})\, d\Omega. \tag{A.10}$$

When the definition of the specific enthalpy $h = u + \frac{p}{\varrho}$ (Equation 2.15) is inserted, energy conservation can be written in differential form as:

$$\frac{\partial(\varrho\, u)}{\partial t} + \nabla \cdot (\varrho\, h\, \mathbf{v}) - \nabla\cdot\big(\lambda_{\mathrm{i}}\, \nabla T\big) = 0. \tag{A.11}$$

A.2.2 Mass Balance Equations

To account for mass-transfer processes of the components between the phases, it is advantageous to formulate the mass balance equations (Equation A.4) derived for multi-phase flow in porous media (without mass-transfer processes) for each component (Class (2001), Class et al. (2002)). An extra variable is introduced into the equations, X^{C}_{α}, representing the mass fraction of component C in phase α. The component C refers to CO_2 and water, whereas the phase α includes a water-rich phase and a CO_2-rich phase. When a rigid porous media ($\frac{\partial \phi}{\partial t} = 0$)is considered, and a term to account for the diffusion of the components in the water-rich phase (cf. Section 2.3.3) is included, the mass balance equations can be written as:

$$\begin{aligned}
&\underbrace{\phi \frac{\partial\Big(\sum_{\alpha}(\varrho_{\alpha}\, X^{\mathrm{C}}_{\alpha}\, S_{\alpha})\Big)}{\partial t}}_{\text{storage}} \\
&- \underbrace{\sum_{\alpha} \nabla\cdot\Big(\varrho_{\alpha}\, X^{\mathrm{C}}_{\alpha}\, \mathbf{k}\, \lambda_{\alpha}(\nabla p_{\alpha} - \varrho_{\alpha}\, \mathrm{g}\, \nabla z)\Big)}_{\text{advective transport}} \\
&- \underbrace{\nabla\cdot\Big(\mathrm{D}^{\mathrm{C}}_{\mathrm{pm}}\, \varrho_{\mathrm{w}}\, \nabla X^{\mathrm{C}}_{\mathrm{w}}\Big)}_{\text{diffusive transport}} \\
&- \underbrace{q^{\mathrm{C}}}_{\text{source/sink}} = 0, \qquad C \in \{\mathrm{w}, \mathrm{CO_2}\},\ \alpha \in \{\mathrm{w}, \mathrm{CO_2}\}.
\end{aligned} \tag{A.12}$$

The different terms can clearly be identified, i.e. a storage term, an advective transport term, a diffusive transport term, and a term considering sources and sinks.

A.2.3 Energy Balance Equation

To derive the energy balance equation, local thermodynamic equilibrium is assumed, i.e. the temperature of all phases (including the solid phase) is identical locally. Thus, a single energy balance is sufficient to describe the entire system. Porosity ϕ and phase saturations S_α are introduced into the storage term to describe the physical processes on the macroscale. Furthermore, the storage term is split into a part describing the energy stored in the fluids, and a part describing the energy stored in the porous medium. The multi-phase extension of Darcy's law (Equation 2.30) is inserted for the phase velocities. After a term to describe diffusive energy transport in the water-rich phase and a term to account for energy sources and sinks have been added, the energy balance equation is written as:

$$\underbrace{\phi \frac{\partial\Big(\sum_\alpha (\varrho_\alpha\, u_\alpha\, S_\alpha)\Big)}{\partial t}}_{\text{energy storage in the fluids}} + \underbrace{(1-\phi)\frac{\partial(\varrho_\mathrm{s}\, c_\mathrm{s}\, T)}{\partial t}}_{\text{energy storage in the matrix}}$$
$$- \underbrace{\nabla\cdot(\lambda_\mathrm{pm}\,\nabla T)}_{\text{heat conduction}}$$
$$- \underbrace{\sum_\alpha \nabla\cdot\Big(\varrho_\alpha\, h_\alpha\, \mathbf{k}\, \lambda_\alpha(\nabla p_\alpha - \varrho_\alpha\, \mathrm{g}\, \nabla z)\Big)}_{\text{heat transport due to advection}}$$
$$- \underbrace{\sum_\mathrm{C} \nabla\cdot\Big(\mathrm{D}^\mathrm{C}_\mathrm{pm}\, \varrho_\mathrm{w}\, h^\mathrm{C}_\mathrm{w}\, \nabla X^\mathrm{C}_\mathrm{w}\Big)}_{\text{heat transport due to diffusion}}$$
$$- \underbrace{q^h}_{\text{source/sink}} = 0, \qquad \alpha \in \{\mathrm{w}, \mathrm{CO_2}\}. \tag{A.13}$$

where ϱ_s is the solid grain density, c_s is the specific heat capacity of the soil grains, λ_pm is the local heat conductivity as a function of the heat conductivity of the matrix and the fluids, of porosity, and of the phase saturations (cf. Section 2.3.5), and $\mathrm{D}^\mathrm{C}_\mathrm{pm}$ is the diffusion coefficient of the components in the porous medium.

A.2.4 Closure Relations

In addition to the closure relations made for the multi-phase mathematical model (Section A.1.3), some more simplifying assumptions, constitutive relations, and auxiliary conditions are necessary to be able to solve this extended set of balance equations of the non-isothermal multi-phase multi-component mathematical model.

Simplifying Assumptions
In addition to the mechanical equilibrium valid for the 2p-module (considering the capillary pressure difference between the phases on the macroscale) in the mathematical model for non-isothermal multi-phase multi-component processes, local thermal and chemical equilibrium is of importance (cf. Section 2.2.5). Assuming local thermal equilibrium allows the solution of just one energy balance for the system, instead of one energy balance for each phase. Assuming local chemical equilibrium allows the calculation of the mass fraction of a component in all phases by knowing the mass fraction of a component in one phase (Miller et al., 1996). Thus, any mass transfer kinetics are neglected and mass fractions of components are instantaneously in equilibrium among the phases.

Equation of State
Equations of state cannot only be defined for pure substances (cf. Section A.1.3), but also for mixtures of substances. To describe mixtures, mixing rules have to be set up, taking into account the properties of the pure substances and the interaction effects between the substances. This is discussed in Section 2.1.4.

Constitutive Relations
In addition to the constitutive relations given in Section A.1.3, rules for the mass transfer between the phases need to be found for the multi-component model considered here. This is discussed in Section 2.3.7.

Auxiliary Conditions
To close the system of equations for the multi-component model considered here, one additional auxiliary condition is necessary. The condition follows directly from the definition of the mass fractions of the components in the phases, i.e. mass fractions have to add up to one in each phase (Equation 2.3).

A.2.5 Primary Variables

The set of three partial differential equations (Equations A.12 and A.13) and closure relations is solved for the primary variables. For the non-isothermal two-phase two-component system considered here, the solution of three independent primary variables is necessary. Since in this system phases can appear and disappear locally (cf. Section 2.1.3), one set of primary variables is not sufficient to describe every possible state of the physical system. In this system, it is possible to have both phases present locally, or only either one of the phases (water-rich or CO_2-rich phase). When both phases are present, the set of primary variables is switched when either $S_w \geq 1.0$, i.e. the disappearance of the CO_2-rich phase and only the water-rich phase is present, or $S_w \leq 0.0$, i.e. the disappearance of the water-rich phase and only the CO_2-rich phase is present. Table A.1 summarises the different phase states with the corresponding primary variables and substitution criteria.

Phase state	Present ph.	Primary variables	Substitution criteria	
			W-rich phase appears	CO_2-rich phase appears
Both phases	w, CO_2	p_{CO2}, T, S_w	–	–
W-rich phase	w	p_{CO2}, T, X_w^{CO2}	–	$X_w^{CO2} \geq (X_w^{CO2})_{max}$
CO_2-rich ph.	CO_2	p_{CO2}, T, X_{CO2}^w	$X_{CO2}^w \geq (X_{CO2}^w)_{max}$	–

Table A.1: Primary variables and substitution criteria for the 2p2cni-module (Bielinski, 2006).

A detailed description of the process-adaptive algorithm for the substitution of the primary variables and the implementation in the numerical simulator used here is given in Class et al. (2002) and Bielinski (2006).

A.3 Initial and Boundary Conditions

Differential equations A.4 for the multi-phase model and Equations A.12 and A.13 for the non-isothermal multi-phase multi-component model describe a transient flow and transport problem in porous media for which adequate initial and boundary conditions need to be defined for the actual set of primary variables. Initial conditions define the state of the system at the beginning of the simulation, whereas boundary conditions define the state at the boundary of the model domain. The simulation software MUFTE-UG (Section 2.5) offers two kinds of boundary conditions:

Dirichlet type: The Dirichlet boundary condition defines the value of a primary variable at the boundary of the model domain (e.g. $S_w, p_{CO2}, T, X_{CO2}^w, X_w^{CO2}$).

Neumann type: The Neumann boundary condition describes the gradient of a primary variable at the boundary; it is therefore a flux of a quantity perpendicular to the boundary of the model domain. Here, this is a mass or energy flux.

A.4 Discretisation in Space and Time

To solve the system of differential equations numerically, they have to be discretised in space and time. For the discretisation in space, the Box method (Helmig (1997), Bastian and Helmig (1999)) is used. For the discretisation in time, a fully implicit Euler scheme is applied, i.e. a finite difference method of first order with time-step size Δt. It is unconditionally stable for arbitrary time steps. However, the time-step size might be varied in the solution process (given in Section A.5) according to the performance of the applied method to find a satisfactory solution. For the sake of simplicity, only the discretisation of the multi-phase

multi-component mass balance equations is shown.

Integrating the differential form of the mass balance equation A.12 over the model domain yields the weak form of the equations:

$$\begin{aligned}
&\int_\Omega \phi \frac{\partial\Big(\sum_\alpha (\varrho_\alpha X_\alpha^{\mathrm{C}} S_\alpha)\Big)}{\partial t}\, d\Omega \\
&- \int_\Omega \sum_\alpha \nabla\cdot\Big(\varrho_\alpha X_\alpha^{\mathrm{C}}\, \mathbf{k}\, \lambda_\alpha \left(\nabla p_\alpha - \varrho_\alpha\, \mathrm{g}\, \nabla z\right)\Big)\, d\Omega \\
&- \int_\Omega \nabla\cdot\Big(\mathrm{D}_{\mathrm{pm}}^{\mathrm{C}}\, \varrho_{\mathrm{w}} \nabla X_{\mathrm{w}}^{\mathrm{C}}\Big)\, d\Omega \\
&- \int_\Omega q^{\mathrm{C}}\, d\Omega = 0, \qquad C \in \{\mathrm{w}, \mathrm{CO_2}\},\ \alpha \in \{\mathrm{w}, \mathrm{CO_2}\}.
\end{aligned} \tag{A.14}$$

The discrete values of the primary variables u (e.g. $S_{\mathrm{w}}, p_{\mathrm{CO2}}, T, X_{\mathrm{CO2}}^{\mathrm{w}}, X_{\mathrm{w}}^{\mathrm{CO2}}$) are given at the nodes of the finite element mesh. In between these nodes, the values are approximated using a basis function N_{j} for node j:

$$\tilde{u} = \sum_{\mathrm{j}=1}^{n_{\mathrm{nodes}}} \hat{u}_{\mathrm{j}} \cdot N_{\mathrm{j}}, \tag{A.15}$$

where n_{nodes} is the number of nodes of the finite element mesh. Figure A.1 shows the basis function, which is a C^0 Lagrangian polynomial.

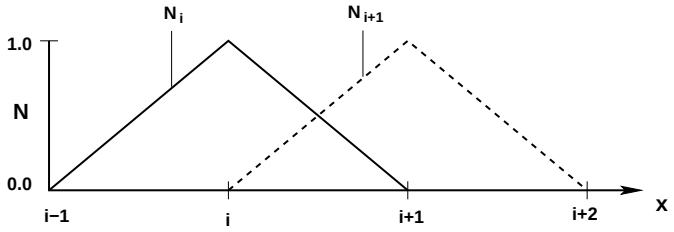

Figure A.1: Basis function for the respective node in the 1-D case. The basis function is one at the respective node and zero at all other nodes.

Inserting the approximated values of the primary variables into the balance equations results in an error ε. The weighted mean error shall become zero over the model domain.

$$\int_\Omega W_{\mathrm{i}} \cdot \varepsilon\, d\Omega \stackrel{!}{=} 0, \quad \mathrm{i} = 1, 2, \ldots, n_{\mathrm{nodes}}, \tag{A.16}$$

where W is the weighting function.

The mass matrix (M_{ij}) is defined as

$$M_{\mathrm{ij}} = \int_{\Omega} W_{\mathrm{i}}\, N_{\mathrm{j}}\, d\Omega. \tag{A.17}$$

The total potential of phase α can be written as

$$\hat{\Psi}_{\alpha \mathrm{i}} := p_{\alpha \mathrm{i}} - \varrho_{\alpha \mathrm{i}}\, \mathrm{g}\, z_{\mathrm{i}}. \tag{A.18}$$

Following application of the implicit Euler scheme for the time discretisation and inclusion of the definitions made in Equations A.15 to A.18, Equation A.14 is then rewritten as

$$\begin{aligned}
&\frac{\phi}{\Delta t} \sum_{\mathrm{j} \in \eta_{\mathrm{i}}} M_{\mathrm{ij}} \left(\left(\sum_{\alpha} \left(\varrho_{\alpha}\, \hat{X}^{\mathrm{C}}_{\alpha}\, \hat{S}_{\alpha} \right) \right)^{(\mathrm{t}+\Delta \mathrm{t})}_{\mathrm{j}} - \left(\sum_{\alpha} \left(\varrho_{\alpha}\, \hat{X}^{\mathrm{C}}_{\alpha}\, \hat{S}_{\alpha} \right) \right)^{\mathrm{t}}_{\mathrm{j}} \right) \\
&- \int_{\Omega} \sum_{\alpha} \sum_{\mathrm{j} \in \eta_{\mathrm{i}}} W_{\mathrm{i}}\, \nabla \cdot \left(\left(\varrho_{\alpha}\, \mathbf{k}\, \lambda_{\alpha} \right)^{(\mathrm{t}+\Delta \mathrm{t})}_{\mathrm{ij}} \left(\hat{X}^{\mathrm{C}}_{\alpha}\, N_{\mathrm{j}} \right)^{(\mathrm{t}+\Delta \mathrm{t})} \nabla N_{\mathrm{j}} \right) d\Omega \left(\hat{\Psi}_{\alpha \mathrm{j}} - \hat{\Psi}_{\alpha \mathrm{i}} \right)^{(\mathrm{t}+\Delta \mathrm{t})} \\
&- \int_{\Omega} \sum_{\mathrm{j} \in \eta_{\mathrm{i}}} W_{\mathrm{i}}\, \nabla \cdot \left(\left(\mathrm{D}^{\mathrm{C}}_{\mathrm{pm}}\, \varrho_{\mathrm{w}} \right)^{(\mathrm{t}+\Delta \mathrm{t})}_{\mathrm{ij}} \nabla N_{\mathrm{j}} \right) d\Omega \left(\hat{X}^{\mathrm{C}}_{\mathrm{wj}} - \hat{X}^{\mathrm{C}}_{\mathrm{wi}} \right)^{(\mathrm{t}+\Delta \mathrm{t})} \\
&- \int_{\Omega} \left(W_{\mathrm{i}}\, \hat{q}^{\mathrm{C}}_{\mathrm{i}} \right)^{(\mathrm{t}+\Delta \mathrm{t})} d\Omega \; = 0,
\end{aligned} \tag{A.19}$$

where η_{i} is a set of nodes including all neighbouring nodes of the considered node i.

A mass lumping technique is introduced, assigning all entries of the mass matrix to its main diagonal (Huber and Helmig, 1999):

$$M^{\mathrm{lumped}}_{\mathrm{ij}} = \begin{cases} V_{\mathrm{i}} & \text{for} \quad \mathrm{i} = \mathrm{j} \\ 0 & \text{for} \quad \mathrm{i} \neq \mathrm{j} \end{cases} \tag{A.20}$$

Additionally, the source term is lumped by $\int_{\Omega} W_{\mathrm{i}}\, q^{\mathrm{C}}_{\mathrm{i}}\, d\Omega = V_{\mathrm{i}}\, q^{\mathrm{C}}_{\mathrm{i}}$.

Applying the product rule $\int_{\Omega} \nabla \cdot (W_{\mathrm{i}} \cdot \mathbf{F})\, d\Omega = \int_{\Omega} (\nabla W_{\mathrm{i}} \cdot \mathbf{F})\, d\Omega + \int_{\Omega} (W_{\mathrm{i}} \nabla \cdot \mathbf{F})\, d\Omega$ and applying the Green-Gaussian integral rule (Helmig, 1997) as $\int_{\Omega} \nabla \cdot (W_{\mathrm{i}} \cdot \mathbf{F})\, d\Omega = \int_{\Gamma} (W_{\mathrm{i}} \cdot \mathbf{F}) \cdot \mathbf{n}\, d\Gamma$ yields after rearrangement:

$$\int_{\Omega} (W_{\mathrm{i}} \nabla \cdot \mathbf{F})\, d\Omega = \int_{\Gamma} (W_{\mathrm{i}} \cdot \mathbf{F}) \cdot \mathbf{n}\, d\Gamma - \int_{\Omega} (\nabla W_{\mathrm{i}} \cdot \mathbf{F})\, d\Omega. \tag{A.21}$$

Equation A.21 is introduced exemplarily to the advective flux term in Equation A.19:

$$\begin{aligned}
&\int_{\Omega} \sum_{\alpha} \sum_{\mathrm{j}\in\eta_\mathrm{i}} W_\mathrm{i} \nabla \cdot \left((\varrho_\alpha \mathbf{k} \lambda_\alpha)_{\mathrm{ij}}^{(\mathrm{t}+\Delta\mathrm{t})} (\hat{X}_\alpha^\mathrm{C} N_\mathrm{j})^{(\mathrm{t}+\Delta\mathrm{t})} \nabla N_\mathrm{j} \right) d\Omega \, (\hat{\Psi}_{\alpha\mathrm{j}} - \hat{\Psi}_{\alpha\mathrm{i}})^{(\mathrm{t}+\Delta\mathrm{t})} \\
&= \int_{\Gamma} \sum_{\alpha} \sum_{\mathrm{j}\in\eta_\mathrm{i}} \left(W_\mathrm{i} \cdot \left((\varrho_\alpha \mathbf{k} \lambda_\alpha)_{\mathrm{ij}}^{(\mathrm{t}+\Delta\mathrm{t})} (\hat{X}_\alpha^\mathrm{C} N_\mathrm{j})^{(\mathrm{t}+\Delta\mathrm{t})} \nabla N_\mathrm{j} \right) \right) \mathbf{n} \, d\Gamma \, (\hat{\Psi}_{\alpha\mathrm{j}} - \hat{\Psi}_{\alpha\mathrm{i}})^{(\mathrm{t}+\Delta\mathrm{t})} \\
&- \int_{\Omega} \sum_{\alpha} \sum_{\mathrm{j}\in\eta_\mathrm{i}} \nabla W_\mathrm{i} \left((\varrho_\alpha \mathbf{k} \lambda_\alpha)_{\mathrm{ij}}^{(\mathrm{t}+\Delta\mathrm{t})} (\hat{X}_\alpha^\mathrm{C} N_\mathrm{j})^{(\mathrm{t}+\Delta\mathrm{t})} \nabla N_\mathrm{j} \right) d\Omega \, (\hat{\Psi}_{\alpha\mathrm{j}} - \hat{\Psi}_{\alpha\mathrm{i}})^{(\mathrm{t}+\Delta\mathrm{t})} \qquad \text{(A.22)}
\end{aligned}$$

For the discretisation in space, the Box method (Helmig (1997), Bastian and Helmig (1999)) is used; this is a node-centred (vertex-centred) finite volume method based on the Galerkin finite element method. To create the primary finite element mesh, the model domain is split into elements that connect at the nodes of the mesh (see Figure A.2). A secondary mesh is constructed by connecting the midpoints of the element edges with the barycentres of the elements. Thus, each element is split into a number of sub-control volumes. The sub-control volumes around the respective point form a box. The fluxes between the boxes are approximated at the integration points, which lie at the centre of each sub-control volume face.

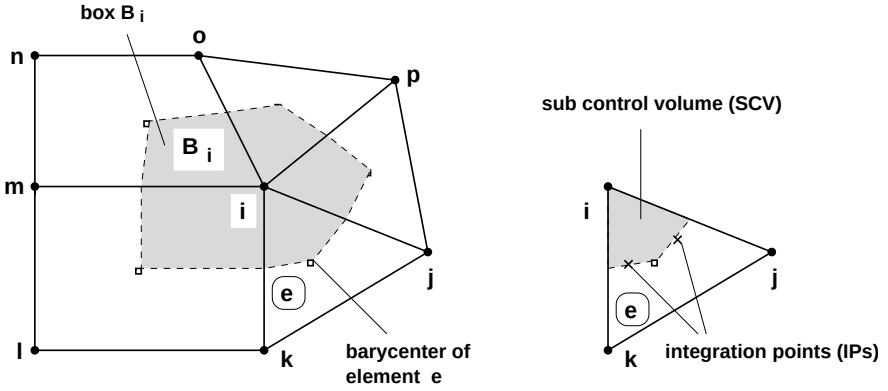

Figure A.2: Finite element mesh (solid lines) and finite volume mesh (dashed lines) composed of several sub control volumes (Helmig, 1997).

The Box method employs a weighting function as shown in Figure A.3. Since the weighting function is constantly one inside the respective box, the gradient ∇W_i equals zero. Hence, the last term in Equation A.22 vanishes.

To obtain a stable and non-oscillating solution, it is necessary to evaluate the mobilities λ_α, the densities ϱ_α, and mass fractions of the components X_α^C in the advective term at the upstream node (Helmig, 1997). The upstream node can be identified by its larger total potential, compared to the total potential of the downstream node. This is referred to as

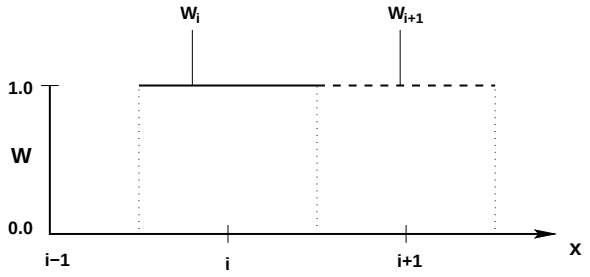

Figure A.3: Weighting function (W) for the respective node in the 1-D case. For the box method discussed here, the weighting function is one inside the respective box and zero elsewhere.

"fully-upwinding":

$$\mathrm{upw}(i,j) = \begin{cases} \mathrm{i} & \text{if} \quad (\Psi_{\alpha\mathrm{j}} - \Psi_{\alpha\mathrm{i}}) \leq 0 \\ \mathrm{j} & \text{if} \quad (\Psi_{\alpha\mathrm{j}} - \Psi_{\alpha\mathrm{i}}) > 0 \end{cases} \tag{A.23}$$

The coefficients in the diffusive flux term are evaluated by arithmetic averaging between adjacent nodes.

Finally, after inclusion of the mass lumping (Equation A.20), application of the Green-Gaussian integral rule (Equation A.21) to the advective and diffusive flux terms (shown exemplarily for the advective flux term in Equation A.22), introduction of the fully-upwinding technique (Equation A.23) and on the assumption weighting functions as shown in Figure A.3, Equation A.19 is rewritten as:

$$\begin{aligned} &\frac{\phi}{\Delta t} V_\mathrm{i} \left(\Big(\sum_\alpha (\varrho_\alpha \, \hat{X}^\mathrm{C}_\alpha \, \hat{S}_\alpha) \Big)^{(\mathrm{t}+\Delta\mathrm{t})}_\mathrm{j} - \Big(\sum_\alpha (\varrho_\alpha \, \hat{X}^\mathrm{C}_\alpha \, \hat{S}_\alpha) \Big)^{\mathrm{t}}_\mathrm{j} \right) \\ &- \int_\Gamma \sum_\alpha \sum_{\mathrm{j} \in \eta_\mathrm{i}} \Big((\varrho_\alpha \, \lambda_\alpha \, \hat{X}^\mathrm{C}_\alpha)^{(\mathrm{t}+\Delta\mathrm{t})}_\mathrm{upw} \, \mathbf{k} \, \nabla N_\mathrm{j} \, \mathbf{n} \Big) \, d\Gamma \, (\hat{\Psi}_{\alpha\mathrm{j}} - \hat{\Psi}_{\alpha\mathrm{i}})^{(\mathrm{t}+\Delta\mathrm{t})} \\ &- \int_\Gamma \sum_{\mathrm{j} \in \eta_\mathrm{i}} \Big((\mathrm{D}^\mathrm{C}_\mathrm{pm} \, \varrho_\mathrm{w})^{(\mathrm{t}+\Delta\mathrm{t})}_\mathrm{ij} \, \nabla N_\mathrm{j} \, \mathbf{n} \Big) \, d\Gamma \, (\hat{X}^\mathrm{C}_\mathrm{wj} - \hat{X}^\mathrm{C}_\mathrm{wi})^{(\mathrm{t}+\Delta\mathrm{t})} \\ &- V_\mathrm{i} \, (\hat{q}^\mathrm{C}_\mathrm{i})^{(\mathrm{t}+\Delta\mathrm{t})} \, d\Omega \; = 0. \end{aligned} \tag{A.24}$$

A.5 Linearisation and Solution

The discretised equations are strongly non-linear, mainly because of the constitutive relations (see Sections A.1.3 and A.2.4). They are linearised by a Newton-Raphson method (Helmig, 1997) before being solved. In general form, the set of non-linear differential equations of the vector of primary variables $\mathbf{u}$ at the current node can be written as:

$$\mathbf{R}(\mathbf{u}) = 0, \tag{A.25}$$

A Taylor series expansion, neglecting higher-order terms, leads to:

$$\mathbf{R}\Big(\mathbf{u}^{(\mathrm{t}+\Delta\mathrm{t},\mathrm{n}+1)}\Big) \approx \mathbf{R}\Big(\mathbf{u}^{(\mathrm{t}+\Delta\mathrm{t},\mathrm{n})}\Big) + \Big(\frac{\partial \mathbf{R}}{\partial \mathbf{u}}\Big)^{(\mathrm{t}+\Delta\mathrm{t},\mathrm{n})} \cdot \Big(\mathbf{u}^{(\mathrm{t}+\Delta\mathrm{t},\mathrm{n}+1)} - \mathbf{u}^{(\mathrm{t}+\Delta\mathrm{t},\mathrm{n})}\Big) \tag{A.26}$$

where $\mathrm{t}+\Delta\mathrm{t}$ indicates the time level the solution is sought for and n respectively n+1 is the number of the iteration cycle. Following application of Equation A.25 and the introduction of the Jacobian matrix as $\mathbf{J} = \frac{\partial \mathbf{R}}{\partial \mathbf{u}}$, the solution vector of the next iterative cycle can be written as:

$$\mathbf{u}^{(\mathrm{t}+\Delta\mathrm{t},\mathrm{n}+1)} = \mathbf{u}^{(\mathrm{t}+\Delta\mathrm{t},\mathrm{n})} - \Big(\mathbf{J}^{\mathrm{t}+\Delta\mathrm{t},\mathrm{n}}\Big)^{-1} \cdot \mathbf{R}\Big(\mathbf{u}^{(\mathrm{t}+\Delta\mathrm{t},\mathrm{n})}\Big). \tag{A.27}$$

The Jacobian matrix $\mathbf{J}$ can be calculated using a central difference scheme as:

$$\mathbf{J}_{\mathrm{ij}}^{(\mathrm{t}+\Delta\mathrm{t},\mathrm{n})} \approx \frac{R_{\mathrm{i}}(\ldots, u_{\mathrm{j}\text{-}1}, u_{\mathrm{j}} + \Delta u_{\mathrm{j}}, u_{\mathrm{j}+1}, \ldots) - R_{\mathrm{i}}(\ldots, u_{\mathrm{j}\text{-}1}, u_{\mathrm{j}} - \Delta u_{\mathrm{j}}, u_{\mathrm{j}+1}, \ldots)}{2\,\Delta u_{\mathrm{j}}}, \tag{A.28}$$

where $\Delta u_{\mathrm{j}} = \delta \cdot u_{\mathrm{j}}$ and δ is a small increment (e.g. δ=10^{-8}).

For the solution of the linearised equations, MUFTE-UG offers various sophisticated methods, e.g. the bi-conjugated gradient method (Bastian et al., 1997) or the multi-grid method (Class et al., 2002).

B Detailed derivation of Equations 4.21, 4.22, and 4.25

Inserting Equations 4.12 to 4.17 into the pressure and water-phase saturation Equations (Equations 4.8, 4.9 and 4.10) leads to a dimensionless pressure equation

$$\widehat{\nabla}\cdot \hat{\mathbf{v}}_{\mathrm{tot}} = 0, \tag{B.1}$$

$$\hat{\mathbf{v}}_{\mathrm{tot}} \cdot \mathrm{v}_{\mathrm{cr}} = -\lambda\,\mathbf{k}\left(\frac{1}{l_{\mathrm{cr}}}\,\widehat{\nabla p_{\mathrm{w}}}\,p_{\mathrm{cr}} + f_{\mathrm{CO2}}\,\frac{1}{l_{\mathrm{cr}}}\,\widehat{\nabla p_{\mathrm{c}}}\,p_{\mathrm{cr}} - \mathrm{g}\,\frac{1}{l_{\mathrm{cr}}}\,\widehat{\nabla z}\,l_{\mathrm{cr}}\sum_{\alpha} f_{\alpha}\,\varrho_{\alpha}\right), \tag{B.2}$$

$$\tag{B.3}$$

and to a dimensionless saturation equation

$$\begin{aligned}\phi\,\frac{\partial S_{\mathrm{w}}}{\partial \hat{t}\cdot t_{\mathrm{cr}}} &+ \frac{1}{l_{\mathrm{cr}}}\,\widehat{\nabla}\cdot\left(f_{\mathrm{w}}\,\hat{\mathbf{v}}_{\mathrm{tot}}\,\cdot \mathrm{v}_{\mathrm{cr}}\right)\\ &+\frac{1}{l_{\mathrm{cr}}}\,\widehat{\nabla}\cdot\left(f_{\mathrm{w}}\,\lambda_{\mathrm{CO2}}(\varrho_{\mathrm{w}}-\varrho_{\mathrm{CO2}})\,\mathbf{k}\,\mathrm{g}\,\frac{1}{l_{\mathrm{cr}}}\,\widehat{\nabla z}\,l_{\mathrm{cr}}\right)\\ &+\frac{1}{l_{\mathrm{cr}}}\,\widehat{\nabla}\cdot\left(f_{\mathrm{w}}\,\lambda_{\mathrm{CO2}}\,\mathbf{k}\,\frac{1}{l_{\mathrm{cr}}}\,\widehat{\nabla p_{\mathrm{c}}}\,p_{\mathrm{cr}}\right) = 0.\end{aligned} \tag{B.4}$$

Some reformulation (using e.g. $f_{\mathrm{CO2}} = \frac{\lambda_{\mathrm{CO2}}}{\lambda}$) yields for the pressure equation

$$\widehat{\nabla}\cdot \hat{\mathbf{v}}_{\mathrm{tot}} = 0, \tag{B.5}$$

$$\begin{aligned}\hat{\mathbf{v}}_{\mathrm{tot}} = -\Bigg[&\widehat{\nabla p_{\mathrm{w}}}\,\frac{p_{\mathrm{cr}}\,\lambda\,\mathbf{k}}{l_{\mathrm{cr}}\,\mathrm{v}_{\mathrm{cr}}} + \widehat{\nabla p_{\mathrm{c}}}\,\frac{p_{\mathrm{cr}}\,\lambda_{\mathrm{CO2}}\,\mathbf{k}}{l_{\mathrm{cr}}\,\mathrm{v}_{\mathrm{cr}}}\\ &- \widehat{\nabla z}\,\frac{\mathrm{g}\,\mathbf{k}\,\lambda}{\mathrm{v}_{\mathrm{cr}}}\,\frac{l_{\mathrm{cr}}}{l_{\mathrm{cr}}}\underbrace{(\varrho_{\mathrm{w}}-\varrho_{\mathrm{CO2}})\left((f_{\mathrm{w}}-f_{\mathrm{CO2}}) + \frac{\varrho_{\mathrm{w}}\,f_{\mathrm{CO2}}}{\varrho_{\mathrm{w}}-\varrho_{\mathrm{CO2}}} + \frac{\varrho_{\mathrm{CO2}}\,f_{\mathrm{w}}}{\varrho_{\mathrm{w}}-\varrho_{\mathrm{CO2}}}\right)}_{\sum_{\alpha} f_{\alpha}\,\varrho_{\alpha}}\Bigg],\end{aligned} \tag{B.6}$$

and for the saturation equation

$$\begin{aligned}\frac{\partial S_{\mathrm{w}}}{\partial \hat{t}} &+ \underbrace{\frac{t_{\mathrm{cr}}}{\phi\, l_{\mathrm{cr}}}}_{\mathrm{v}_{\mathrm{cr}}^{-1}}\, \widehat{\nabla}\cdot\Big(f_{\mathrm{w}}\,\hat{\mathbf{v}}_{\mathrm{tot}}\,\cdot \mathrm{v}_{\mathrm{cr}}\Big) \\ &+ \underbrace{\frac{t_{\mathrm{cr}}}{\phi\, l_{\mathrm{cr}}}}_{\mathrm{v}_{\mathrm{cr}}^{-1}}\, \widehat{\nabla}\cdot\Big(f_{\mathrm{w}}\,\lambda_{\mathrm{CO2}}(\varrho_{\mathrm{w}}-\varrho_{\mathrm{CO2}})\,\mathbf{k}\,\mathrm{g}\,\widehat{\nabla}\hat{z}\Big) \\ &+ \underbrace{\frac{t_{\mathrm{cr}}}{\phi\, l_{\mathrm{cr}}}}_{\mathrm{v}_{\mathrm{cr}}^{-1}}\, \widehat{\nabla}\cdot\Big(f_{\mathrm{w}}\,\lambda_{\mathrm{CO2}}\,\mathbf{k}\frac{1}{l_{\mathrm{cr}}}\,\widehat{\nabla}\widehat{p_{\mathrm{c}}}\,p_{\mathrm{cr}}\Big)=0.\end{aligned} \tag{B.7}$$

Some further reformulation (using e.g. $\lambda = \frac{1}{\mu_{\mathrm{CO2}}}(\frac{\mu_{\mathrm{CO2}}}{\mu_{\mathrm{w}}}k_{\mathrm{r,w}} + k_{\mathrm{r,CO2}})$, and $\lambda_{\mathrm{CO2}} = \frac{k_{\mathrm{r,CO2}}}{\mu_{\mathrm{CO2}}}$) yields for the pressure equation

$$\widehat{\nabla}\cdot\,\hat{\mathbf{v}}_{\mathrm{tot}} = 0, \tag{B.8}$$

$$\begin{aligned}\hat{\mathbf{v}}_{\mathrm{tot}} = -\Bigg[&\widehat{\nabla p_{\mathrm{w}}}\;\underbrace{\frac{\mathrm{k}\,p_{\mathrm{cr}}}{\mu_{\mathrm{CO2}}\,\mathrm{v}_{\mathrm{cr}}\,l_{\mathrm{cr}}}}_{\mathrm{Ca}}\;\underbrace{\Big(\frac{\mu_{\mathrm{CO2}}}{\mu_{\mathrm{w}}}\,k_{\mathrm{r,w}}+k_{\mathrm{r,CO2}}\Big)}_{\mathrm{A}} + \widehat{\nabla}\widehat{p_{\mathrm{c}}}\;\underbrace{\frac{\mathrm{k}\,p_{\mathrm{cr}}}{\mu_{\mathrm{CO2}}\,\mathrm{v}_{\mathrm{cr}}\,l_{\mathrm{cr}}}}_{\mathrm{Ca}}\;k_{\mathrm{r,CO2}} \\ &- \widehat{\nabla}\hat{z}\;\underbrace{\frac{(\varrho_{\mathrm{w}}-\varrho_{\mathrm{CO2}})\,\mathrm{g}\,\mathrm{k}}{\mu_{\mathrm{CO2}}\,\mathrm{v}_{\mathrm{cr}}}}_{\mathrm{Gr}}\;\underbrace{\frac{\mu_{\mathrm{CO2}}}{\mu_{\mathrm{w}}}\,k_{\mathrm{r,w}}+k_{\mathrm{r,CO2}}}_{\mathrm{A}} \\ &\underbrace{\Big((f_{\mathrm{w}}-f_{\mathrm{CO2}})+\frac{\varrho_{\mathrm{w}}\,f_{\mathrm{CO2}}}{\varrho_{\mathrm{w}}-\varrho_{\mathrm{CO2}}}+\frac{\varrho_{\mathrm{CO2}}\,f_{\mathrm{w}}}{\varrho_{\mathrm{w}}-\varrho_{\mathrm{CO2}}}\Big)}_{\mathrm{B}}\Bigg],\end{aligned} \tag{B.9}$$

and for the saturation equation

$$\begin{aligned}\frac{\partial S_{\mathrm{w}}}{\partial \hat{t}} &+ \widehat{\nabla}\cdot\Big(f_{\mathrm{w}}\,\hat{\mathbf{v}}_{\mathrm{tot}}\Big) \\ &+ \widehat{\nabla}\cdot\Big(\underbrace{f_{\mathrm{w}}\,k_{\mathrm{r,CO2}}}_{\mathrm{C}}\;\underbrace{\frac{(\varrho_{\mathrm{w}}-\varrho_{\mathrm{CO2}})\,\mathrm{g}\,\mathrm{k}}{\mu_{\mathrm{CO2}}\,\mathrm{v}_{\mathrm{cr}}}}_{\mathrm{Gr}}\;\widehat{\nabla}\hat{z}\Big) \\ &+ \widehat{\nabla}\cdot\Big(\underbrace{f_{\mathrm{w}}\,k_{\mathrm{r,CO2}}}_{\mathrm{C}}\;\underbrace{\frac{\mathrm{k}\,p_{\mathrm{cr}}}{\mu_{\mathrm{CO2}}\,\mathrm{v}_{\mathrm{cr}}\,l_{\mathrm{cr}}}}_{\mathrm{Ca}}\;\widehat{\nabla}\widehat{p_{\mathrm{c}}}\Big)=0.\end{aligned} \tag{B.10}$$

C Tables

Risk contour line [log kg]	A	B	R^2
0.001	1.5487	-3.9691	0.9953
1	1.4654	-3.2771	0.9967
2	1.4024	-2.7152	0.9980
3	1.3565	-2.1370	0.9976
4	1.4615	-2.3706	0.9887
5	1.6048	-2.7717	0.9956
6	1.3875	-0.6535	0.9991
7	1.0798	2.8553	0.9981

Table C.1: Power-fitted coefficients A and B in Equation 7.7 to calculate risk contour lines. R^2 indicates goodness of fit (that is the ratio of the sum of the squares of the regression to the total sum of the squares) between {0,1}, where a value closer to one indicates better fit.

Time contour line [days]	A_0	A_1	A_2	A_3	A_4	A_5	A_6	A_7	A_8	A_9	R^2
1000	1.0685E+00	1.4859E-01	-1.5375E-03	8.0130E-06	-2.3983E-08	4.2862E-11	-4.5849E-14	2.8163E-17	-8.8019E-21	9.8655E-25	0.9997
2000	5.0088E+00	4.9038E-02	-4.6774E-04	2.0879E-06	-5.2227E-09	7.7607E-12	-6.9974E-15	3.7556E-18	-1.1029E-21	1.3634E-25	0.9998
3000	7.4770E+00	-3.9704E-03	-7.6240E-06	7.2986E-08	-1.9675E-10	2.5317E-13	-1.7582E-16	6.6951E-20	-1.2949E-23	9.6473E-28	0.9995
4000	8.4316E+00	-1.9807E-02	9.8945E-05	-2.7483E-07	4.3676E-10	-4.2399E-13	2.5517E-16	-9.2601E-20	1.8511E-23	-1.5627E-27	0.9987
5000	8.0576E+00	-1.0807E-02	3.9636E-05	-8.7095E-08	1.1024E-10	-8.6559E-14	4.2855E-17	-1.2960E-20	2.1768E-24	-1.5516E-28	0.9973
6000	8.1624E+00	-1.0943E-02	3.8833E-05	-8.0753E-08	9.6220E-11	-7.0288E-14	3.1944E-17	-8.7698E-21	1.3262E-24	-8.4625E-29	0.9974
7000	8.3008E+00	-1.1898E-02	4.2956E-05	-8.8591E-08	1.0433E-10	-7.4669E-14	3.2931E-17	-8.7074E-21	1.2621E-24	-7.6946E-29	0.9964

Table C.2: Coefficients A_i fitted to Equation 7.8 to calculate time contour lines. R^2 indicates goodness of fit (that is the ratio of the sum of the squares of the regression to the total sum of the squares) between {0,1}, where a value closer to one indicates better fit.

D Output List

D.1 Peer-Reviewed

- Kopp, A., Binning, P.J., Johannsen, K., Class, H. and Helmig, R., Risk Analysis for Leakage through Abandoned Wells in Geological CO_2 Storage, submitted to Energy Conversion and Management, 2009.
- Kopp, A., Ebigbo, A., Bielinski, A., Class, H. and R. Helmig, Numerical simulation of temperature changes due to CO_2 injection in geological reservoirs, AAPG Studies 59: Carbon dioxide sequestration in geological media – State of the science, Grobe, M. and Pashin, J.C. and Dodge, R.L. (Editors), in press, 2009.
- Kopp, A., Class, H. and Helmig, R., Investigations on CO_2 storage capacity in saline aquifers - Part 1: Dimensional analysis of flow processes and reservoir characteristics, Int. J. Greenhouse Gas Control, 3(3), 263–276, DOI:10.1016/j.ijggc.2008.10.002, 2009.
- Kopp, A., Class, H. and Helmig, R., Investigations on CO_2 storage capacity in saline aquifers - Part 2: Estimation of storage capacity coefficients, Int. J. Greenhouse Gas Control, 3(3), 277–287, DOI:10.1016/j.ijggc.2008.10.001, 2009.
- Bielinski, A., Kopp, A., Schütt, H. and Class, H., Monitoring of CO_2 plumes during storage in geological formations using temperature signals: numerical investigation, Int. J. Greenhouse Gas Control, 2, 319–328, DOI: 10.1016/ j.ijggc.2008.02.008, 2008.
- Hurter, S., Garnett, A., Bielinski, A. and Kopp, A.,Thermal Signature of Free-Phase CO_2 in Porous Rocks: Detectability of CO_2 by Temperature Logging, Society of Petroleum Engineers, SPE 109007, DOI: 10.2118/109007-MS, 2007.
- Class, H., Bielinski, A., Helmig, R., Kopp, A. and Ebigbo, A., Numerische Simulation der Speicherung von CO_2 in geologischen Formationen, Chemie Ingenieur Technik, 78(4), 445–452, Special Issue: Kohlendioxid und Klimaschutz, DOI: 10.1002/cite.200500186, 2006.

D.2 Non Peer-Reviewed (selected)

- Kopp, A., Probst, P., Class, H., Hurter, S. and Helmig, R., Estimation of CO_2 Storage Capacity Coefficients in Geologic Formations, Energy Procedia, 1(1), 2863–2870, 9th International Conference on Greenhouse Gas Control Technologies Proceedings, DOI:10.1016/j.egypro.2009.02.060, 2009.

- Johannsen, K., Kopp, A., Tourunen, O. and Kleist, J., Studying CO_2 Sequestration with the Power of Supercomputing, European Research Consortium for Informatics and Mathematics (ERCIM) 74, 17–18, 2008.

- Class, H., Ebigbo, A. and Kopp, A., Numerical modeling of CO_2 storage in geological formations - recent developments and challenges, 1. French-German Symposium on Geological Storage of CO_2, Science Report No.9, Geoforschungszentrum Potsdam, 51–58, 2007.

- Kopp, A., Class, H. and Helmig, R., Treibhausgase in der Bodenfalle, UNI-Kurier 1/2007,99, EU-Projekt CO_2SINK: Numerische Simulation der Kohlendioxidspeicherung, 2007.

- Kopp, A., Bielinski, A., Ebigbo, A., Class, H. and Helmig, R., Numerical Investigation of Temperature Effects during the Injection of Carbon Dioxide into Brine Aquifers, Gale, J. Bolland, O. (Editors): 8th International Conference on Greenhouse Gas Control Technologies, (GHGT-8), Trondheim, Norway, June 19th–22nd, http://www.ieagreen.org.uk/ghgt8.html.

- Kopp, A. and Sheta, H., Grid Generation for Complex Geological Systems in Mining Areas, European Union Marie Curie Conferences and Training Courses, 2006.

- Assteerawatt, A., Bastian, P., Bielinski, A., Breiting, T., Class, H., Ebigbo, A., Eichel, H., Freiboth, S., Helmig, R., Kopp, A., Niessner, J., Ochs, S.O., Papafotiou, A., Paul, M., Sheta, H., Werner, D. and Ölmann, U., MUFTE-UG: Structure, Applications and Numerical Methods, Newsletter, International Groundwater Modeling Centre, Colorado School of Mine, 2005. Volume XXIII (2), 2005.

Institut für Wasserbau
Universität Stuttgart

Pfaffenwaldring 61
70569 Stuttgart (Vaihingen)
Telefon (0711) 685 - 64717/64749/64752/64679
Telefax (0711) 685 - 67020 o. 64746 o. 64681
E-Mail: iws@iws.uni-stuttgart.de
http://www.iws.uni-stuttgart.de

Verzeichnis der Mitteilungshefte

1 Röhnisch, Arthur: *Die Bemühungen um eine Wasserbauliche Versuchsanstalt an der Technischen Hochschule Stuttgart*,
und
Fattah Abouleid, Abdel: *Beitrag zur Berechnung einer in lockeren Sand gerammten, zweifach verankerten Spundwand*, 1963

2 Marotz, Günter: *Beitrag zur Frage der Standfestigkeit von dichten Asphaltbelägen im Großwasserbau*, 1964

3 Gurr, Siegfried: *Beitrag zur Berechnung zusammengesetzter ebener Flächentragwerke unter besonderer Berücksichtigung ebener Stauwände, mit Hilfe von Randwert- und Lastwertmatrizen*, 1965

4 Plica, Peter: *Ein Beitrag zur Anwendung von Schalenkonstruktionen im Stahlwasserbau*, und Petrikat, Kurt: *Möglichkeiten und Grenzen des wasserbaulichen Versuchswesens*, 1966

5 Plate, Erich: *Beitrag zur Bestimmung der Windgeschwindigkeitsverteilung in der durch eine Wand gestörten bodennahen Luftschicht*,
und
Röhnisch, Arthur; Marotz, Günter: *Neue Baustoffe und Bauausführungen für den Schutz der Böschungen und der Sohle von Kanälen, Flüssen und Häfen; Gestehungskosten und jeweilige Vorteile*, sowie Unny, T.E.: *Schwingungsuntersuchungen am Kegelstrahlschieber*, 1967

6 Seiler, Erich: *Die Ermittlung des Anlagenwertes der bundeseigenen Binnenschiffahrtsstraßen und Talsperren und des Anteils der Binnenschiffahrt an diesem Wert*, 1967

7 *Sonderheft anläßlich des 65. Geburtstages von Prof. Arthur Röhnisch mit Beiträgen von* Benk, Dieter; Breitling, J.; Gurr, Siegfried; Haberhauer, Robert; Honekamp, Hermann; Kuz, Klaus Dieter; Marotz, Günter; Mayer-Vorfelder, Hans-Jörg; Miller, Rudolf; Plate, Erich J.; Radomski, Helge; Schwarz, Helmut; Vollmer, Ernst; Wildenhahn, Eberhard; 1967

8 Jumikis, Alfred: *Beitrag zur experimentellen Untersuchung des Wassernachschubs in einem gefrierenden Boden und die Beurteilung der Ergebnisse*, 1968

9 Marotz, Günter: *Technische Grundlagen einer Wasserspeicherung im natürlichen Untergrund*, 1968

10 Radomski, Helge: *Untersuchungen über den Einfluß der Querschnittsform wellenförmiger Spundwände auf die statischen und rammtechnischen Eigenschaften*, 1968

11 Schwarz, Helmut: *Die Grenztragfähigkeit des Baugrundes bei Einwirkung vertikal gezogener Ankerplatten als zweidimensionales Bruchproblem*, 1969

12 Erbel, Klaus: *Ein Beitrag zur Untersuchung der Metamorphose von Mittelgebirgsschneedecken unter besonderer Berücksichtigung eines Verfahrens zur Bestimmung der thermischen Schneequalität*, 1969

13 Westhaus, Karl-Heinz: *Der Strukturwandel in der Binnenschiffahrt und sein Einfluß auf den Ausbau der Binnenschiffskanäle*, 1969

14 Mayer-Vorfelder, Hans-Jörg: *Ein Beitrag zur Berechnung des Erdwiderstandes unter Ansatz der logarithmischen Spirale als Gleitflächenfunktion*, 1970

15 Schulz, Manfred: *Berechnung des räumlichen Erddruckes auf die Wandung kreiszylindrischer Körper*, 1970

16 Mobasseri, Manoutschehr: *Die Rippenstützmauer. Konstruktion und Grenzen ihrer Standsicherheit*, 1970

17 Benk, Dieter: *Ein Beitrag zum Betrieb und zur Bemessung von Hochwasserrückhaltebecken*, 1970

18 Gàl, Attila: *Bestimmung der mitschwingenden Wassermasse bei überströmten Fischbauchklappen mit kreiszylindrischem Staublech*, 1971, vergriffen

19 Kuz, Klaus Dieter: *Ein Beitrag zur Frage des Einsetzens von Kavitationserscheinungen in einer Düsenströmung bei Berücksichtigung der im Wasser gelösten Gase*, 1971, vergriffen

20 Schaak, Hartmut: *Verteilleitungen von Wasserkraftanlagen*, 1971

21 *Sonderheft zur Eröffnung der neuen Versuchsanstalt des Instituts für Wasserbau der Universität Stuttgart mit Beiträgen von* Brombach, Hansjörg; Dirksen, Wolfram; Gàl, Attila; Gerlach, Reinhard; Giesecke, Jürgen; Holthoff, Franz-Josef; Kuz, Klaus Dieter; Marotz, Günter; Minor, Hans-Erwin; Petrikat, Kurt; Röhnisch, Arthur; Rueff, Helge; Schwarz, Helmut; Vollmer, Ernst; Wildenhahn, Eberhard; 1972

22 Wang, Chung-su: *Ein Beitrag zur Berechnung der Schwingungen an Kegelstrahlschiebern*, 1972

23 Mayer-Vorfelder, Hans-Jörg: *Erdwiderstandsbeiwerte nach dem Ohde-Variationsverfahren*, 1972

24 Minor, Hans-Erwin: *Beitrag zur Bestimmung der Schwingungsanfachungsfunktionen überströmter Stauklappen*, 1972, vergriffen

25 Brombach, Hansjörg: *Untersuchung strömungsmechanischer Elemente (Fluidik) und die Möglichkeit der Anwendung von Wirbelkammerelementen im Wasserbau*, 1972, vergriffen

26 Wildenhahn, Eberhard: *Beitrag zur Berechnung von Horizontalfilterbrunnen*, 1972

27 Steinlein, Helmut: *Die Eliminierung der Schwebstoffe aus Flußwasser zum Zweck der unterirdischen Wasserspeicherung, gezeigt am Beispiel der Iller*, 1972

28 Holthoff, Franz Josef: *Die Überwindung großer Hubhöhen in der Binnenschiffahrt durch Schwimmerhebewerke*, 1973

29 Röder, Karl: *Einwirkungen aus Baugrundbewegungen auf trog- und kastenförmige Konstruktionen des Wasser- und Tunnelbaues*, 1973

30 Kretschmer, Heinz: *Die Bemessung von Bogenstaumauern in Abhängigkeit von der Talform*, 1973

31 Honekamp, Hermann: *Beitrag zur Berechnung der Montage von Unterwasserpipelines*, 1973

32 Giesecke, Jürgen: *Die Wirbelkammertriode als neuartiges Steuerorgan im Wasserbau*, und Brombach, Hansjörg: *Entwicklung, Bauformen, Wirkungsweise und Steuereigenschaften von Wirbelkammerverstärkern*, 1974

33 Rueff, Helge: *Untersuchung der schwingungserregenden Kräfte an zwei hintereinander angeordneten Tiefschützen unter besonderer Berücksichtigung von Kavitation*, 1974

34 Röhnisch, Arthur: *Einpreßversuche mit Zementmörtel für Spannbeton - Vergleich der Ergebnisse von Modellversuchen mit Ausführungen in Hüllwellrohren*, 1975

35 *Sonderheft anläßlich des 65. Geburtstages von Prof. Dr.-Ing. Kurt Petrikat mit Beiträgen von*: Brombach, Hansjörg; Erbel, Klaus; Flinspach, Dieter; Fischer jr., Richard; Gàl, Attila; Gerlach, Reinhard; Giesecke, Jürgen; Haberhauer, Robert; Hafner Edzard; Hausenblas, Bernhard; Horlacher, Hans-Burkhard; Hutarew, Andreas; Knoll, Manfred; Krummet, Ralph; Marotz, Günter; Merkle, Theodor; Miller, Christoph; Minor, Hans-Erwin; Neumayer, Hans; Rao, Syamala; Rath, Paul; Rueff, Helge; Ruppert, Jürgen; Schwarz, Wolfgang; Topal-Gökceli, Mehmet; Vollmer, Ernst; Wang, Chung-su; Weber, Hans-Georg; 1975

36 Berger, Jochum: *Beitrag zur Berechnung des Spannungszustandes in rotationssymmetrisch belasteten Kugelschalen veränderlicher Wandstärke unter Gas- und Flüssigkeitsdruck durch Integration schwach singulärer Differentialgleichungen*, 1975

37 Dirksen, Wolfram: *Berechnung instationärer Abflußvorgänge in gestauten Gerinnen mittels Differenzenverfahren und die Anwendung auf Hochwasserrückhaltebecken*, 1976

38 Horlacher, Hans-Burkhard: *Berechnung instationärer Temperatur- und Wärmespannungsfelder in langen mehrschichtigen Hohlzylindern*, 1976

39 Hafner, Edzard: *Untersuchung der hydrodynamischen Kräfte auf Baukörper im Tiefwasserbereich des Meeres*, 1977, ISBN 3-921694-39-6

40 Ruppert, Jürgen: *Über den Axialwirbelkammerverstärker für den Einsatz im Wasserbau*, 1977, ISBN 3-921694-40-X

41 Hutarew, Andreas: *Beitrag zur Beeinflußbarkeit des Sauerstoffgehalts in Fließgewässern an Abstürzen und Wehren*, 1977, ISBN 3-921694-41-8, vergriffen

42 Miller, Christoph: *Ein Beitrag zur Bestimmung der schwingungserregenden Kräfte an unterströmten Wehren*, 1977, ISBN 3-921694-42-6

43 Schwarz, Wolfgang: *Druckstoßberechnung unter Berücksichtigung der Radial- und Längsverschiebungen der Rohrwandung*, 1978, ISBN 3-921694-43-4

44 Kinzelbach, Wolfgang: *Numerische Untersuchungen über den optimalen Einsatz variabler Kühlsysteme einer Kraftwerkskette am Beispiel Oberrhein*, 1978, ISBN 3-921694-44-2

45 Barczewski, Baldur: *Neue Meßmethoden für Wasser-Luftgemische und deren Anwendung auf zweiphasige Auftriebsstrahlen*, 1979, ISBN 3-921694-45-0

46 Neumayer, Hans: *Untersuchung der Strömungsvorgänge in radialen Wirbelkammerverstärkern*, 1979, ISBN 3-921694-46-9

47 Elalfy, Youssef-Elhassan: *Untersuchung der Strömungsvorgänge in Wirbelkammerdioden und -drosseln*, 1979, ISBN 3-921694-47-7

48 Brombach, Hansjörg: *Automatisierung der Bewirtschaftung von Wasserspeichern*, 1981, ISBN 3-921694-48-5

49 Geldner, Peter: *Deterministische und stochastische Methoden zur Bestimmung der Selbstdichtung von Gewässern*, 1981, ISBN 3-921694-49-3, vergriffen

50 Mehlhorn, Hans: *Temperaturveränderungen im Grundwasser durch Brauchwassereinleitungen*, 1982, ISBN 3-921694-50-7, vergriffen

51 Hafner, Edzard: *Rohrleitungen und Behälter im Meer*, 1983, ISBN 3-921694-51-5

52 Rinnert, Bernd: *Hydrodynamische Dispersion in porösen Medien: Einfluß von Dichteunterschieden auf die Vertikalvermischung in horizontaler Strömung*, 1983, ISBN 3-921694-52-3, vergriffen

53 Lindner, Wulf: *Steuerung von Grundwasserentnahmen unter Einhaltung ökologischer Kriterien*, 1983, ISBN 3-921694-53-1, vergriffen

54 Herr, Michael; Herzer, Jörg; Kinzelbach, Wolfgang; Kobus, Helmut; Rinnert, Bernd: *Methoden zur rechnerischen Erfassung und hydraulischen Sanierung von Grundwasserkontaminationen*, 1983, ISBN 3-921694-54-X

55 Schmitt, Paul: *Wege zur Automatisierung der Niederschlagsermittlung*, 1984, ISBN 3-921694-55-8, vergriffen

56 Müller, Peter: *Transport und selektive Sedimentation von Schwebstoffen bei gestautem Abfluß*, 1985, ISBN 3-921694-56-6

57 El-Qawasmeh, Fuad: *Möglichkeiten und Grenzen der Tropfbewässerung unter besonderer Berücksichtigung der Verstopfungsanfälligkeit der Tropfelemente*, 1985, ISBN 3-921694-57-4, vergriffen

58 Kirchenbaur, Klaus: *Mikroprozessorgesteuerte Erfassung instationärer Druckfelder am Beispiel seegangsbelasteter Baukörper*, 1985, ISBN 3-921694-58-2

59 Kobus, Helmut (Hrsg.): *Modellierung des großräumigen Wärme- und Schadstofftransports im Grundwasser*, Tätigkeitsbericht 1984/85 (DFG-Forschergruppe an den Universitäten Hohenheim, Karlsruhe und Stuttgart), 1985, ISBN 3-921694-59-0, vergriffen

60 Spitz, Karlheinz: *Dispersion in porösen Medien: Einfluß von Inhomogenitäten und Dichteunterschieden*, 1985, ISBN 3-921694-60-4, vergriffen

61 Kobus, Helmut: *An Introduction to Air-Water Flows in Hydraulics*, 1985, ISBN 3-921694-61-2

62 Kaleris, Vassilios: *Erfassung des Austausches von Oberflächen- und Grundwasser in horizontalebenen Grundwassermodellen*, 1986, ISBN 3-921694-62-0

63 Herr, Michael: *Grundlagen der hydraulischen Sanierung verunreinigter Porengrundwasserleiter*, 1987, ISBN 3-921694-63-9

64 Marx, Walter: *Berechnung von Temperatur und Spannung in Massenbeton infolge Hydratation*, 1987, ISBN 3-921694-64-7

65 Koschitzky, Hans-Peter: *Dimensionierungskonzept für Sohlbelüfter in Schußrinnen zur Vermeidung von Kavitationsschäden*, 1987, ISBN 3-921694-65-5

66 Kobus, Helmut (Hrsg.): *Modellierung des großräumigen Wärme- und Schadstofftransports im Grundwasser*, Tätigkeitsbericht 1986/87 (DFG-Forschergruppe an den Universitäten Hohenheim, Karlsruhe und Stuttgart) 1987, ISBN 3-921694-66-3

67 Söll, Thomas: *Berechnungsverfahren zur Abschätzung anthropogener Temperaturanomalien im Grundwasser*, 1988, ISBN 3-921694-67-1

68 Dittrich, Andreas; Westrich, Bernd: *Bodenseeufererosion, Bestandsaufnahme und Bewertung*, 1988, ISBN 3-921694-68-X, vergriffen

69 Huwe, Bernd; van der Ploeg, Rienk R.: *Modelle zur Simulation des Stickstoffhaushaltes von Standorten mit unterschiedlicher landwirtschaftlicher Nutzung*, 1988, ISBN 3-921694-69-8, vergriffen

70 Stephan, Karl: *Integration elliptischer Funktionen*, 1988, ISBN 3-921694-70-1

71 Kobus, Helmut; Zilliox, Lothaire (Hrsg.): *Nitratbelastung des Grundwassers, Auswirkungen der Landwirtschaft auf die Grundwasser- und Rohwasserbeschaffenheit und Maßnahmen zum Schutz des Grundwassers*. Vorträge des deutsch-französischen Kolloquiums am 6. Oktober 1988, Universitäten Stuttgart und Louis Pasteur Strasbourg (Vorträge in deutsch oder französisch, Kurzfassungen zweisprachig), 1988, ISBN 3-921694-71-X

72 Soyeaux, Renald: *Unterströmung von Stauanlagen auf klüftigem Untergrund unter Berücksichtigung laminarer und turbulenter Fließzustände*,1991, ISBN 3-921694-72-8

73 Kohane, Roberto: *Berechnungsmethoden für Hochwasserabfluß in Fließgewässern mit überströmten Vorländern*, 1991, ISBN 3-921694-73-6

74 Hassinger, Reinhard: *Beitrag zur Hydraulik und Bemessung von Blocksteinrampen in flexibler Bauweise*, 1991, ISBN 3-921694-74-4, vergriffen

75 Schäfer, Gerhard: *Einfluß von Schichtenstrukturen und lokalen Einlagerungen auf die Längsdispersion in Porengrundwasserleitern*, 1991, ISBN 3-921694-75-2

76 Giesecke, Jürgen: *Vorträge, Wasserwirtschaft in stark besiedelten Regionen; Umweltforschung mit Schwerpunkt Wasserwirtschaft*, 1991, ISBN 3-921694-76-0

77 Huwe, Bernd: *Deterministische und stochastische Ansätze zur Modellierung des Stickstoffhaushalts landwirtschaftlich genutzter Flächen auf unterschiedlichem Skalenniveau*, 1992, ISBN 3-921694-77-9, vergriffen

78 Rommel, Michael: *Verwendung von Kluftdaten zur realitätsnahen Generierung von Kluftnetzen mit anschließender laminar-turbulenter Strömungsberechnung*, 1993, ISBN 3-92 1694-78-7

79 Marschall, Paul: *Die Ermittlung lokaler Stofffrachten im Grundwasser mit Hilfe von Einbohrloch-Meßverfahren*, 1993, ISBN 3-921694-79-5, vergriffen

80 Ptak, Thomas: *Stofftransport in heterogenen Porenaquiferen: Felduntersuchungen und stochastische Modellierung*, 1993, ISBN 3-921694-80-9, vergriffen

81 Haakh, Frieder: *Transientes Strömungsverhalten in Wirbelkammern,* 1993, ISBN 3-921694-81-7

82 Kobus, Helmut; Cirpka, Olaf; Barczewski, Baldur; Koschitzky, Hans-Peter: *Versucheinrichtung zur Grundwasser und Altlastensanierung VEGAS, Konzeption und Programmrahmen*, 1993, ISBN 3-921694-82-5

83 Zang, Weidong: *Optimaler Echtzeit-Betrieb eines Speichers mit aktueller Abflußregenerierung*, 1994, ISBN 3-921694-83-3, vergriffen

84 Franke, Hans-Jörg: *Stochastische Modellierung eines flächenhaften Stoffeintrages und Transports in Grundwasser am Beispiel der Pflanzenschutzmittelproblematik*, 1995, ISBN 3-921694-84-1

85 Lang, Ulrich: *Simulation regionaler Strömungs- und Transportvorgänge in Karstaquiferen mit Hilfe des Doppelkontinuum-Ansatzes: Methodenentwicklung und Parameteridentifikation*, 1995, ISBN 3-921694-85-X, vergriffen

86 Helmig, Rainer: *Einführung in die Numerischen Methoden der Hydromechanik*, 1996, ISBN 3-921694-86-8, vergriffen

87 Cirpka, Olaf: *CONTRACT: A Numerical Tool for Contaminant Transport and Chemical Transformations - Theory and Program Documentation* -, 1996, ISBN 3-921694-87-6

88 Haberlandt, Uwe: *Stochastische Synthese und Regionalisierung des Niederschlages für Schmutzfrachtberechnungen*, 1996, ISBN 3-921694-88-4

89 Croisé, Jean: *Extraktion von flüchtigen Chemikalien aus natürlichen Lockergesteinen mittels erzwungener Luftströmung*, 1996, ISBN 3-921694-89-2, vergriffen

90 Jorde, Klaus: *Ökologisch begründete, dynamische Mindestwasserregelungen bei Ausleitungskraftwerken*, 1997, ISBN 3-921694-90-6, vergriffen

91 Helmig, Rainer: *Gekoppelte Strömungs- und Transportprozesse im Untergrund - Ein Beitrag zur Hydrosystemmodellierung*-, 1998, ISBN 3-921694-91-4, vergriffen

92 Emmert, Martin: *Numerische Modellierung nichtisothermer Gas-Wasser Systeme in porösen Medien,* 1997, ISBN 3-921694-92-2

93 Kern, Ulrich: *Transport von Schweb- und Schadstoffen in staugeregelten Fließgewässern am Beispiel des Neckars*, 1997, ISBN 3-921694-93-0, vergriffen

94 Förster, Georg: *Druckstoßdämpfung durch große Luftblasen in Hochpunkten von Rohrleitungen 1997*, ISBN 3-921694-94-9

95 Cirpka, Olaf: *Numerische Methoden zur Simulation des reaktiven Mehrkomponententransports im Grundwasser*, 1997, ISBN 3-921694-95-7, vergriffen

96 Färber, Arne: *Wärmetransport in der ungesättigten Bodenzone: Entwicklung einer thermischen In-situ-Sanierungstechnologie*, 1997, ISBN 3-921694-96-5

97 Betz, Christoph: *Wasserdampfdestillation von Schadstoffen im porösen Medium: Entwicklung einer thermischen In-situ-Sanierungstechnologie*, 1998, ISBN 3-921694-97-3

98 Xu, Yichun: *Numerical Modeling of Suspended Sediment Transport in Rivers*, 1998, ISBN 3-921694-98-1, vergriffen

99 Wüst, Wolfgang: *Geochemische Untersuchungen zur Sanierung CKW-kontaminierter Aquifere mit Fe(0)-Reaktionswänden,* 2000, ISBN 3-933761-02-2

100 Sheta, Hussam: *Simulation von Mehrphasenvorgängen in porösen Medien unter Einbeziehung von Hysterese-Effekten*, 2000, ISBN 3-933761-03-4

101 Ayros, Edwin: *Regionalisierung extremer Abflüsse auf der Grundlage statistischer Verfahren*, 2000, ISBN 3-933761-04-2, vergriffen

102 Huber, Ralf: *Compositional Multiphase Flow and Transport in Heterogeneous Porous Media*, 2000, ISBN 3-933761-05-0

103 Braun, Christopherus: *Ein Upscaling-Verfahren für Mehrphasenströmungen in porösen Medien*, 2000, ISBN 3-933761-06-9

104 Hofmann, Bernd: *Entwicklung eines rechnergestützten Managementsystems zur Beurteilung von Grundwasserschadensfällen*, 2000, ISBN 3-933761-07-7

105 Class, Holger: *Theorie und numerische Modellierung nichtisothermer Mehrphasenprozesse in NAPL-kontaminierten porösen Medien,* 2001, ISBN 3-933761-08-5

106 Schmidt, Reinhard: *Wasserdampf- und Heißluftinjektion zur thermischen Sanierung kontaminierter Standorte*, 2001, ISBN 3-933761-09-3

107 Josef, Reinhold:, *Schadstoffextraktion mit hydraulischen Sanierungsverfahren unter Anwendung von grenzflächenaktiven Stoffen*, 2001, ISBN 3-933761-10-7

108 Schneider, Matthias: *Habitat- und Abflussmodellierung für Fließgewässer mit unscharfen Berechnungsansätzen*, 2001, ISBN 3-933761-11-5

109 Rathgeb, Andreas: *Hydrodynamische Bemessungsgrundlagen für Lockerdeckwerke an überströmbaren Erddämmen*, 2001, ISBN 3-933761-12-3

110 Lang, Stefan: *Parallele numerische Simulation instätionärer Probleme mit adaptiven Methoden auf unstrukturierten Gittern*, 2001, ISBN 3-933761-13-1

111 Appt, Jochen; Stumpp Simone: *Die Bodensee-Messkampagne 2001, IWS/CWR Lake Constance Measurement Program 2001*, 2002, ISBN 3-933761-14-X

112 Heimerl, Stephan: *Systematische Beurteilung von Wasserkraftprojekten,* 2002, ISBN 3-933761-15-8

113 Iqbal, Amin: *On the Management and Salinity Control of Drip Irrigation,* 2002, ISBN 3-933761-16-6

114 Silberhorn-Hemminger, Annette: *Modellierung von Kluftaquifersystemen: Geostatistische Analyse und deterministisch-stochastische Kluftgenerierung,* 2002, ISBN 3-933761-17-4

115 Winkler, Angela: *Prozesse des Wärme- und Stofftransports bei der In-situ-Sanierung mit festen Wärmequellen,* 2003, ISBN 3-933761-18-2

116 Marx, Walter: *Wasserkraft, Bewässerung, Umwelt - Planungs- und Bewertungsschwerpunkte der Wasserbewirtschaftung,* 2003, ISBN 3-933761-19-0

117 Hinkelmann, Reinhard: *Efficient Numerical Methods and Information-Processing Techniques in Environment Water,* 2003, ISBN 3-933761-20-4

118 Samaniego-Eguiguren, Luis Eduardo: *Hydrological Consequences of Land Use / Land Cover and Climatic Changes in Mesoscale Catchments*, 2003, ISBN 3-933761-21-2

119 Neunhäuserer, Lina: *Diskretisierungsansätze zur Modellierung von Strömungs- und Transportprozessen in geklüftet-porösen Medien*, 2003, ISBN 3-933761-22-0

120 Paul, Maren: *Simulation of Two-Phase Flow in Heterogeneous Poros Media with Adaptive Methods*, 2003, ISBN 3-933761-23-9

121 Ehret, Uwe: *Rainfall and Flood Nowcasting in Small Catchments using Weather Radar*, 2003, ISBN 3-933761-24-7

122 Haag, Ingo: *Der Sauerstoffhaushalt staugeregelter Flüsse am Beispiel des Neckars - Analysen, Experimente, Simulationen -,* 2003, ISBN 3-933761-25-5

123 Appt, Jochen: *Analysis of Basin-Scale Internal Waves in Upper Lake Constance,* 2003, ISBN 3-933761-26-3

124 Hrsg.: Schrenk, Volker; Batereau, Katrin; Barczewski, Baldur; Weber, Karolin und Koschitzky, Hans-Peter: *Symposium Ressource Fläche und VEGAS - Statuskolloquium 2003, 30. September und 1. Oktober 2003,* 2003, ISBN 3-933761-27-1

125 Omar Khalil Ouda: *Optimisation of Agricultural Water Use: A Decision Support System for the Gaza Strip,* 2003, ISBN 3-933761-28-0

126 Batereau, Katrin: *Sensorbasierte Bodenluftmessung zur Vor-Ort-Erkundung von Schadensherden im Untergrund*, 2004, ISBN 3-933761-29-8

127 Witt, Oliver: *Erosionsstabilität von Gewässersedimenten mit Auswirkung auf den Stofftransport bei Hochwasser am Beispiel ausgewählter Stauhaltungen des Oberrheins*, 2004, ISBN 3-933761-30-1

128 Jakobs, Hartmut: *Simulation nicht-isothermer Gas-Wasser-Prozesse in komplexen Kluft-Matrix-Systemen*, 2004, ISBN 3-933761-31-X

129 Li, Chen-Chien: *Deterministisch-stochastisches Berechnungskonzept zur Beurteilung der Auswirkungen erosiver Hochwasserereignisse in Flussstauhaltungen,* 2004, ISBN 3-933761-32-8

130 Reichenberger, Volker; Helmig, Rainer; Jakobs, Hartmut; Bastian, Peter; Niessner, Jennifer: *Complex Gas-Water Processes in Discrete Fracture-Matrix Systems: Upscaling, Mass-Conservative Discretization and Efficient Multilevel Solution,* 2004, ISBN 3-933761-33-6

131 Hrsg.: Barczewski, Baldur; Koschitzky, Hans-Peter; Weber, Karolin; Wege, Ralf: *VEGAS - Statuskolloquium 2004,* Tagungsband zur Veranstaltung am 05. Oktober 2004 an der Universität Stuttgart, Campus Stuttgart-Vaihingen, 2004, ISBN 3-933761-34-4

132 Asie, Kemal Jabir: *Finite Volume Models for Multiphase Multicomponent Flow through Porous Media*. 2005, ISBN 3-933761-35-2

133 Jacoub, George: *Development of a 2-D Numerical Module for Particulate Contaminant Transport in Flood Retention Reservoirs and Impounded Rivers,* 2004, ISBN 3-933761-36-0

134 Nowak, Wolfgang: *Geostatistical Methods for the Identification of Flow and Transport Parameters in the Subsurface,* 2005, ISBN 3-933761-37-9

135 Süß, Mia: *Analysis of the influence of structures and boundaries on flow and transport processes in fractured porous media*, 2005, ISBN 3-933761-38-7

136 Jose, Surabhin Chackiath: *Experimental Investigations on Longitudinal Dispersive Mixing in Heterogeneous Aquifers,* 2005, ISBN: 3-933761-39-5

137 Filiz, Fulya: *Linking Large-Scale Meteorological Conditions to Floods in Mesoscale Catchments,* 2005, ISBN 3-933761-40-9

138 Qin, Minghao: *Wirklichkeitsnahe und recheneffiziente Ermittlung von Temperatur und Spannungen bei großen RCC-Staumauern*, 2005, ISBN 3-933761-41-7

139 Kobayashi, Kenichiro: *Optimization Methods for Multiphase Systems in the Subsurface - Application to Methane Migration in Coal Mining Areas*, 2005, ISBN 3-933761-42-5

140 Rahman, Md. Arifur: *Experimental Investigations on Transverse Dispersive Mixing in Heterogeneous Porous Media,* 2005, ISBN 3-933761-43-3

141 Schrenk, Volker: *Ökobilanzen zur Bewertung von Altlastensanierungsmaßnahmen,* 2005, ISBN 3-933761-44-1

142 Hundecha, Hirpa Yeshewatesfa: *Regionalization of Parameters of a Conceptual Rainfall-Runoff Model*, 2005, ISBN: 3-933761-45-X

143 Wege, Ralf: *Untersuchungs- und Überwachungsmethoden für die Beurteilung natürlicher Selbstreinigungsprozesse im Grundwasser,* 2005, ISBN 3-933761-46-8

144 Breiting, Thomas: *Techniken und Methoden der Hydroinformatik - Modellierung von komplexen Hydrosystemen im Untergrund*, 2006, 3-933761-47-6

145 Hrsg.: Braun, Jürgen; Koschitzky, Hans-Peter; Müller, Martin: *Ressource Untergrund: 10 Jahre VEGAS: Forschung und Technologieentwicklung zum Schutz von Grundwasser und Boden,* Tagungsband zur Veranstaltung am 28. und 29. September 2005 an der Universität Stuttgart, Campus Stuttgart-Vaihingen, 2005, ISBN 3-933761-48-4

146 Rojanschi, Vlad: *Abflusskonzentration in mesoskaligen Einzugsgebieten unter Berücksichtigung des Sickerraumes,* 2006, ISBN 3-933761-49-2

147 Winkler, Nina Simone: *Optimierung der Steuerung von Hochwasserrückhaltebecken-systemen,* 2006, ISBN 3-933761-50-6

148 Wolf, Jens: *Räumlich differenzierte Modellierung der Grundwasserströmung alluvialer Aquifere für mesoskalige Einzugsgebiete*, 2006, ISBN: 3-933761-51-4

149 Kohler, Beate: *Externe Effekte der Laufwasserkraftnutzung*, 2006, ISBN 3-933761-52-2

150 Hrsg.: Braun, Jürgen; Koschitzky, Hans-Peter; Stuhrmann, Matthias: *VEGAS-Statuskolloquium 2006,* Tagungsband zur Veranstaltung am 28. September 2006 an der Universität Stuttgart, Campus Stuttgart-Vaihingen, 2006, ISBN 3-933761-53-0

151 Niessner, Jennifer: *Multi-Scale Modeling of Multi-Phase - Multi-Component Processes in Heterogeneous Porous Media*, 2006, ISBN 3-933761-54-9

152 Fischer, Markus: *Beanspruchung eingeerdeter Rohrleitungen infolge Austrocknung bindiger Böden,* 2006, ISBN 3-933761-55-7

153 Schneck, Alexander: *Optimierung der Grundwasserbewirtschaftung unter Berücksichtigung der Belange der Wasserversorgung, der Landwirtschaft und des Naturschutzes*, 2006, ISBN 3-933761-56-5

154 Das, Tapash: *The Impact of Spatial Variability of Precipitation on the Predictive Uncertainty of Hydrological Models,* 2006, ISBN 3-933761-57-3

155 Bielinski, Andreas: *Numerical Simulation of CO_2 sequestration in geological formations*, 2007, ISBN 3-933761-58-1

156 Mödinger, Jens: *Entwicklung eines Bewertungs- und Entscheidungsunterstützungssystems für eine nachhaltige regionale Grundwasserbewirtschaftung*, 2006, ISBN 3-933761-60-3

157 Manthey, Sabine: *Two-phase flow processes with dynamic effects in porous media - parameter estimation and simulation,* 2007, ISBN 3-933761-61-1

158 Pozos Estrada, Oscar: *Investigation on the Effects of Entrained Air in Pipelines,* 2007, ISBN 3-933761-62-X

159 Ochs, Steffen Oliver: *Steam injection into saturated porous media – process analysis including experimental and numerical investigations*, 2007, ISBN 3-933761-63-8

160 Marx, Andreas: *Einsatz gekoppelter Modelle und Wetterradar zur Abschätzung von Niederschlagsintensitäten und zur Abflussvorhersage, 2007,* ISBN 3-933761-64-6

161 Hartmann, Gabriele Maria: *Investigation of Evapotranspiration Concepts in Hydrological Modelling for Climate Change Impact Assessment*, 2007, ISBN 3-933761-65-4

162 Kebede Gurmessa, Tesfaye: *Numerical Investigation on Flow and Transport Characteristics to Improve Long-Term Simulation of Reservoir Sedimentation*, 2007, ISBN 3-933761-66-2

163 Trifković, Aleksandar: *Multi-objective and Risk-based Modelling Methodology for Planning, Design and Operation of Water Supply Systems*, 2007, ISBN 3-933761-67-0

164 Götzinger, Jens: *Distributed Conceptual Hydrological Modelling - Simulation of Climate, Land Use Change Impact and Uncertainty Analysis*, 2007, ISBN 3-933761-68-9

165 Hrsg.: Braun, Jürgen; Koschitzky, Hans-Peter; Stuhrmann, Matthias: *VEGAS – Kolloquium 2007,* Tagungsband zur Veranstaltung am 26. September 2007 an der Universität Stuttgart, Campus Stuttgart-Vaihingen, 2007, ISBN 3-933761-69-7

166 Freeman, Beau: *Modernization Criteria Assessment for Water Resources Planning; Klamath Irrigation Project, U.S.*, 2008, ISBN 3-933761-70-0

167 Dreher, Thomas: *Selektive Sedimentation von Feinstschwebstoffen in Wechselwirkung mit wandnahen turbulenten Strömungsbedingungen*, 2008, ISBN 3-933761-71-9

168 Yang, Wei: *Discrete-Continuous Downscaling Model for Generating Daily Precipitation Time Series*, 2008, ISBN 3-933761-72-7

169 Kopecki, Ianina: *Calculational Approach to FST-Hemispheres for Multiparametrical Benthos Habitat Modelling,* 2008*,* ISBN 3-933761-73-5

170 Brommundt, Jürgen: *Stochastische Generierung räumlich zusammenhängender Niederschlagszeitreihen*, 2008, ISBN 3-933761-74-3

171 Papafotiou, *Alexandros: Numerical Investigations of the Role of Hysteresis in Heterogeneous Two-Phase Flow Systems*, 2008, ISBN 3-933761-75-1

172 He, Yi: *Application of a Non-Parametric Classification Scheme to Catchment Hydrology*, 2008, ISBN 978-3-933761-76-7

173 Wagner, Sven: *Water Balance in a Poorly Gauged Basin in West Africa Using Atmospheric Modelling and Remote Sensing Information*, 2008, ISBN 978-3-933761-77-4

174 Hrsg.: Braun, Jürgen; Koschitzky, Hans-Peter; Stuhrmann, Matthias; Schrenk, Volker: *VEGAS-Kolloquium 2008 Ressource Fläche III*, Tagungsband zur Veranstaltung am 01. Oktober 2008 an der Universität Stuttgart, Campus Stuttgart-Vaihingen, 2008, ISBN 978-3-933761-78-1

175 Patil, Sachin: *Regionalization of an Event Based Nash Cascade Model for Flood Predictions in Ungauged Basins*, 2008, ISBN 978-3-933761-79-8

176 Assteerawatt, Anongnart: *Flow and Transport Modelling of Fractured Aquifers based on a Geostatistical Approach,* 2008, ISBN 978-3-933761-80-4

177 Karnahl, Joachim Alexander: *2D numerische Modellierung von multifraktionalem Schwebstoff- und Schadstofftransport in Flüssen*, 2008, ISBN 978-3-933761-81-1

178 Hiester, Uwe: *Technologieentwicklung zur In-situ-Sanierung der ungesättigten Bodenzone mit festen Wärmequellen,* 2009, ISBN 978-3-933761-82-8

179 Laux, Patrick: *Statistical Modeling of Precipitation for Agricultural Planning in the Volta Basin of West Africa,* 2009, ISBN 978-3-933761-83-5

180 Ehsan, Saqib: *Evaluation of Life Safety Risks Related to Severe Flooding,* 2009, ISBN 978-3-933761-84-2

181 Prohaska, Sandra: *Development and Application of a 1D Multi-Strip Fine Sediment Transport Model for Regulated Rivers,* 2009, ISBN 978-3-933761-85-9

182 Kopp, Andreas: *Evaluation of CO_2 Injection Processes in Geological Formations for Site Screening,* 2009, ISBN 978-3-933761-86-6

Die Mitteilungshefte ab der Nr. 134 (Jg. 2005) stehen als pdf-Datei über die Homepage des Instituts: www.iws.uni-stuttgart.de zur Verfügung.